

EXPERIMENTS ON FREE SHEAR LAYER TRANSITION

by

RICHARD WALTER MIKSAD

B.S.M.E. Bradley University (1963)
M.S. Cornell University (1964)

SUBMITTED IN PARTIAL FULFILLMENT
OF THE REQUIREMENTS FOR THE
DEGREE OF DOCTOR OF SCIENCE

at the

MASSACHUSETTS INSTITUTE OF TECHNOLOGY

May 14, 1970

SIGNATURE OF AUTHOR: _____
Department of Meteorology, May 14, 1970

CERTIFIED BY: _____
Thesis Supervisor

ACCEPTED BY: _____
Chairman, Departmental Committee on
Lindgren Graduate Students

WITHDRAWN
OCT 4 1971
LIBRARIES
MIT LIBRARIES

EXPERIMENTS ON FREE SHEAR LAYER TRANSITION

Richard Walter Miksad

Submitted to the Department of Meteorology, on May 14, 1970
in partial fulfilment of the requirements for the degree of Doctor
of Science.

ABSTRACT

An experimental investigation of the transition of a free shear layer from laminar flow to turbulent breakdown is described. Primary emphasis is placed on the non-linear stages of transition. Both the natural and forced transitions are studied. Hot-wire anemometry techniques are used, and controlled perturbations are introduced by sound excitation techniques.

The effects of single and dual frequency excitation are investigated. Experimental interest is centered on the transition triggered by single frequency excitation. The forced transitions are found to differ from the natural transition. For example, the downstream evolution of the mean flow is dependent on the scale of the particular forced disturbances present.

The overall transition from laminar instability to turbulent breakdown covered about five wavelengths of distance. The transition encompassed six distinct regions of activity. Harmonic and sub-harmonic modes were present in both the single and dual frequency experiments. However, the latter was dominated by non-linear combination modes, and was sensitive to the relative phases of the two excitation signals.

The results show that linear stability theory does predict the basic instability. The fundamental mode grows as predicted by linear theory even after non-linear modes are generated. Downstream variations predicted by a quasi-uniform model did not appear. However, quasi-uniform calculations do give an indication of which fundamental modes are favored by local mean conditions for non-linear activity.

Fundamental mode growth rates deviated from exponential values

at amplitudes of order 4%. No specific critical amplitude was found for the onset of non-linear activity. In general, non-linear modes appeared before the disturbance amplitude reached 2%.

The importance of non-linear modes in organizing the transition was demonstrated. The existence of critical Reynolds numbers for the onset of new finite amplitude instabilities, and bands of Reynolds numbers over which finite amplitude equilibration occurred, gave added reinforcement to Landau's original concept of successive instabilities. The final breakdown to turbulence was found to involve a three-dimensional longitudinal vortex structure. The influence of the discrete upstream spectra was found to persist into the turbulent breakdown regions. Weak secondary instabilities were also observed.

A critical disturbance amplitude of 2% was found for the breakdown of linear superposition theory in the mixed frequency experiments. Non-linear mode competition was observed between the growing fundamentals, and the added presence of combination modes caused a redistribution of disturbance energy and not an increase. The phase of the excitation field was found to a factor in the preferred generation of combination modes.

Thesis supervisor : Erik Mollo-Christensen
Title : Professor of Meteorology

TABLE OF CONTENTS

| | |
|---|----|
| ABSTRACT | 2 |
| FOREWORD | 8 |
| SUMMARY | 12 |
| I. INTRODUCTION | 24 |
| II. EXPERIMENTAL APPARATUS AND INSTRUMENTATION | 44 |
| II.1 Wind Tunnel | 44 |
| II.2 Test Section | 50 |
| II.3 Hot-Wire Monometer System | 54 |
| II.4 Auxiliary Instrumentation | 56 |
| III. EXPERIMENTAL MEASUREMENTS AND TECHNIQUES | 60 |
| III.1 Data Collection | 60 |
| III.2 Coordinate Reference Frame | 62 |
| III.3 Initial Conditions | 63 |
| III.4 Generation of Controlled Disturbances | 64 |
| III.5 Mean Flow Measurements | 66 |
| (a) Mean velocity profiles | 66 |
| (b) Dynamic pressure profiles | 68 |
| (c) Static pressure distribution | 69 |
| III.6 Fluctuating Flow Measurements | 70 |
| (a) Frequency spectra | 70 |
| (b) Spatial distribution of spectral amplitudes | 71 |
| (c) Spatial distribution of spectral phase angles | 72 |
| (d) Frequency response transfer function | 73 |
| III.7 Smoke Pictures | 75 |

| | | |
|------|--|-----|
| IV. | NATURAL VERSUS FORCED TRANSITION | 77 |
| IV.1 | Characteristic Scales and Reference Parameters | 80 |
| IV.2 | Qualitative Aspects of the Natural Transition | 84 |
| | (a) Natural input spectra | 85 |
| | (b) Mean entrance conditions | 86 |
| | (c) Test section velocity field | 87 |
| | (d) Natural transition spectra | 89 |
| IV.3 | Qualitative Aspects of the Forced Transition | 93 |
| | (a) Intensity of speaker induced disturbances | 95 |
| | (b) Speaker location and the generation of a symmetric or asymmetric forcing field | 97 |
| | (c) Amplitude response curves of the forced transition | 97 |
| | (d) Role of excitation field phase symmetry | 99 |
| V. | FORCED TRANSITION (QUANTITATIVE RESULTS) | 109 |
| V.1 | Initial Growth Rates and Most Unstable Forced Mode | 111 |
| V.2 | Downstream Evolution of the Forced Transition Spectrum | 113 |
| | (a) ω_{fs1} and ω_{II} forced transitions | 114 |
| | (b) $(\omega_A + \omega_B)$ mixed mode transitions | 115 |
| | (c) Summary of observed interactions with asymmetric field forcing | 116 |
| | (d) Transition spectra with symmetric field forcing | 117 |
| V.3 | Downstream Evolution of the Unstable Disturbance Field | 120 |
| | (a) Evolution of the r.m.s. velocity field | 120 |
| | (b) Maximum values of the r.m.s. velocities | 122 |

| | | |
|-------------|--|-----|
| (c) | Evolution of the vertically integrated disturbance energy | 122 |
| V.4 | Downstream Evolution of the U(x,y) Mean Velocity Fields | 124 |
| V.5 | Further Details of the ω_{II} Transition | 125 |
| (a) | Additional details of the ω_{II} transition mean flow | 126 |
| (b) | Downstream phase variations (i.e. wavelength measurements) | 126 |
| (c) | Vertical phase variations | 129 |
| (d) | Three-dimensional structure | 131 |
| VI. | DISCUSSION OF THE TRANSITION PROCESS | 190 |
| VI.1 | Single Mode Forced Transition | 191 |
| Region I: | Linear Transition | 191 |
| (a) | Stability of the initial wake profile | 192 |
| (b) | Successive downstream quasi-uniform calculations | 197 |
| (c) | Comparison of experiment to the quasi-uniform model | 200 |
| (d) | The effect of local scale conditions on non-linear activity | 203 |
| (e) | Effect of test section boundaries | 208 |
| Region II: | Weakly Non-Linear Behavior | 209 |
| Region III: | Finite Amplitude Equilibrium | 215 |
| (a) | Equilibration amplitudes | 216 |
| (b) | Calculation of the second Landau coefficient | 218 |
| (c) | Influence of the critical layer | 221 |
| (d) | Dependence of equilibration on local Reynolds number | 222 |
| (e) | Physical significance of the second Landau coefficient | 226 |
| (f) | Simplified model of the equilibration process | 228 |
| Region IV: | Second Region of Sub-Harmonic Growth | 229 |
| (a) | Sub-harmonic generation by finite | 229 |

| | |
|---|-----|
| amplitude interactions | |
| (b) Vortex model for sub and 3/2 harmonic generation | 233 |
| Region V: Onset of Three-Dimensional Behavior and the Termination of Fundamental Mode Equilibration | 240 |
| Region VI: Final Breakdown | 243 |
| VI.2 Mixed Mode Transition | 244 |
| (a) Validity of the linear superposi- tion principle | 245 |
| (b) Role of non-linear combination modes | 246 |
| (c) Mode suppression due to non-linear effects | 248 |
| (d) Role of disturbance phase in shear layer breakdown | 250 |
| APPENDIX | 253 |
| A-1 Linear Trapezoidal Stability Model | 253 |
| A-2 Sound Generation of Vorticity Pertur- bations | 256 |
| A-3 Wavelength, Phase Speed and Phase Angle | 261 |
| A-4 Hot-Wire Calibration | 267 |
| BIBLIOGRAPHY | 270 |

FOREWORD

"It is the instability of the atmosphere which makes it less predictable than tides and eclipses. It is instability which renders empirical methods of prediction only moderately successful."

Edward N. Lorenz (1969)

Although studies of oceanic and atmospheric motions have attained a reasonable degree of achievement, our knowledge of the governing physical laws is still incomplete and a proper modeling of nature is presently beyond reach. Scaling arguments and linearization schemes have been used with great success to isolate given oceanic or atmospheric phenomena from the wealth of other motions which occur simultaneously in nature. However, all scales of motion communicate with each other to one extent or another, and energy is transferred both up and down the spectrum of disturbance motions. For example, the small scale surface mixing of atmospheric momentum provides the source of energy for the global wind driven circulation, and baroclinic mechanisms can generate internal waves which may interact and exchange energy with surface gravity waves or inertial oscillations. Unstable small scale atmospheric disturbances often derive their energy from the mean state and in growing in intensity they in turn interact with and alter the global or hemispheric weather patterns.

As in all fluid systems, the mechanics of interaction are determined by the Reynolds stress terms which express the exchange of momen-

tum by disturbance motions. Scaling techniques essentially eliminate the non-linear influence of other motions by breaking the Reynolds stress into two parts. One part expresses an average influence of other scales of motion and is commonly referred to as an eddy stress, or turbulent viscosity. The eddy stress term tacitly acknowledges the presence of phenomena of other scales without being specific about their structure or influence. The remaining portion of the Reynolds stress term is contained within the scaled equations themselves and expresses the interaction of the considered scale of motion with itself or with other motions of a similar scale. For lack of a better name they can be referred to as the "scaled Reynolds stress" terms.

It has been common practice to parameterize the non-linear exchange mechanisms represented by the eddy stress. However, we do not understand the physical laws governing these terms and it is not apparent that they may be appropriately accounted for by using average values to express their effect. To further increase the analytic tractability of scaled models, the scaled non-linear terms are usually eliminated by linearization schemes.

The inherent non-linear behavior of fluid systems make the use of such linearization schemes an often implausible artifice when modeling the real world, and a lack of knowledge regarding non-linear exchange mechanisms make parameterization of the eddy stress term very difficult and suspect in most cases.

An obvious two-fold problem exists in the atmospheric sciences. Not only can present theories not adequately assess the importance and

influence of other scales of motion on a given phenomenon but the characteristics of the non-linear behavior of the desired scale of motion cannot be satisfactorily taken account of.

Efforts have been made to measure at least some of the in situ non-linear behavior and interactions of oceanic and atmospheric motions, (i.e. Starr, 1968). However, the complexity and diversity of scales involved make a prior knowledge of the more general physical aspects of non-linear behavior essential for any meaningful interpretation. Although recent advances in non-linear mechanics have established many promising theories, a dearth of confirming experimental information exists. Theoretical models are by necessity abstract and idealized. In situ confirmations are hard to achieve since controlled conditions approximating those required by theory cannot be established. A logical alternative is to conduct controlled laboratory experiments which can isolate specific non-linear phenomena. Ideally these experiments should be initially concerned with the study of non-linear behavior in general, and not with generating spurious and misunderstood Reynolds stress data. One cannot hope to understand Reynolds stresses until the fundamental non-linear mechanisms which form the building blocks for this term are understood.

The majority of oceanic and atmospheric motions are not what are normally referred to as boundary layer flows. The boundaries do act as constraints for certain scales of motion, but the dynamic processes involved are often those characteristic of free shear layers, and this is a logical area for laboratory investigation.

Although baroclinic effects are extremely important in nature, it is felt that a reasonable understanding of the barotropic problem must be achieved before the complicating influence of stratification can be effectively studied. However, in order to be able to meaningfully investigate the effects of stratification once the homogeneous problem is at least partially understood, the experiment conducted here was designed so that a thermal stratification could be impressed on the free shear layer at a later date. In this way, future work on non-linear baroclinic effects can be made relative to a base problem established in the same apparatus. Variations due to stratification can then be hopefully identified with certainty. All too often, seemingly significant variations in the work of two researchers can be belatedly traced to spurious differences in the experimental apparatus used, and not to phenomenological differences in the problems being studied.

The purpose of this thesis has been to conduct an experimental study of the non-linear behavior of a homogeneous free shear layer from the viewpoint of stability theory and transition. Emphasis has been placed on determining the important non-linear mechanisms which are involved in the transition of an initially laminar free shear layer to a quasi-turbulent state. Direct measurement of Reynolds stresses or baroclinic effects will be left for future work. It is hoped that the information obtained will provide direction for further advances in the area of non-linear interactions, the influence of which is so germane to all fluid systems.

Experiments on Free Shear Layer Transition
SUMMARY

The stability and transition of a laminar, two-dimensional free shear layer is studied. The basic flow is formed by the merging of two laminar boundary layers in the wake of a separating splitter plate. The resulting mean flow is an asymmetric shear layer with two inflexion points and hence vorticity peaks. The upper layer vorticity is an order of magnitude greater than that of the bottom layer and dominates the transition.

Natural Transition:

The natural transition was excited by a clean quasi-white noise disturbance field. It was dominated in the initial stages of transition by a broad band of amplifying disturbances, which were centered about the maximally unstable mode predicted by a linear parallel flow stability model. This model was based on the mean velocity at the initial point of instability. However, the non-linear modes which appeared downstream were not multiples of the initially most unstable fundamental mode. They were found to be multiples of the fundamental mode which best fit the local mean conditions at the downstream location where the disturbances reached finite amplitudes. In general, the natural transition revealed the following basic points:

(i) Even though the scale of the mean flow changes with downstream distance, the dominant fundamental mode over the entire linear zone of transition was that mode preferred by the mean velocity field at the initial point of instability.

(ii) The non-linear mechanisms involved in the transition are sensitive to the local scale of the mean flow at the point where finite amplitude effects become important.

(iii) The non-linear modes may not receive their energy directly from the fundamental mode. The fundamental may act as a catalyst which allows the non-linear modes to obtain energy directly from the mean flow.

(iv) The natural transition involves amplifying disturbances which have randomly shifting phases.

Natural vs. Forced Transitions

The most dramatic aspect of the forced transitions is the strong organizing effect that a slight but continuous disturbance input can exert on the transition. Instead of a broad band of intermittently amplifying disturbances, only that frequency component picked out for controlled excitation is observed to amplify. In several respects the organizing effect of the excitation field prevented the forced transition from being an accurate representation of the natural behavior of the flow. This was particularly true for the evolution of the mean flow and the non-linear stages of transition.

Experiments with symmetric and asymmetric excitation fields established the asymmetric phase structure of the naturally unstable fundamental modes. Higher frequency non-linear modes were basically symmetric in phase across the center line. Similar experiments demonstrated that a symmetric forcing field could stimulate the direct excitation of non-linear modes.

Forced Transitions

Three basic controlled experiments were conducted. Primary emphasis was placed on the transition of ω_{II} the most unstable mode of the initial laminar velocity field. The transition of ω_{fs1} an initially less unstable mode which was preferred by downstream mean conditions for non-linear activity was also studied. Finally, some experiments concerning the simultaneous transition of two excited

fundamental modes were also conducted. The three forced transitions will be respectively referred to as the ω_{II} , ω_{fs1} , and $(\omega_A + \omega_B)$ transitions.

Specific data were taken to evaluate the applicability of existing theories concerning the linear and non-linear aspects of the transition process. In general the forced transitions were found to exhibit a distinct sequence of instabilities which were similar in character to the sequential instability concept of Landau (1944). Critical Reynolds numbers for the onset of new instabilities were found, and bands of Reynolds numbers were found over which disturbance equilibration occurred. The behavior of the ω_{II} transition was of greatest interest since the initial conditions for its existence were well understood and verified by theoretical calculations. Also, ω_{II} underwent the most distinct sequence of transition processes, many of which were describable by existing theories, and provided a classic example of an evolving flow undergoing a "slow transition".

The mixed frequency experiments presented many interesting questions. Its results were used to investigate the bounds on the superposition principle of linear theory, the phenomena of non-linear mode suppression, the role of combination modes, and the effects of disturbance phase on the transition. Its results will be summarized last.

Single Mode Forced Transitions

The experimental results showed that the ω_{II} transition en-

compassed six basic stages of behavior: a linear region (i.e. obey disturbances linear theory), a weakly non-linear region, a region of finite amplitude equilibration, a region of finite amplitude triggered instabilities, a region of three-dimensional distortions, and a final stage of turbulent breakdown. These stages will be discussed in order of downstream appearance for the ω_{II} transition. In general the ω_{fsl} transition exhibited a similar transition sequence.

Region I: Linear Transition ($0.0 \rightarrow 0.9 \lambda_{II}$)

The linear region of transition extended for about one wavelength of downstream distance. The amplified instabilities originated in the laminar wake and not in the splitter plate boundary layers. Parallel flow linear stability theory correctly predicted the basic instability of the initial laminar flow. Even though the scale of the mean flow changed with downstream distance, the dominant fundamental mode over the entire linear region of transition was that mode preferred by the mean velocity field at the initial point of instability. Downstream changes in growth rate, etc., as predicted by a series of quasi-uniform stability calculations were not observed. It was concluded that the initial profile at which instability first occurs acts as an energy centering device for later downstream stations. The centering of energy at the frequency of the most unstable upstream mode acts to suppress any subtle changes in disturbance characteristics that might be introduced by downstream scale variations.

Cross-stream measurements of the disturbance phase and mean velo-

city profiles showed that both the initial disturbances and the mean flow were strongly two-dimensional.

Measurements also showed that the small geometry of the test section led to the stabilization of long wave modes below $\alpha_r = 0.175$. This result was in reasonable agreement with a model proposed by Howard (1964).

Region II : Weak Non-Linear Behavior ($0.9 \rightarrow 1.8 \lambda_{II}$)

The generation of non-linear modes characterized this second region of transition. Even after non-linear modes appeared the fundamental mode continued to grow at its initial exponential rate. The generated harmonic and sub-harmonic modes grew exponentially and often at rates which exceeded that of the fundamental.

The first non-linear modes appeared within one wavelength of downstream distance. The amplitude of the ω_{II} fundamental mode was of order 2% at this point. Second harmonics appeared first, while sub and 3/2-harmonics were generated when the fundamental mode reached a slightly larger amplitude of order 4%. Third harmonics and higher modes appeared last.

In general it was found that lower frequency, larger scale modes such as ω_{fs1} could generate strong non-linear activity while at much smaller amplitudes than ω_{II} . As verified by quasi-uniform calculations the explanation involved the fact that the larger scale of ω_{fs1} fit in better with the local downstream scale of the mean shear. Since

the Reynolds stress term governs transfer energy from the mean flow to the disturbances it is clear that both the scale and amplitude of the fundamental modes, which interact with the mean flow, must be considered when defining a limit on linear behavior.

The sub and 3/2 harmonic modes were extremely intermittent in this region and were of very small magnitude. These two facts may explain why other investigators have not noticed as early an appearance of sub-harmonic activity as this investigator did. The mechanisms responsible for the sub-harmonic generation are not clear. However, a heuristic model indicated that a weak parametric resonance effect may be sufficient to trigger the sub-harmonic mode and cause it to grow at the observed rates.

Region III : Finite Amplitude Equilibration ($1.8 \rightarrow 2.5 \lambda_{II}$)

Towards the end of region II all modes, including the fundamental, were observed to deviate from their exponential growths and equilibrate into finite amplitude oscillations. The equilibration reflected the influence of non-linear bounds on disturbance energy growth. The equilibration occurred at about two downstream wavelengths, and the amplitude of the ω_{II} fundamental mode was of order 12%. The equilibration amplitudes were found to vary inversely with frequency and the longer wave fundamental modes along with their non-linear harmonics grew to much larger amplitudes. The experimental data was used to calculate the second Landau coefficients for various fundamental modes.

The magnitude of the Landau coefficient, and hence the intensity of the amplitude-limiting non-linear effects, was found to increase with frequency. The Reynolds number range over which equilibration occurred was found to vary inversely with frequency.

The equilibration amplitude was also found to be dependent on the local Reynolds number and obeyed a relation similar to that put forward by Stuart (1958) for plane Poiseuille flow. A simple equilibration model based on this result showed that the generation of harmonics and sub-harmonics do not play an important role in the equilibration process. The important effect is the feedback mechanism established by the distortion of the mean flow by the fundamental mode Reynolds stress, and the subsequent distortion of the fundamental by the distorted mean flow.

Region IV : Second Region of Sub-Harmonic Growth ($2.5 \rightarrow 3.2 \lambda_{II}$)

In many respects this region has a very unique character. Even though the energy of the fundamental mode is still in equilibration, the sub-harmonic mode starts a second region of very strong growth. The existence of a distinct sub-harmonic equilibration zone between the two-regions of sub-harmonic growth indicate that the destabilizing mechanisms differ in the two regions. Sub-harmonic growth in region II was found to be due to either a parametric mechanism, or a weakly non-linear interaction. In contrast, the second onset of sub-harmonic growth is definitely due to finite amplitude effects.

The occurrence of a second region of sub-harmonic growth provided

a classic example of Landau's concept of successive instabilities. Here, a finite amplitude equilibrium oscillation due to an earlier instability apparently causes the flow to be unstable for a new type of disturbance; namely the sub-harmonic mode.

The overall features of the sub-harmonic growth were found to be in agreement with the theoretical results of Kelly (1967). A fundamental mode threshold amplitude of 10 to 12% was found necessary in both experiment and theory for the triggering of sub-harmonic growth. The experimentally measured growth rates were roughly half of that predicted by theory. This may be due to the dispersive and intermittent nature of the spatially growing sub-harmonic modes. Kelly's model considered a non-dispersive temporal flow.

A vortex model, which considered the mutual slipping of like signed vortex pairs was found to give a physical explanation of sub-harmonic generation. A series of smoke pictures taken in this region supported the physical importance of vortex slipping. An extension of this vortex model to a symmetric wake demonstrated how the symmetry of the mean velocity field inhibits vortex slipping and hence sub-harmonic formation.

Region V : Termination of Fundamental Mode Equilibration and the
Onset of Three-Dimensional Spanwise Behavior ($3.2 \rightarrow 4.75 \lambda_{II}$)

The termination of fundamental mode equilibration at $\sim 3.2 \lambda_{II}$ was accompanied by the onset of three-dimensional spanwise distortions. The distortions quickly organized into a longitudinal stream wise

vortex structure similar to that discussed by Benney & Lin (1960). The spanwise wavelength of the vortex structure decreased with growing three-dimensional activity.

Similar three-dimensional structures have been found in flows, such as viscous boundary layers and symmetric wakes, which do not exhibit sub-harmonic oscillations. Thus the presence of finite amplitude sub-harmonic oscillations do not appear to be directly responsible for the three-dimensional behavior of asymmetric shear layers. The existence of a three-dimensional instability seems to be a necessary precursor for the turbulent breakdown of shear layers in general.

Region VI : Final Turbulent Breakdown ($4.75 \rightarrow 5.75 \lambda_{II}$)

The final breakdown of the organized structure of the transition spectra is accompanied by a commensurate increase in three-dimensional activity. All synchronization with the upstream oscillations was lost and at about five downstream wavelengths the disturbance field abruptly filled out into a broad band spectrum. The presence of weak, intermittent secondary instabilities were observed at the upper edge of the shear layer, but no evidence of high frequency turbulent bursts was found.

Mixed Mode Transition

The mixed mode transition was triggered by simultaneously exciting the flow at two frequencies ω_A and ω_B where

$$\omega_A \sim \omega_{fs1}$$

$$\omega_B \sim \omega_{II}$$

The resulting transition was dominated by ω_B , the maximally unstable mode of the linear region.

Sum and difference combination modes which were generated by the interaction of ω_A and ω_B dominated the non-linear stages of transition. In general, the difference frequency mode underwent the same transition sequence as the sub-harmonic modes of the single frequency experiments did. The sum frequency mode paralleled the behavior of the harmonic modes of the single mode experiments. The presence of additional non-linear combination modes appeared to cause a redistribution of disturbance energy and not an increase. The preferred appearance of combination modes may have been due to the constant phase relation between the excitation signals.

The excited fundamental modes grew simultaneously as predicted by linear theory until ω_B reached an amplitude of 2%. This point marked the upper limit of the region in which the disturbances obeyed the linear superposition principle. The breakdown of superposition was reflecting in the appearance of non-linear combination modes and the suppression of the ω_A fundamental. Calculations based on the

work of Stuart (1962) showed that the two fundamental modes competed for energy. The non-linear coupling of the two modes explained the suppression of ω_A . The coupling effects of ω_B on ω_A was an order of magnitude greater than the non-linear effects of ω_A upon itself. This was verified by comparing the mixed transition results to the ω_{fs1} transition.

Arguments based on the presence of a few finite amplitude disturbances with random or intermittantly changing phases were shown to model many of the facets of shear layer breakdown.

CHAPTER I

INTRODUCTION

"Although the turbulent motion has been extensively discussed in the literature from different points of view, the very essence of this phenomenon is still lacking sufficient clearness. To the author's opinion, the problem may appear in a new light if the process of initiation of turbulence is examined thoroughly."

L. D. Landau (1944)

The formal problem of stability can be stated as follows: Given an equilibrium state of a physical system, a departure from equilibrium is considered, and the question is asked as to whether in the course of time, or space, the system will tend towards its initial equilibrium configuration. Departures from equilibrium are physically initiated by random noise or by the introduction of known controlled disturbances. Mathematically, a new composite flow field is postulated, consisting of the initial equilibrium state and a disturbance of given functional form. Requiring the disturbed equilibrium state to satisfy the non-linear Navier-Stokes equations and proper boundary conditions serves to formalize analytical stability theory. The relations governing the mean and disturbance fields are obtained in this manner. The non-linearity of the system manifests itself in the presence of terms representing the inertial transport of momentum by the disturbance motions (the so-called Reynolds stress). These terms couple the disturbances to each other, and to the mean flow field, so that an exchange of energy may be effected

between the mean flow and the disturbances of various scales. This mutual interplay leads to a continual modification, and distortion of the composite flow field, and a possible generation and subsequent interaction of new fluctuations. It is apparent that on a physical basis, the "mean part" of the flow field will not necessarily remain the original laminar flow, but must be so defined so that at all times it represents the suitably averaged mean field in the presence of disturbances. Only in the classic linear limit, where the influence of disturbance interaction is so small that it has a negligible effect on the mean flow, will the original laminar profile give a good approximation to the mean state. In fact, if the analytic system proves unstable, the initial profile cannot truly exist in the real world and must be considered as just a convenient possible idealized functioning of the system.

The earliest analytic efforts were extensions of the well established linear perturbation schemes of analytic mechanics. Since linear schemes cannot account for the distortion of the mean flow due to disturbance growth, the validity of such schemes are limited to very slight departures from equilibrium. They can only truly predict the possible "onset" of instability due to an infinitesimal disturbance and none of the subsequent effects. One need only observe a rising filament of smoke to be convinced that the start of sinuous motion is only the beginning of the overall process of transition to turbulence. If all real world disturbances were infinitesimal, linear theories could always give a prediction of the onset of instability. However, many physi-

cal systems which are predicted stable to infinitesimal disturbances, are physically known to be unstable. The answer often lies in considering the non-linear finite amplitude behavior of systems subject to large departures from equilibrium.

In general, linear stability theory can quite often predict the possible occurrence of instability for infinitesimal departures from equilibrium. It cannot establish the connection between laminar instability and turbulence, nor can it predict the response to intense deviations from equilibrium. The stability problem must necessarily be considered from its more general non-linear viewpoint in order to achieve an understanding of how, and under what conditions, turbulence, or a possibly new equilibrium state may occur from an initial laminar instability. Furthermore, a study of the non-linear aspects of transition can serve not only to expose the unique characteristics of a given system, but also to elucidate some of the more general characteristics of non-linear behavior of fluid systems in general. It is perhaps this last aspect of non-linear transition that is most appealing and fascinating to physical scientists who study the behavior of atmospheric and oceanic motions.

Previous Literature

Stability experiments are really initial value problems which involve the introduction and growth of arbitrary perturbations. However, due to analytic difficulties, relatively little theoretical attention has been expended on initial value stability analysis. Some general

results do exist for the temporal behavior of certain systems. Howard and Drazin (1965), and Betchov and Criminale (1967) have surveyed the existing work and reconcile the normal mode approach usually taken, with that of the continuous disturbance spectrum required in an initial value analysis or an arbitrary disturbance. Their results show that the asymptotic solutions of the linearized integral relations governing the disturbance growths have singular wave like solutions which grow exponentially with time. The singular solutions can be shown to be equivalent to those obtained from a normal mode analysis of the linearized, differential stability equations. The growth of the remaining frequencies in the continuous spectra are found to decay as $(1/t)$. Asymptotically, only the discrete normal mode spectra will lead to actual instability and the remainder of the continuous spectra need not be considered for a temporal stability analysis. Similar arguments can presumably be made for spatial initial value problems, but rigorous justifications do not seem to be present in the literature.

Historically the experimental work of Reynolds (1883) and the theoretical analysis of Helmholtz (1868) and Kelvin (1871) marked the beginnings of hydrodynamic stability theory. Reynolds' classic experiments verified the causal relation between mean flow conditions and the onset of disturbance growth. The extensive efforts of Rayleigh (1878-1919) served to formalize the inviscid linear stability theory, and with minor additions have served as the basis for most subsequent work. Rayleigh established the analytic equations governing inviscid stability and, in an extension of Kelvin's work on piece-wise continuous linear

profiles, analyzed the stability of various symmetric and asymmetric free shear layers. Rayleigh also proved that a necessary condition for inviscid temporal instability is that the velocity profile should have an inflexion point. Fjortoft (1950) proved the stronger necessary condition that the absolute value of the mean vorticity must have a maximum somewhere inside the flow domain. Tollmien (1935) showed that in certain cases such as for symmetric velocity profiles in channel or boundary layer flows, the existence of an inflexion point is also a sufficient condition for inviscid instability. Howard (1964) has further shown that each inflexion point will introduce a separate mode of instability.

Although Rayleigh attempted some discussion of viscous effects, it was Orr (1907) and Sommerfeld (1908) who established the stability equations for a viscous linear stability model. Taylor (1915) used Reynolds' stress arguments to note how the presence of frictionless boundaries prevented the transfer of momentum necessary to maintain an unstable disturbance when the mean velocity profile did not have an inflexion point. Taylor further concluded that viscosity may allow momentum to be diffused from the boundaries and hence have a destabilizing effect. This was later verified by Lin (1955). Tollmien (1929) and later Schlichting (1933) obtained solutions to the viscous Orr-Sommerfeld equations for a parallel boundary layer. Schubauer and Skramsted (1943) experimentally confirmed the existence of Tollmien-Schlichting waves, and Lin (1955) showed that the instability mechanism of shear layers which are not influenced by boundaries (i.e. free shear

layers) is an inviscid one caused by vorticity interactions. Viscosity was found to act only as a damping influence. Calculations by Lesson (1950) and Esch (1957) for viscous free boundary layers showed that for large Reynolds numbers, the viscous solutions asymptotically approached the inviscid values. Experiments by Sato (1960, 1961, 1966) on symmetric and axisymmetric jets and wakes verified these results.

Most linear models assume a parallel and non-developing flow, and consequently the expanding characteristics of strongly evolving flows such as jets and wakes cannot be accounted for. Lanchon and Eckhaus (1964) have used the growing boundary layer thickness to define new non-dimensional coordinates in an attempt to model quasi-parallel flows. The new coordinates implicitly contained the boundary layer growth and the stability equations were derived in terms of these coordinates. Viscous effects could be included for boundary layers. For free shear layers, only an inviscid approximation which neglected viscous stresses and terms in the expansion velocity normal to the layer was considered.

Recent attempts to model the developing aspects of the flow by "quasi-uniform" temporal models have met with limited success. Quasi-uniform models calculate the eigenvalues and growth rates at succeeding downstream stations by using actual measured mean profiles. The results are then compared to experiment. Mattingly (1968) used both spatial, and quasi-uniform temporal theories to model a measured symmetric wake. His results confirm Gaster's conviction that only for a very limited class of slowly expanding flows will a group velocity transformation model experimental results. In general, temporal, or quasi-uniform

temporal theories unsuccessfully model spatially evolving flows.

Most stability models have considered the temporal growth of a disturbance, rather than the spatial downstream growth normally present in physical shear layers. In order to compare temporal results with experimental data on spatially evolving flows the temporal growth rates have been normally transferred to a spatial frame by either a phase velocity transformation (Schubauer and Skramsted, 1947) for non-dispersive systems, or by a group velocity transformation for dispersive disturbances as suggested by Gaster (1962). However, Gaster (1965) has pointed out that group velocity transformations are valid only for weakly amplified disturbances and will not give meaningful results for rapidly expanding flows such as jets and wakes which exhibit strong disturbance amplifications.

Sato (1956, 1959) used sound perturbations from a speaker to artificially excite disturbances and verified the exponential spatial growth of disturbances in the initial stages of the free shear layer transition. His growth rates were only in order of magnitude agreement with temporal theory, and the phase reversals of the primary fluctuation did not agree at all with theory. Contrary to theory, the phase velocity was found to depend on frequency. Michalke (1964) used a hyperbolic tangent profile to make a refined continuous profile temporal analysis and found the same discrepancies. Freymuth (1966) made a careful experimental study of a free shear layer shed from the edge of a jet with a large ratio of diameter to boundary layer thickness. The results were again unsuccessfully compared to existing temporal

theories and Freymuth concluded that only a spatial stability analysis could explain the initial stability of expanding flows. Michalke (1965) made a numerical analysis of a hyperbolic tangent profile using a spatial stability theory and computed the eigenvalues and eigenfunctions for complex wave numbers and real frequencies. The results obtained closely modeled the experimental results of Freymuth and Sato. Both phase reversals and the dependence of phase velocity on frequency were correctly predicted.

The inadequacies and peculiarities of linear theories can be discussed ad infinitum. Clearly a disturbance, however well described by linear theory, cannot grow indefinitely. Nature will always act in one way or another to reduce the increasing stress. One is led to expect that non-linear mechanisms may impart at least a partial bound on the disturbance growth and provide a release valve by means of which the disturbance can shed some of its excess energy and so to speak "calm down".

The introduction of non-linear bounds on disturbance growth has been observed by many investigators. G. I. Taylor (1923) in studying the instability of a flow between two rotating coaxial cylinders noted that long before the onset of turbulence and well within the finite amplitude range, several successive equilibrium states appeared as the differential shear was increased. In each case, the disturbances had a definite finite amplitude and the mean flow exhibited a definite deviation from the original laminar state. Taylor concluded that the effect of the second order non-linear terms was to prevent the distur-

bances from increasing indefinitely in activity.

The concept of non-linear equilibrium states for growing finite amplitude disturbances was proposed by Landau (1944). In his classic paper, Landau postulated that transition processes in general may involve a passage through a series of equilibrium states as determined by the mean flow parameters. This concept of successive instabilities was summarized by Stuart (1958):

...The occurrence of instability in a flow may lead to the replacement of the original laminar flow by a new laminar flow, which consists of a mean flow with a superimposed finite disturbance. This flow may be expected to persist for a certain range of Reynolds number above the critical value and then to become unstable at some Reynolds number against a new (second) type of disturbance. A new equilibrium flow, consisting of a mean flow with two superimposed modes of disturbance, is then conceivable for a range of Reynolds numbers above the second critical value. As the Reynolds number is raised still further, additional modes of disturbance may appear successively until at sufficiently large Reynolds numbers the flow is so highly disturbed as to be considered turbulent.

Coles (1965) has coined the expressions, "transition by spectral evolution" and "catastrophic transition", to differentiate between what appears to be two distinct types of transition sequences. Taylor's experiments on rotating cylinders (where only the inner cylinder was rotated) seem to fall into the "spectral evolution" class. Here, as the differential shear is increased, an orderly sequence of finite amplitude, equilibrium flows appears. As the shear is increased further, small scale irregularities and turbulent structures gradually appear. In this evolutionary process, the disturbance spectrum changes gradually from a discrete form, to a continuous turbulent spectrum without the

appearance of intermittent behavior.

Evolving flows such as expanding viscous boundary layers seem to fall into the "catastrophic transition" class. Here, disturbances pass through different Reynolds number regimes as they proceed downstream. The flow evolves very quickly from laminar flow to turbulence without the establishment of any regions of finite amplitude equilibrium oscillations.

The basic difference between the two classes of transition is really determined by the residence time a disturbance can spend at a critical value of the flow parameter. In the Taylor flow, one can maintain the Taylor number at any desired value. In boundary layers a disturbance is convected without control from one value of critical Reynolds number to another. The time scale of residence is too small for the disturbance to equilibrate in any given Reynolds number band. Physically this means that the critical Reynolds numbers are spaced very close together, and the time scale necessary for equilibration is much larger than the residence time in any given band.

However, some evolving flows such as jets and wakes do exhibit distinct equilibration regions of finite amplitude oscillations. Here, there is a wider band of local Reynolds numbers in which equilibration can occur and the wake disturbances (in contrast to boundary layers which seem to have narrow equilibration bands) effectively have a longer residence time in which successful equilibration can occur. In effect then, wake disturbances pass more slowly through an equilibration zone, and the terms "fast" and "slow" transitions have been used to discriminate between these two types of evolving flows. A

"slow" transition flow is really a hybrid of Coles' two classes.

Non-linear disturbances are normally referred to as existing under "supercritical" conditions if they appear at values of the local Reynolds numbers which are above the critical value for linearized instability, and as existing under "subcritical" conditions if they occur at Reynolds numbers below the linear critical value. In the latter case the initiation of instability is due to finite amplitude effects, and although finite amplitude effects are important for some systems, only the appearance of non-linear effects under supercritical conditions will be considered here.

The development of non-linear stability theories for evolving flows has proved extremely difficult. Even slight changes in the value of the local Reynolds number or other mean parameters can produce strong non-linear effects which have to be taken into account. Most of the detailed theories have been developed for flows, such as plane Poiseuille flow, which exhibit a constant Reynolds number throughout the flow. Hence analytically, the Reynolds number can be varied at will in order to search for possible bands of Reynolds number in which equilibration can occur.

Stuart (1958) studied the non-linear behavior of plane Poiseuille flow, and the flow between two rotating cylinders. An integral energy balance technique was used which only took into account the mean flow distortion due to the Reynolds stress action of the fundamental and the consequent modification of the fundamental. The analysis produced an equation first discussed by Landau (1944) governing the asymptotic

finite amplitude of the fundamental disturbance oscillation. Stuart's results showed that the method gave good agreement for flows, such as that between two rotating cylinders, in which the overall or "integral" properties are important. For plane Poiseuille flow and others governed by the Orr-Sommerfeld relations, the precise spatial details of the flow are important and the integral method had less validity and gave poor quantitative agreement with experimental data.

In a later series of papers Stuart (1960a, b, 1962, 1967) often used the analytic convenience of constant Reynolds number Poiseuille flow to attack the problem from the viewpoint of the Orr-Sommerfeld equations directly. The effects of harmonic generation were taken into account and both subcritical and supercritical behavior were considered. The nature of the limiting non-linear solutions of the equations as the Reynolds number tended towards a critical value was considered. Again a Landau relation, of more complicated form was found and the results showed that equilibrium disturbances can exist under both subcritical and supercritical conditions near a particular critical value of Reynolds number.

Watson (1960) developed a valid perturbation expansion of the non-linear, time dependent Navier-Stokes equations and obtained some formal analytic solutions for Couette flow. The method of solution is similar to that put forward by Stuart and essentially uses an undetermined time dependent amplitude function in place of the exponential growth of linear theory. Expansions in terms of the undetermined amplitude parameter are made and give rise to a Landau type equation. Disturbances

were found to grow exponentially for small values of the amplitude parameter. However at larger amplitudes an asymptotic equilibrium oscillation of a definite finite amplitude, which was independent of the initial disturbance amplitude, was found. This, as discussed earlier, is very similar to the behavior of the laminar wake observed behind cylindrical bodies for certain Reynolds number ranges. Liu (1969) extended the work of Stuart and Watson and others to the case of spatially growing disturbances.

Research on the non-linear transition of evolving flows achieved a significant milestone with the experimental work of Klebanoff, Tidstrom and Sargent (1962). Most of our present knowledge of non-linear transitions is based on boundary layer studies; it proves useful to note the important elements of the boundary layer transition process. Using a vibrating ribbon to generate controlled two-dimensional and three-dimensional disturbances, the nature of boundary layer transition from laminar to turbulent flow was systematically explored. The sequence of events in the boundary layer transition can be summarized as follows. First, two-dimensional linear Tollmien-Schlichting waves developed in the boundary layer at points beyond the critical Reynolds number. The originally two-dimensional linear waves developed strong three-dimensional effects before any noticeable non-linear features were observed. As the wave grew in amplitude, non-linear longitudinal vortex structures evolved which then established local regions of high shear. Intermittent bursts of high frequency oscillations appeared at these regions and eventually formed series of randomly distributed turbulent spots

that eventually became numerous enough to develop a fully turbulent flow.

Klebanoff's work indicated that the three-dimensional effects play a very significant role in the breakdown process of boundary layers. Three-dimensional distortions appeared before noticeable non-linear effects were observed, and seemed to be a necessary prelude to the non-linear aspects of the transition. The importance of three-dimensional effects was further illustrated by the theoretical work of Benny (1961) and Lin and Benny (1964). They showed that the interaction of a two- and three-dimensional wave could produce a streamwise vortex flow as experimentally observed. Klebanoff concluded that strong development of the three-dimensional structure seemed to be an inherent property of the transition which was independent of any external or random excitation.

As pointed out earlier, however, in the context of "fast" and "slow" transitions experimental studies have shown that the character of the non-linear transition and breakdown stages of free shear layers are in many respects very different from that of viscous boundary layer flows.

In considering free shear layer transition one must, at least in principle, make a strong distinction between the behavior of symmetric and asymmetric mean flows. As will be discussed, a symmetric wake (or jet) tends to exhibit a more organized, non-linear behavior than an asymmetric flow (such as a single separated shear layer). However, many observed characteristics of free shear layer transition are found

to be common to both flows, and when studying a physical flow which is not purely symmetric or asymmetric, it often proves useful to identify those aspects of the transition which are characteristic of symmetric wakes on one hand, and asymmetric free shear layers on the other.

Also the difference between "high" and "low" speed modes of wake instability must be considered. In the high speed mode the instabilities are due to vorticity concentrations shed from the unstable boundary layers of the body forming the wake. These are often referred to as bluff body experiments. In the low speed mode, the instability arises in the wake of the body. The body only acts to establish the geometry of the shear layer formed in its wake.

This thesis is concerned with the low speed mode of transition and all following comments will pertain to free shear layers in which the instabilities arise in the initially laminar wake.

The experiments of Sato and Kuriki (1961) and Sato and Okada (1966) determined that the initial stages of transition in a symmetric wake were characterized by the presence of two-dimensional, antisymmetric disturbances which were described by linear theory. However the linear region was limited in extent, and non-linear effects were found to dominate the major portion of transition. The primary fluctuation observed in the linear region was also prominent in the non-linear zone, although its growth was found to progressively deviate from its initial exponential behavior as downstream transition proceeded. The appearance of higher ordered harmonics was characteristic of the non-linear zone.

and the flow was found to be highly two-dimensional. After the non-linear, two-dimensional behavior was established, three-dimensional non-linear distortions were noticeable, and the fluctuations gradually developed into turbulence without any noticeable sudden breakdowns or intermittent turbulent bursts.

Lin and Benny (1964) used various arguments based on the possible sources of secondary instabilities to explain the gradual breakdown of free shear layers in contrast to boundary layers. They concluded that the strong expanding nature of free shear layers may preclude any efficient organization of three-dimensional effects which might otherwise give rise to intensive regions of local shear and hence violent new instabilities.

Linear spatial amplification theories by Mattingly (1968) and others have confirmed Sato's results that antisymmetric u' disturbances are more unstable than symmetric disturbances for symmetric wakes. Ko, Kubota and Lees (1969) used the experimental data of Sato and Kuriki to conduct a theoretical non-linear spatial analysis for a symmetric wake. Using a two-dimensional antisymmetric disturbance and its harmonic many of the important experimentally observed features were explained, including the streamwise amplitude variation of the primary fluctuation. The analysis was basically an extension of Stuart's equilibrium state calculations.

Although a considerable body of theoretical knowledge exists on the linear stability of asymmetric flows, very little theoretical or experimental attention has been paid to the non-linear problem. Two basic

experimental approaches have been used to form separated asymmetric free shear layers. Sato (1956, 1959) used the flow behind a rearward facing step to form a single free shear layer, while others, such as Wille (1963) have used the outer edge of plane and circular jets with large core areas to study asymmetric free shear layers. For jets with a large ratio of core diameter to shear layer thickness, the outer edge shear layers can be considered as non-interacting free shear layers and not strongly coupled as in jet flows. For plane jets, the two edges are independent while the behavior is more complicated and circumferentially linked for circular jets with large cores. In at least one respect, namely the appearance of sub-harmonic oscillations, the non-linear behavior of asymmetric free shear layers differs quite dramatically from that of narrow symmetric wakes (or jets) and boundary layers.

Several investigators, Sato (1956, 1959), Wille (1963), Browand (1966), and Bradshaw (1966), have noted that the non-linear transition regions of asymmetric free shear layers characteristically exhibit sub-harmonic oscillations with a frequency one-half of the primary oscillation observed in the linear zone. In a series of experiments similar to those on symmetric wakes Sato observed that with the exception of the unexplained presence of sub-harmonic oscillations, the general characteristics of the transition process mirrored that of symmetric wakes. A laminar→linear→non-linear→three-dimensional→turbulent breakdown sequence was observed. As with symmetric wakes no pronounced presence of intermittent turbulent bursts were observed and the transition to turbulence was a gradual and irregular process. Wille (1963) observed sub-

harmonic oscillations in the transition of jet-formed free shear layers, and concluded they were due to the interaction and fusion of vortices which were observed to develop in the late stages of transition. Models which attempt to explain sub-harmonic development due to wake spreading do not seem to be valid since no sub-harmonic response is observed in similarly spreading symmetric wakes. Michalke (1965) used a linear theory to explain the formation of vortices in a hyperbolic tangent profile wake. Using the calculated linear results as a shape function for Stuart's non-linear theory, the vorticity distributions obtained were found to be similar to those experimentally observed by Wille. Abernathy and Kronauer (1962) surveyed the prior work on non-linear interaction of finite amplitude vortex sheets constructed from alternating points vortices. The results indicate a finite amplitude tendency for an infinite single vortex sheet to evolve into a row of concentrated vortices.

Browand (1966) investigated the non-linear transition region of a separated free shear layer and experimentally determined that the sub-harmonic appeared when the primary oscillation reached about 10% of the free stream velocity. The sub-harmonic growth was observed to be intermittent and the generation of third harmonics of the sub-harmonic was observed. Browand used a model of a single row of alternating vortices to qualitatively explain the generation of sub-harmonics. The model was similar to one proposed earlier by Sato.

Browand's data indicated the presence of a secondary instability in the final stages of transition. Limited measurements of three-dimensional effects indicated that the flow was strongly two-

dimensional in the initial region of sub-harmonic growth. However, these were not extended to cover the actual region where the transition to turbulence occurred.

Kelly (1967) studied the non-linear behavior of a parallel, temporally growing asymmetric free shear layer. His results indicate that secondary instabilities associated with the finite amplitude behavior of the primary fluctuation can act to selectively reinforce the sub-harmonic frequencies. Kelly's results also indicate that the 3/2-harmonic may be selectively reinforced by finite amplitude effects. Using a hyperbolic tangent profile, reasonable qualitative agreement with Browand's data was achieved.

Freythuth (1966) made a series of smoke pictures in a separated jet wake and correlated the results with hot-wire measurements. The results demonstrated that phase reversals occurred in the linear region long before smoke vortices appeared and concluded that the presence of vortices cannot necessarily be inferred from the existence of phase reversals in the velocity fluctuations. His pictures showed a tendency for "vortex slipping" in the non-linear zone and he further conjectured that this was the cause of the appearance of sub-harmonics.

Bradshaw (1966) has also observed the formation of sub-harmonics and based on flow-visualization pictures, concluded that the final breakdown to turbulence may occur via the longitudinal vortices predicted by Benny (1961). Benny's calculations, although discussed earlier in the context of boundary layer transition, were rather general and applicable to parallel flows in general. His actual calculations were in fact

for a hyperbolic tangent free shear layer, and it is highly likely that three-dimensional effects may play a more significant role in the transition process of free shear layers than previously considered. The lack of experimental results on the spanwise behavior of free shear layers render the subject an open area.

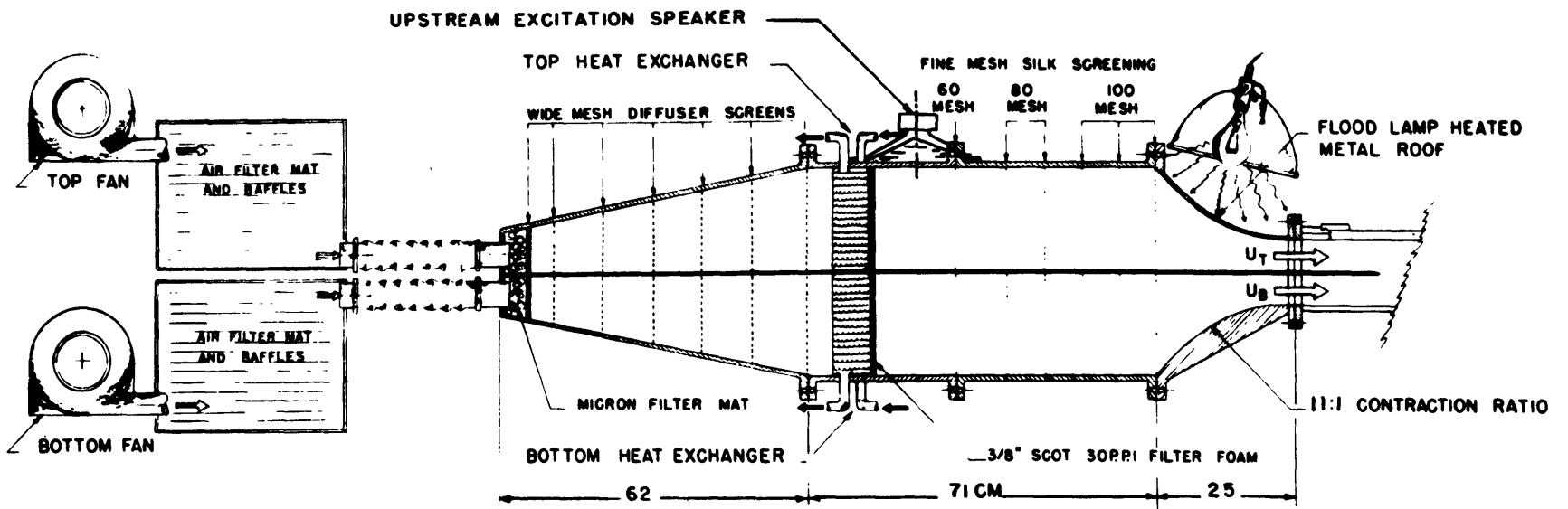
CHAPTER II

EXPERIMENTAL APPARATUS AND INSTRUMENTATION

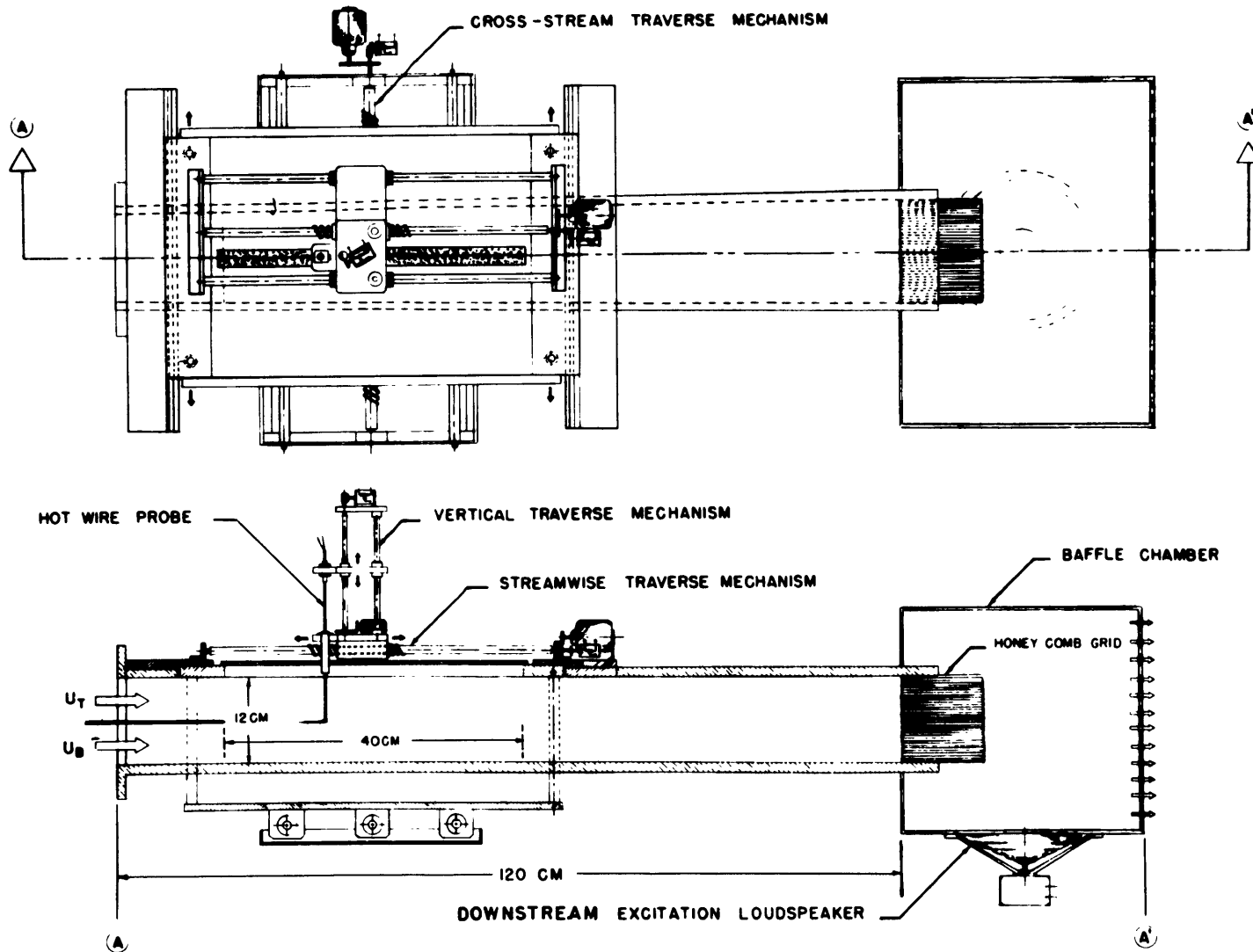
II.1 Wind Tunnel

The basic test apparatus is a low turbulence, open return wind tunnel of wood construction, with facilities for generating velocity and temperature gradients in the mean flow field. The main unit of the tunnel (shown in figures 2.1 to 2.4) is square in cross section, and is divided into two sections by means of a horizontal splitter plate assembly. The splitter plate runs the entire length of the tunnel, and extends to the test section entrance. Each section is effectively an independent wind tunnel, and consists of a variable speed centrifugal blower, a baffle chamber to dampen blower induced pressure oscillations, a wide angle diffuser, a setting chamber incorporating a variable temperature heat exchanger, and a 11:1 contraction zone to accelerate the flow into the test section. With this dual configuration the top and bottom streams can be maintained at different speeds and mean temperatures. A stratified, or non-stratified, free shear layer can be generated by merging the two streams in the wake of the dividing splitter plate.

The centrifugal blowers are two stage units with separate impellor units for motor cooling and blower outputs. The blower outputs were extremely stable; the operating r.p.m. varied by less than 1% over the course of an experiment. Short term variations in blower output were not noticeable; however, high frequency pressure fluctuations caused



LOW TURBULENCE, STRATIFIED FLOW, WIND TUNNEL
 FIGURE 2.1



TEST SECTION FOR STRATIFIED, FREE SHEAR LAYER EXPERIMENTS

FIGURE 2.2

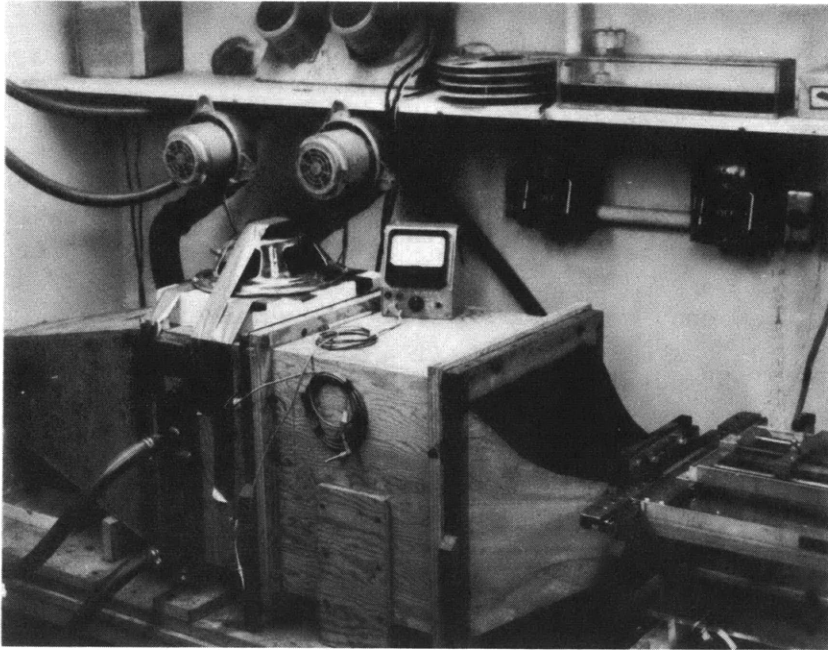


FIGURE 2.3

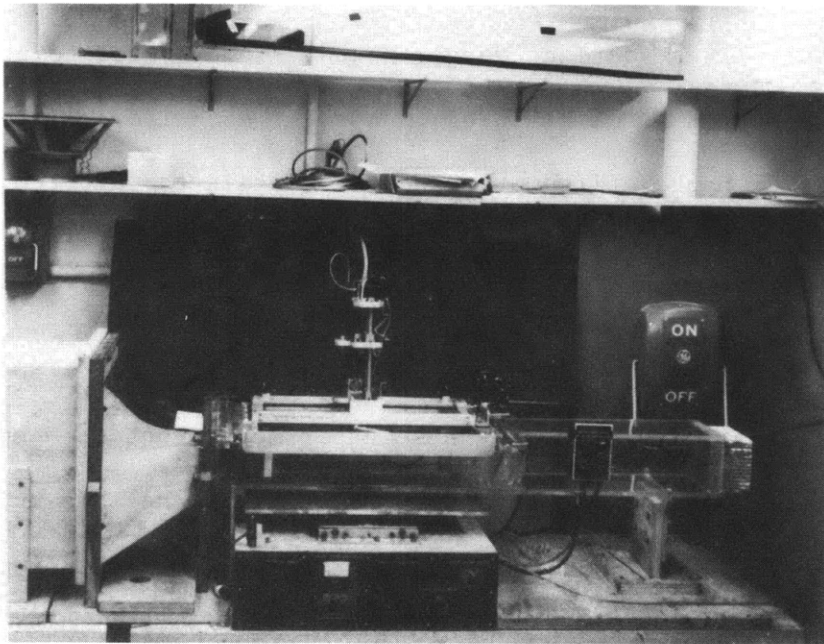


FIGURE 2.4

by irregularities in the eight bladed impellor were present. To alleviate this condition barrel shaped baffle chambers with a honeycomb and filter mat interior were used to isolate the blowers from the wind tunnel. Several small openings were used to couple the chambers with the ambient room. The impedance of the openings tended to damp any low frequency resonances within the chambers.

The baffle chambers were connected to the tunnel diffusers by 6.35 cm flexible hosing. A dust filtration unit, consisting of several interspaced layers of fine mesh silk screening and Faber H. P. micron filter matting, was placed at the diffuser entrances. These were then followed by a staggered series of coarse mesh wire screening which were used to smooth the expanding flow. The micron filters have a mean rated efficiency of 95% for 5 micron sized particles and larger. The effectiveness of the micron filters decreased with use, and on final data runs, the filter sections were renewed. This proved to be of considerable importance in maintaining consistent hot-wire calibrations.

The heat exchange units were used to maintain the air temperature of the incoming streams at a desired constant value. The units were constructed from standard automobile radiator cores adapted with the proper headers to fit the dimensions of the tunnel. The units were not used for differential heating in these experiments, but were employed to maintain the incoming top and bottom streams at the same uniform and constant reference temperature. The importance of minimizing mean temperature irregularities has been pointed out by Corrsin (1963). Slight density variations due to temperature non-uniformities are accelerated

at different rates in the contraction zone and can lead to noticeable velocity irregularities. As noted by Corrsin, a 1°C hot spot can lead to a 0.1% velocity perturbation in the test section. The exchangers also acted to thermally shield the hot-wire sensor from spurious temperature loadings due to variations in the ambient or blower operating temperatures. This helped to prevent changes in the probe calibration during the course of an experiment.

The heat exchangers produced one drawback, however. The radiator cores generated a mild large scale eddy structure in each stream. A 1.5 cm layer of Scot 30 PPI Fiter Foam, was placed behind the radiator cores to damp the generated eddies. This is a porous, reticulated, polyurethane foam, and proved very effective in reducing the intensity of the radiator eddy structure to acceptable levels.

To further reduce flow irregularities, a series of six silk damping screens were installed. The mesh size of the screens was cascaded from largest to smallest in the flow direction. The screens were placed at 400 mesh length intervals to allow sufficient decay time of the fine mixing eddy structure generated by the screens. An excitation loud speaker was mounted on the roof of the settling chamber at a position mid-way between the radiator core and the first silk screen. It is assumed that the screens acted to distribute the induced velocity fluctuations uniformly over the top stream.

The flow was accelerated from the settling chamber into the test section through an 11:1 contraction stage. This ratio is on the marginally low side of the values assumed necessary for low turbulence wind

tunnels. Values greater than 10:1, and preferably in the range of 20:1 are considered necessary to induce sufficient axial strain to reduce the relative turbulence level of the accelerated flow. Care must be taken to avoid boundary layer separation on the contraction walls. A carefully designed contraction zone from a previous wind tunnel was used. The effectiveness of this zone was demonstrated by the low turbulence levels and uniform profiles of the exiting flows. On leaving the contraction zone the exiting streams of air run parallel for 15 cm, and then merge in the wake of the splitter plate.

The tunnel configuration as described, gave a usable test section velocity range of 25 cm/sec to 500 cm/sec, and a differential temperature difference between the two streams of 10°C to 60°C. The free stream turbulence levels measured two centimeters before the splitter plate and were found to be 0.01% and 0.06% for the top and bottom streams, respectively, when operating at their final mean speeds of 200 cm/sec and 38 cm/sec. The turbulence levels varied slightly with time, but with judicious replacement of filters, the stated values could be closely adhered to.

II.2 Test Section

The test section in which the experiment was conducted is shown in figure 2.2. The walls, and non-structural elements of the tunnel are made from 1.60 cm plexiglass. The initial cross-sectional area at the splitter plate edge is 12 x 13.5 cm. The side walls of the test section expand in the downstream direction in order to eliminate

flow acceleration due to boundary layer growth on the walls. The final downstream exit cross section is 20 x 12 cm. The main feature of the test section is a multiple direction, traversing unit. This unit can be viewed as three traverses, each moveable in a different coordinate direction, mounted successively on top of one another.

The hot-wire, or pressure probes, are mounted on the traveler of the vertical traverse. It is guided in its vertical movements by an airfoil shaped collar. The probe-airfoil assembly (see figures 2.5 and 2.6) enters the test section through a 50 cm long slot, machined in the test section roof. Two strips of silicon impregnated rubber are mounted flush with roof and are butted together to meet mid-way over the slot, and seal the opening. The airfoil shape of the guide allows it to move longitudinally along the interface of the two rubber strips without breaking the seal.

The vertical traverse unit is then mounted on the traveler of the streamwise traverse as shown in figure 2.5. This allowed the probe to be moved along the downstream axis of the tunnel while being maintained at any desired height. The bed of the streamwise traverse formed the roof of the test section. This bed is made of 1.9 cm plexiglass and rests on two brass rails which allow the roof to slide in the cross-stream direction. The roof is coupled to the traveler of the cross-stream traverse by two vertical connecting rods. The cross-stream traveler incorporates two linear ball-bearing bushings, which ride on parallel steel shafts. The unit is advanced by a lead screw geared to a variable speed D.C. motor. The vertical and streamwise traverse units

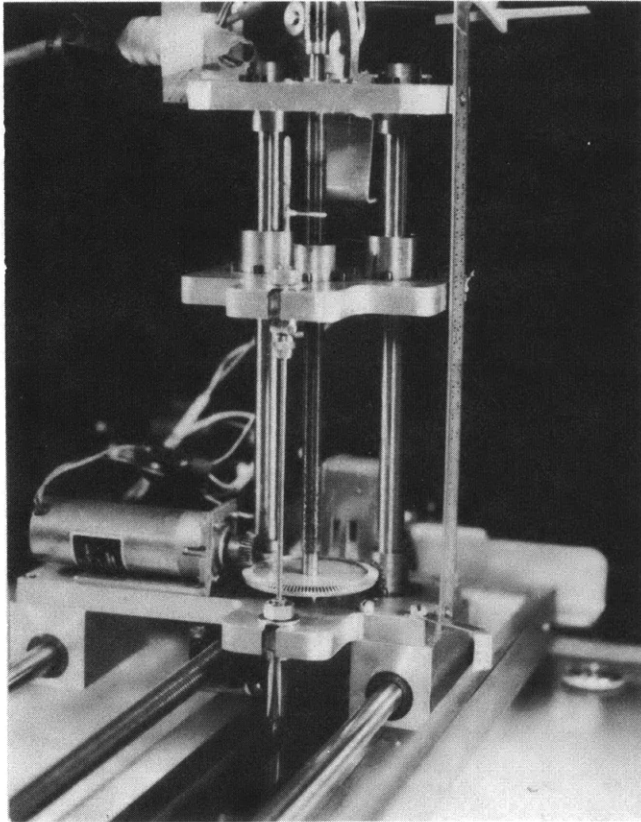


FIGURE 2.5

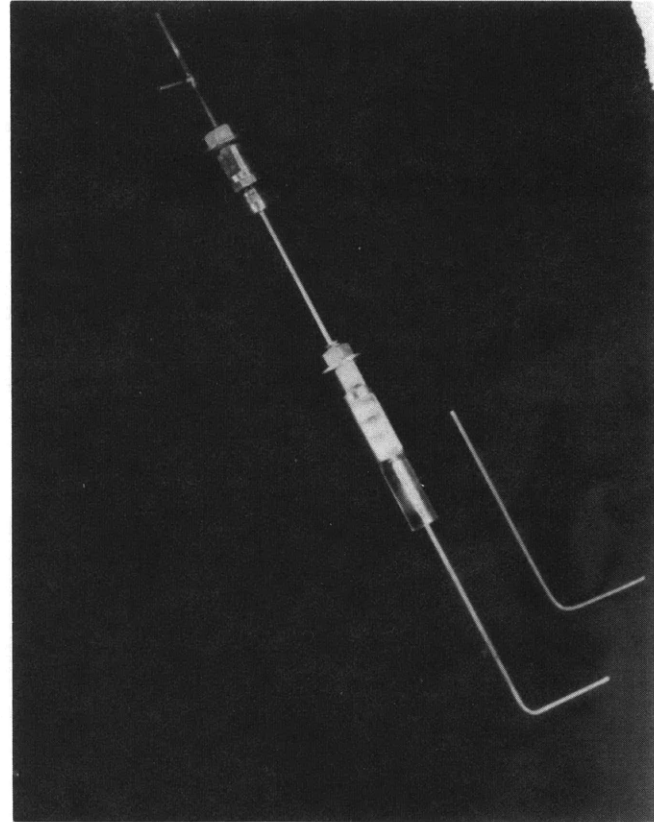


FIGURE 2.6

also utilize the same basic linear bushing, parallel shaft, motor-driven lead screw design. Each traverse can be operated independently of the others.

The sliding roof of the tunnel is structurally supported by the cross-stream traverse connecting rods, and is shimmed to clear the top edge of the side walls by 0.15 mm. The remaining air gap is sealed by attaching a strip of silicon-impregnated rubber to the upper side walls so that it rubs against the lower edge of the roof.

Each traverse is driven by a variable speed D.C. motor, powered by an accurate voltage control unit. The vertical traverse speed can be varied from 0.1 mm/sec to 2.0 mm/sec. The streamwise and cross-stream traverses could be driven from 0.2 mm/sec to 5.0 mm/sec. Vernier scale indicators were used to position the three traverses. The vertical traverse could be repositioned to ± 0.15 mm. The streamwise and cross-stream traverses could be positioned to ± 0.25 mm. Ten-turn precision potentiometers were geared to each traverse drive. The voltage output of these pots were converted to an F.M. signal by a multiple channel, voltage-controlled oscillator. In this way a very accurate, frequency modulated signal proportional to the spatial position of the probe, could be continuously monitored with a digital counter and was available in a convenient format for analog tape recording. The traverse geometry allowed the probe to explore the last 8 cm of the splitter plate in order to establish the initial flow conditions. The effective total length of the test section that could be explored was 30 cm downstream of the plate, and 8 cm upstream of the plate. Several configura-

tions were used for the trailing edge of the splitter plate. The most satisfactory design was a 15-cm length of 0.165 cm epoxy-fiberglass plate. This plate is commercially available with very precise tolerances on the surface finish and levelness. This type of epoxy sheet is almost impervious to nicks and scratches. The trailing edge was machined to form a slowly tapering edge.

The air exited the test section through a 10-cm length of aluminum honeycomb. The independence of the honeycomb acted to decouple the test section from the eddy structure generated by the exhaust air as it is dumped into the room. To further reduce this effect, and to also decouple the test section flow from ambient room effects, a final baffle chamber was installed. This chamber also served as a mounting platform for the rear excitation loud speaker.

II.3. Hot-Wire Monometer System and Sensors

A Shapiro-Edwards, Model 50, Constant Current Hot-Wire Monometer system (see figures 2.7) was used to measure the mean and fluctuating characteristics of the flow. The system was modified to include a differential, variable integration time, D.C. amplifier. When used in conjunction with the standard, A.C. amplifier supplied with the unit the instantaneous values of the mean and fluctuating flow could be monitored, and simultaneously recorded. This allowed use of the optimum dynamic ranges of the magnetic tape recorder, and associated analog instrumentation. This proved necessary since the ratio of fluctuation intensity to mean voltage level of the probe signal often approaches the

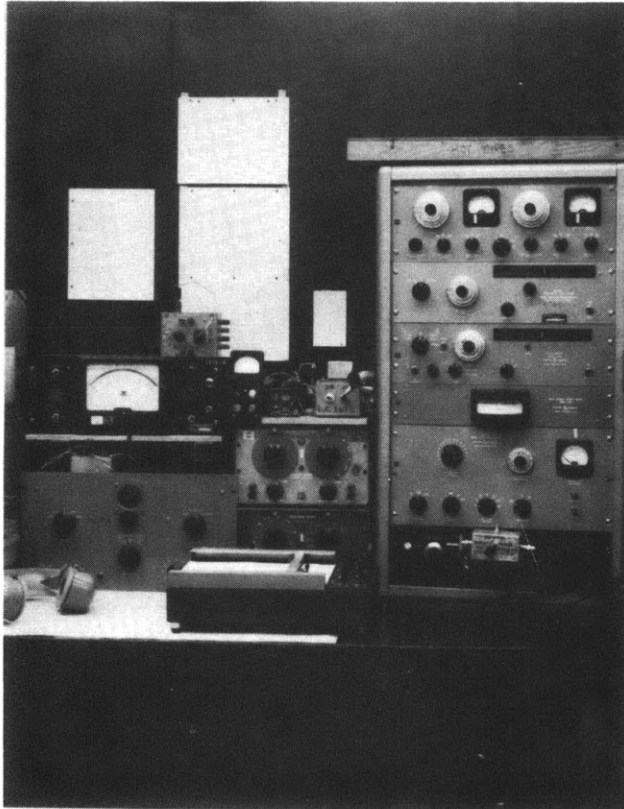


FIGURE 2.7

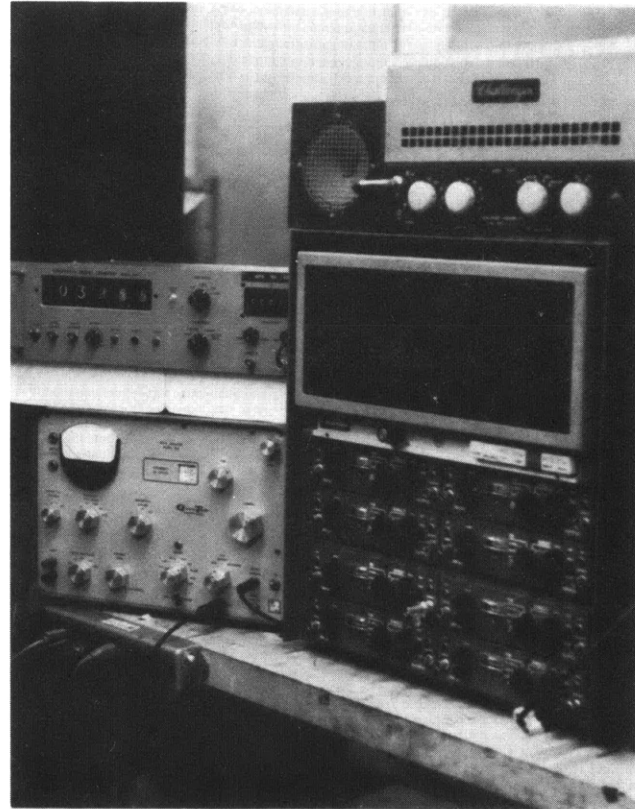


FIGURE 2.8

quoted dynamic signal-to-noise range of the tape recorder and other analog equipment. The remainder of the anemometer system contains a precision current control unit for providing current to the probe sensor; bridge and potentiometer circuits for measuring sensor resistance, current and voltage; a square wave generator and mean square percentage meter for calibration purposes; and a low noise, variable gain, A.C. amplifier with a useful frequency range of 1 Hz to 321 K Hz.

The probes are of the standard home-grown garden variety. Considerable attention has been paid by numerable authors [see Browand (1966) for example] to their construction, and various idiosyncracies. The probes used here were made from 3.05 mm stainless steel, hypodermic tubing. The sensor supports were standard # 13 sewing needles, and were soldered to wire leads connected to the current control unit. The actual sensor was a 1.5 mm length of 3.8 micron platinum wire, which was soldered across the needle tips to complete the circuit.

II.4 Auxiliary Instrumentation

Pressure Manometer System and Probes

An M.K.S. Baratron, Type 144, low pressure, capacitance manometer was used to measure the distribution of the mean static, and stagnation pressures. The linearity of the analog output was better than $\pm 0.1\%$. The sensor head has an overall differential pressure range of 0.0003 mm Hg to 3.000 mm Hg. The 0.10 and 0.03 Hg scales were used in these experiments.

An N.P.L. modified Prandtl design pitot-static probe was used for measuring dynamic pressure variations. The probe is shown in figure 26. For measurements of static pressure variations, a second reference static pressure probe was used in conjunction with the static side of the Prandtl probe. The pressure probe had the same general dimensions as the hot-wire probe and utilized the same airfoil guide system.

Magnetic Tape Recorder:

An 8-channel, Precision Instrument, Model PI-6200 magnetic tape recorder was used for recording of the experimental data. On final data runs, the traverse position frequency, mean probe voltage, fluctuating probe voltage, reference forcing frequency, and an audio identification of each run and test station were recorded on individual channels. The data was then played back as input into the normal analog reduction and data - processing equipment.

Spectrum Analyzer:

The main bulk of data analysis and reduction was performed with a Quan-Tech Model 304 Spectrum Analyzer. It has a frequency range of 1 Hz to 5000 Hz, and three selectable pass bands of 1 Hz, 10 Hz and 100 Hz at 3 db down. These are of the maximally flat 4 section Butterworth type with 24 db slopes. The input sensitivity is 30 V to 100 volts full scale in 10 db steps. The dynamic range is 70 db for Fourier Analyses. The unit has an internal, variable speed, sweep oscillator which permits automatic scanning of the entire or discrete portions of the frequency spectra. The averaging time, analysis bandwidth, sweep speed, sweep width and center frequency can be varied

for optimum results. D.C. analog outputs are available which are linearly proportional to the sweep voltage, instantaneous tuning frequency, and r.m.s. meter outputs of the filtered signal. In addition, the restored filtered input signal and B.F.O. tuning frequency of the heterodyne filter are available as sine wave outputs.

An extremely useful function of the analyzer was its ability to be used as an "externally tuned", narrow band-pass filter. When tuned with a stable external signal, virtually all center frequency drift can be eliminated. This makes the use of the 1 Hz pass-band possible for very accurate and maximally discriminating analysis.

The analyzer was used in conjunction with an x-y plotter to produce graphic plots of frequency spectra, modal amplitude envelopes, frequency response functions, and phase information.

Function Generator: A Hewlett-Packard Model 202A Low Frequency Function Generator was used to provide a stable forcing frequency to the excitation speakers. The forcing signal was used as the reference signal for phase and wavelength measurements.

Preset Counter: A Universal Preset Counter, Model 2019 was used for various monitoring purposes. A multiple input switching network was used so that the function generator forcing frequency, probe shedding frequency, spectrum analyzer tuning frequency, and traverse voltage oscillator outputs could be monitored as desired. The period count mode was used for greatest accuracy.

Phase Meter: A Technology Instrumentation Corporation Model 320-AB Phase Meter was used to measure the phase angle between the reference forcing signal, and the desired filtered fluctuating velocity signal.

A multistep frequency divider/multiplier unit was used in conjunction with the meter to compare the various harmonics with the standard reference forcing frequency.

Oscilloscope: A Tektronix Model 520A Dual-Beam Oscilloscope was used to monitor the instantaneous responses of the hot-wire and pressure probes.

Digital Voltmeter: A Hickok, Model DP100, Digital D.C. Voltmeter was used to monitor the various D.C. analog outputs.

Strobotac: A General Radio, Model 631-B Strobotac was employed to monitor the speeds of the two centrifugal blowers during the course of a run. It was also used as a synchronous light source for smoke pictures by clocking the strobotac with the function generator forcing frequency.

X-Y Plotter: A Mosley Model 703A X-Y Plotter was used as the last stage in the analog data reduction. The various spectrum analyzer analog outputs, traverse pot voltages, phase meter analog output, etc., were converted into graphical information with this unit.

X-Y Digitizer: A Wayne-George, Model T60/36/10, X-Y Digitizer was used in conjunction with an I.B.M. 526 Printing Summary Punch to convert graphic information, obtained from the x-y plotter, into a digital format for computer processing.

CHAPTER III
EXPERIMENTAL MEASUREMENTS AND TECHNIQUES

The stability characteristics of unstable flows are extremely sensitive to the initial state of the flow, and the presence of spurious disturbances. If measurements are made on a day to day basis, considerable care must be exercised in repeating the exact same initial states and operational conditions each time. This necessarily introduces an inherent uncertainty, as slight differences will always occur between runs no matter how much care is taken. To avoid this problem, each final experiment was run only once under established conditions and all necessary information was obtained at the same time. This approach eliminated any question of the relative validity of the measured variables.

III.1 Data Collection

The approach taken here was to use in-line data reduction for the preliminary experiments in order to establish the qualitative aspects of the transition. Once satisfied that the correct conditions existed, and armed with a general picture of the transition process, the experiment was instrumented so that all necessary information was simultaneously recorded on an 8 channel magnetic tape recorder. The recorder then served as a passive information storage interface in the normal in-line data reduction scheme as shown in figure 3.1. The presence of a storage interface will be implicitly assumed in the discussions that

follow. The only data not processed from tape recordings were the qualitative frequency spectra taken as preliminary information and the dynamic and static pressure distributions which were of necessity taken at a later date and processed directly.

The actual sequence of data taking in each experiment consisted of making a series of continuous vertical traverses at successive downstream stations spaced 0.5 cm apart on the tunnel centerline. During each traverse, the mean and fluctuating components of the probe voltage were recorded as continuous functions of the vertical coordinate. When searching for the presence of three-dimensional, spanwise effects, data was recorded as a function of the cross-stream coordinate, z , for various (x, y) stations. For each traverse, the data recorded and the variables obtained by later data processing are listed below.

| <u>Recorded Data</u> | <u>Processed Variable</u> |
|---------------------------------------|----------------------------|
| 1. V.C.O. Traverse Frequency $E(x_i)$ | Traverse Coordinate, x_i |
| 2. Audio Amplifier Forcing ω_f | ω_f |
| 3. Fluctuating Wire Voltage | $u'_{rms}(x_i, t)$ |
| 4. Mean Wire Voltage, $E(x_i)$ | $U(x_i)$ |
| 5. ω_{fs1} Reference Signal | ω_{fs1} |
| 6. ω_{II} Reference Signal | ω_{II} |
| 7. Audio Identification | Confidence |

Since the total probe signal is recorded, one traverse record contains all necessary information on the mean velocity and various spectral components of the fluctuation velocities at the given downstream

station. Each replay of the taped record corresponds to a physically repeated traverse, taken under exactly the same experimental conditions each time. The need for actual repeated traverses during an experiment is eliminated. Figure 3.1 shows the overall data processing scheme.

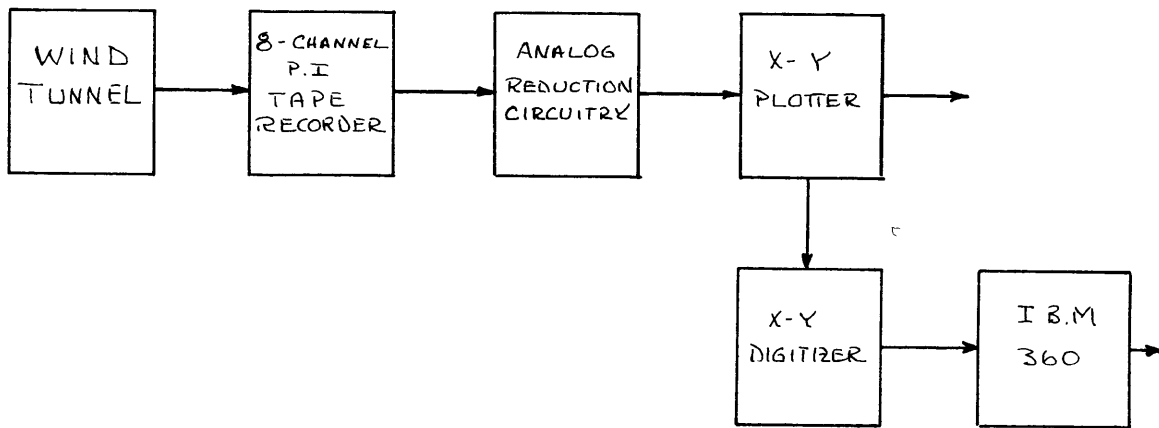


Figure 3.1: Overall Data Processing Scheme

III.2 Coordinate Reference Frame

A coordinate frame, shown in figure 3.2, with origin at the center of the splitter plate trailing edge was used for laboratory reference. The (0, 0, 0) position was established by visually aligning the probe tip with the surface of the plate. Half the measured plate thickness was then subtracted from this reading and taken as the y-axis zero. The x-axis zero was set by advancing the probe towards the plate edge and noting the position where no light could be seen between the probe tip and plate edge, when sighting along the edge in a bright light.

The z-axis zero was taken as the tunnel centerline. The useful (x, y, z) traverse space was: $(-5.00 < x < 25.00 \text{ cm}; -6.00 < y < 5.00 \text{ cm}; -6.00 < z < 6.00 \text{ cm})$.

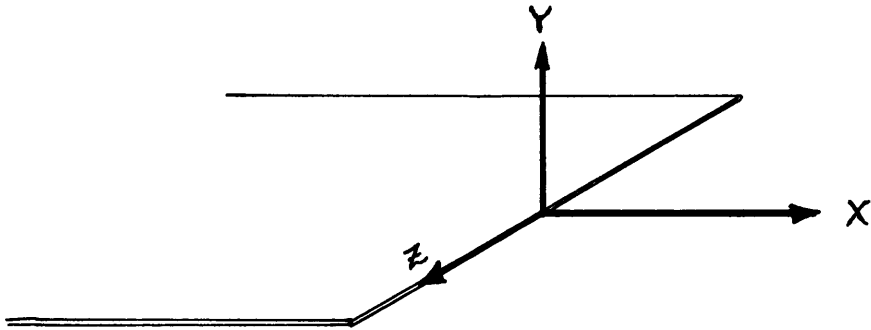


Figure 3.2 : Laboratory Coordinate Frame is Referenced to the Splitter Plate Edge

III.3 Initial Conditions

The entrance mean speed, temperature, turbulence level, and forcing disturbance intensity, were checked before and after each run in the free stream of each section. Random checks of these parameters were also made during the course of a run. Points 1 cm upstream of the plate edge and 2.75 cm into the free stream were chosen as the reference point for measuring entrance conditions for each stream. These points were also used as the reference point for free stream static pressure measurements.

Entrance mean velocities were established by measuring the shedding frequency of a cylindrical rod positioned in the top and bottom streams respectively. Using the data of Roshko (1954), the mean speeds were calculated as $202.50 \pm 2.00 \text{ cm/sec}$ and $38.50 \pm .50 \text{ cm/sec}$. The over-

all accuracy of the mean velocity data was important for reduction equations and could be considered as $\pm 2\%$.

The mean temperatures of the entering streams were measured before and after each run. A drift of $+ 0.5^{\circ}\text{C}$ was observed during a four hour period when the heat exchanges were used to maintain a constant reference temperature. Erratic, random variations in stream temperature were observed when the heat exchanges were not used. This has apparently been a source of severe calibration errors for past researchers.

Initial conditions on the natural, and forced disturbances were determined from frequency spectra taken first without forcing to establish the natural disturbance input, and then with forcing to analyze the cleanness and intensity of the forced signal relative to the natural level. These spectra are presented and discussed in Chapter IV.

III.4 Generation of Controlled Disturbances

As indicated earlier, a crucial factor in this experiment was the introduction of a suitable controlled disturbance. The success of this procedure, and the characteristics of the generated disturbances will be discussed in Chapter IV. The technical aspects will be touched on here.

Two, 8 watt, 30 cm, low frequency speakers were positioned on the tunnel so as to generate two distinct disturbance fields . The rear speaker was mounted at the test section exhaust and introduced a uniform

disturbance over the whole flow field. The front speaker was positioned over the top stream settling chamber and connected to the chamber by a small hole. This speaker basically introduced disturbances into the top stream only. The transition characteristics of the flow were found to vary with the location of the forcing speaker. This required, especially for the mixed forcing mode ($\omega_A + \omega_B$) that only one speaker be used to excite the flow. Final data runs were made using the upstream speaker. A comparison of the relative effects of the two types of forcing fields was also made.

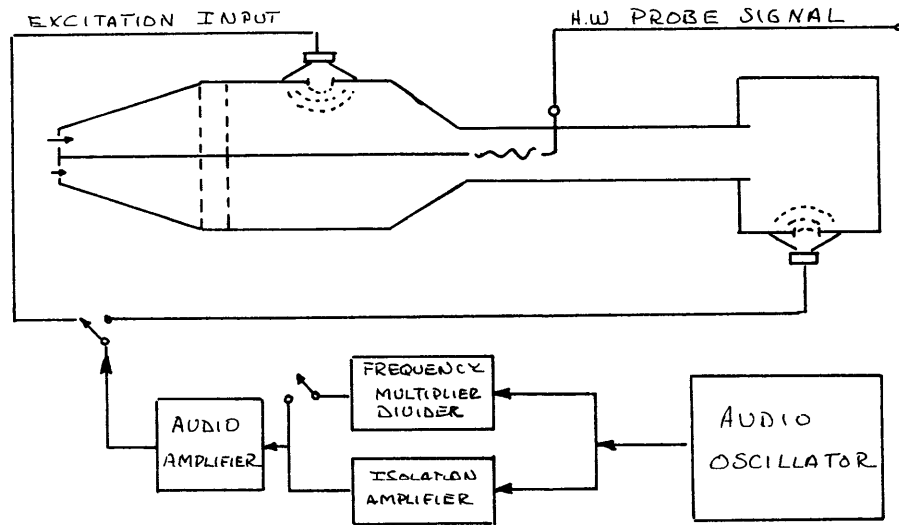


Figure 3.3: Schematic of the Speaker Excitation Circuit

The speakers were driven by a low frequency audio oscillator (see figure 3.3). In the mixed forcing mode, the output of the oscillator was fed into a frequency multiplier-divider circuit (M-D) to produce ω_A and ω_B from the same reference frequency. The (M-D) cir-

cuits were built around Texas Instrument, integrated logic chips, operational amplifiers, and Schmidt triggers. Buffer amplifiers were used to isolate the output stages which were fed to the speaker through a solid state audio amplifier.

The outputs of the M-D circuits were of the form

$$\omega_{\text{out}} = n\omega_{\text{in}}/m \quad n = 1, 3, 5 \quad m = 1, 2, 4$$

and were also fed to respective channels on the tape recorder for referencing purposes. The speakers were found to have excellent linear response in the 15-90 Hz frequency range. Resonance points in the speaker response were found at 10 and 110 Hz; the between region exhibited very little non-linear distortion and was reasonably flat in amplitude response.

III.5 Mean Flow Measurements

(a) Mean Velocity Profiles:

Graphic plots of the mean probe voltage were made simultaneously as the data were being recorded on tape. The integrated mean probe voltage was passed through a Voltage Controlled Oscillator (V.C.O.) and recorded as an f.m. modulated signal on the direct record mode. When played back on the f.m. mode, the tape recorder's internal V.C.O. produced a D.C. signal which could then be plotted and checked against the in-line plot mode during the run. This provided an excellent overall check of the storage interface analog reduction system.

Besides giving a systems check, direct in-line plotting of the

mean voltage profiles provided a useful visual check of the appropriateness of the time constants introduced by the probe traversing speed, and the D.C. integrator. In traversing through space, the probe necessarily averages the signal over a spatial volume proportional to the wire width, wire diameter, and distance traversed in a unit time. The integrator in addition adds a temporal averaging time to the already spatial averaged signal. A judicious combination of the two must be used to avoid distorting the recorded data. One technique, and in practice the most effective, is to observe whether any hysteresis exists when the output voltage on the down and return traverses are plotted over each other. With an integrator time constant of 0.3 seconds, and a traverse speed of 0.25 mm/sec, no hysteresis effects were noticeable. The two traces overlay one another perfectly even in regions of sharp gradients where time constant biasing would be most pronounced.

The data reduction circuitry for mean profiles is schematically shown below.

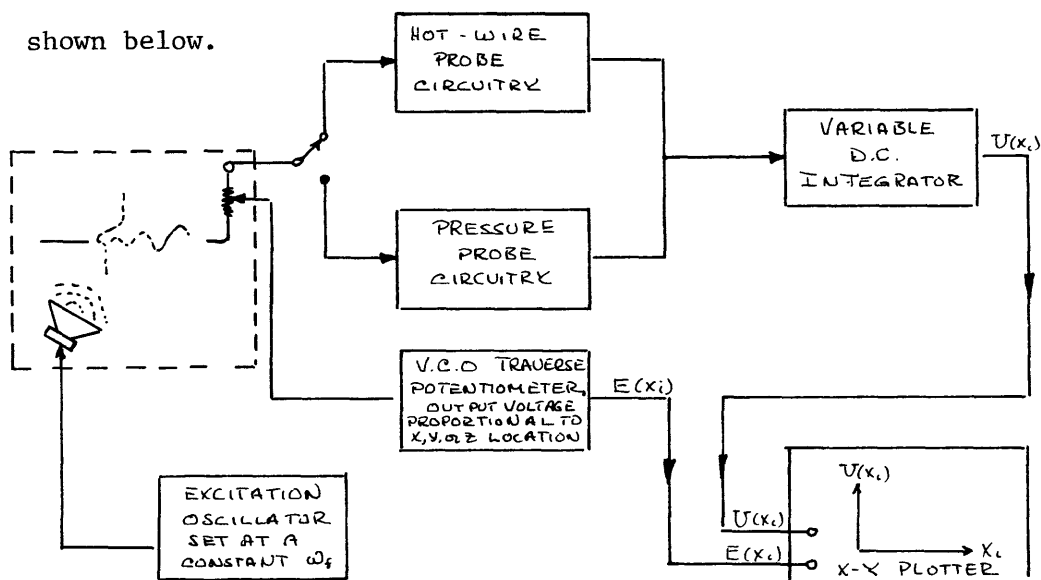


Figure 3.4: Schematic of the Mean Flow Measurements Circuitry

Since the calibration curves for the mean and fluctuating velocities depend critically on an exact knowledge of the mean wire voltage, probe current and the hot and cold resistances, it was necessary to measure these variables as initial and end conditions for each traverse. The values at the start of each run were initialized with $I = I_0 = 30.00$ ma. This gave the true mean voltage (and hence velocity) as referenced to the proceeding stations. Also, since the constant current supply for the probe is really just a large ballast resistor in series with the probe and a voltage source, changes in the probe resistance as the wire passes into regions of different velocity alter the current from its initial value. This variation will change the probe's overheat ratio, and hence the appropriate calibration constants at each point. By using a digital computer to process the data in conjunction with an iteration scheme for computing changes in wire current, the calibration constants, and hence mean velocity for each point could be easily, and cheaply computed. The measurements of the probe voltage, current, etc., taken at the end of the traverse were used to check the accuracy of the iteration scheme.

(b) Dynamic Pressure Profiles:

Plots of the vertical distribution of dynamic pressure were made at several downstream stations to provide a cross-check on the hot-wire velocity data. A standard, "N.P.L. Improved Form, Prandt '1 Type", pitot-static probe was used. Because of the difference in physical size, and response time between the pressure probe and hot-wire, several factors had to be considered in choosing an appropriate series of appro-

priate stations for comparing the two techniques. The pressure probe spatially averages the flow field over a very large volume compared to the hot-wire. Regions of the flow field, where strong spatial gradients of mean velocity existed, were often of a scale comparable to the pressure probe geometry and could not be accurately measured. It was finally decided to make the dynamic pressure measurements in a region 10 cm downstream where the flow was fully developed and exhibited gradual vertical and streamwise gradients of velocity. The small size of the static pressure ports (0.40 mm) gave rise to a rather sluggish response time, and a very slow traverse speed of 0.15 mm/sec was required to avoid hysteresis effects. Traverses were made at five successive downstream stations from 9.50 cm to 11.00 cm. The circuit schematic is identical to that for mean velocity profiles. An M.K.S. Baratron capacitive pressure system was used to monitor pressure changes and the plotted voltage is proportional to the difference between the stagnation and static pressures sensed by the probe.

(c) Static Pressure Distribution:

Two stagnation probes were used to measure streamwise accelerations of the mean flow. A reference probe was located at the test section entrance, and was calibrated relative to ambient pressure as indicated by a standard precision mercury barometer. The two probes were then aligned at the same (x, y) location but slightly separated in the spanwise coordinate. No pressure differential was observed between the probes at this initial position. The second probe was then slowly traversed downstream at various vertical heights. The differential in static pressure

between the two probes was recorded as a D.C. voltage and plotted against the downstream coordinate.

III.6 Fluctuating Flow Measurements

(a) Frequency Spectra:

Considerable qualitative information was taken in the form of disturbance frequency spectra. Sweep bands of 50, 100 and 500 Hz were used to analyze the entire range of fluctuations present in the transition zone. The schematic circuitry is shown below.

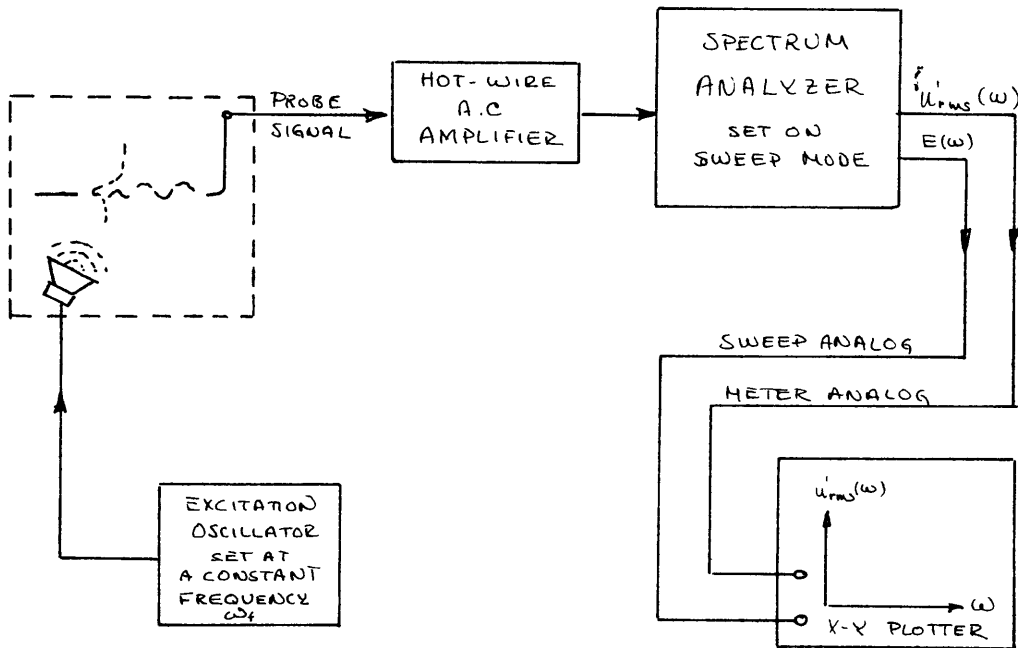


Figure 3.5: Schematic of the Frequency Spectra Circuitry

Spectrum measurements were made using the internal sweep mode and plotting the r.m.s. meter analog of the fluctuating wire voltage against the sweep analog. Calibration plots were made by passing sine and square waves through the unit and observing the amplitude and

clearness of the sine wave spikes and harmonics of the square wave. However, in analyzing real spectral data which had background noise and no strong concentration of energy at any one given frequency, it became clear that considerable attention must be paid to the proper combination of bandwidth, sweep speed, and averaging time used. For maximum discrimination, a bandwidth of 1 Hz (i.e. ± 0.5 Hz @ 3 db down) was used. For relatively clean signals such as the forced transition spectra, a sweep rate of 0.55 Hz/sec and a meter time constant of 0.1 sec was found satisfactory. For rather confused signals such as the natural transition spectra where the energy is randomly distributed among the various unstable disturbance frequencies, a sweep time of 0.55 Hz/sec and an integration time of 10.0 sec was required to show the true average character of the natural transition. This choice essentially corresponds to the criteria suggested by Bendat and Piersol (1966) for random signal analysis.

(b) Spatial Distribution of Spectral Amplitudes:

The r.m.s. amplitude distributions of various significant spectral components were plotted at each downstream station as shown in figure 3.6.

Plots were made as a continuous function of y by using the wave analyzer as a tuned band-pass filter. Because of the closeness of the various harmonics and sub-harmonics a bandwidth of ± 0.5 Hz was used. This required a very close control over the analyzer tuning frequency. By tuning the analyzer with a stable external standard, drift in the tuning center frequency was kept to within $\pm 0.10\%$ over the course of

a traverse. The meter time constant and traverse speeds were again chosen to eliminate hysteresis effects.

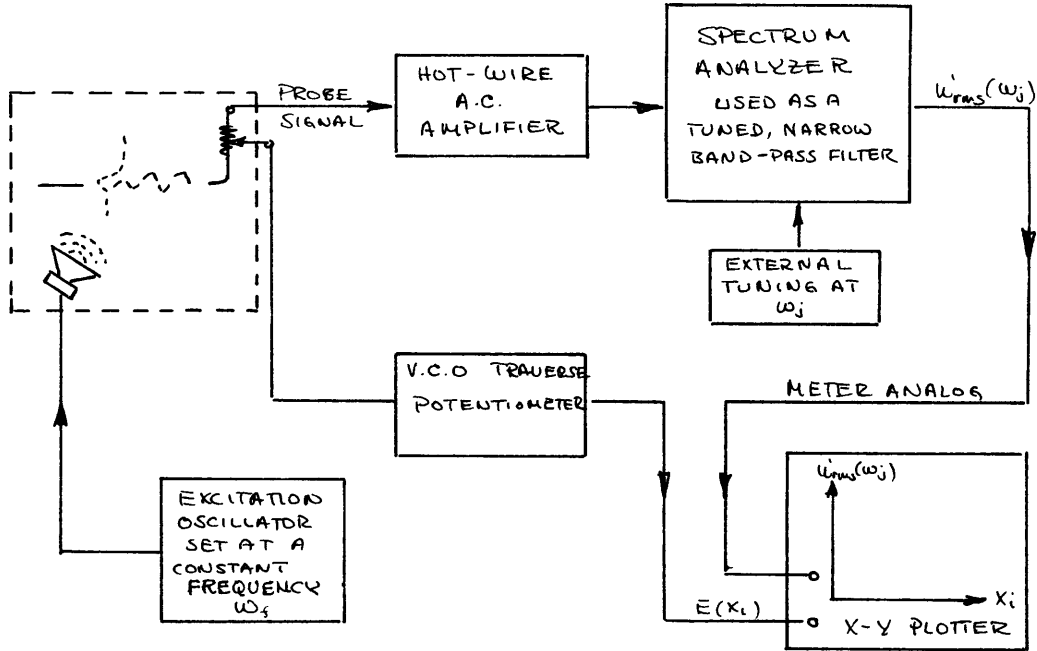


Figure 3.6: Schematic of the u'_{rms} Amplitude Distribution Circuitry

(c) Spatial Distribution of Spectral Phase Angles:

Measurements were made of the spatial variations in disturbance phase angles as measured relative to a standard reference signal. Measurements were taken as continuous functions of the vertical and stream-wise coordinates. The schematic circuitry is shown below in figure 3.7.

The forcing signal of the audio oscillator was used as the reference input to the phase meter when analyzing the spatial phase changes of the primary oscillation. In the mixed-mode experiment, the outputs

of the multiplier-divider were used to give reference values for ω_{fs1} and ω_{II} respectively.

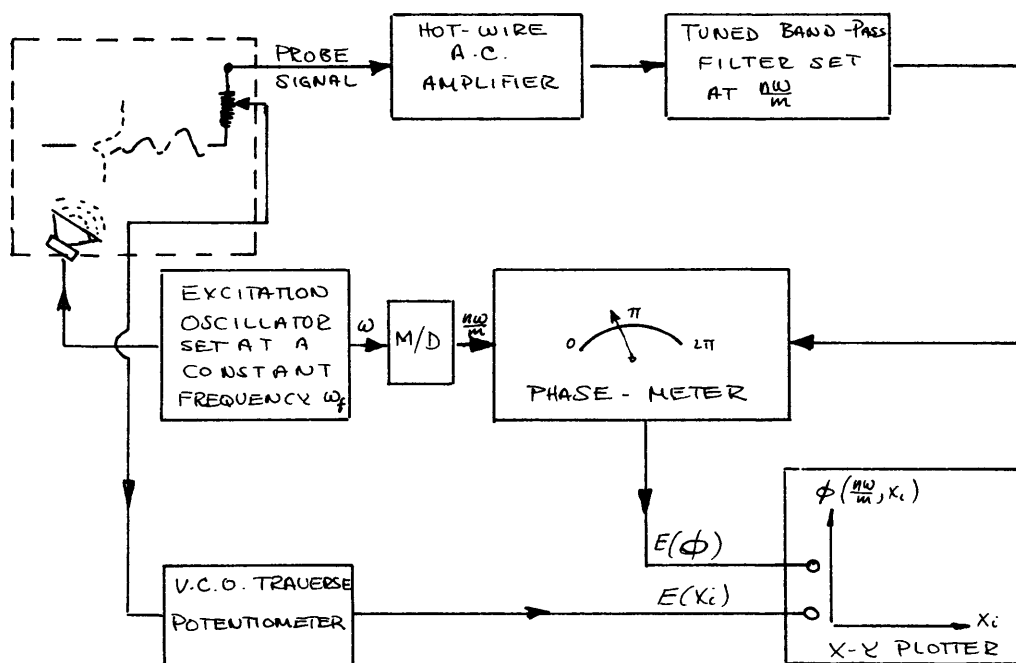


Figure 3.7: Schematic of the Phase Angle and Wavelength Measurement Circuitry

The phase meter was nulled with the driving signal at a reference point in the entrance of the upper stream. By traversing the probe in space, variations relative to this point were measured. This is the same as having a second probe at the reference point, and measuring phase shifts relative to the reference probe. Two distinct variables, at least in name, can be obtained from these phase measurements. These are phase angle and wavelength.

(d) Frequency Response Transfer Function:

The frequency response of a linear system is usually defined as the

ratio of the phaser output to the phaser input, when the system is driven by a sine wave input. In case of the wind tunnel, the sinusoidal driving input can be considered as the disturbance generated by the excitation speaker, and the output as the induced instability response in the linear region of transition. By incorporating the tunnel as a black box element in a closed impedance circuit, the effects of varying excitation speaker location could be studied by observing the response in various regions of the transition. As shown in figure 3.8 the speaker was driven by the B.F.O. output of the wave analyzer and the forced disturbance response was fed back into the analyzer to complete the loop. The amplitude of the forced response at each frequency was then plotted against the sweep analog as the analyzer was slowly swept through a frequency range. This technique proved quite useful in analyzing the influence of the speaker location on the forced transition process.

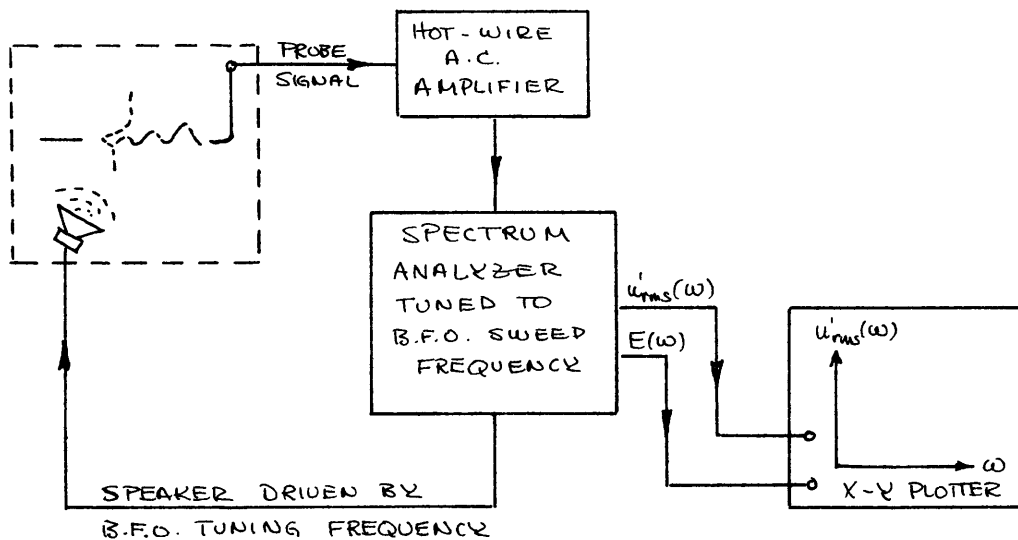


Figure 3.8: Schematic of the Amplitude Response Circuitry

III.7 Smoke Pictures

Smoke pictures were made to determine the qualitative aspects of the transition. A dense, highly visible smoke was generated by blowing air over titanium tetrachloride. Titanium tetrachloride is a hygroscopic salt which is liquid at room temperatures and when brought into contact with air, it combines chemically with the moisture present to form a vapor of high optical density. A small drop of liquid will emit a dense cloud of smoke for several minutes.

In order to introduce the smoke into the test section without placing any foreign bodies into the upstream flow, a modified version of the original splitter plate was constructed (see figure 3.9 below):

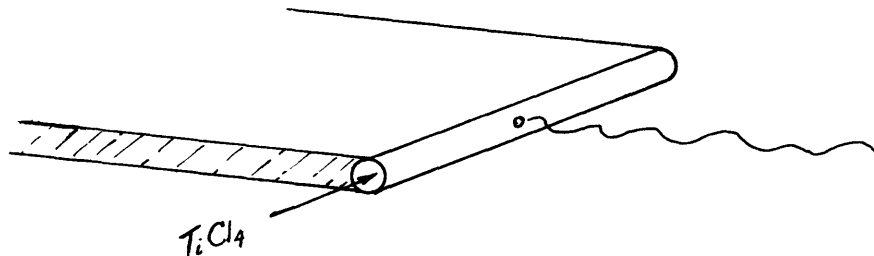


Figure 3.9: Modified Splitter Plate for Smoke Pictures

A length of stainless steel hypodermic tubing was soldered to the edge of a sheet of brass plate whose dimensions were identical to the original plate. The soldered joint was polished and smoothed to eliminate any surface irregularities. The tube then formed the trailing edge of the plate. One end of the tube was plugged, and a small hole was drilled in the wind tunnel side wall so as to align with the open end of the tube when the plate was installed in the tunnel. A small hole

was drilled in the center of the tube to emit the generated smoke into the wake immediately behind the plate. The smoke generating flask was connected to the plate by a male insert which fitted into the open side of the tubing through the tunnel wall. The configuration worked quite well and did not alter the flow field in any noticeable manner.

CHAPTER IV

NATURAL VERSUS FORCED TRANSITION

Stability experiments must be conducted with respect to the unavoidable level of disturbances which are intrinsic to the particular apparatus used or system being studied. These intrinsic disturbances determine the systems natural response to an input perturbation. Although it is not possible in a physically realizable flow, one would ideally like the natural input noise to consist of a wide-band of infinitesimal disturbances which have a relatively uniform power spectra over all frequencies (i.e. nearly "white noise"). In this manner no one frequency interval is singled out for a biased energy input and the system can undergo its own natural selection process for disturbance amplification.

With adequate care, wind tunnels can be designed so that over the frequency range of experimental interest the natural input spectra can be made to approach a "quasi-white noise" character. Then each frequency receives a relatively equal energy input on a random basis and the disturbance spectra will be dominated by the modes preferred by the instability process for maximum amplification. However, a quasi-white noise input must be considered as an ultimate goal for any physical system. Small variations in the character of the mean and input disturbance conditions inevitably occur, and often cause the observed maximally unstable mode to vary by as much as 10% from instant to instant. No single, distinct, maximally unstable mode will normally appear.

Rather, a band of highly amplified waves will appear. Since any one of the modes in this band will be intermittently dominant, quantitative measurements of natural transitions are extremely difficult.

To circumvent this natural intermittence, various techniques of generating controlled artificial disturbances can be used to selectively excite a desired mode. Because an artificial energy input can be made continuous in the time domain, the continuously excited frequency component will grow on a coherent basis relative to its intermittently excited neighbors. In this manner, the preferred growth of any unstable mode can be triggered. Of course, in order to have the artificially forced mode correspond to the natural case, the qualitative structure of the forced excitation field must be similar to that of the natural noise at that frequency (i.e. if the natural noise input is localized, so should the forced input, etc.). The forced and natural input should differ only in relative continuity of input and perhaps slightly in magnitude. If these conditions are met (and they normally are not), then the sole effect of the artificial excitation will be to impart a selective bias (i.e. spike) on the input noise spectra. The selectively excited mode can be expected to exhibit on a continuous basis the same properties of growth and modal structure that on a natural basis appear only instantaneously and intermittently.

This is really the name of the stability game since unlike many mechanical systems, real life geophysical systems do not receive continuous and coherent energy inputs. What we really want to obtain is an understanding of what the instantaneous natural characteristics of

an unstable system are. Because our present investigatory tools do not allow us to measure the natural transition in sufficient detail, we must achieve an understanding via the back door and conduct controlled experiments which, in the limit of satisfying all proper criteria, will model the natural behavior of the system.

Some techniques of excitation such as vibrating ribbons (Klebanoff, 1962) can generate controlled disturbances on a local basis and are useful in boundary layer experiments. However, the mechanical configuration of the apparatus used here seemed to preclude the use of ribbon techniques, and as in past experiments on jets and wakes the generation of perturbation vorticity by radiated sound waves was chosen as a means to excite the flow and trigger the transition.

Hindsight has shown, however, that a localized excitation field would have been far more useful. Any difficulties that may have been involved with the construction of a localized ribbon system would probably have been of far less magnitude than those problems encountered with a sound wave forcing field.

As was conclusively demonstrated, the forced transition of the sound excited flow could, and did, vary from the observed natural transition. In order to fully understand the implications of the forcing techniques used, a careful investigation was made of the natural transition process and of the effects of using various techniques of sound excitation.

In the work that follows, the qualitative character of the natural and forced transitions will be discussed in order to establish the gen-

eral scope of the problem. Conclusions will be drawn as necessary to provide insight into just why certain experimental approaches were used. A detailed quantitative presentation of the experimental results will be left until Chapter V, and will be discussed in Chapter VI.

IV.1 Characteristic Scales and Reference Parameters

The initial mean velocity profile immediately behind the splitter plate at $x = x_0$, was used for establishing most reference scales,

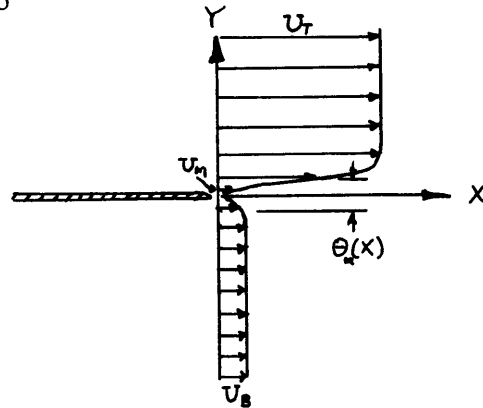


Figure 4.1: Schematic plot of the mean velocity field just behind the splitter plate.

where $x_0 = 0.2$ cm.

The overall character of the flow could be established by a length scale based on $\theta_m(x)$ the local momentum thickness, a velocity scale based on the maximum free stream velocity U_T , and the dimensionless ratio

$$\mu = \frac{U_T - U_B}{U_T + U_B}$$

which for the present experiments was $\mu = .700$. The ratio $\mu = 0.700$ distinguishes the flow studied here from the two limiting cases: $\mu = 0$ for symmetric wakes (or jets), and $\mu = 1.0$ for single separated free shear

layers where $U_B=0$. The ratio μ also expresses the fact that the frequency of disturbance oscillation as observed in the laboratory frame is dependent not only on the magnitude of the maximum shear, but also on the mean convective speed at which the disturbances are carried along by the mean flow.

The actual ratio of free stream velocities is

$$\frac{U_B}{U_T} = 0.175$$

while the maximum velocity differences across the upper and lower shear layers respectively are

$$\frac{U_T - U_M}{U_T} = 0.950 \quad (\text{upper layer}) @ x = x_0$$

$$\frac{U_B - U_M}{U_T} = 0.131 \quad (\text{lower layer}) @ x = x_0$$

The initial momentum thickness $\theta_m(x_0)$ was used when forming dimensionless variables for comparison with theory. This was taken to be the sum of the momentum thicknesses of the two entrance boundary layers.

$$\theta_m(x_0) = 0.121 \text{ cm}$$

Since it is often convenient to refer to downstream distances in terms of primary mode wavelength, the wavelengths λ_{II} and λ_{fs1}

$$\lambda_{II} = 4.35 \text{ cm}$$

$$\lambda_{fs1} = 7.80 \text{ cm}$$

of the maximally unstable mode and a preferred downstream free shear

layer mode will also be used. These values were experimentally measured and agreed reasonably well with the results of a spatial stability model based on the mean velocity profile at x_0 . More interestingly, the values also agreed with the characteristic scale of the shear layer "cat's eyes" discussed in section V.5.

Considerable effort proved the futility of trying to establish a single length scale for dimensionalization throughout the entire flow field. The presence of downstream derivatives of all variables, the existence of several regions of strong flow expansion (i.e. non-parallel behavior), local variations in wavelength, and the lack of pure symmetry or pure asymmetry of the initial profile precluded the use of any one particular scaling variable.

In order to avoid a myriad of confusing scaling arguments, most plots are presented with the length scale axis in dimensional form. When it proves convenient, scaling arguments will be made for various regions of the flow, but these will usually be in terms of the cat's eye wavelength and will be expressly noted when used.

The initial Reynolds number of the wake, as based on the initial momentum thickness and maximum free stream velocity, is

$$R(x \approx 0.20) = \frac{U_T \theta_m(x_0)}{\nu} \sim 160$$

The Reynolds numbers of the splitter plate boundary layers, as based on the local momentum thickness just prior to separation from the plate, are of the order of 100 and are hence below the critical value for boundary layer instability. The two results indicate that any amplifying

disturbances observed in the wake are due to an instability of the laminar wake and not of the plate boundary layers. The wake Reynolds number is well within the inviscid range for free shear layers.

Note that the free stream speed of the fastest moving layer is used for dimensionalization; any dimensional parameter based on U_B would be meaningless in the limit $U_B \rightarrow 0$. Also, any parameter based on the overall velocity difference ($U_T - U_B$) would not be representative since the initial instability is dominated by the upper shear layer difference ($U_T - U_M$).

The disturbance oscillations are expressed in dimensionless form by

$$u'(\underline{x}, t) = \sqrt{2} u'_{\text{rms}}(\underline{x}) e^{i(\alpha_r x - \beta_r t + \phi_2 + \phi_3)} e^{-\alpha_i x}$$

where

$$\begin{aligned} \alpha_r &= \frac{2\pi \cdot 2\theta_m(x_o)}{\lambda} && = \text{dimensionless wavenumber} \\ \beta_r &= \frac{2\pi\omega \cdot 2\theta_m(x_o)}{U_T} && = \text{dimensionless radian frequency} \\ \alpha_i &= \alpha_i^* \cdot 2\theta_m(x_o) && = \text{dimensionless spatial growth rate} \\ u_{\text{rms}}^* &= \frac{u_{\text{rms}}^*}{U_T} && = \text{dimensionless r.m.s. amplitude} \end{aligned}$$

and ϕ_2 and ϕ_3 are the vertical and spanwise phase angles.

The experimentally observed frequencies ranged as follows:

$$\begin{aligned} (0.075 < \beta_r < 0.32) & \quad \text{initial linear modes} \\ (0.075 < \beta_r < 1.50) & \quad \text{overall transition.} \end{aligned}$$

* An asterisk denotes a dimensional variable.

As indicated above, the correct length scale for comparing experimental data to linear theory was found to be $2\theta_m(x_o)$.

IV.2 Qualitative Aspects of the Natural Transition

Previous investigations of shear layer transitions have often identified the dominant unstable mode from frequency spectra made at the earliest convenient downstream position where a clear and obvious singly peaked energy spectrum existed. This practice can be both misleading and incorrect.

In any unstable and spatially developing flow, the various growing linear and non-linear modes evolve differently with downstream distance, and consequently can have radically different vertical modal structures. At best, frequency spectra taken in such flows can be considered only as qualitative information whose proper interpretation is unhappily more often an art than a science. For example, since non-linear effects can appear quite suddenly and much earlier than usually suspected, one could be easily lured into using a spectra dominated by non-linear modes to demonstrate the existence of a purportedly linear mode.

Also, depending on the vertical modal structure of the frequencies present (i.e. symmetric, asymmetric, etc.), one can easily assign a given mode the wrong relative importance, or order of appearance. For example, a flow comprised of a symmetric and asymmetric mode is schematically illustrated below. Spectra taken at various heights in this imaginary system clearly illustrate the pitfalls involved in being too eager to attach great significance to any one particular piece of spec-

tral information.

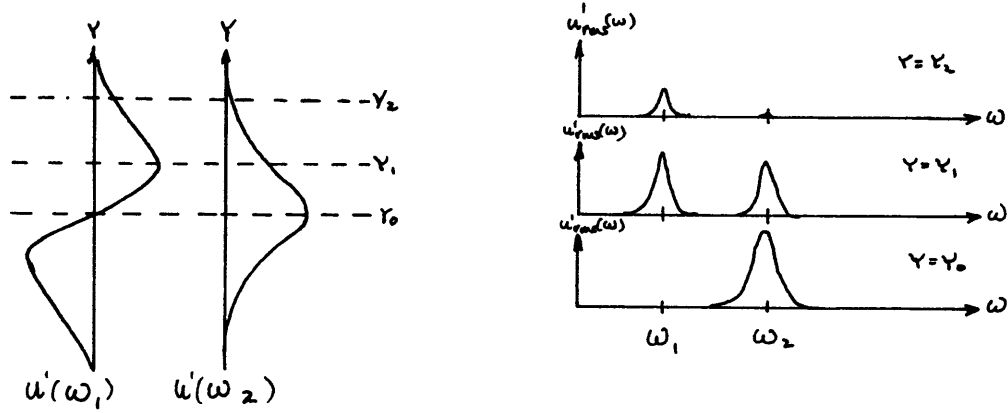


Figure 4.2.

(a) Natural Input Spectra

The distribution of natural input noise was measured in the boundary layers and free streams of both entrance sections. Most of the natural disturbance energy was concentrated in the lower frequencies (see figure 4.6) and no spurious spikes of input noise were present. The distribution of disturbance energy closely approached a quasi-white noise behavior. Erroneous spectral results could be obtained by choosing too fast a frequency scan rate or too large a meter time constant. The criteria established by Bendat and Piersol (1966) were found to give repeatable and consistent results.

The free stream turbulence levels were measured in the upper and lower streams and are given below

$$\text{r.m.s. turbulence level} = \begin{array}{l} 0.01\% \text{ top layer free stream} \\ 0.06\% \text{ bottom layer free stream} \end{array}$$

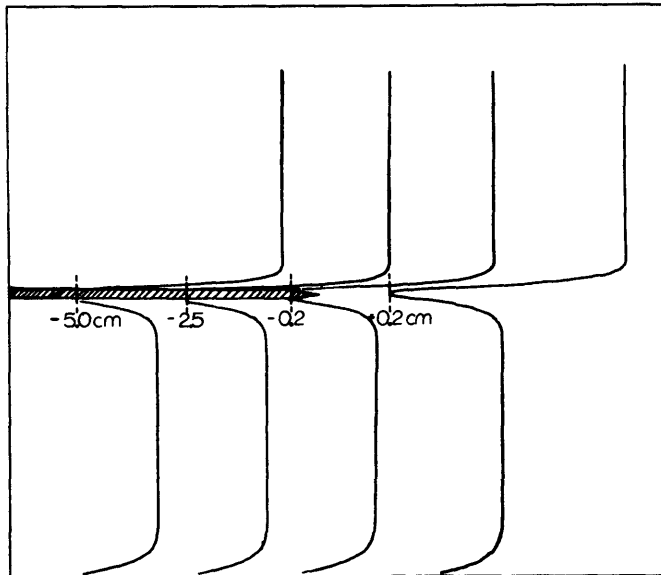


Figure 4.5: Profiles of mean hot-wire voltage at test section entrance ($x_0 = 0.2$ cm), and at various stations over the splitter plate.

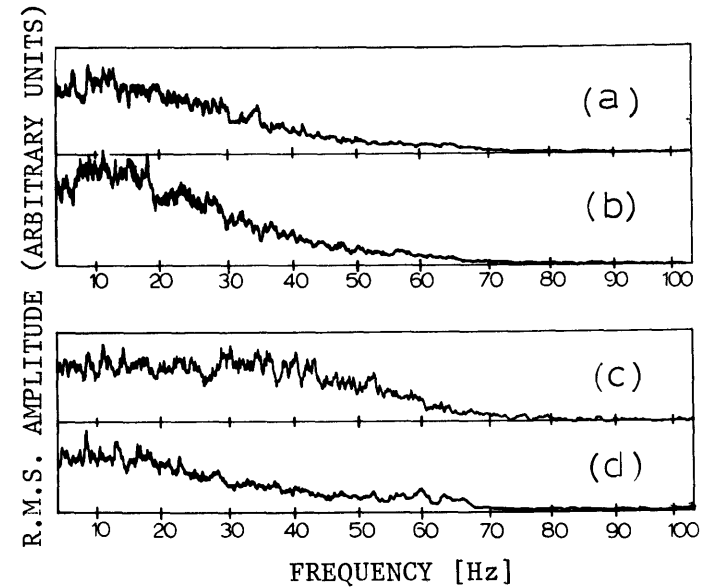


Figure 4.6: Natural input disturbance spectra at test section entrance. (a) upper layer freestream; (b) upper plate boundary layer; (c) lower plate boundary layer; (d) lower layer free-stream.

The r.m.s. turbulence level was somewhat higher in the slower bottom stream. The average magnitude $\langle u' \rangle$ of the natural u' fluctuations in a 1.0 Hz frequency interval near the maximally unstable mode was of the order of 0.0015%.

$$\langle u' \rangle = \frac{u'_{\text{rms}} (\omega_{II} \pm 0.5 \text{ Hz})}{U_T} * 100 \sim 0.0015\%$$

Although the input spectra were sensitive to ambient variations and to external mechanical vibrations, repeated spectra taken at random intervals during the course of the experiment indicated that the measured turbulence levels varied only slightly with time and the overall distribution of natural input energy remained qualitatively constant.

Plots of the natural disturbance spectra in the top and bottom splitter plate boundary layers were also made and are shown in figure 4.6. They have the same qualitative distribution as the free stream spectra and show no evidence of disturbances due to possible boundary layer instabilities. The entrance mean profiles over the plate were checked and were found to be laminar and free of unstable fluctuations. After separation from the trailing edge of the plate the boundary layers coalesced to form an initially laminar and highly two dimensional free shear layer.

(b) Mean Entrance Conditions

The mean flow profiles over the last 5 cm of the splitter plate are shown in figure 4.5. The plots are of the mean hot wire voltage and while they are not expressed in terms of velocity they do illustrate

several important points. First, the free stream flow is very uniform and parallel. The mean profiles are extremely flat in the free stream. The mean flow is slightly accelerated near the edge of the top plate boundary layer at x_0 . However, this does not seem significant and is probably due to the accelerative effects of the contraction zone. The hot wire probe used to measure these profiles was broken before a proper calibration could be made. However, a rough reduction scheme which used typical calibration constants from previous wires indicated that the top and bottom layers were characteristic of slightly accelerated Blasius boundary layers.

The two dimensionality of the initial free shear layer (and input disturbance spectra) was verified by making a series of spanwise traverses at different vertical heights and measuring variations in mean velocity and disturbance spectra. Both the mean and disturbance conditions did not exhibit any significant spanwise variations in the central 8 x 8 cm region of the test section entrance. Slight corner vortices were found at the plate wall boundaries but were not of significant intensity nor spatial extent to influence the central flow. Corner vortices of approximately 1 cm. diameter did exist along the bottom floor of the tunnel. These vortices tended to spread in spanwise extent with downstream distance and may have caused some three-dimensional distortions of the later downstream profiles. However, they did not exert any observable influence on the initial entrance profiles.

(c) Test Section Mean Velocity Field

The initial mean velocity field was formed by the two merging

boundary layers and possessed two inflexion points of opposite sign (i.e. two mean vorticity peaks). With progressive downstream distance, the two layers coalesced to form a single inflexion point shear layer. Static pressure measurement showed no free stream static pressure gradients and to a good approximation the test section flow can be considered non-accelerated.

The evolution of the mean streamwise velocity $U(x,y)$ is shown in figure 4.7 for the unforced natural transition. The downstream mean velocity field is presented in an isometric-orthographic three-dimensional format. A contour projection is also shown and gives an indication of how the mean velocity field spreads with downstream distance. The axis convention is shown below, in figure 4.3.

The mean velocity plot represents a series of vertical traverses across the shear layer in the test section center plane. Each plot contains 50 vertical traverses made at 0.5 cm downstream intervals and covers roughly six primary wavelengths of transition.

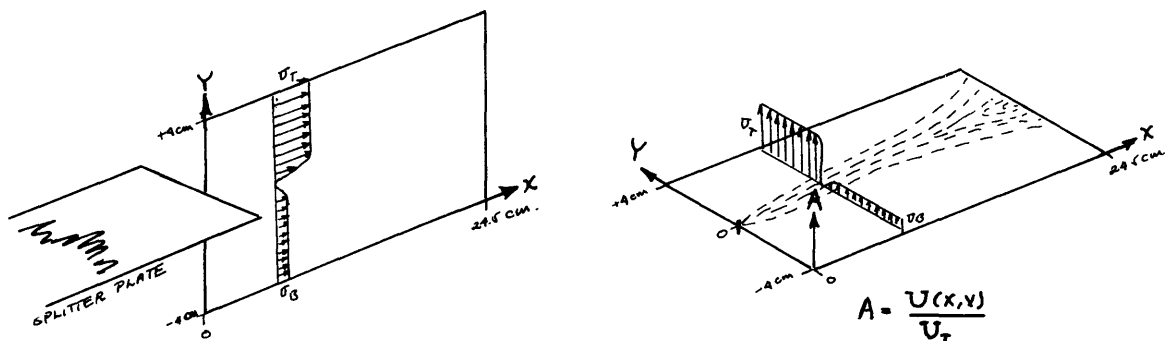


Figure 4.3: Axis convention used in all contour and 3-D isometric, orthographic data presentations. Only the scale of the amplitude axis will vary between plots of different data.

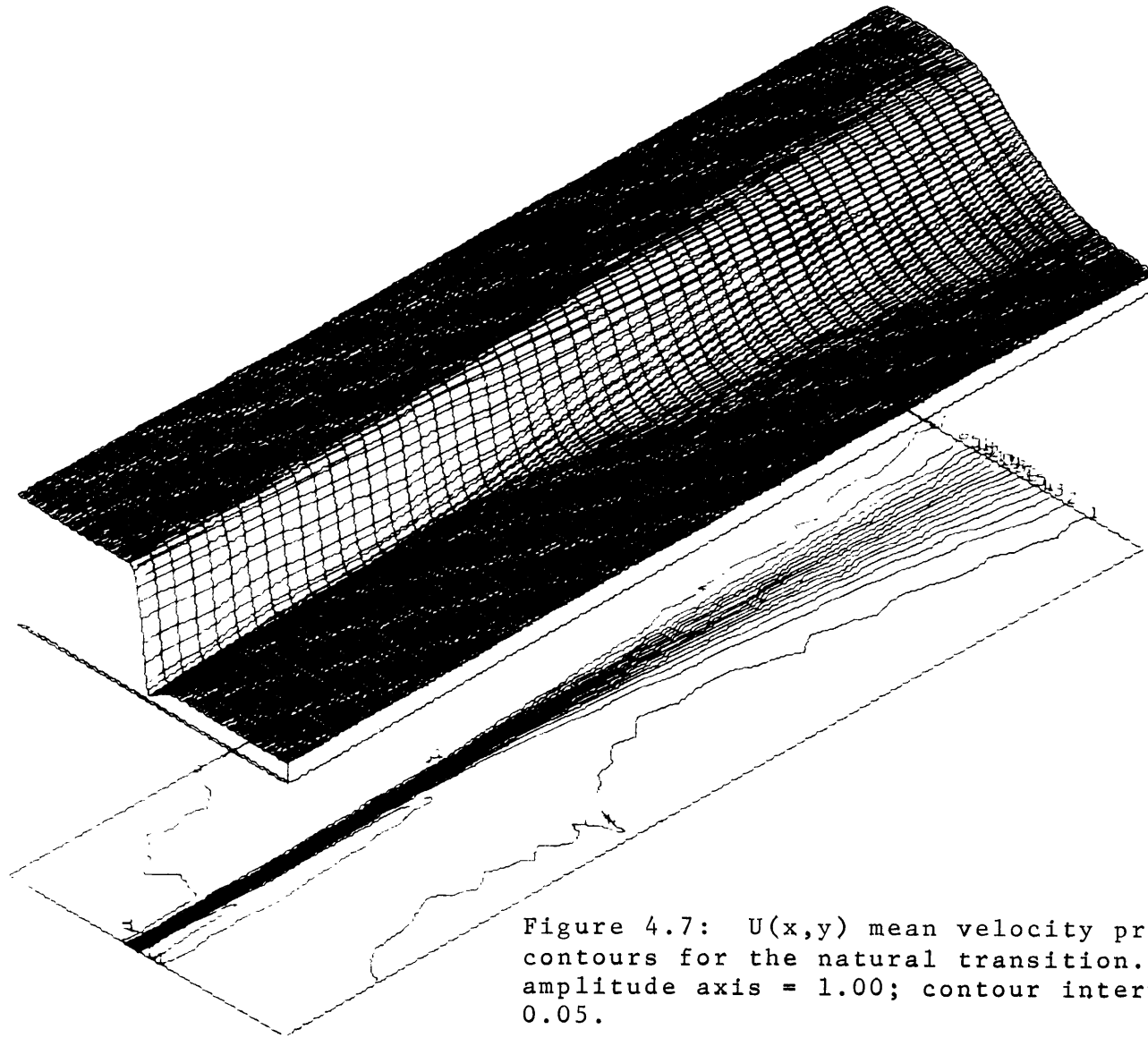


Figure 4.7: $U(x,y)$ mean velocity profiles and contours for the natural transition. U/U_T amplitude axis = 1.00; contour interval = 0.05.

(d) Natural Transition Spectra

Several interesting aspects of the natural transition were evident from a series of spectra taken at 1 cm downstream intervals. Preliminary measurements indicated that the activity of the majority of frequency components could be observed at a vertical height slightly above (2 mm) the plate center line. The spectra are shown in figure 4.8 and indicate that a wide band of unstable oscillations are initially excited by the natural input noise. These oscillations amplify with downstream distance. The band of initially excited modes (5 to 48 Hz) roughly coincides with the spectra of input disturbances in the top stream.

In the initial stages of transition no one particular frequency interval dominates the transition. However, within a wavelength ω_{II} of downstream distance, a band centered at 32 Hz starts to dominate the field, and within 1.5 wavelengths, this band evidently contains the most amplified modes. The most unstable mode in the initial portion of the natural transition (where the disturbance amplitudes are infinitesimal and hence linearized theory is valid) is clearly near 32 Hz.

A discrete band of higher frequency disturbances appeared at 6.00 cm and signaled the onset of finite amplitude behavior. The elements of this higher frequency band were not centered at harmonic multiples of the dominant 32 Hz fundamental band. Rather, they seemed to be centered about multiples of 40 Hz. This was entirely unexpected and prompted further investigation.

In the early stages of transition spectra taken at different ver-

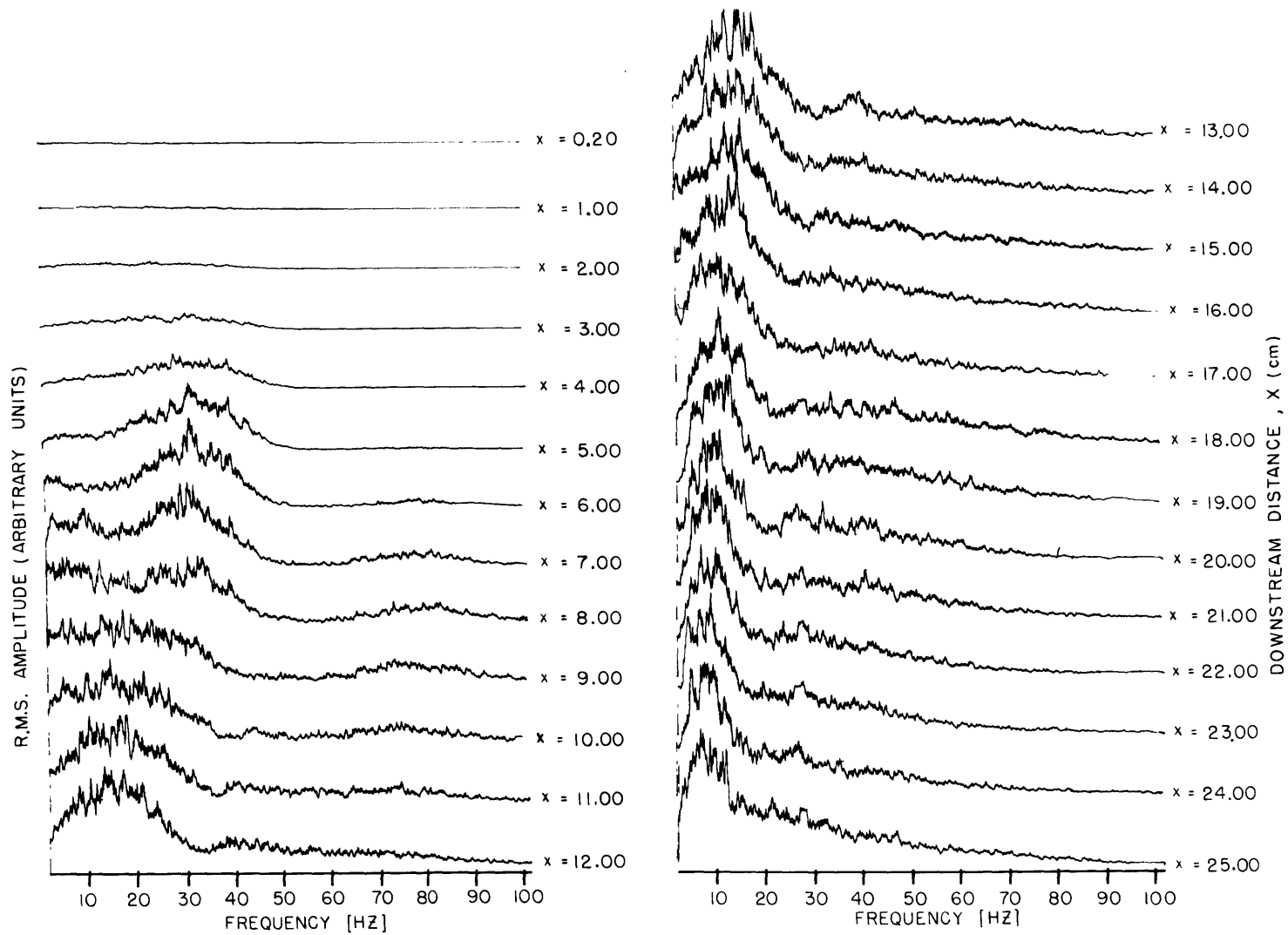


Figure 4.8: Downstream frequency spectra of the natural transition excited by a quasi-white noise disturbance input ($y = 0.2$ cm).

tical levels showed the same spectral content. However, after about wavelength λ_{II} of downstream distance the disturbance spectra taken at different heights showed distinct variations in spectral content. Figure 4.9 shows a series of spectra taken at several vertical heights at $x = 7.00$ cm. Near the center line, a very distinct band of disturbances centered at 45 Hz is present. Also present are some harmonic and strong low frequency modes. The low frequency modes seem to be sub-harmonics of the primary 32 Hz band.

The 45 Hz band merges with the 32 Hz band of fundamentals on either side of the center line. This makes discrimination difficult at any point other than the center line where the asymmetric fundamentals die off. The apparent symmetry of the 45 Hz band and antisymmetry of the 32 Hz band are in accord with the work of past researchers who have found that the fundamental linearized modes are antisymmetric and non-linear harmonic modes are basically symmetric.

Although it is clear, then, that the elements of the 80-90 Hz band are probably harmonics of the 45 Hz band, the origin of the latter band was still unknown. Initially it was thought that it may have represented the non-linear generation of 3/2-harmonics of the fundamental 32 Hz modes. The presence of sub-harmonics and the work of Kelly (1967) suggested this as a weak, but distinct possibility. Another series of spectra taken at different heights (figure 4.10) at a later downstream position showed that the influence of the 32 Hz band died off with the appearance of strong non-linear modes. The transition spectra was then dominated by two bands centered at 20 Hz and 40 Hz. The decrease in

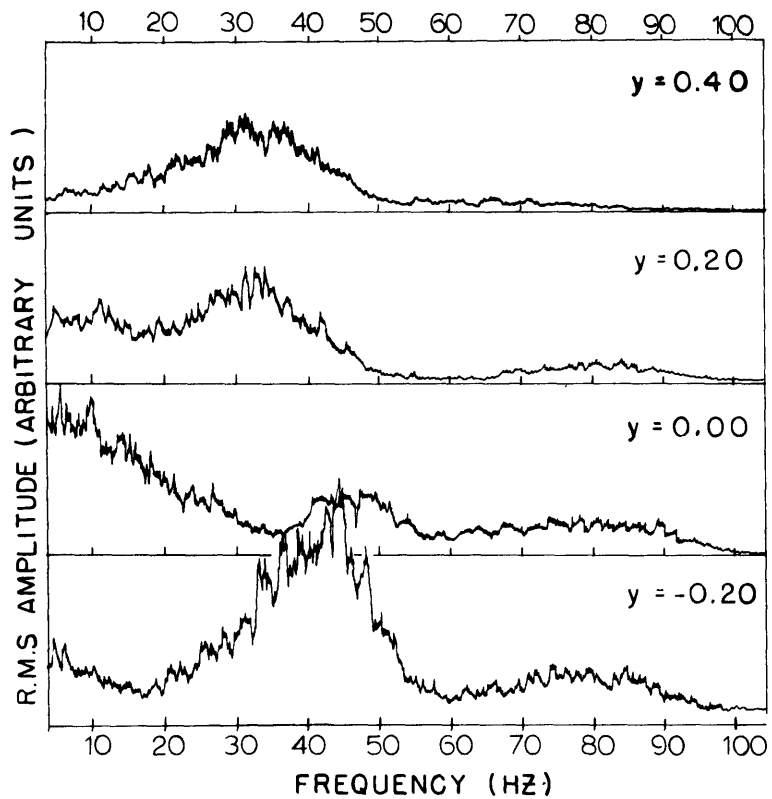


Figure 4.9: Frequency spectra of the natural transition at different values of y for $x = 7.00$ cm.

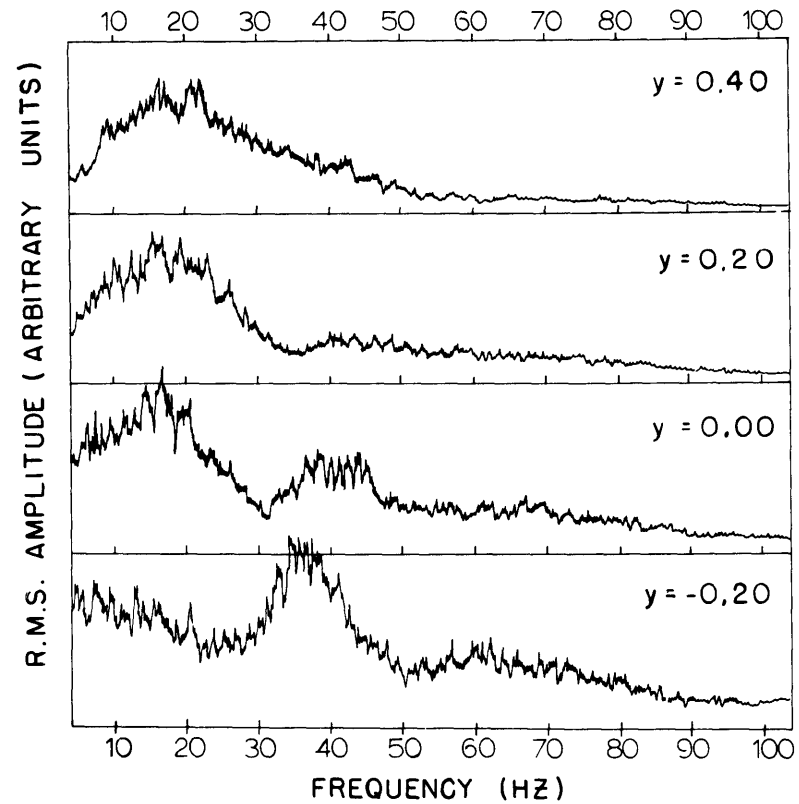


Figure 4.10: Frequency spectra of the natural transition at different values of y for $x = 12.00$ cm.

center frequency of the 45 Hz band from 45 to 40 Hz can be shown (section VI.1) to be due to the spreading of the mean flow.

Based on this second series of spectra, one may infer that the 20 Hz band may represent sub-harmonics of the 40 Hz modes (or in other words, sub-harmonics of the 3/2-harmonics of the primary mode. This however was later shown to be wrong. In fact a subsequent experiment showed that the elements of the 45-40 Hz band were the second harmonics of a latent band of 22.5 Hz instabilities centered about 22.5 Hz.

This latter behavior was evident during one series of preliminary runs in which an upstream segment of the settling chamber splitter plate assembly was misaligned and generated spurious disturbances in the 10 to 34 Hz range. The results of this series of measurements will often be referred to as the natural transition induced by a non quasi-white noise input spectra (or in other words a dirty input spectra). As indicated in figure 4.11, the natural transition excited by a dirty input spectra showed a pronounced preference for the simultaneous amplification of two discrete fundamental modes. These modes were centered at 22.5 Hz and 29.5 Hz respectively. A careful investigation of the input spectra showed slight concentrations of disturbance energy at 10, 15, 21, 24 and 34 Hz. These were apparently due to eddies shed by the protruding lip of the plate. The intensity of these spurious inputs were only slightly more pronounced than the normal input noise and were of the same general order of magnitude^{*}. No concentrations appeared at the

* It is worth noting that the slightest level of coherent noise input can cause the transition spectra to show distinct peaks. This is in direct contrast to the broad band spectra excited by the clean input spectra.

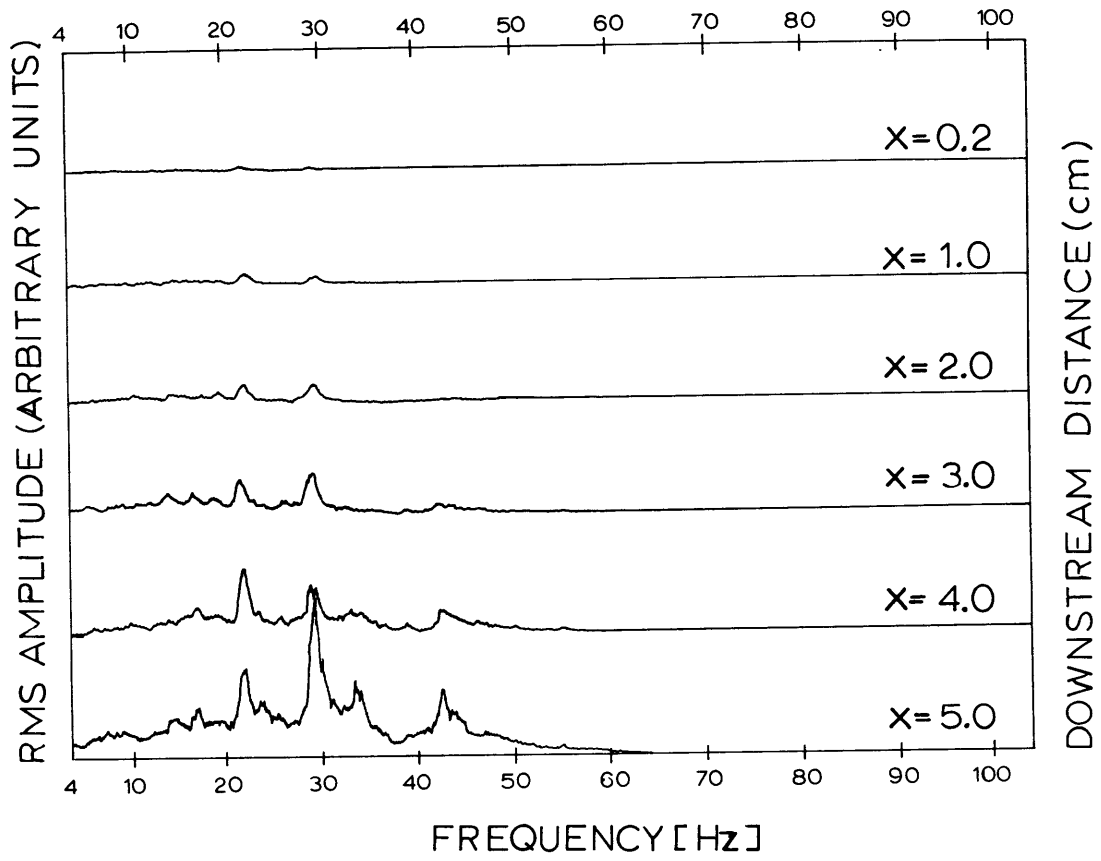


Figure 4.11: Downstream frequency spectra of the natural transition excited by a non quasi-white noise disturbance input ($y=0.2$ cm)

exact values of 22.5 Hz and 29.5 Hz. The strong downstream appearance of a mode at 45 Hz (i.e. the second harmonic of 22.5 Hz) was evident within one wavelength. A weak mode at 34 Hz also is present but this is felt to be due to the input noise at that frequency.

It was still not clear, however, why the harmonic of the 22.5 Hz mode should appear so strongly when the flow was excited by a clean quasi-white noise input spectra. In the latter case there is certainly no preferred energy input into or near the 22.5 Hz fundamental.

Analysis of a linear stability model (see section VI.1) based on the initial asymmetric wake configuration at $x = x_0$ showed that two different modes of instability (mode I and mode II) existed. The mode I instabilities (due to the bottom inflexion point) were of extremely low frequency and had such long wavelengths that they could not be detected in the existing apparatus. The mode II instabilities were due to the upper inflexion point, and the maximally unstable mode II oscillation (i.e. ω_{II}) was found to correspond to the 29.5 Hz instability. The results of a later series of quasi-uniform stability calculations, showed that as the mean flow lost its wake-like structure and evolved towards a free shear layer configuration, the maximally unstable mode II oscillation approached the 22.5 Hz value at the point where non-linear harmonic modes appeared. Since the 22.5 Hz instability is characteristic of the basic free shear layer structure of the flow, it will be often referred to as ω_{fsl} .

It was evident from the calculations that with downstream distance the evolving nature of the mean flow increasingly favored the presence of

lower frequency fundamental modes. The larger initial growth rate of ω_{II} and its sizeable amplitude in the regions where ω_{fs1} is favored probably explain why ω_{II} still dominated the downstream transition spectra even though the local mean conditions favor the growth of ω_{fs1} .

The fact that harmonics of ω_{fs1} rather than those of ω_{II} are favored for non-linear reinforcement demonstrates the influence and importance of local mean conditions on the non-linear behavior of the transition.

It was interesting to note that the natural transition induced by the dirty input spectra mentioned earlier showed a strong downstream tendency for the ω_{II} and ω_{fs1} modes to interact and produce not only various harmonics and sub-harmonics of their respective frequencies, but also non-linear combination modes. This behavior will be more thoroughly discussed in later chapters.

IV.3 Qualitative Aspects of the Forced Transition

Although the use of sound waves for disturbance excitation has found considerable acceptance in the literature, the results presented here clearly demonstrate that the character of the forced transition can be altered from that of the natural case. In particular, it was found that the location of the excitation speaker, and the manner in which the sound waves are introduced into the test section, had a considerable influence on the transition. The exact mechanisms by which sound waves generate vorticity perturbations in a shear layer are not clear. A heuristic explanation is given in appendix A.2. However, only the quali-

tative aspects of the problem will be touched on here.

Sound waves of the frequency range used in this experiment have wavelengths of order 10 meters. This is several times the length of the tunnel and, on a relative basis, sound perturbations are instantaneously generated in a uniform manner throughout the length of the test section. However, the characteristic wavelengths of the unstable shear layer modes are several orders of magnitude smaller than that of sound waves, and it is not at all clear just how sound waves trigger shear oscillations of the proper wavelength.

One approach has been to assume that the sound field establishes the time response (i.e. frequency) of the shear perturbations, but the layer acts (in some unknown manner) to allow the existence only of wavelengths which fit the system's dispersion relation for the given impressed frequency. The other school of thought asserts that the sound field may induce instantaneous shifts in the pressure distribution at the edge of the splitter plate forming the wake. This may then produce the appropriate smaller scale vorticity oscillations necessary to fit the shear layer dispersion constraints. This is discussed further in appendix A.2.

If a shifting of the pressure field is responsible for generating the proper scale oscillations, then the excitation can probably be considered as being localized at the test section entrance. If so, only the alteration of the input spectra need be considered when analyzing the effects of the forcing field.

However, if mechanisms which can act throughout the entire flow

field are responsible, then the influence of a volume excitation field must be considered. Such a field will influence the downstream non-linear regions of transition as well as the initial input spectra. In this respect it can act as a possible constraint on the flow, and prevent the disturbances generated in the linear zone from evolving in a natural manner in the non-linear regions.

(a) Intensity of Speaker Induced Disturbances

Initial investigations showed that the lowest amplitude u'_f of controlled excitation which would lock the transition into the desired frequency was a disturbance whose total energy input was roughly equivalent to the total energy of the natural background noise (i.e. as measured by the input turbulence level).

$$[u'_f]^2 = O\left[\int_{\omega} u'_N{}^2(\omega) d\omega\right]$$

Figure 4.9 shows the relative levels of disturbance r.m.s. values when the flow is forced with an order $[u'_f]$ excitation.

The intensity of speaker excitation was measured at the entrance free stream reference points over the splitter plate. Measurements made at various other locations indicated that the excitation field had no noticeable vertical modal structure and that the forced disturbance field was uniform across each entering stream.

A careful check of the induced fluctuations showed the speaker diaphragm produced slight harmonics of the excitation signal. However, with the exception of the mixed forcing case, the harmonic fluctuations were always one to two orders of magnitude smaller than the fundamental, and

below the average natural noise level. In the mixed mode experiments where the speaker was simultaneously driven by two signals ω_A and ω_B , a fairly noticeable component near $(\omega_B - \omega_A)$ was present in the input spectra. This can be seen in figure 5.1 where the forced input spectra are shown for each of the three cases studied here.

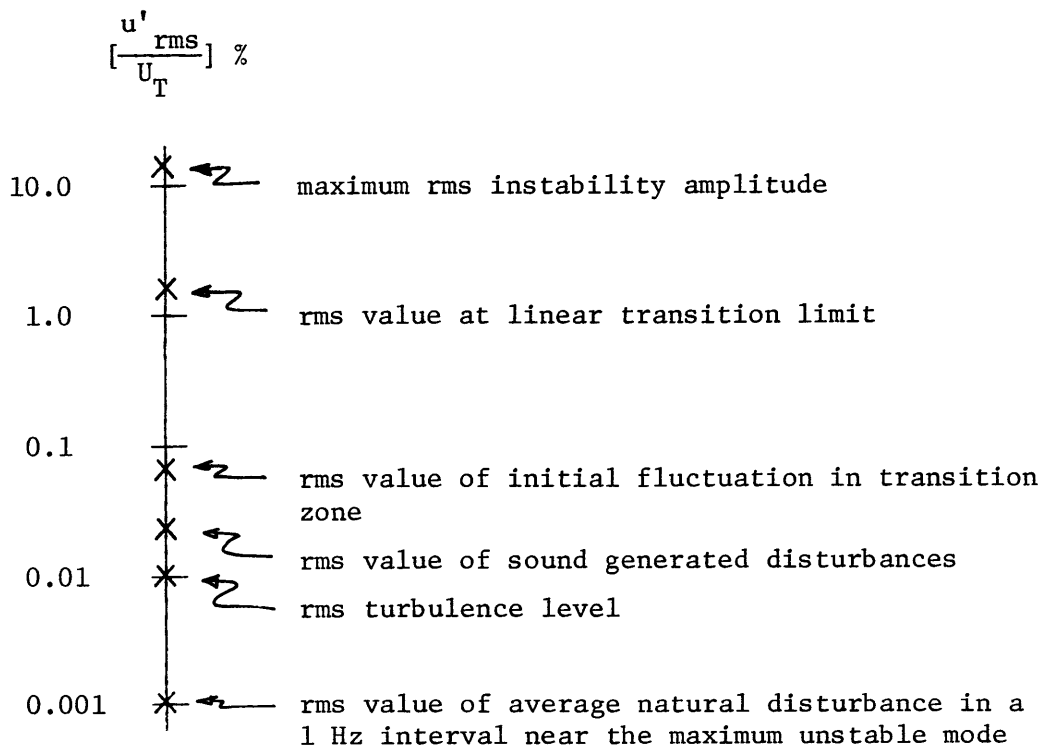


Figure 4.4: Relative r.m.s. values of significant disturbance quantities. Many of the disturbance spectra are presented in arbitrary units. The % r.m.s. scale factors shown above can be used to obtain a rough estimate of the relative r.m.s. velocity scale of each plot.

(b) Speaker Location and the Generation of a Symmetric or Asymmetric Forcing Field

As indicated in figures 2.1 and 2.2, two speaker locations were used for the final experiments. Actually, several speaker locations were tried, but the results showed that the only basic difference lay in whether the speaker induced excitations were in phase or somewhat asymmetric and out of phase in different regions of the test section.

A symmetric excitation field was obtained by placing the speakers at virtually any position or angle at a location downstream of the test section. With this orientation the speaker projected disturbances directly into the entire flow field. The excited disturbances were uniformly distributed and were basically in phase across the transition zone.

An asymmetric forcing field was generated by orienting the speaker upstream of the test section and in such a manner that it radiated directly into the upper stream while leaving the bottom stream undisturbed. The continuous upstream splitter plate isolated the two streams and made the technique feasible. As later measurements were to show, this phase asymmetry was a crucial factor in exciting the proper fundamental modes.

(c) Amplitude Response Curves of the Forced Transitions

The role of the symmetry (or asymmetry) of the excitation field was illustrated by measuring the amplitude response curves of the unstable oscillations when the flow was excited with both types of forcing fields. Amplitude response curves are experimentally made by position-

ing the probe at a given location in the shear layer and then incrementally increasing the frequency (but not amplitude) of forcing. The amplitude of the triggered mode of shear layer instability is noted, and plotted against frequency to give the amplitude response portion of the system's transfer function.*

The amplitude responses were measured for both asymmetric and symmetric forcing and are presented in figures 4.12 and 4.13 respectively. In the initial stages of transition, the asymmetric field tended to excite the same band of disturbances that were found to be naturally unstable. However, by $x = 5.00$ cm a tendency for lower modes near ω_{fs1} to be excited is evident, and by $x = 7.50$ cm lower frequency modes that tend to fit the free shear layer geometry are preferentially excited. This really says that if the upstream behavior had not been investigated we would conclude somewhat erroneously that the maximally unstable mode of the system was near ω_{fs1} . What we have really found is that ω_{fs1} is the locally preferred downstream mode. The second band of disturbance responses at $x = 6.00$ cm are those of the second harmonics of the free shear layer modes. Since this is a region of strong non-linear interactions, it is not surprising that harmonics can be directly excited.

The response curves for symmetric forcing demonstrated an entirely different behavior. Although a slight tendency for the excitation of the 20-30 Hz band of naturally unstable fundamental modes is evident in

* Note: Amplitude response curves are not equivalent to frequency spectra and will not make any sense if interpreted as such.

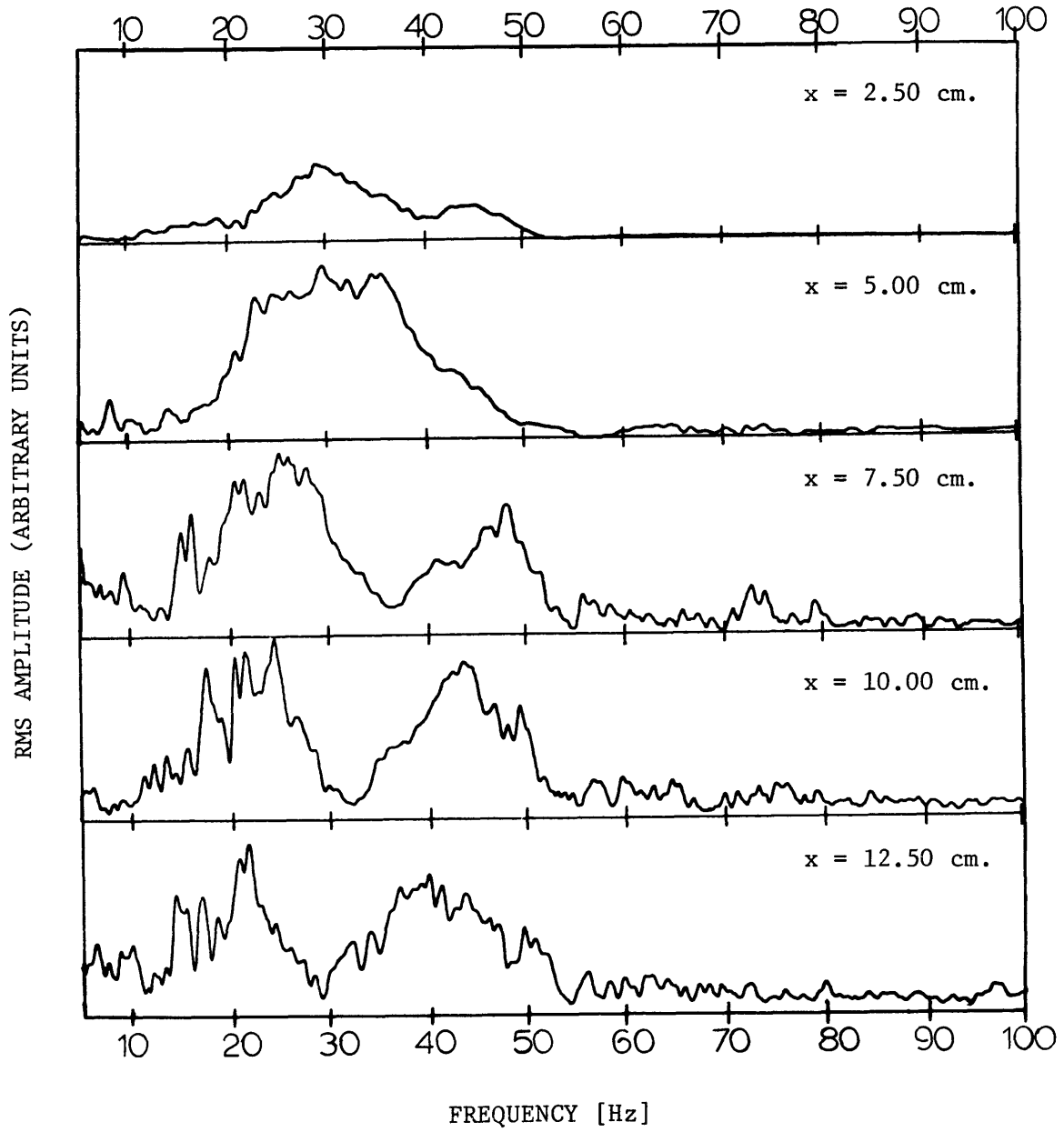


Figure 4.12: Amplitude response curves at different values of x when the shear layer is excited with an asymmetric forcing field. ($y = 0.4$ cm)

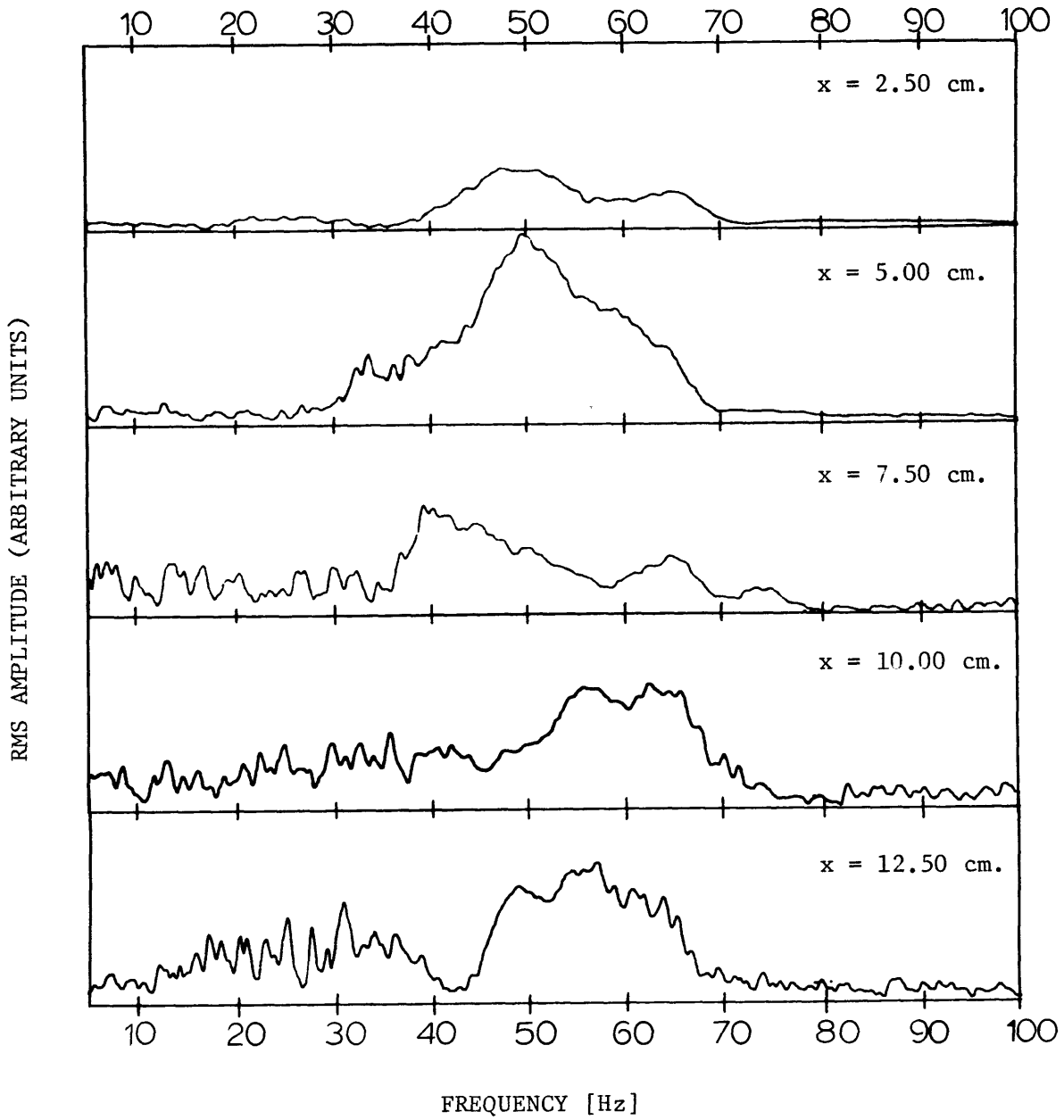


Figure 4.13: Amplitude response curves at different values of x when the shear layer is excited with a symmetric forcing field. ($y = 0.4$ cm)

the initial linear zone of transition, the maximum forced response is elicited from two bands of higher ordered modes centered about 49 and 65 Hz respectively. By 6.00 cm downstream, a double peaked response centered near the 2nd and 3rd harmonics of ω_{fs1} is found.

In general, it was clear that the symmetric forcing field tended to excite spurious higher order modes and not the modes preferred by the natural transition. Conversely, the asymmetric forcing preferentially excited the same instabilities that were observed in the natural transition.

It is also worth noting that with both types of forcing the maximally excited frequencies tend to drop with downstream distance, (i.e. note the gradual shift of the peak in figure 4.11 which at 7.50 cm is centered at 65 Hz and at 12.50 cm is at 55 Hz).

(d) Role of Excitation Field Phase Symmetry

As mentioned earlier and as later measurements verified, higher order non-linear modes have a greater tendency for symmetry of phase than do the fundamental modes which were all characteristically asymmetric in phase. One would intuitively expect then that the asymmetric forcing field would be more efficient in reinforcing the fundamental modes. This was verified by measuring the vertical phase and amplitude distributions of ω_{fs1} and ω_{II} when the flow was excited by the upstream and downstream speakers respectively. The results are shown in figure 4.14.

The phase distribution of the fundamental modes, when excited by the downstream speaker, showed a tendency for asymmetry, but were not strongly locked into phase with the forcing signal. Apparently, the fun-

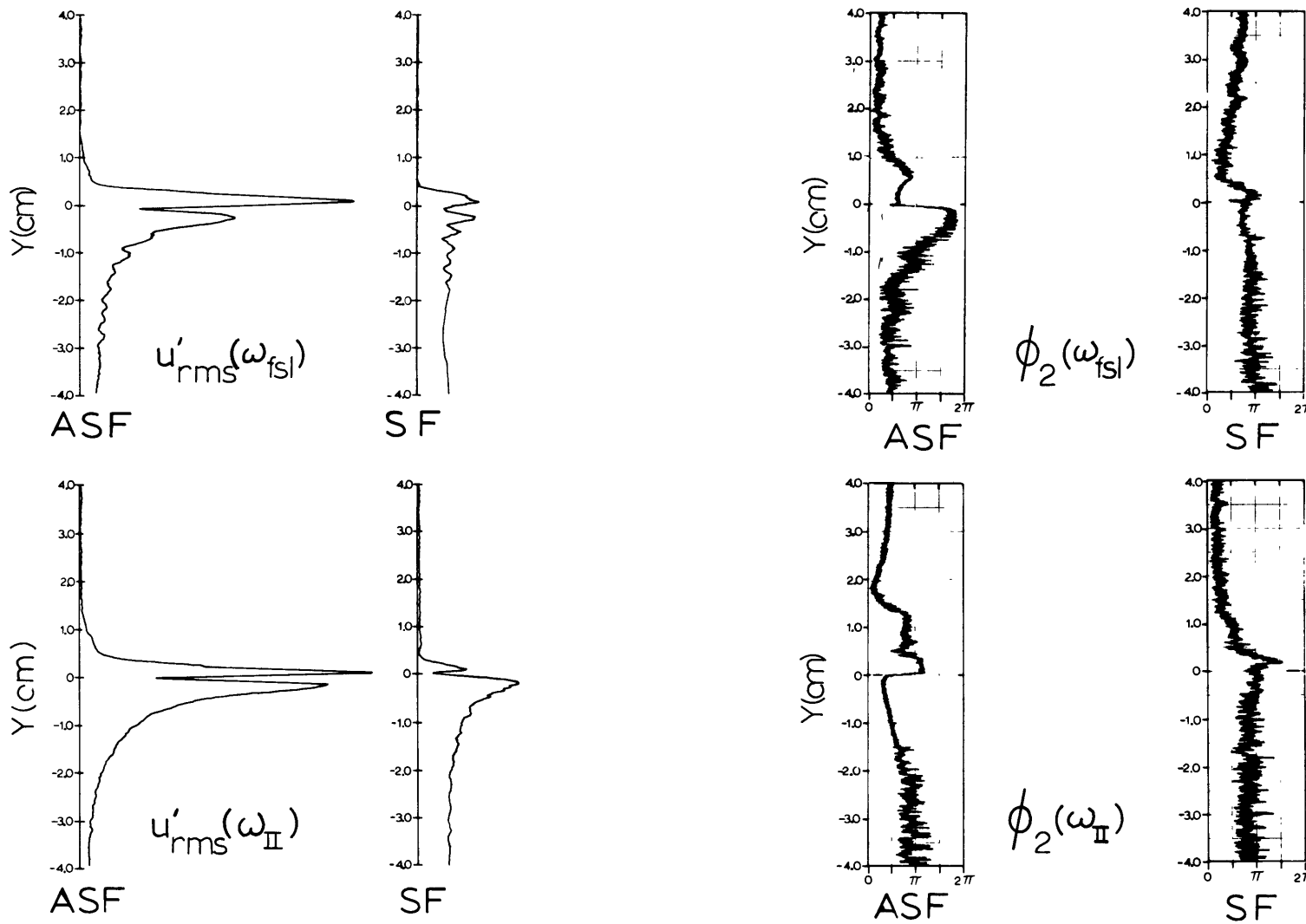


Figure 4.14: Vertical profiles of the u'_{rms} amplitudes and phase angles of the ω_{II} and ω_{fsl} forced modes. ASF-- asymmetric excitation field, SF-- symmetric excitation field.

damental modes resist the impressed symmetry and intermittently try to assert their asymmetric form; hence the noisy nature of the symmetric field phase plots.

Similar measurements for higher order harmonic modes showed that although they could be weakly reinforced by the asymmetric field of the upstream speaker, they were preferentially excited by the downstream speaker and showed a greater symmetry of phase.

The basic conclusion here is that the most unstable free shear layer mode which is experimentally observed is strongly asymmetric in phase. This agrees with the theoretical results for spatially growing free shear layers. One would intuitively expect the transition process may be altered if the preferred mode is not left free to seek its desired phase configuration. The results show that the fundamental mode exerts a strong tendency to establish an asymmetric distribution even if the impressed force field is symmetric in nature.

Except when expressly noted, following discussions of the forced transition will concern experimental data taken when the flow was excited by an asymmetric forcing field generated by the upstream speaker.

CHAPTER V

FORCED TRANSITION (QUANTITATIVE RESULTS)

The results of chapter IV demonstrate that the evolving nature of the shear layer exerts an influence on both the linear and non-linear regions of transition. This stimulated a study of the transition not only in terms of the most unstable mode ω_{II} of the initially asymmetric wake, but also in terms of the free shear layer mode ω_{fsl} whose harmonic modes seem to be favored for non-linear downstream reinforcement.

As will be evident from the data presented in this chapter, a comparison of the forced transitions of ω_{II} and ω_{fsl} will demonstrate some aspects of the influence of disturbance scale and local mean conditions on the linear and non-linear mechanisms involved in the transition. It will be seen that the ω_{II} mode exhibits the most clearly identifiable stages of transition as it passes from laminar instability to turbulent breakdown*. The overall transitions are similar in both forced cases. However, in some respects both forced transitions differ from that of the natural transition.

Pursuing these differences further, it was evident from the natural transition induced by a non-quasi white noise input that non-linear

*The term "turbulence" will only be used in the context of describing the flow when all modes present have lost any coherent relation to the excitation signal. Hence, it will be used as a euphemism for chaos and not for any profound scientific description.

combination modes play an important role. A controlled mixed mode experiment in which the flow is simultaneously forced at two frequencies, ω_A and ω_B , was conducted to study the importance of combination modes. The results gave a more representative picture of real life systems which are subjected to a multiplicity of disturbance inputs. The mixed transition presented an order of magnitude increase in complexity and only certain significant features were investigated.

In the material that follows the primary emphasis will be placed on obtaining a clear overall picture of the general transition process. The four experiments conducted here will be referred to as:

1. ω_N : Natural transition;
2. ω_{fs1} : Free shear layer transition;
3. ω_{II} : Initial wake transition;
4. $\omega_A + \omega_B$: Mixed mode transition.

In each forced transition an asymmetric forcing field is used to generate the initial disturbance field. The natural transition is assumed to be excited by a quasi-white noise disturbance input.

The specific details of the ω_{II} transition will be investigated more thoroughly than the other three cases, especially in terms of the influence of the mean flow field on the transition process. The ω_{II} transition will then be used as a vehicle for interpreting the ω_N , ω_{fs1} and $(\omega_A + \omega_B)$ transitions.

To avoid descriptive repetition, the data of all three forced transitions will be presented in this chapter en masse rather than in three isolated units. Most comments will pertain to the ω_{II} transition,

and the second half of this chapter will be entirely concerned with the details of the ω_{II} transition.

V.1 Initial Growth Rates and Most Unstable Forced Mode

A series of growth rate measurements were made (for asymmetric excitation) by setting the forcing oscillator at a given frequency and then observing the downstream growth of the excited oscillations at that frequency. Plots of the vertical variations of r.m.s. velocity were made and the values of the maximum peaks were used as a measure of growth rate. The experimentally determined growth rates, $-\alpha_i$, are plotted in figure 5.1 where:

$$u'(\underline{x}, t) = \sqrt{2} u'_{rms}(\underline{x}, \beta_r) e^{i(\alpha_r x - \beta_r t + \phi_2 + \phi_3)} e^{-\alpha_i x}$$

Also shown in figure 5.1 are the growth rates predicted by a linear stability model based on the mean profile at x_0 . The experimentally determined maximally unstable mode was at $\beta_r = 0.218$ while linear spatial and temporal theories predicted maximally unstable modes at $\beta_r = 0.2217$ and 0.2090 respectively. The theoretically predicted growth rates were in good agreement with experiment for small wave numbers, but were normally $\sim 20\%$ in error for the most unstable mode.

As the forcing frequency was extended beyond the most unstable mode, the growth rates decreased as theoretically predicted until at $\beta_r = 0.296$ when they started to increase again at much larger values than noted for the primary modes. These points represent the direct excitation of harmonic modes and are noted as darkened triangles. As indi-

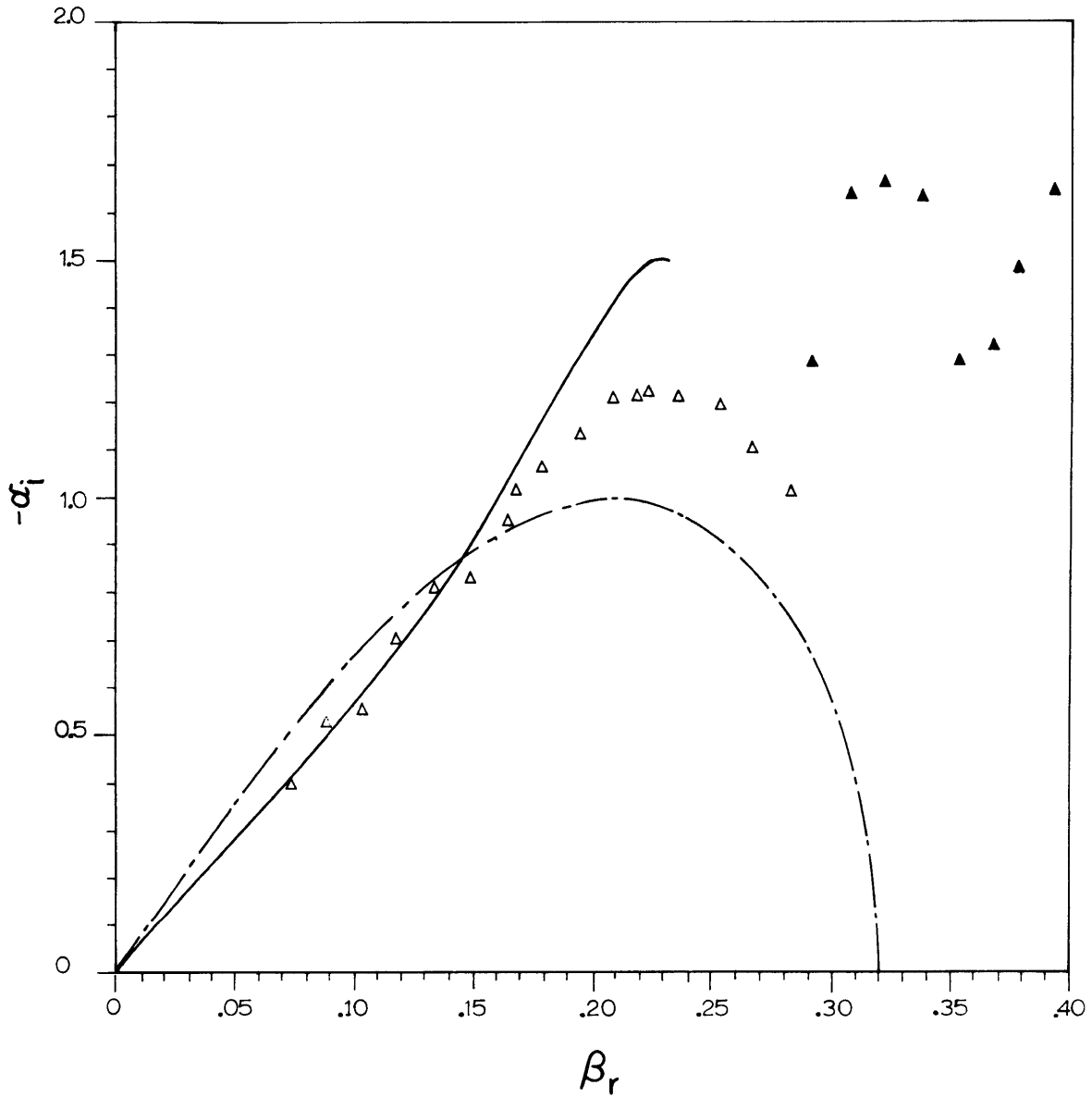


Figure 5.1: Spatial growth rates $-\alpha_1$ of the unstable fundamental modes in the linear region of transition. Asymmetric forcing field used for disturbance excitation. Darkened triangles are directly excited non-linear modes. (Δ -experimental points;—results of a linear spatial stability model;---results of a linear temporal stability model. Theoretical calculations based on the mean velocity profile at x_0 .

cated, two additional maximums were observed. One was centered directly at $\beta_r = 0.326$ which is close to the 2nd harmonic of ω_{fs1} ; the second peak appeared to be growing such that a maximum would be occurring near $\beta_r = 0.4350$ which is near the 2nd harmonic of ω_{II} .

An important point to note here concerns the observed location of initial growth. For all modes below $\beta_r = 0.296$, growth started immediately behind the plate, and continued to do so for at least 1.5 downstream wavelengths of the particular mode considered. However, the modes above $\beta_r = 0.296$ did not appear nor start to grow until a wavelength or more (again of the particular mode considered) of downstream distance had elapsed.

It is not clear why harmonic modes can be directly excited. However the crucial point here is that the asymmetric field preferentially excites the natural fundamental modes. The growths of these fundamental modes are basically described by linear theory. The additional fact that harmonic modes can be directly excited must be attributed to non-linear effects and will be discussed further in chapter VI.

V.2 Downstream Evolution of the Forced Transition Spectrum

The input spectra with and without forcing are shown in figure 5.7 for each experiment. The forced energy input, as stated earlier was just slightly larger than the overall natural r.m.s. turbulence level, and was sharply centered at the excitation frequency, or frequencies.

The downstream evolution of the forced transition spectra are shown in figures 5.9, 5.10, and 5.11 for the ω_{II} , ω_{fs1} and $(\omega_A + \omega_B)$ tran-

sitions respectively. One is immediately struck by the organizing effect of the forcing field on the transition spectra. Even the very slightest forcing acted to phase-lock or synchronize the disturbance fluctuations with the excitation field. With very slight forcing (i.e. \ll r.m.s. turbulence level) infrequent, but bothersome, phaseshifts would occur, and the final forcing amplitude was chosen to be the smallest amplitude which would eliminate most intermittent shifting.

(a) ω_{fs1} and ω_{II} Forced Transitions

The ω_{fs1} and ω_{II} transitions were characterized by their initial single frequency growth, the early appearance of clear 2nd and 3rd harmonics, and the later downstream emergence of intermittent sub- and 3/2-harmonics of the primary mode. A slight downstream tendency for ω_{fs1} to exert itself even when the flow is forced at ω_{II} was evident from $x=2.0$ to $x = 6.0$ cm. However, there seemed to be no tendency for ω_{II} to appear in the early stages of the ω_{fs1} forced transition spectra. It is interesting to note also how the ω_{II} forcing had a stronger organizing effect on the downstream transition spectra.

Although the ω_{fs1} spectra had more initial activity in the sub-harmonic and 3/2-harmonic range, the ω_{II} transition seemed more effective in generating strong 1/2 and 3/2-harmonics. In both cases, the exact frequency of the 1/2 and 3/2-harmonics which were reinforced by the transition constantly shifted in value. These modes were not as strongly phase related to the primary frequency as the higher harmonics were. Any attempt to measure the total energy content, or growth of the

sub and 3/2 modes required the use of a much broader band-pass filter (i.e. ± 5 Hz) than the sharply centered higher harmonics did (i.e. ± 0.5 Hz). The onset point of 3/2 and sub-harmonic generation could not be accurately determined from spectra measurements alone.

Measurements in the 100 Hz - 200 Hz frequency interval indicated the slight presence of 4th, 5th, and 6th harmonics in both transitions. However these were of small energy content and appeared for only a short distance (i.e. 7.0 to 13.0 cm) and quickly died away.

(b) $(\omega_A + \omega_B)$ Mixed Mode Transition

For these experiments, the flow was excited simultaneously by ω_{fs1} and ω_{11} . The amplitude of the two excitation inputs were equal and identical to the values used when the flow was singly excited. Both excitation signals were derived from the same reference signal by means of a solid state multiplier-divider circuit and had a constant phase angle relation to each other (see figure 5.8).

The most striking feature of the mixed transition is its extremely strong organizing effect. Instead of a shifting broad-band filling in of the spectra, very sharply centered frequencies are excited and reinforced. Not only do non-linear $n\omega/m$ ($n = 1, 2, 3 \dots; m = 1, 2$) modes appear for each of the two primary modes, but non-linear combination modes of the form $(n\omega_A/m + p\omega_B/q)$ ($n, p = 1, 2, 3 \dots; m, q = 1, 2$) appear. When in apparent competition with a sub-harmonic or 3/2-harmonic mode for energy input, these combination modes seem to win out and dominate the transition.

Growth rate measurements showed that ω_A and ω_B grow exponentially in the initial wavelength of transition at the same rates that ω_{fs1} and ω_{II} did in their singly forced transitions. It was also evident that even though ω_{fs1} was found to grow to larger amplitudes than ω_{II} in the single experiments, $\omega_B \wedge \omega_{II}$ grew to much larger values than $\omega_A \wedge \omega_{fs1}$ did. As with the singly forced experiments, non-linear modes did not appear for at least a wavelength of downstream distance. The first non-linear modes to appear in the spectra were $(\omega_A + \omega_B)$ and $[\omega_A + (\omega_A + \omega_B)]$, with the spectrum quickly filling in after that with $(\omega_B - \omega_A)$ and various other discrete modes. As shown in figure 5.12 higher frequency combination modes were also generated in the 100 to 200 Hz range. However, their spatial extent and energy contents were much less than the lower frequency modes.

As a curiosity measurement, the transition sequence when the flow was directly excited at $(\omega_B - \omega_A)$ was observed. As shown in figure 5.13 rather than causing the preferred growth of $(\omega_B - \omega_A)$, the excitation caused ω_A and ω_B to grow instead.

(c) Summary of Observed Interactions with Asymmetric Field Forcing

Shown below are three representative spectra taken from the ω_{fs1} , ω_{II} and $\omega_A + \omega_B$ transitions. The probable relation of the various non-linear modes to the forced fundamentals are indicated. Although the weak presence of some modes, such as $\omega_A/2$, $\omega_A + \omega_B/2$, etc., were detected in other regions of the flow, their activity was limited, and their small energy content made a detailed search unrewarding. Table 5.1 lists the significant interactions observed in the three forced transition ex-

Table 5.1:

Maximum r.m.s. amplitudes and signal clarity for the various modes observed in the ω_{II} , ω_{fs1} , and $(\omega_A + \omega_B)$ transitions.

| ω_{II} Transition | | | |
|--------------------------|-----------------------------|--------------------------------------|----------------|
| <u>Mode</u> | <u>β_r</u> | <u>Max u'_{rms} (%)</u> | <u>Clarity</u> |
| ω_{II} | 0.2183 | 12.5 | Very sharp |
| $\omega_{II}/2$ | 0.1091 | 13.0 | Intermittent |
| $3\omega_{II}/2$ | 0.3273 | 4.0 | Intermittent |
| $2\omega_{II}$ | 0.4366 | 5.0 | Very sharp |
| $3\omega_{II}$ | 0.6549 | 2.0 | Sharp |

| ω_{fs1} Transition | | | |
|---------------------------|-----------------------------|--------------------------------------|----------------|
| <u>Mode</u> | <u>β_r</u> | <u>Max u'_{rms} (%)</u> | <u>Clarity</u> |
| ω_{fs1} | 0.1665 | 15.5 | Very sharp |
| $\omega_{fs1}/2$ | 0.0833 | 13.0 | Intermittent |
| $3\omega_{fs1}/2$ | 0.2499 | 3.0 | Intermittent |
| $2\omega_{fs1}$ | 0.3330 | 7.0 | Very sharp |
| $3\omega_{fs1}$ | 0.4995 | 3.5 | Sharp |

Table 5.1:

(continued)

| $(\omega_A + \omega_B)$ Transition | | | |
|---|-----------------------------|--------------------------------------|-----------------------|
| <u>Mode</u> | <u>β_r</u> | <u>Max u'_{rms} (%)</u> | <u>Clarity</u> |
| ω_A | 0.1627 | 3.5 | Very sharp |
| ω_B | 0.2170 | 11.0 | Very sharp |
| $(\omega_B - \omega_A)$ | 0.05417 | 15.0 | Sharp |
| $\omega_A/2$ | 0.08133 | | Very intermittent |
| $\omega_B/2$ | 0.10848 | 8.5 | Intermittent |
| $\omega_A + \omega_B/2$ | 0.27114 | 3.0 | Sharp |
| $3\omega_B/2$ or $2\omega_A$ | 0.3255 | 1.2 | Somewhat intermittent |
| $\omega_A + \omega_B$ | 0.3796 | 2.0 | Sharp |
| $2\omega_B$ or $2\omega_A + \omega_B/2$ | 0.4338 | 4.6 | Very sharp |
| $3\omega_A$ | 0.4880 | 1.25 | Sharp |
| $2\omega_A + \omega_B$ | 0.5423 | 1.1 | Somewhat intermittent |
| $2\omega_B + \omega_A$ | 0.5966 | 1.2 | Sharp |
| $3\omega_B$ | 0.6509 | 1.25 | Sharp |
| $3\omega_A + \omega_B$ | 0.7049 | 1.0 | Sharp |
| $2(\omega_A + \omega_B)$ | 0.7592 | 0.75 | Somewhat intermittent |
| etc. | | | |

periments. As will be evident from the r.m.s. velocity distributions presented in the next section, some modes were more strongly reinforced than others. As a precursor to the data that follow an indication of the characteristic maximum amplitude and relative clarity of signal (i.e. lack of intermittency and sharpness of energy concentration) be noted for each mode.

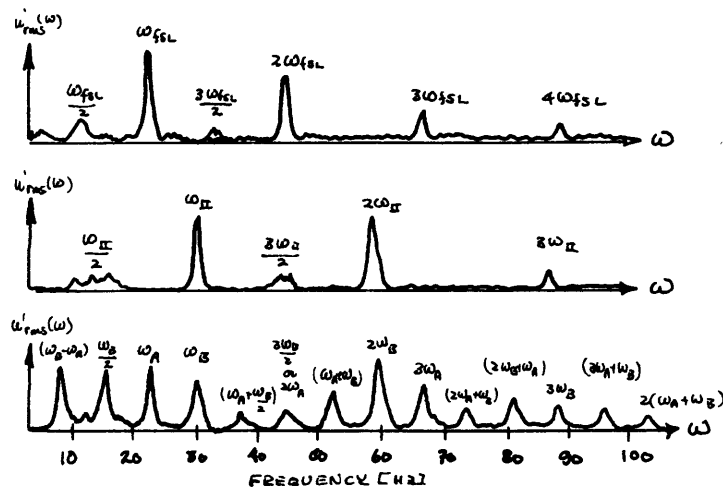


Figure 5.2: Significant modes observed in the ω_{fs1} , ω_{II} , and $\omega_A + \omega_B$ transitions.

(d) Transition Spectra with Symmetric Field Forcing

As discussed in chapter IV, when a symmetric excitation field is used the maximally unstable forced mode was found to be $2\omega_{fs1}$, the second harmonic of ω_{fs1} . A series of downstream spectra are shown in figure 5.14 for the transition excited by forcing directly at the second harmonic of ω_{fs1} . The excited $2\omega_{fs1}$ mode did not start to grow until about a wavelength of downstream distance had elapsed (i.e. $\lambda[2\omega_{fs1}] \sim 1.3$ cm). It was quite interesting to see that the flow followed the same sort of transition sequence as it did when forced at a primary mode frequency

such as ω_{fs1} or ω_{II} . Second and third harmonics of the forced $2\omega_{fs1}$ signal appear along with strong sub- and 3/2-harmonics; a later downstream preference for $\omega_{fs1}/2$ (i.e. the sub-harmonic of the sub-harmonic of the forced $2\omega_{fs1}$ mode) is quite noticeable.

Shown in figures 5.15 and 5.16 are the ω_{II} and ω_{fs1} transitions excited by a symmetric forcing field. A notable degree of intermittency is apparent.

V.3 Downstream Evolution of the Unstable Disturbance Field

(a) Evolution of the R.M.S. Velocity Field

The downstream variations of the r.m.s. values of the $u'(x,y)$ velocity field amplitude distributions are shown in figures 5.22→5.26, 5.28→5.32, and 5.34→5.41 respectively for the significant frequency components observed in the ω_{II} , ω_{fs1} and $(\omega_A + \omega_B)$ transitions. Each plot is the result of a series of continuous vertical traverses across the shear layer. Traverses were made at 0.5 cm downstream intervals. The velocity fields of the $\omega_{fs1}/2$, $3\omega_{fs1}/2$, $\omega_{II}/2$, and $3\omega_{II}/2$ modes were made with a ± 5 Hz filter band in order to compensate for their broad band intermittency. A ± 0.5 Hz filter band was used for the more sharply centered modes. The amplitudes of the r.m.s. longitudinal fluctuations are normalized with the free stream velocity of the top stream (i.e. 200 cm/sec) and are plotted in terms of percentage value [i.e. $(u'/U_T) \cdot 100$].

The plots are presented in an isometric orthographic form for compactness. This format allows an immediate overall picture to be ob-

tained for the downstream evolution of each mode in the transition sequence. Because the plotted surface is considered opaque and hidden points (i.e. those behind a peak, etc.) are deleted, many interesting features are lost from projections made from one viewing angle. Thus, two projections, as noted below, are presented.

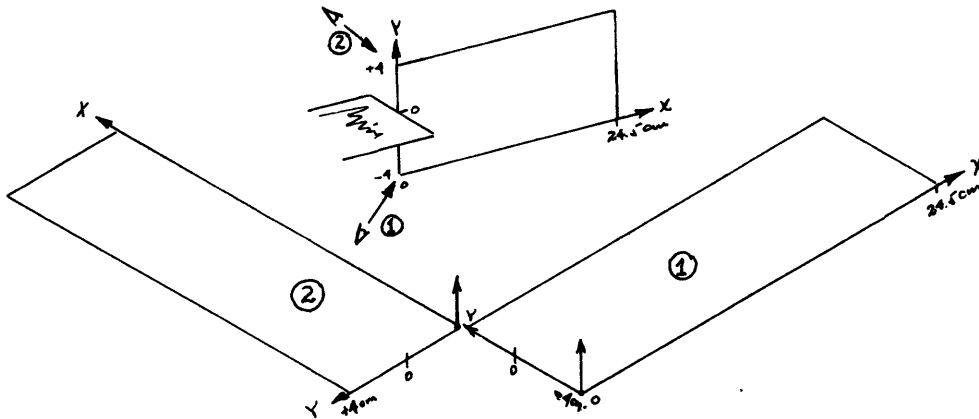


Figure 5.3: Coordinate viewing angles for the contour and 3-D isometric-orthographic data plots.

The overall view provided from two viewing angles demonstrates that other than in the initial stages of transition, it can be misleading and very difficult to obtain a measure of disturbance growth and evolution by following the growth of a given peak, or by measuring the maximum amplitude at each section (i.e. peaks appear, grow and decay and new ones arise at many virtual origins). Also, even in the linear zone of transition, the peaks of a given disturbance were found to grow at different rates.

(b) Maximum Values of the R.M.S. Velocities

Figures 5.42, 5.43 and 5.44 show the downstream evolution of the maximum u'_{rms} amplitudes of the various spectral components in each forced transition. It was surprising to note that most of the non-linear modes grew exponentially in their initial stages of evolution (although this was not completely clear for the 1/2- and 3/2-harmonics). The non-linear modes all abruptly appeared at about one downstream wavelength of the fundamental and grew simultaneously with the primary mode. The 2nd and 3rd harmonics of ω_{fsl} and ω_{II} grow to a finite equilibrium amplitude, remain there for a while, and then decay. However, the sub- and 3/2-harmonics seem to reach an initial equilibrium state, and then start growing again. This same behavior is found in the $(\omega_B - \omega_A)$ and $\omega_B/2$ plots for the mixed transition.

(c) Evolution of the Vertically Integrated Disturbance Energy

The spreading of the disturbance modal structures with downstream distance made it clear that the total energy of a given spectral component could increase even if the peak values did not. Also, some vertical distributions have more peaks than others (i.e. different modal structures) and hence can differ in total energy content from a similarly distributed mode with less, or broader peaks (i.e. compare the four distributions shown below).

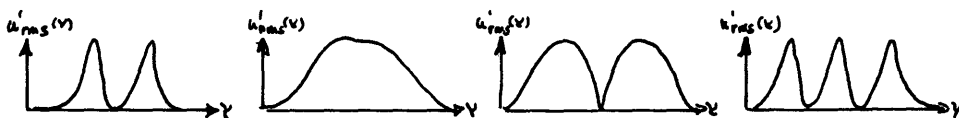


Figure 5.4: Four r.m.s. modal shapes that have the same r.m.s. maximums but different energy contents.

A meaningful way to compare the energy content of various modal shapes is to use an integral measure to eliminate the precise spatial details. An integral energy measure

$$EM(x, \omega_j) = \int_{y=-\infty}^{y=+\infty} \frac{u'_{rms}(x, \omega_j)^2}{U_T^2} \frac{dy}{2\theta_m(x_0)}$$

was used to compare the overall downstream growth of the various modes. $EM(x, \omega_j)$ gives a measure of the u'_{rms} energy content of a given disturbance whose frequency is centered at ω_j .

As a measure of total u'_{rms} disturbance energy, the integrated energies of all modes present were summed at each downstream station.

$$E(x) = \sum_j EM(x, \omega_j)$$

This is a reasonable measure for a disturbance field comprised mainly of discrete modes.

Figures 5.45, 5.46 and 5.47 show the growth of $EM(x, \omega_j)$ for the various significant modes in the three experiments. The total disturbance energy $E(x)$ is plotted in figure 5.48. These curves will be discussed in the next chapter. However, several points of interest can be noted. One immediately notices that the vertical integral of disturbance energy does provide a useful measure of disturbance growth. The scatter observed in the u'_{rms} plots has been eliminated by the integration.

The energy plots exhibit the same basic behavior as the r.m.s. amplitude measurements. Equilibration zones and regions of exponential

growth are present in both the r.m.s. and energy curves. As indicated in figure 5.46, six basic stages of transition can be identified for the ω_{II} transition. These stages are identified as regions I through VI and are extensively discussed in the next chapter.

The disturbance energy grows as the square of the disturbance amplitudes, thus the downstream growth rate of disturbance energy will be proportional to $\exp(-2\alpha_i x)$. Both the r.m.s. and energy curves have been used to calculate disturbance growth rates. The growth rates, regardless of which curves were used, will always be stated in terms of $-\alpha_i$, the u'_{rms} growth rate. To obtain energy curve growth rates one need only multiply by a factor of two.

As has been pointed out by Stuart (1960a) and Kelly (1967) among others, it is often convenient to consider the energy growth in terms of odd and even multiples of the sub-harmonic. The total u'_{rms} energy contained in the odd and even disturbances are presented in figures 5.49 and 5.50 where

$$\begin{aligned} \text{EM (odd)} &= \sum_n \text{EM} \left(x, \frac{\omega_n}{2} \right) & (n = 1, 3, 5 \dots) \\ \text{EM (even)} &= \sum_m \text{EM} \left(x, \frac{\omega_m}{2} \right) & (m = 2, 4, 6 \dots) \end{aligned}$$

V.4 Downstream Evolution of the U(x,y) Mean Velocity Fields

The downstream development of the U(x,y) mean velocity fields are shown in figure 5.17 for the ω_{II} transition and in figures 4.7, 5.27, and 5.33 for the ω_N , ω_{fs1} and $(\omega_A + \omega_B)$ transitions respectively. It is quite clear from both the profile evolution and the respective contour

plots that the evolution of the mean flow is dependent upon the particular transition being studied and hence the disturbance modes which are present. For example, the mean flow abruptly spreads at about $1.0\lambda_{II}$ and $1.0\lambda_{fs1}$ in the ω_{II} and ω_{fs1} transitions, and at $1.0\lambda_B$ where ($\lambda_B \sim \lambda_{II}$) for the mixed mode transition.

V.5 Further Details of the ω_{II} Transition

(a) Additional Details of the ω_{II} Transition Mean Flow

The mean vertical velocity field $V(x, y)$ is shown in figure 5.18. The amplitude scale has been stretched relative to the $U(x, y)$ plots, so for comparison's sake $V(x, y)$ is emphasized out of proportion. A small vertical velocity ($V/U_T \sim 2-6\%$) is observable at the test section entrance and may account for the slow spreading of the initial wake. This up-flow dies off within a wavelength and in fact the spreading of $U(x, y)$ at $\sim 1.0\lambda_{II}$ is reflected in an outward (i.e. away from the center line) mean vertical velocity. The final transition to turbulent motion at $\sim 5\lambda_{II}$ is also accompanied by a spreading of $U(x, y)$ and a strong outward vertical velocity field (i.e. $V/U_T \sim 2-12\%$). Note also, that the equilibration region between $x = 1.8\lambda_{II}$ and $x = 3.20\lambda_{II}$ is marked by a slight ($\sim 2\%$) vertical inflow.

The alteration of the stability characteristics of the ω_{II} mean flow due to the merging of the two layers and the subsequent downstream re-distribution of mean vorticity can be seen in figures 5.19 and 5.20. These figures show the evolution of the mean vertical shear profiles

(i.e. spanwise vorticity) with downstream distance. The dominant influence of the upper shear layer (arbitrarily taken as positive vorticity) and the gradual elimination of the bottom layer inflexion point (i.e. negative vorticity) are clearly evident. The maximum shear is sharply centered and closely approximates a vortex sheet. The vertical vorticity distribution spreads extremely slowly in the initial wavelength of transition. The presence of rather odd appendages to the contours in figure 5.20 are due to the approximation schemes used in the computer contour program.

A useful indication of just how a shear layer is evolving is to measure the downstream momentum gradients, or equivalently $\partial U/\partial x$. The downstream distribution of $\partial U/\partial x$ is given in exaggerated scale in figure 5.21.

(b) Downstream Phase Variations

As discussed more fully in appendix A.3, cyclic variations of phase in the downstream flow direction (see figure 5.51) are normally interpreted in terms of wavelength. Local variations in wavelength were measured by graphically reproducing the standard experimental technique of wavelength measurement (i.e. pick a reference point, x_r , note the phase reading there, then move the probe downstream until the initial phase angle is repeated). Graphically, this corresponded to picking a given point, noting the phase angle and drawing a straight line parallel to the x-axis. Where it intercepts the same value of phase on the next sloping segment of the curve is 2π radians, or one inferred wavelength downstream. Figure 5.52 shows the downstream contours of phase for the

ω_{II} transition in the initial 15.00 cm of flow.

It is evident from the phase contours that a word or two of explanation is in order. What are really shown are the contours of downstream phase variation as observed by an observer riding with the phase velocity of ω_{II} . These are the famous "cat's eyes" of Kelvin which are schematically illustrated below, and discussed further in appendix A.3.

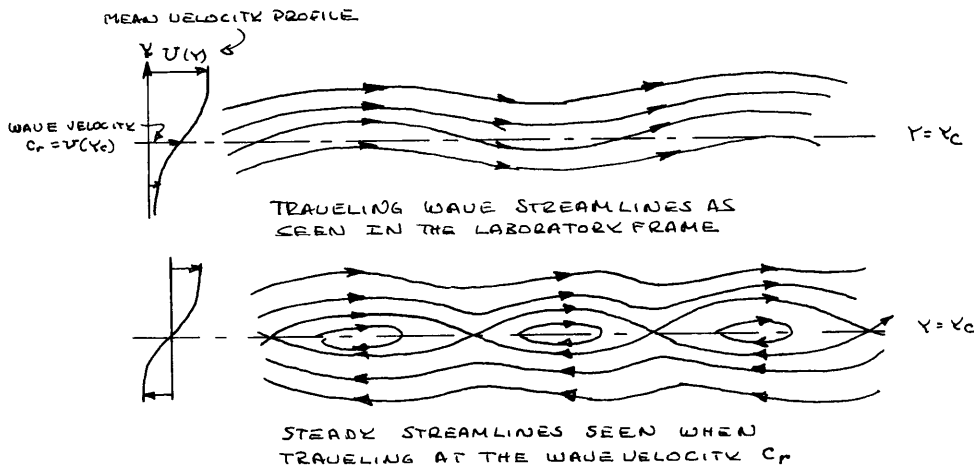


Figure 5.5: Schematic representation of the Kelvin cat's eyes seen by an observer moving with the disturbance wave velocity.

It is felt that past researchers have not appreciated the true meaning of their wavelength measurements (as made by phase repetition) and apparently large scatters in their reported data may be due to the cat's eyes effect (i.e. phase measurements near the critical layer, y_c , will yield smaller apparent wavelengths etc.).

It is interesting to note that the closed contours which should represent the location of the critical layer are located near the plate

center line rather than slightly above it where $U(y_c) = c_r$. It seems that the cat's eyes in this asymmetric wake are centered at the point where the average convective velocity of the two layers equals the disturbance phase velocity (i.e.)

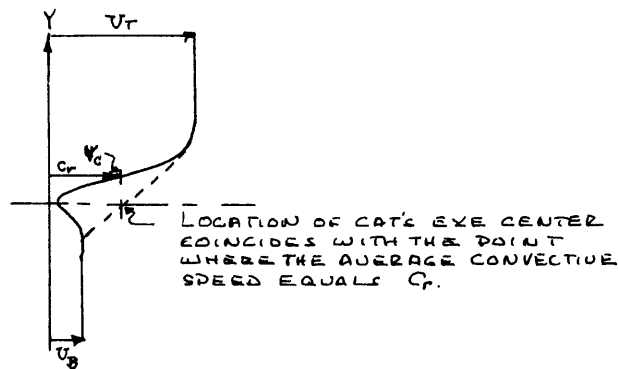


Figure 5.6: Location of the experimentally measured critical layer and the theoretically predicted location, y_c .

The wavelengths are seen to vary with downstream distance and vertical location. However the characteristic streamwise scale of succeeding cat's eyes are relatively similar. For a simple wave train the cat's eye extent would equal the disturbance wavelength, and for lack of a better indication the scale of the cat's eyes will be taken as being representative of fundamental mode wavelength.

The vertical extent of the closed contours gives an indication of the critical layer thickness. Based on the cat's eyes contours the critical layer thickness of the ω_{II} mode is of the order of 0.3 cm. This compares favorably with the theoretically predicted value for ω_{II} which is of the order $(\alpha R)^{-1/3} \sim 0.3$ cm.

(c) Vertical Phase Variations

Shown in figures 5.53 to 5.56 are the variations in phase across the shear layer at each downstream station where a traverse was made. The phase shifts are measured relative to the speaker-induced oscillations at the reference point x_r in the free stream just above the splitter plate edge.

Note that the phase measurements were made by exciting the transition at ω_{II} . The resulting probe signal was filtered to isolate a desired $n \omega_{II}/m$ frequency component. The reference ω_{II} excitation signal was multiplied and divided to give a reference signal of frequency $n\omega_{II}/m$ for comparison with the filtered probe signal. Hence the measurements represent the actual phase relations between the various modes in the ω_{II} transition, and not the phase development when the flow is forced at $n \omega_{II}/m$.

The initial phase distribution of ω_{II} as measured just behind the splitter plate had a very strong 180° asymmetric phase shift. The first few stations were made with high amplification rates and the early profiles probably reflect the phase distribution of the speaker-induced oscillations.

The rapid growth of the unstable ω_{II} mode is reflected in the abrupt formation of a very complex phase profile. This basic profile persisted until ω_{II} reached an equilibrium amplitude at about $x = 11.00$ cm. Here, a strong 180° shift is again established. Smoke pictures showed the formation of a possible discrete vortex structure in this region. In the last wavelength of transition, the phase of ω_{II} became

very intermittent and gradually lost its asymmetric structure. The cat's eye effect is also evident in these as a sausage like necking of the phase profiles with downstream distance.

The phase distributions for $\omega_{II}/2$, $3\omega_{II}/2$ and $2\omega_{II}$ require some qualifying comments. All three modes show phase distributions (and hence implied modal activity) in the initial wavelength of transition. This is in contrast to the energy, and r.m.s. plots which do not indicate any activity in these modes during the first wavelength of transition. This dichotomy can be attributed to several factors. Most important is the fact that the phase meter circuitry required a minimal 500 mv signal for successful operation. Consequently a high gain A.C. amplifier was used to bring the probe signal to the level necessary for comparison with the reference signal. Hence any spurious modes, no matter how small, were to all intents treated as a real 500 mv signal by the meter. The region immediately behind the splitter plate may have contained some spurious oscillations near the frequencies of the harmonic modes, and the meter may have registered the phase of these small but spurious disturbances.

In all three cases, one notices a tendency for the harmonic mode phase profiles to take on a definite character at about $x=3.0$ cm. This is near the point at which non-linear modes first appear in the energy plots.

Since the phase meter will only give a clear steady output voltage when the input frequency exactly matches the reference signal, it is felt that the accuracy of those portions of the phase plots which do not

exhibit a great deal of noise or scatter represents the actual behavior of the desired mode.

A surprising feature of the sub-harmonic behavior is the presence of 90° phase shifts. This indicates a sloshing type behavior where the upper stream sub-harmonic oscillations occur with no bottom stream action and vice versa. This tendency persists until the sub-harmonic begins its second region of growth and loses any coherent phase relation to the ω_{II} forcing signal.

The second harmonic oscillations have a very complex phase structure with less abrupt phase shifts. The sharp 180° jumps exhibited by the primary modes do not appear. Instead more gradual variations occur. The poor phase relation between $2\omega_{II}$ and the $2\omega_{II}$ reference signal (which was derived from the ω_{II} forcing signal) was not expected since the second harmonic is the clearest and most strongly centered non-linear mode present in the transition. Whether the poor phase relation is due to the electronic processing, or really indicates a lack of real phase dependence with the primary is not clear.

(d) Three-Dimensional Structure

Cross-stream variations of the ω_{II} r.m.s. disturbance amplitudes, and the spanwise phase angle $\phi_3(\omega_{II})$ were measured at various vertical levels for selected downstream stations. Downstream intervals of 2.5 cm (i.e. $\sim 0.57\lambda_{II}$) were chosen for analysis.

Perhaps the best indicator of spanwise distortion is the spanwise phase angle ϕ_3 of the primary fluctuation. R.m.s. wavefront distortions can be a misleading indicator. This fact was demonstrated by the verti-

cal r.m.s. profiles of the sub-harmonic mode. The r.m.s. profiles gave no indication of the sloshing behavior which was evident from its vertical phase measurements.

The cross-stream phase variations of the primary mode are shown in figures 5.57 to 5.60. Also shown are the cross-stream variations of the r.m.s. probe voltage (i.e. the variation of the r.m.s. level of the fluctuations across a wave front). It must be noted that the r.m.s. plots are arbitrarily scaled and are not representative of the absolute values of velocity fluctuations. They only show the qualitative distortion of the wave front in comparison to the phase distribution. The magnitude of the r.m.s. distortions have been magnified for visual comparison.

Initial measurements showed that the first indication of spanwise variations in phase coincided with the equilibration of the fundamental mode at $1.8\lambda_{II}$. The spanwise phase distributions (solid lines) in the linear and weakly non-linear regions were relatively flat across the tunnel. For example, the only variations observable at $x = 5.00$ cm are those accompanying the abrupt vertical phase shift across the center line. The scatter at $y = 0.025$ cm may be due to a low frequency shifting of the shear layer cat's eyes. Some spanwise variations of wave front r.m.s. amplitude (dashed lines) are present at $x = 5.00$ cm, and may reflect a pre-existing spanwise variation in the entrance streams. However, measurements made at the test section entrance showed no significant spanwise r.m.s. variations.

Within one and a half wavelengths downstream (i.e. near 7.5 cm)

phase variations were observed at the center line and distortions of the r.m.s. distribution became more emphasized. However, no strong cyclic cross-stream wave structure existed and it is questionable if three-dimensional mechanisms are being brought into play. This point marked the beginning of the equilibration zone.

At $x = 10.00$ the flow actually tends to revert to a more two-dimensional structure with variations in phase and r.m.s. values being less severe. This station is within the equilibrium amplitude zone.

At $x = 12.50$ cm, in coincidence with the onset of strong sub-harmonic growth, the flow again tends to lose its two-dimensional structure. By $x = 15.00$ cm it has reached a highly distorted spanwise structure, 180° spanwise phase changes appear. This highly distorted spanwise structure is reinforced with downstream distance until at $x = 17.50$ cm the entire central portion of the shear layer is strongly three-dimensional.

In summary then it appears that three-dimensional effects are not present in region I nor for the greatest portion of II. However, they seem to weakly appear just prior to the onset of the equilibrium region, III, disappear during region III and again appear in increasing severity in regions IV and V. Spanwise phase measurements were not made in region VI and one can only speculate that the three-dimensionality increased in severity.

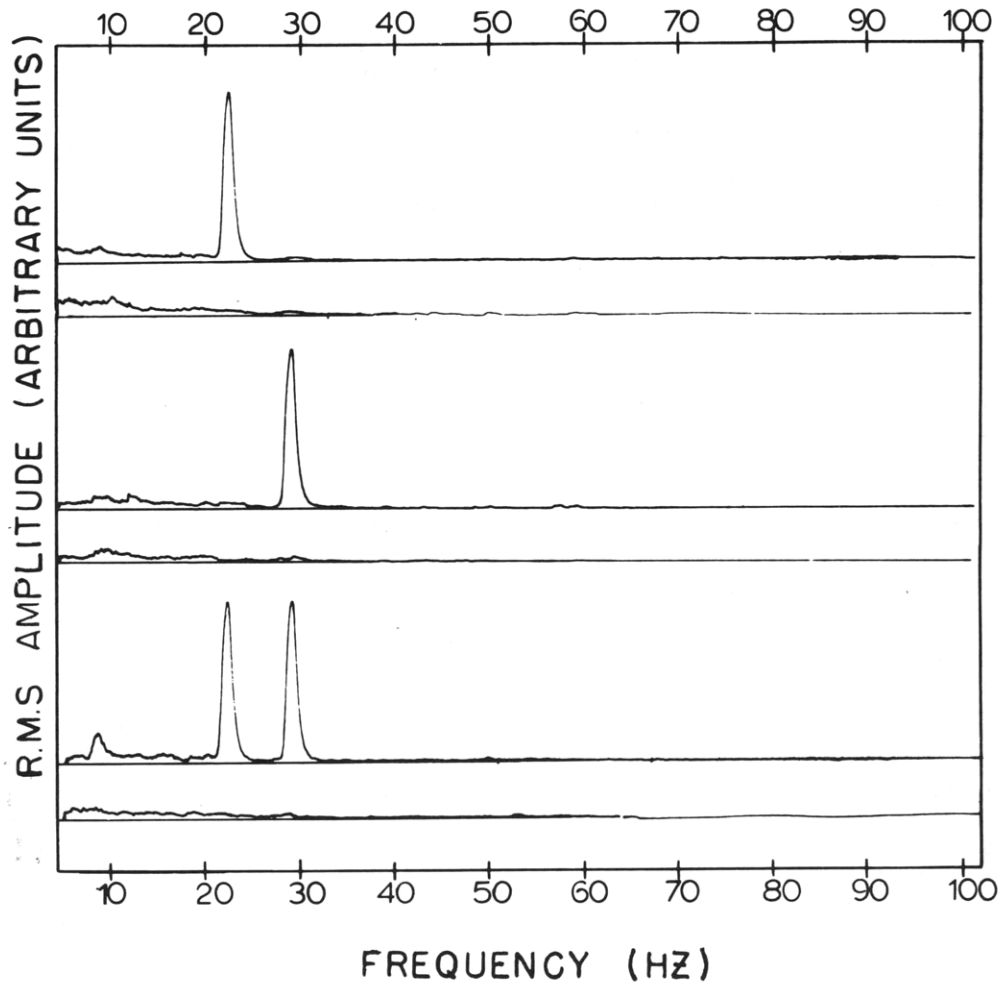


Figure 5.7: Influence of the forced excitation field on the input spectra at the test section entrance. The natural input noise spectra is shown below each forced spectra. (x=0.0, y=4.0 cm)

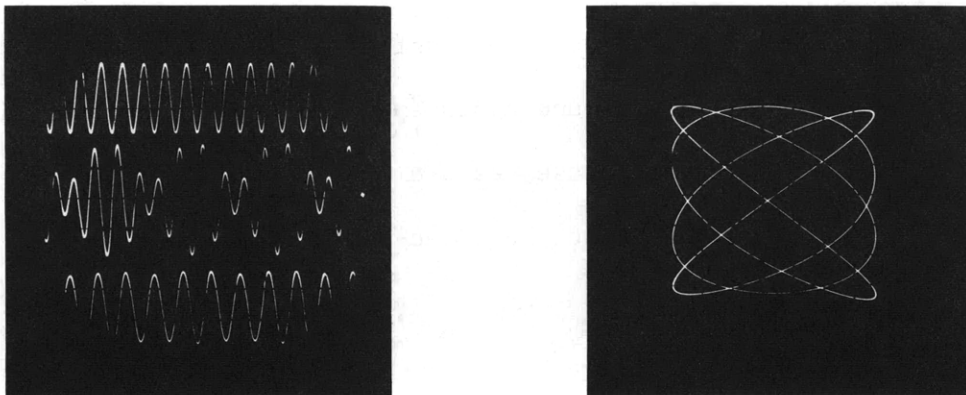


Figure 5.8: (a) Excitation signals of the ω_{II} , $\omega_A + \omega_B$, and ω_{fs1} transitions. (b) Lissajous phase pattern between the ω_A and ω_B excitation signals in the mixed mode transition.

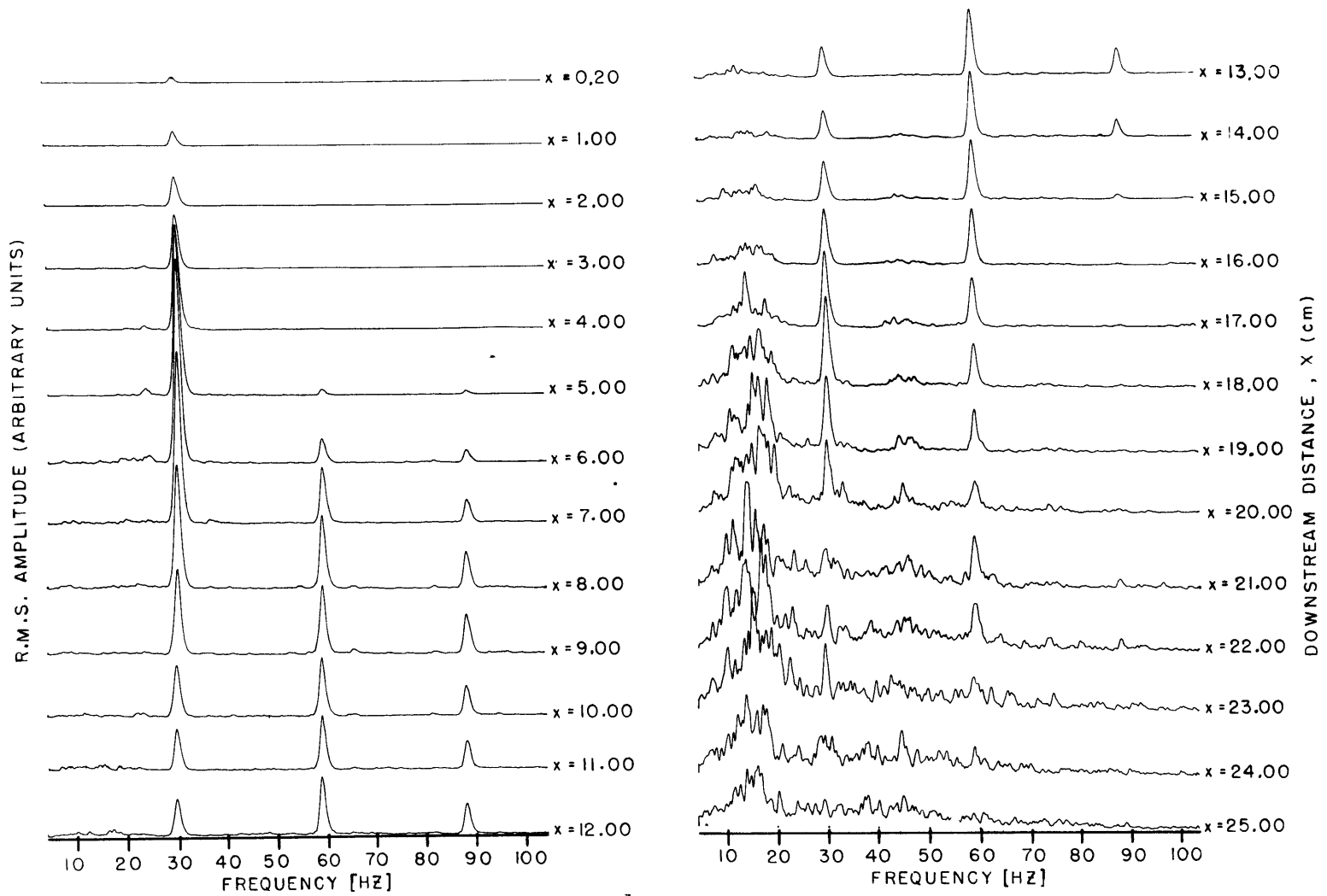


Figure 5.9: Downstream frequency spectra of the ω_{II} forced transition ($y = 0.2$ cm).

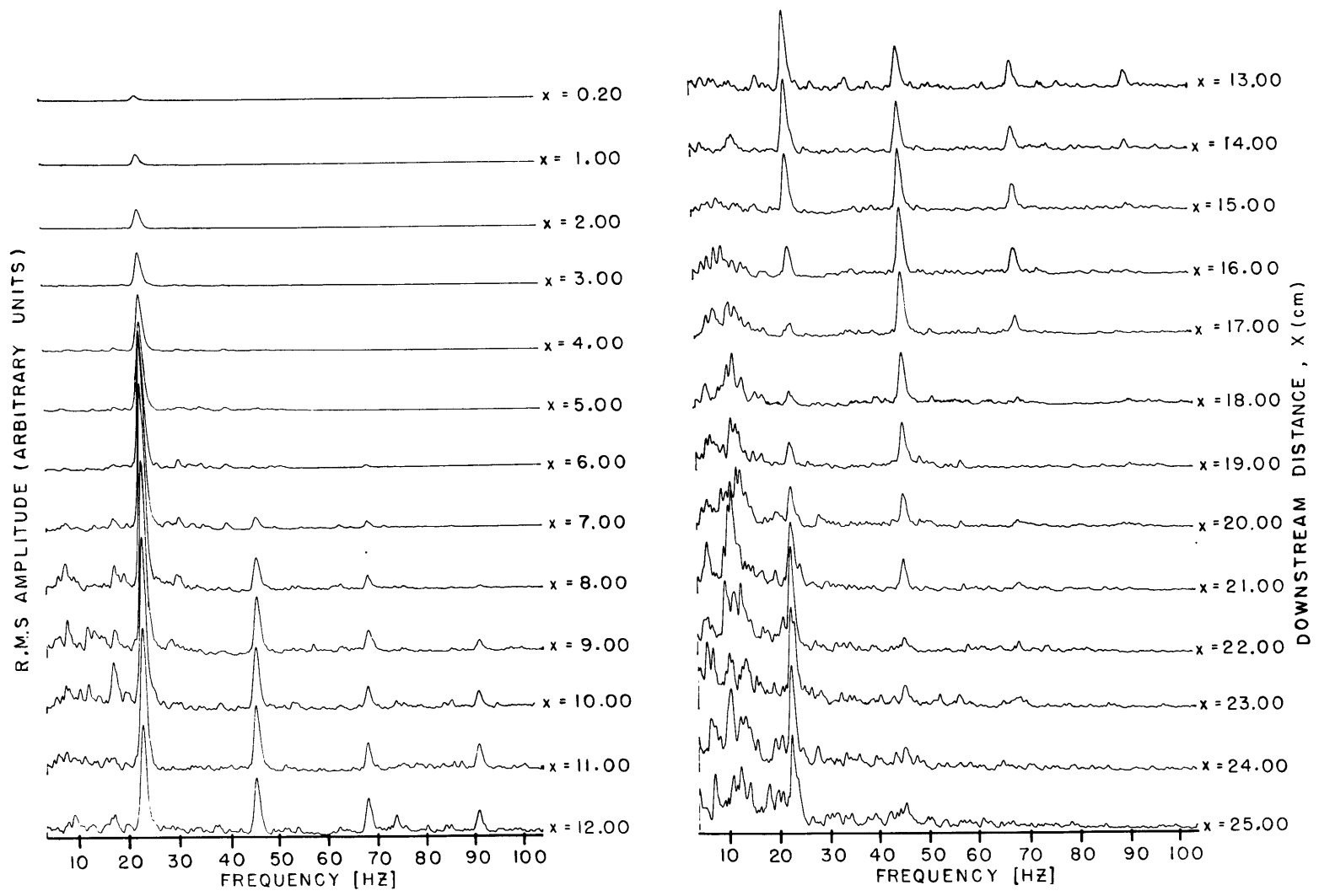


Figure 5.10: Downstream frequency spectra of the ω_{fs1} forced transition ($y = 0.2$ cm).

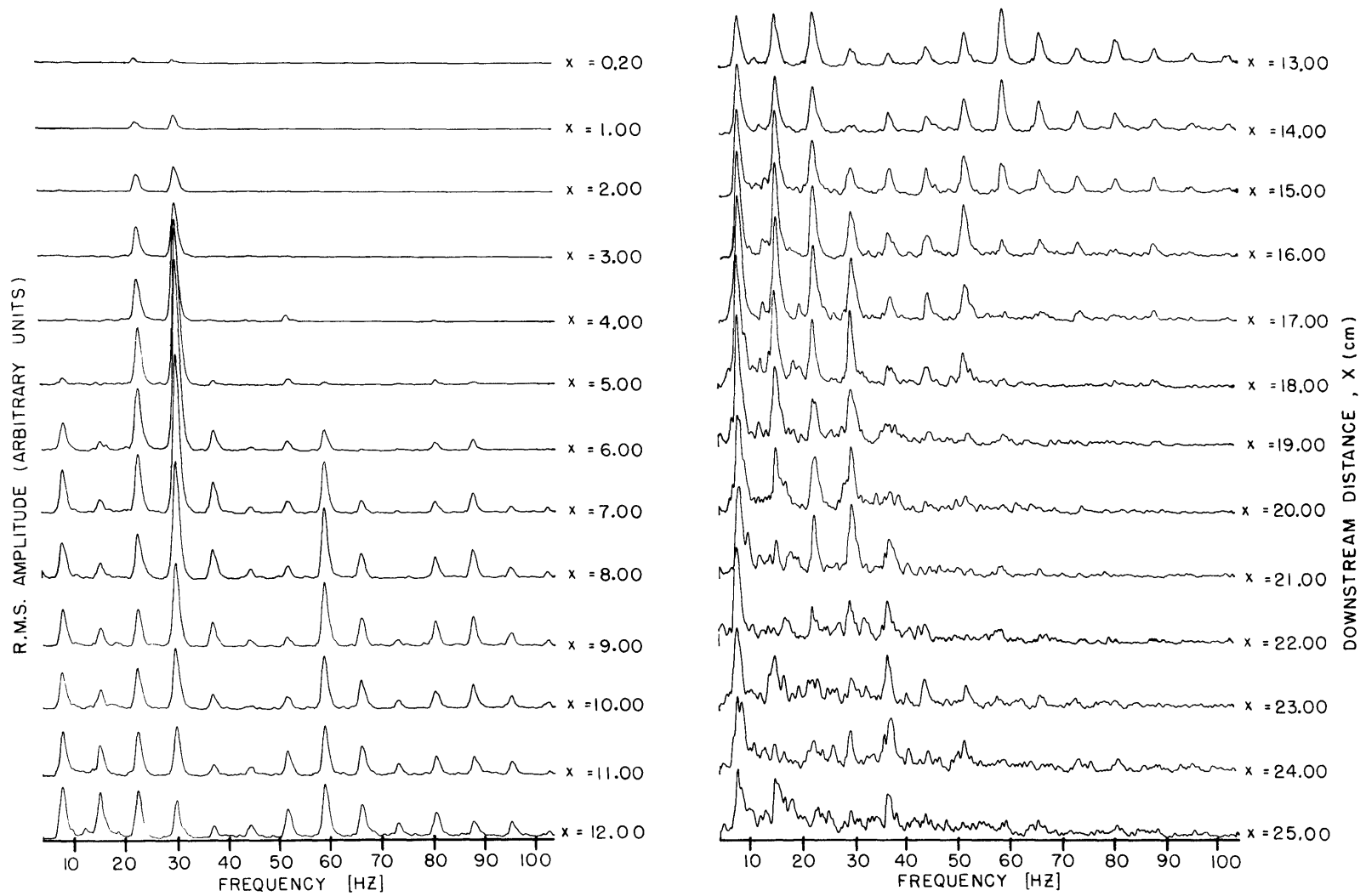


Figure 5.11: Downstream frequency spectra of the $(\omega_A + \omega_B)$ forced transition ($y = 0.2$ cm).

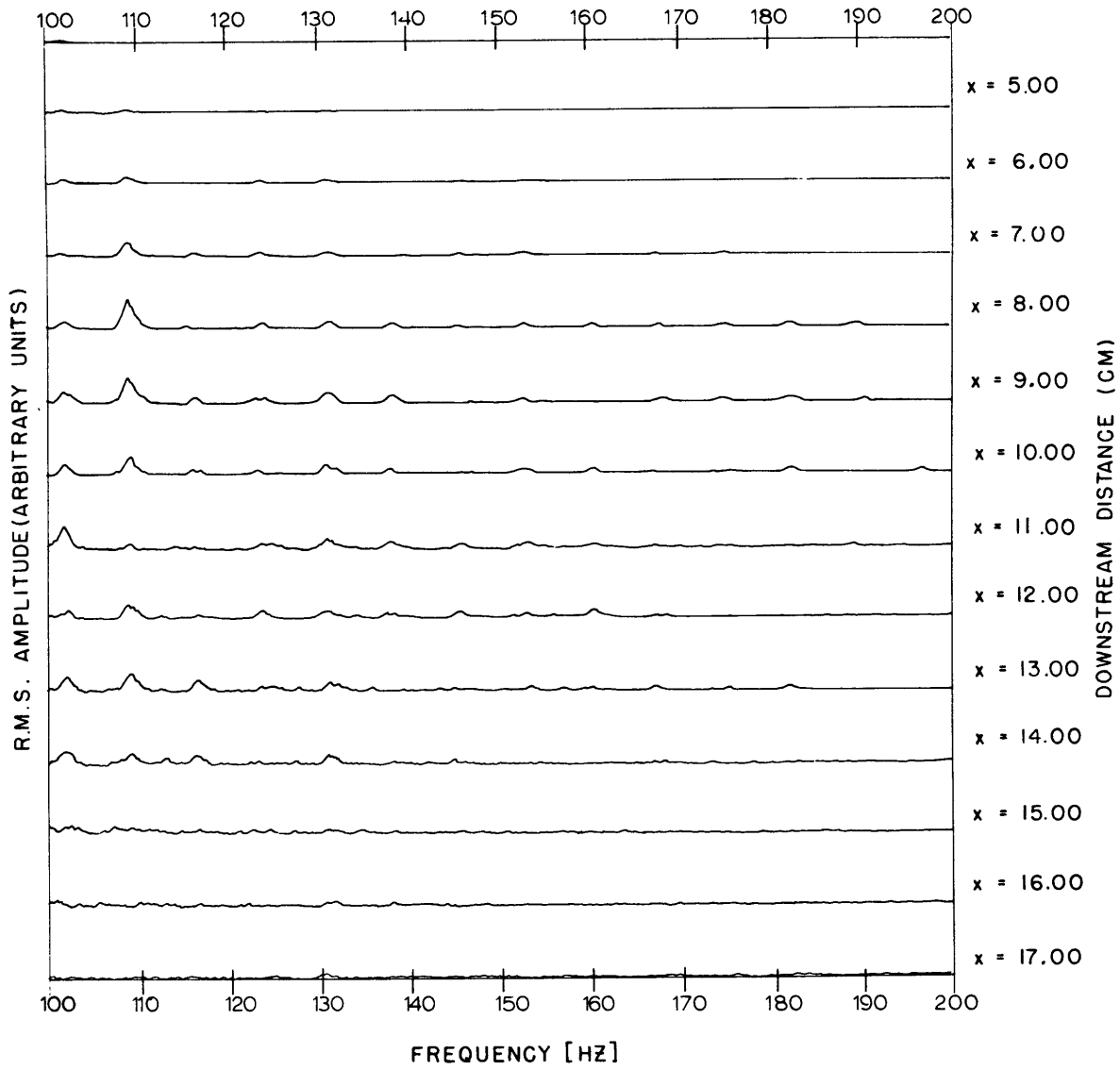


Figure 5.12: Downstream frequency spectra illustrating the presence of higher frequency modes in the mixed mode $(\omega_A + \omega_B)$ forced transition. ($y = 0.2$ cm).

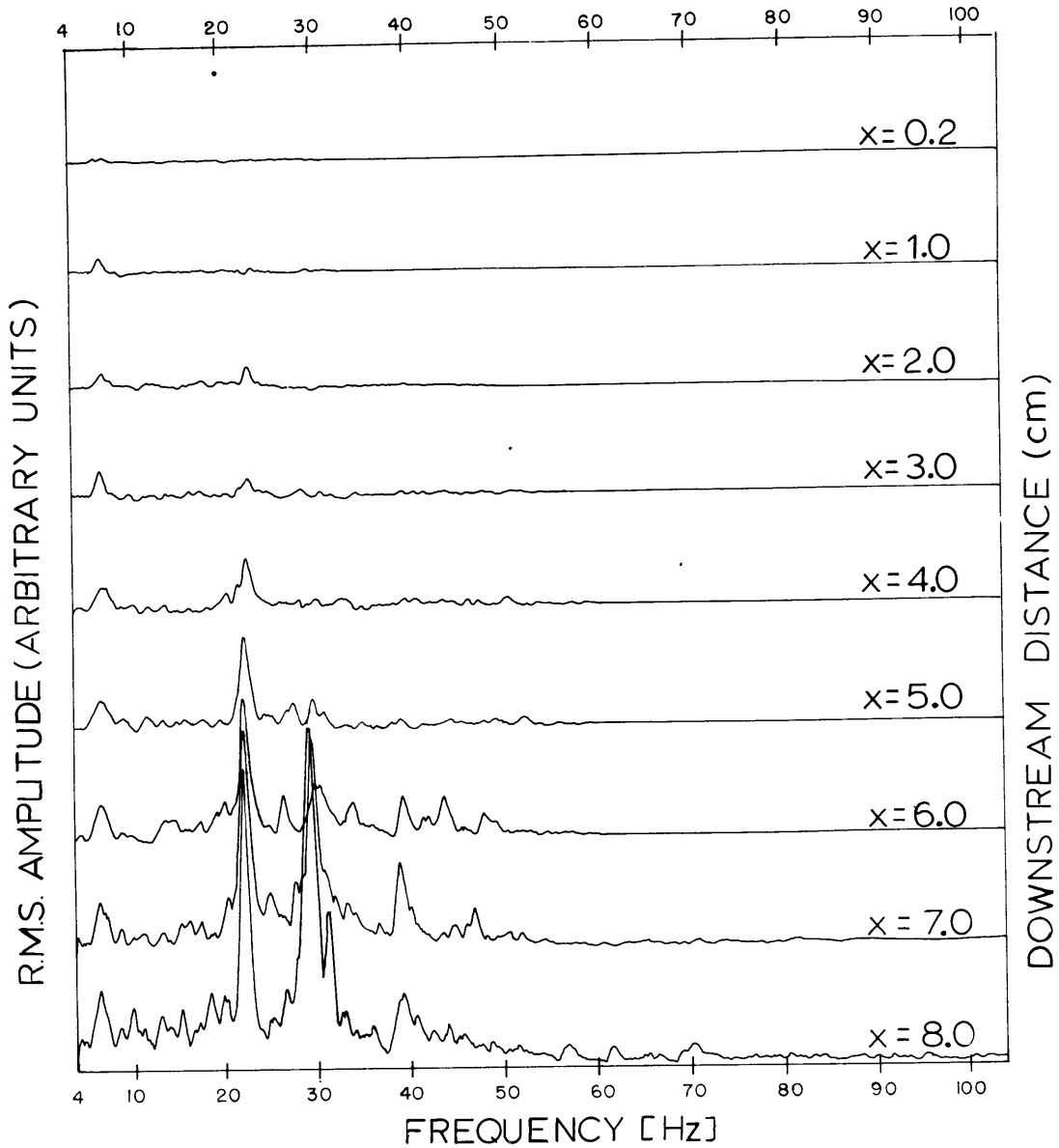


Figure 5.13: Downstream frequency spectra illustrating the reinforcement of ω_A and ω_B when the flow is excited by the difference frequency ($\omega_B - \omega_A$). $y = 0.2$ cm.

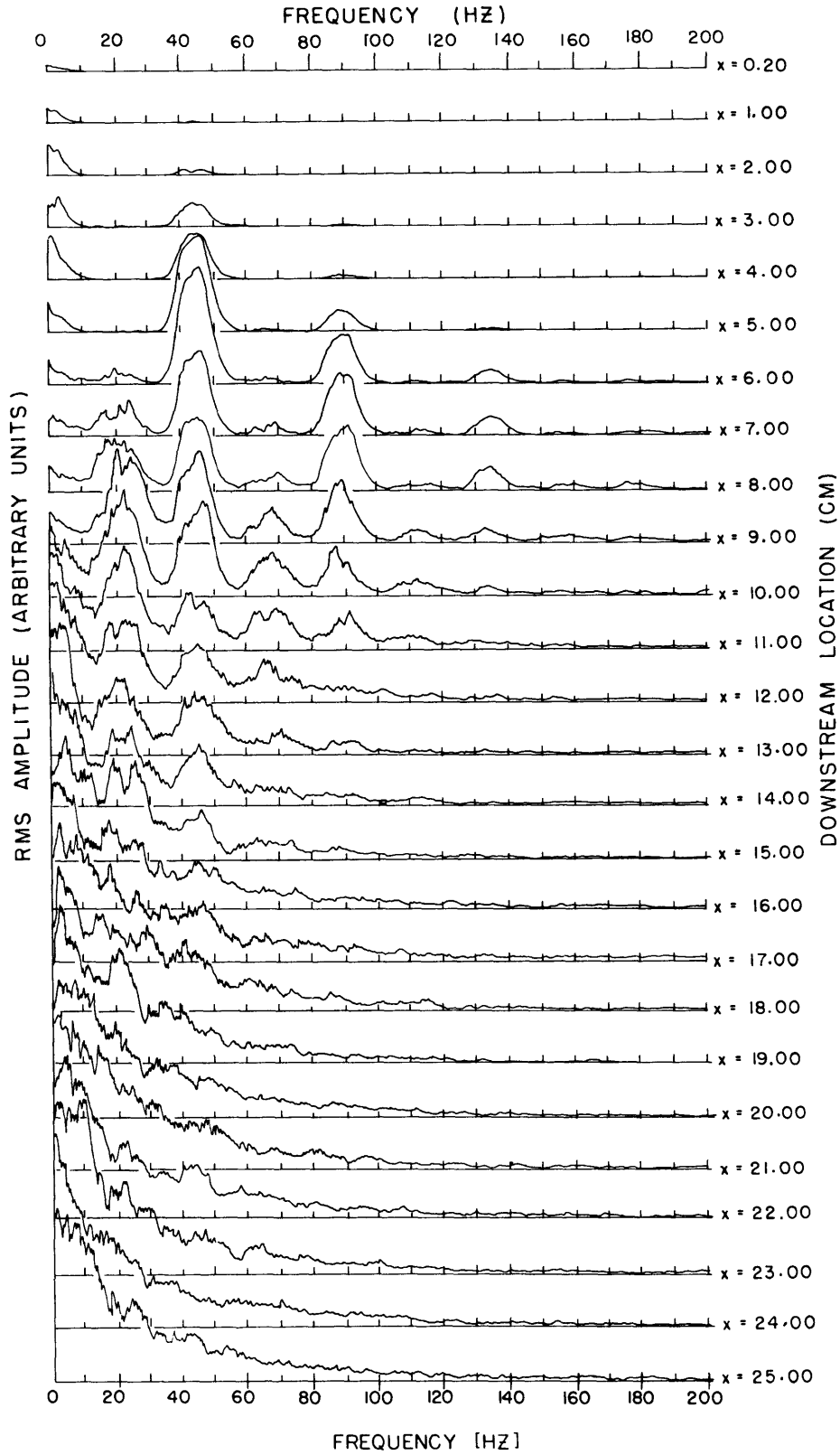


Figure 5.14: Downstream frequency spectra of the transition resulting from the direct excitation of a harmonic mode by a symmetric forcing field. Forcing frequency set at $2\omega_{fs1}$.

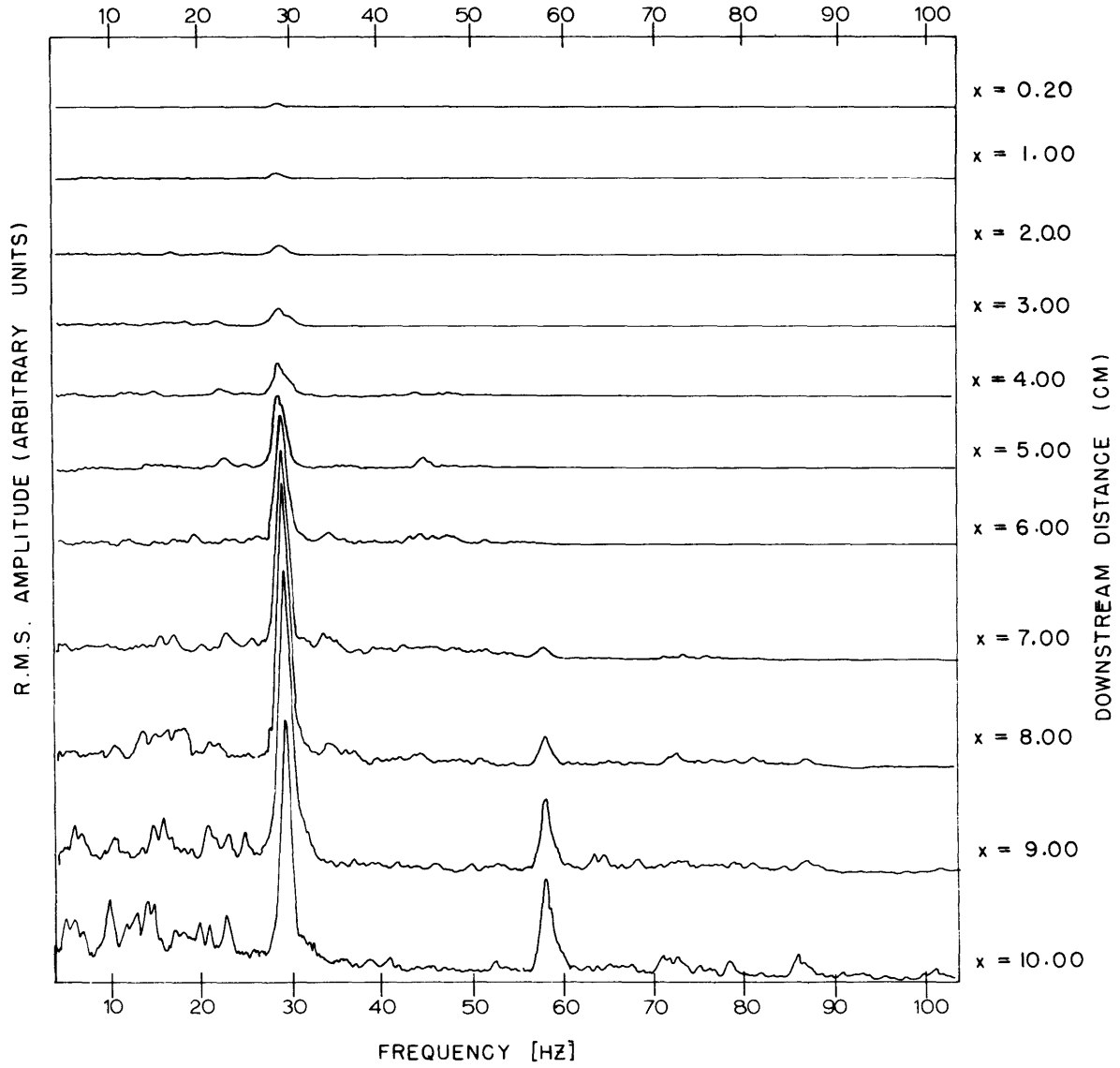


Figure 5.15: Downstream frequency spectra of the forced ω_{II} transition when excited by a symmetric excitation field ($y = 0.2$ cm).

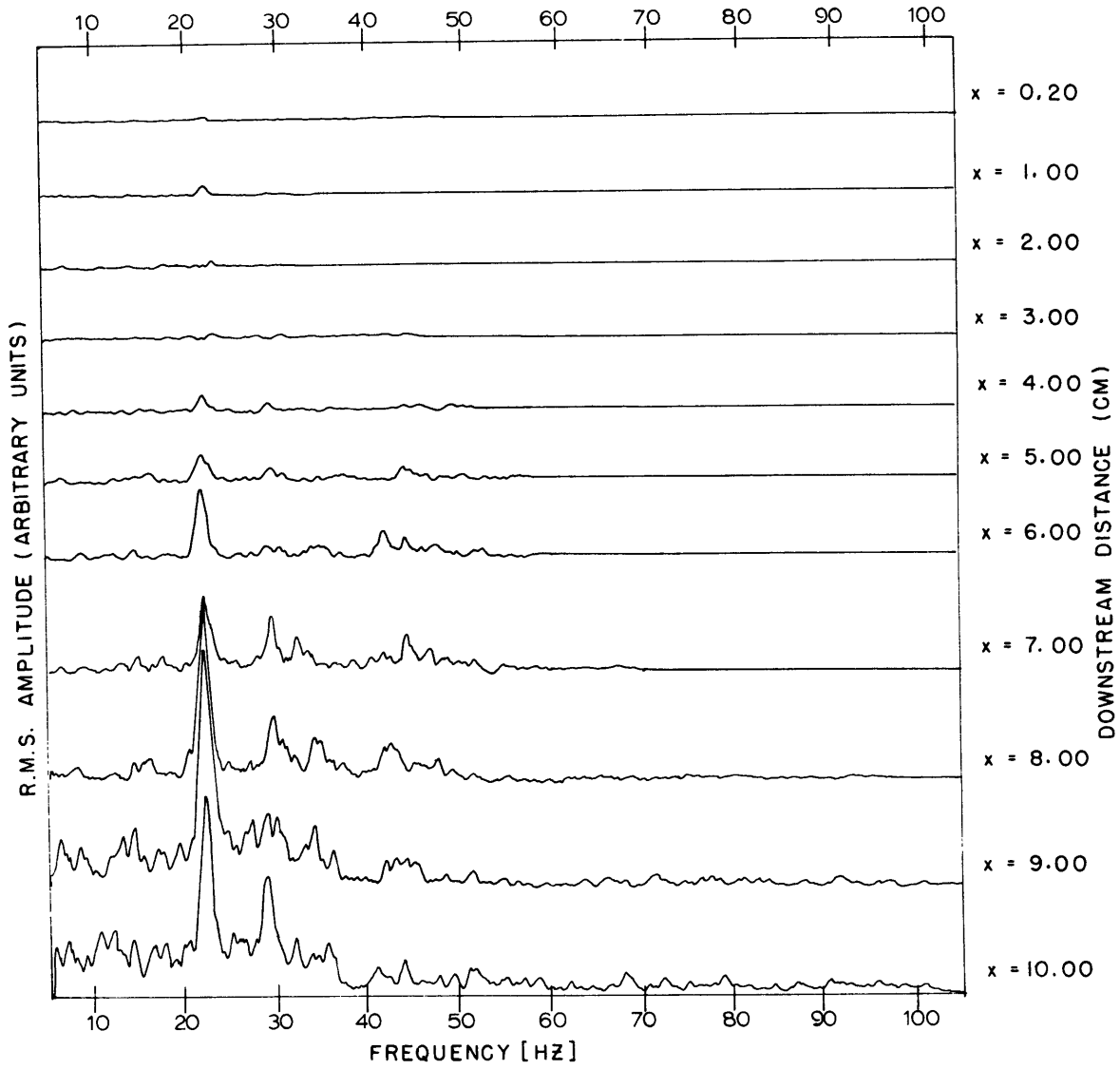


Figure 5.16: Downstream frequency spectra of the forced ω_{fs1} transition when excited by a symmetric excitation field ($y = 0.2$ cm).

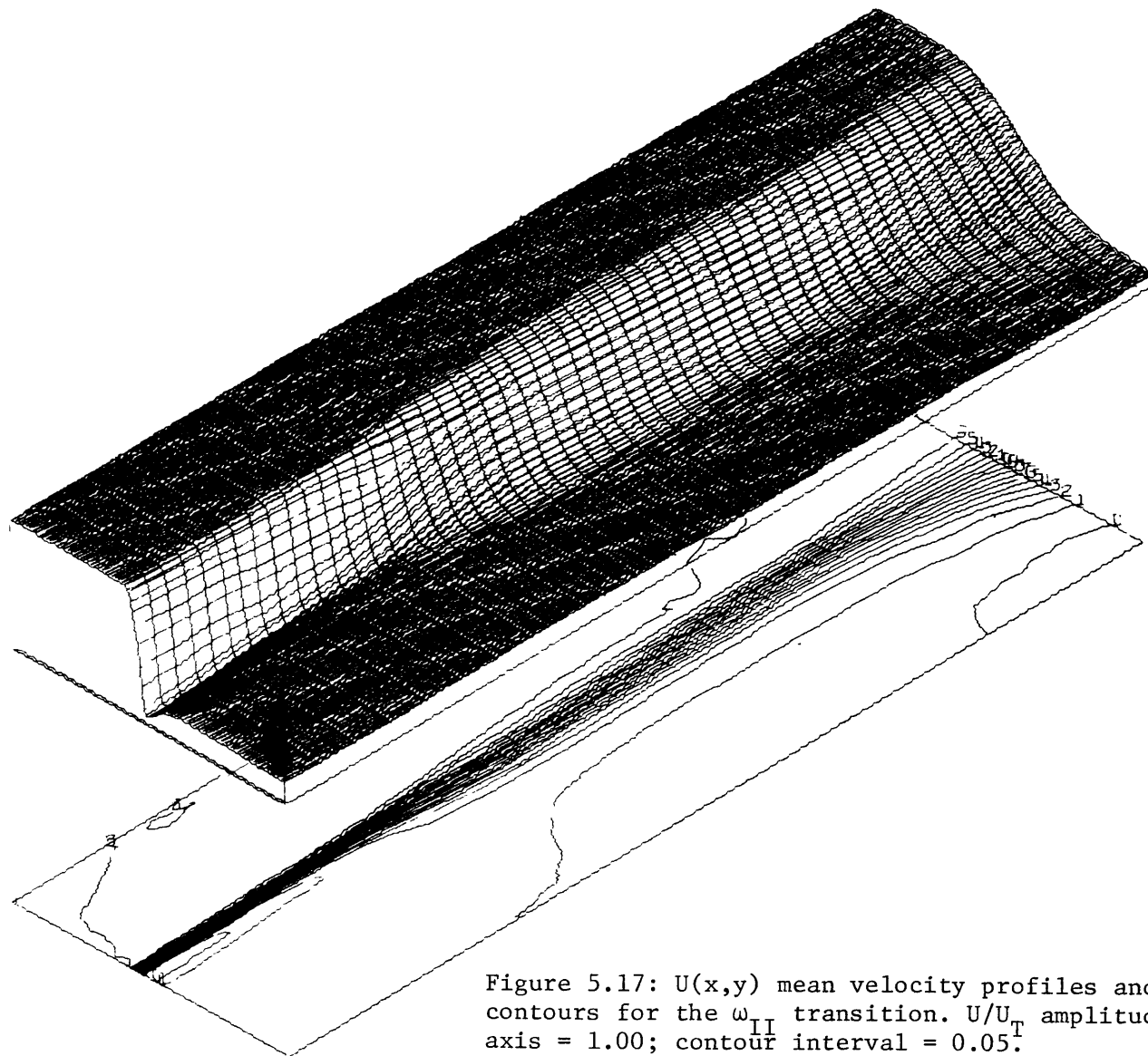


Figure 5.17: $U(x,y)$ mean velocity profiles and contours for the ω_{II} transition. U/U_T amplitude axis = 1.00; contour interval = 0.05.

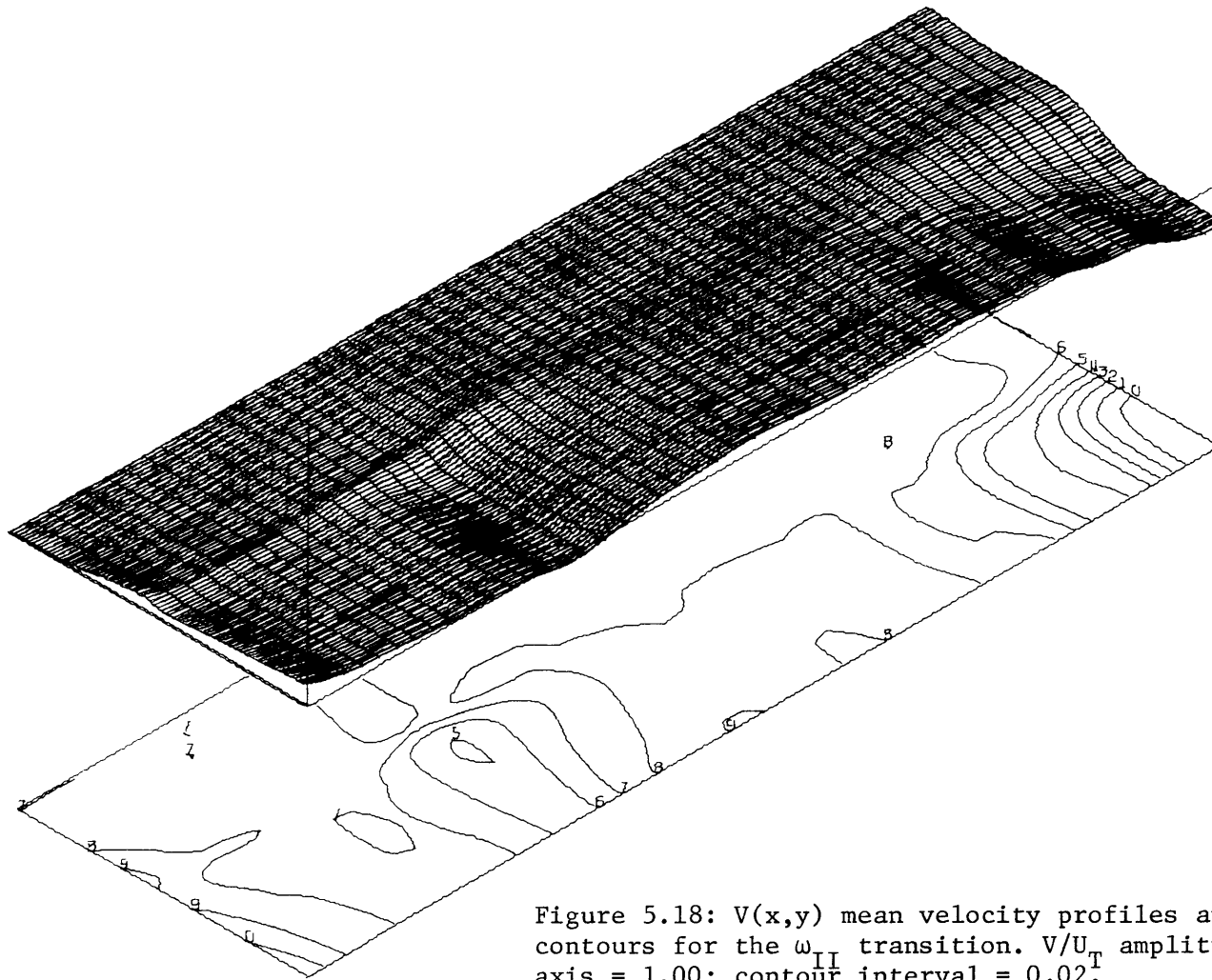


Figure 5.18: $V(x,y)$ mean velocity profiles and contours for the ω_{II} transition. V/U_T amplitude axis = 1.00; contour interval = 0.02.

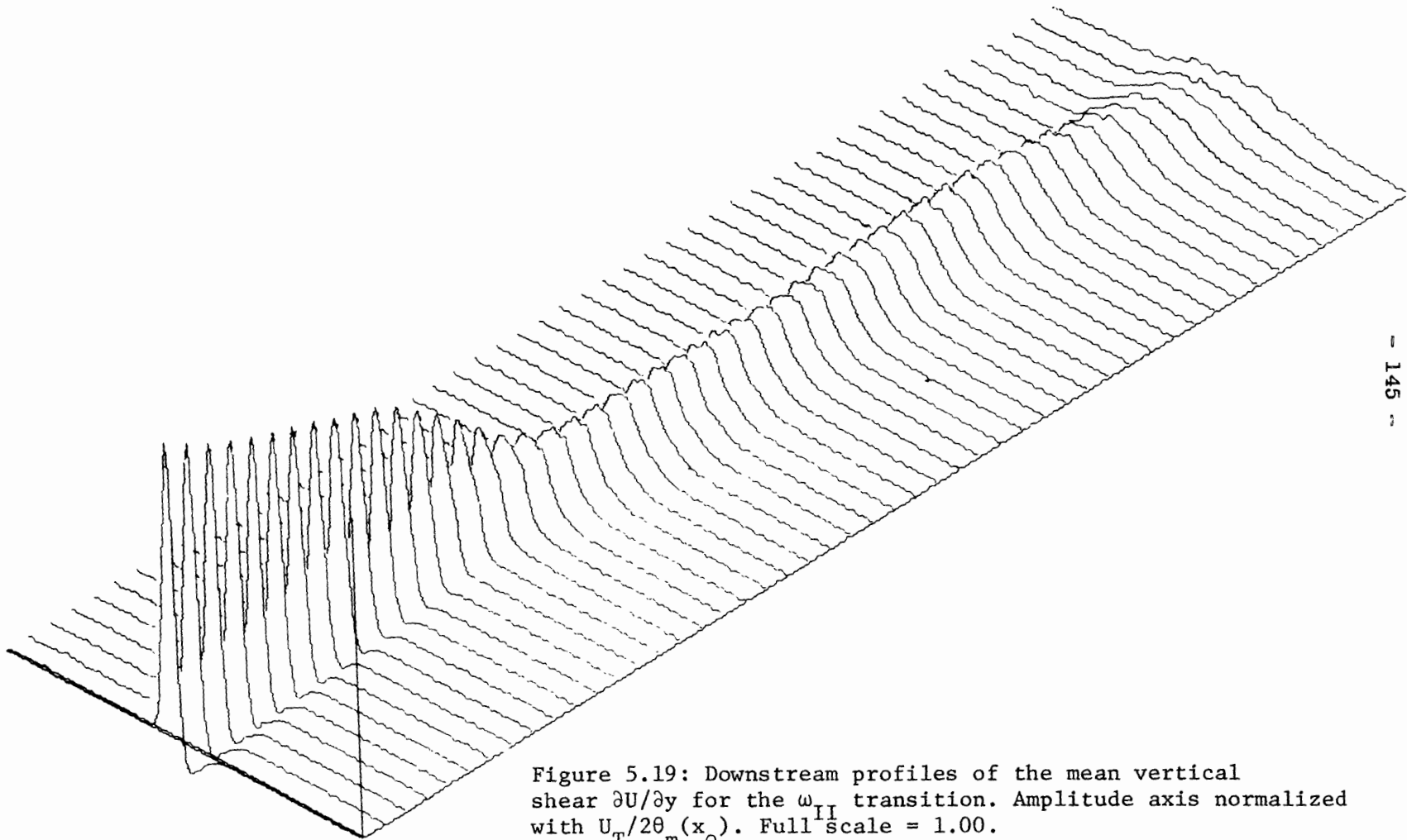


Figure 5.19: Downstream profiles of the mean vertical shear $\partial U / \partial y$ for the ω_{II} transition. Amplitude axis normalized with $U_T / 2\theta_m(x_0)$. Full scale = 1.00.

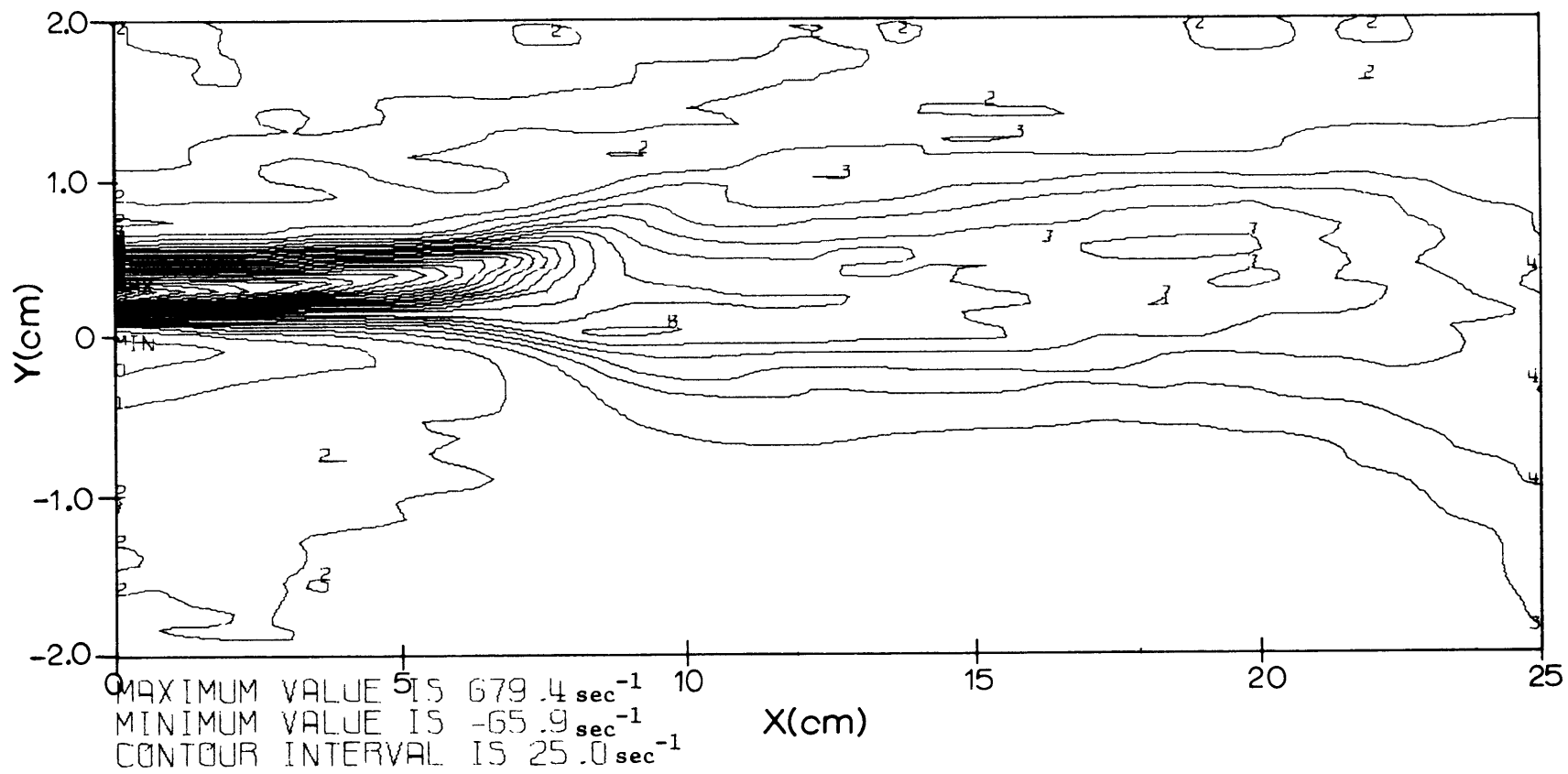


Figure 5.20: Contours of the mean vertical shear in the ω_{II} transition.

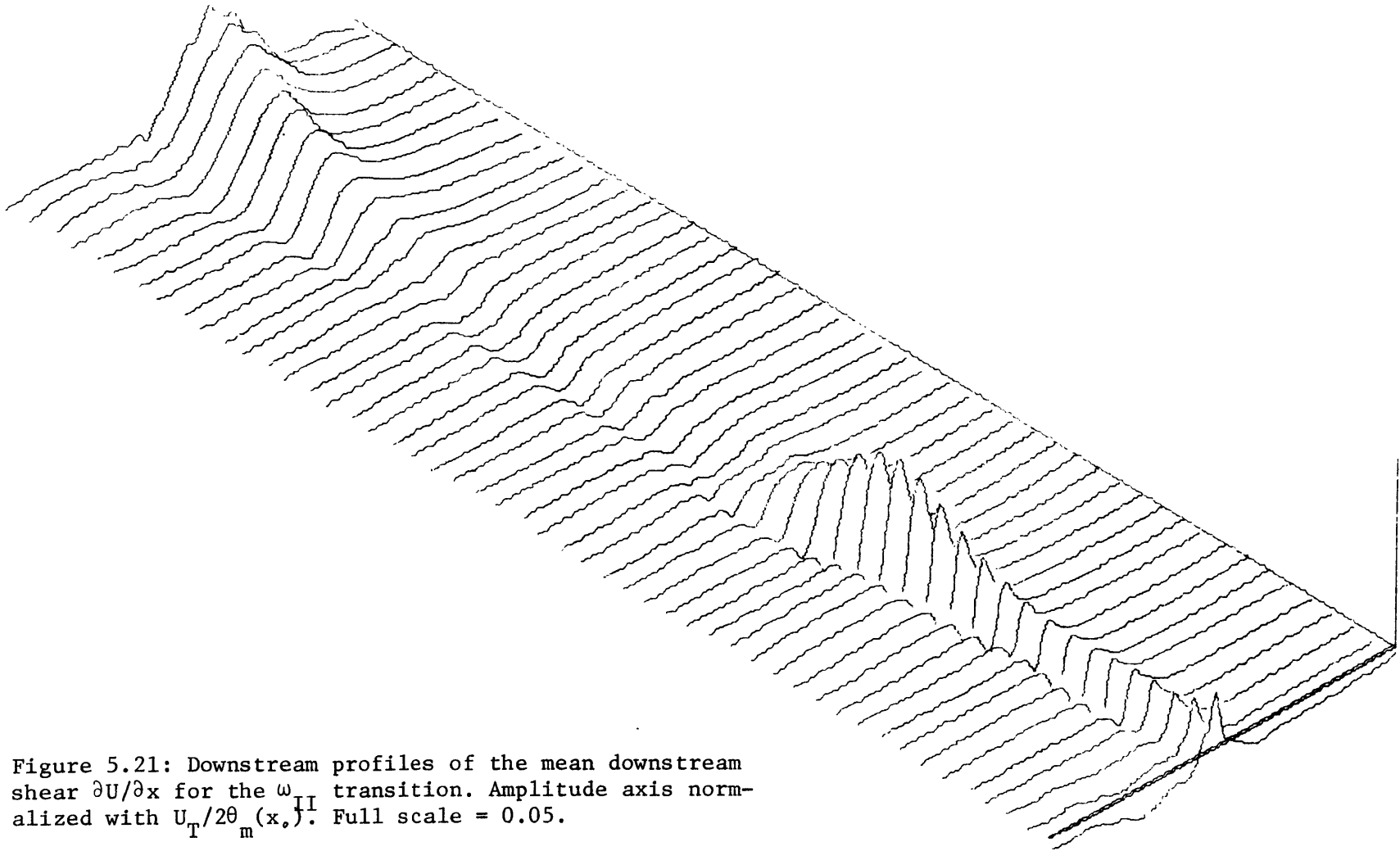


Figure 5.21: Downstream profiles of the mean downstream shear $\partial U/\partial x$ for the ω_{TI} transition. Amplitude axis normalized with $U_T/2\theta_m(x)$. Full scale = 0.05.

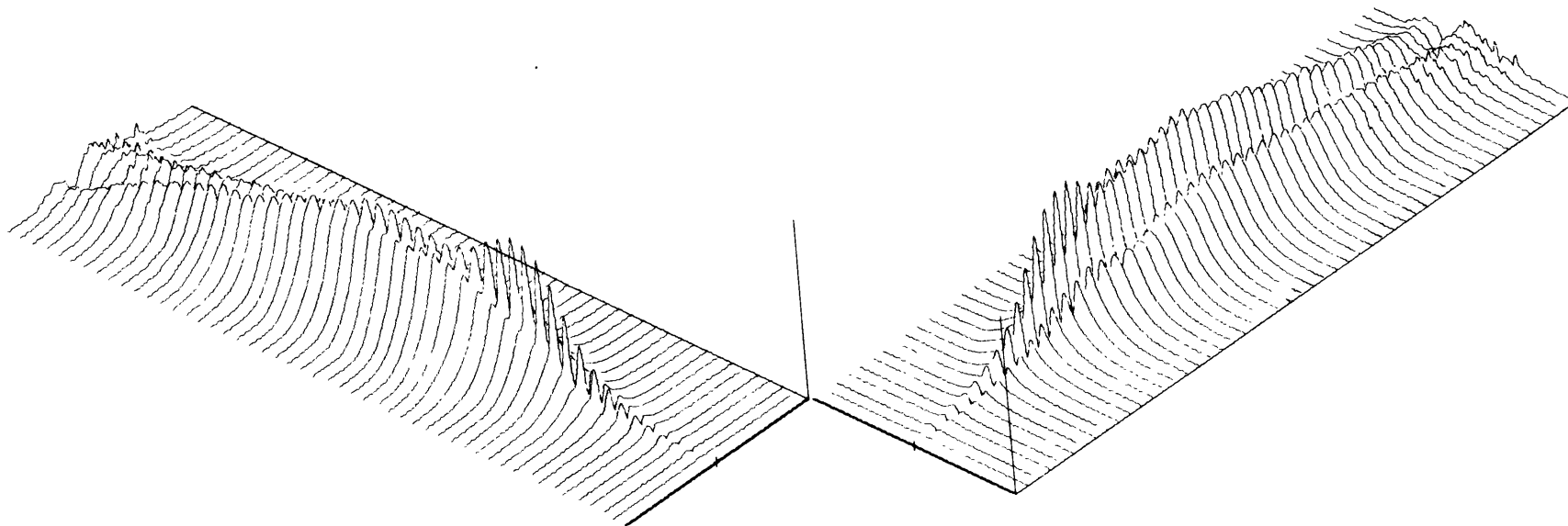


Figure 5.22: Downstream profiles of $u_{rms}(\omega_{II})$.

u_{rms}/U_T amplitude axis = 15.5%.

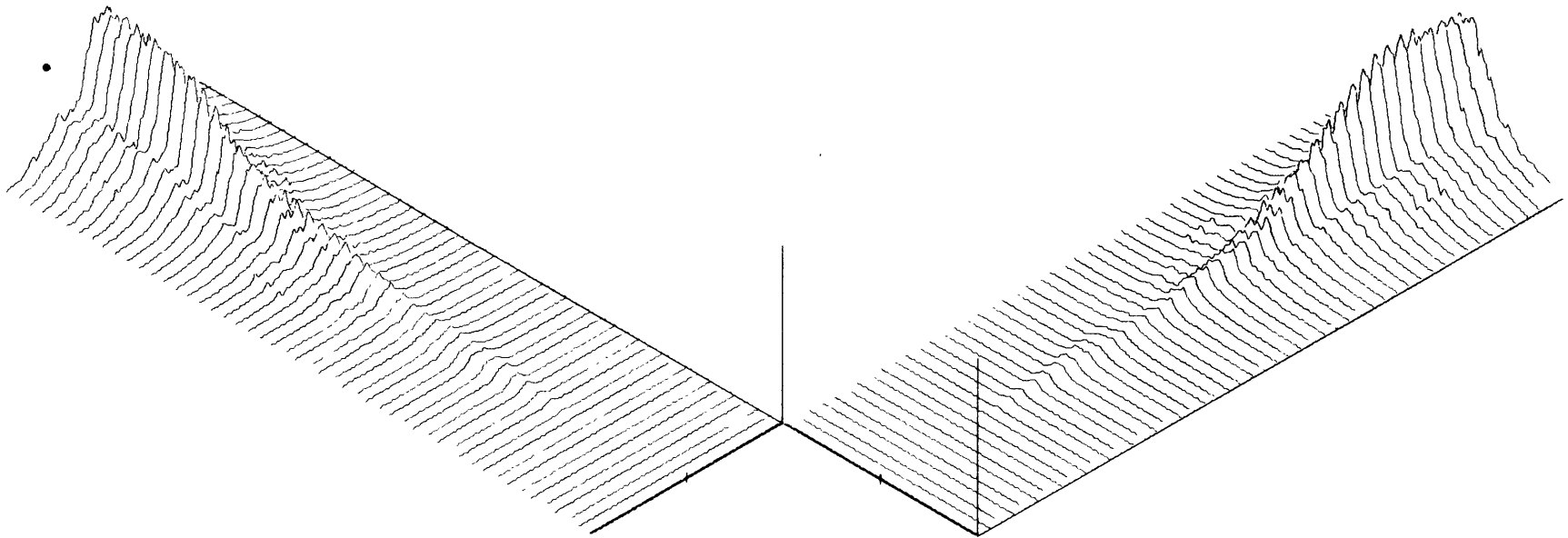


Figure 5.23: Downstream profiles of $u_{\text{rms}}(\omega_{\text{II}}/2)$.

u_{rms}/U_T amplitude axis = 15.5%.

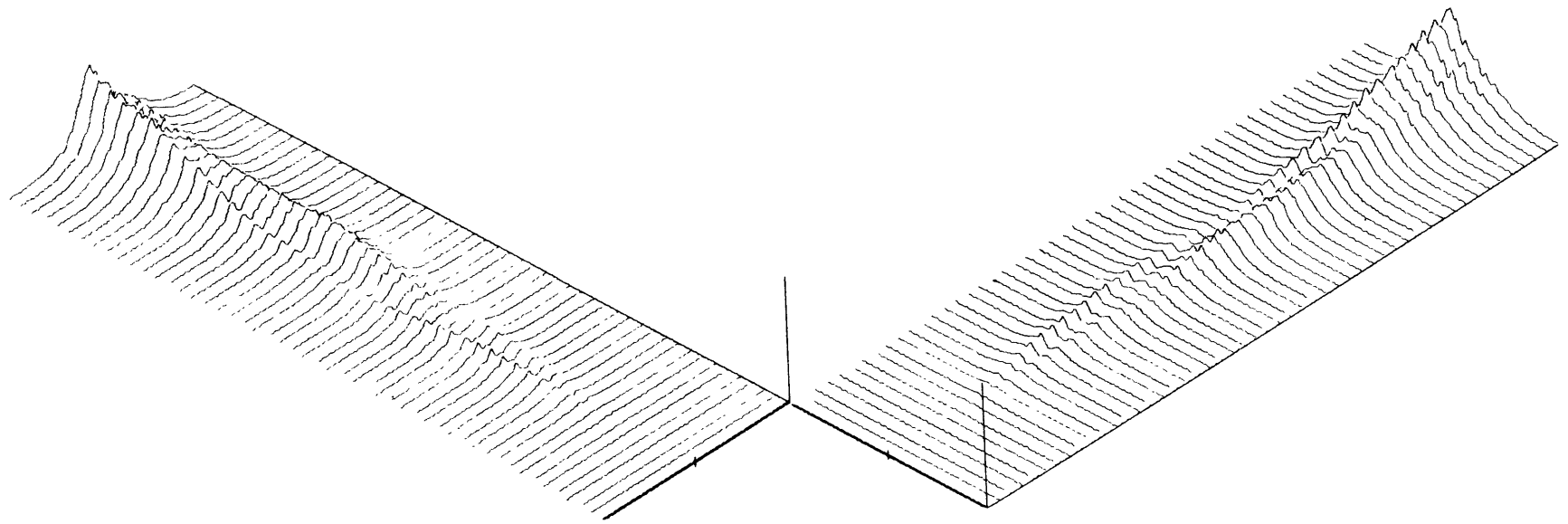


Figure 5.24: Downstream profiles of $u_{\text{rms}}(3 \omega_{\text{II}}/2)$.

$u_{\text{rms}}/U_{\text{T}}$ amplitude axis = 5.5%.

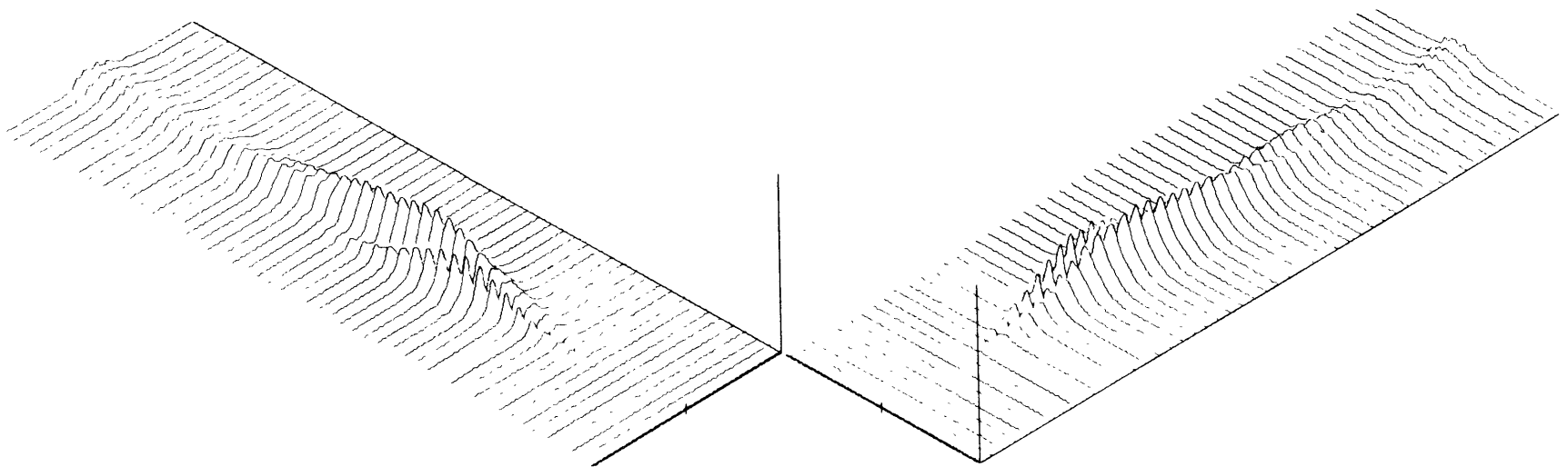


Figure 5.25: Downstream profiles of $u_{\text{rms}}(2\omega_{\text{II}})$.

$u_{\text{rms}}/U_{\text{T}}$ amplitude axis = 15.5%.

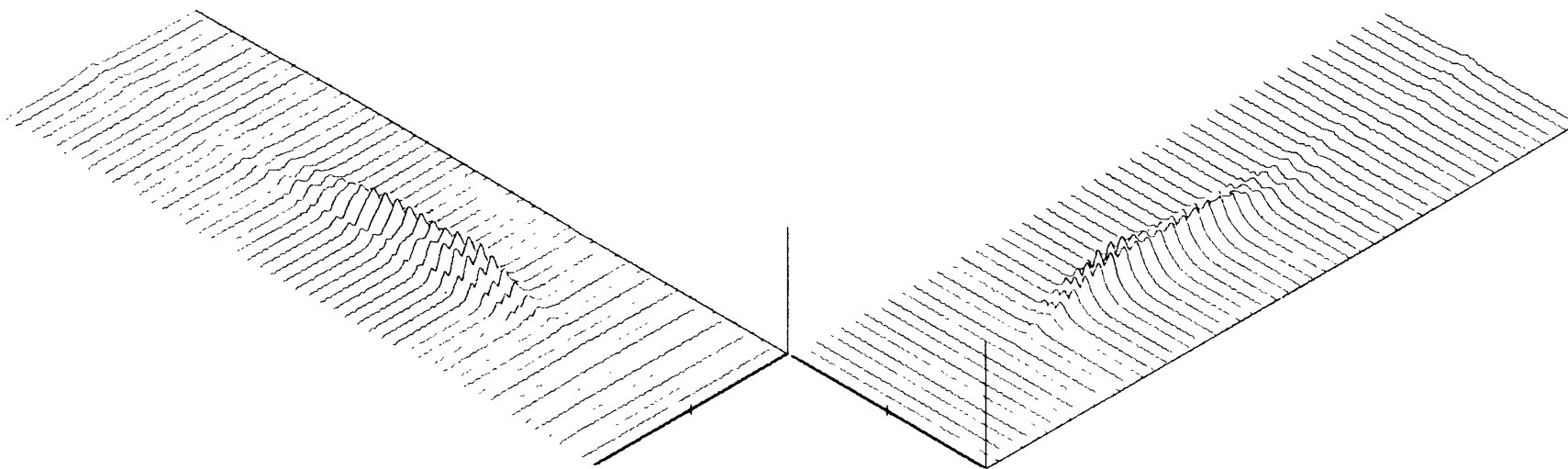


Figure 5.26: Downstream profiles of $u_{\text{rms}}(3\omega_{\text{II}})$.

$u_{\text{rms}}/U_{\text{T}}$ amplitude axis = 5.5%.

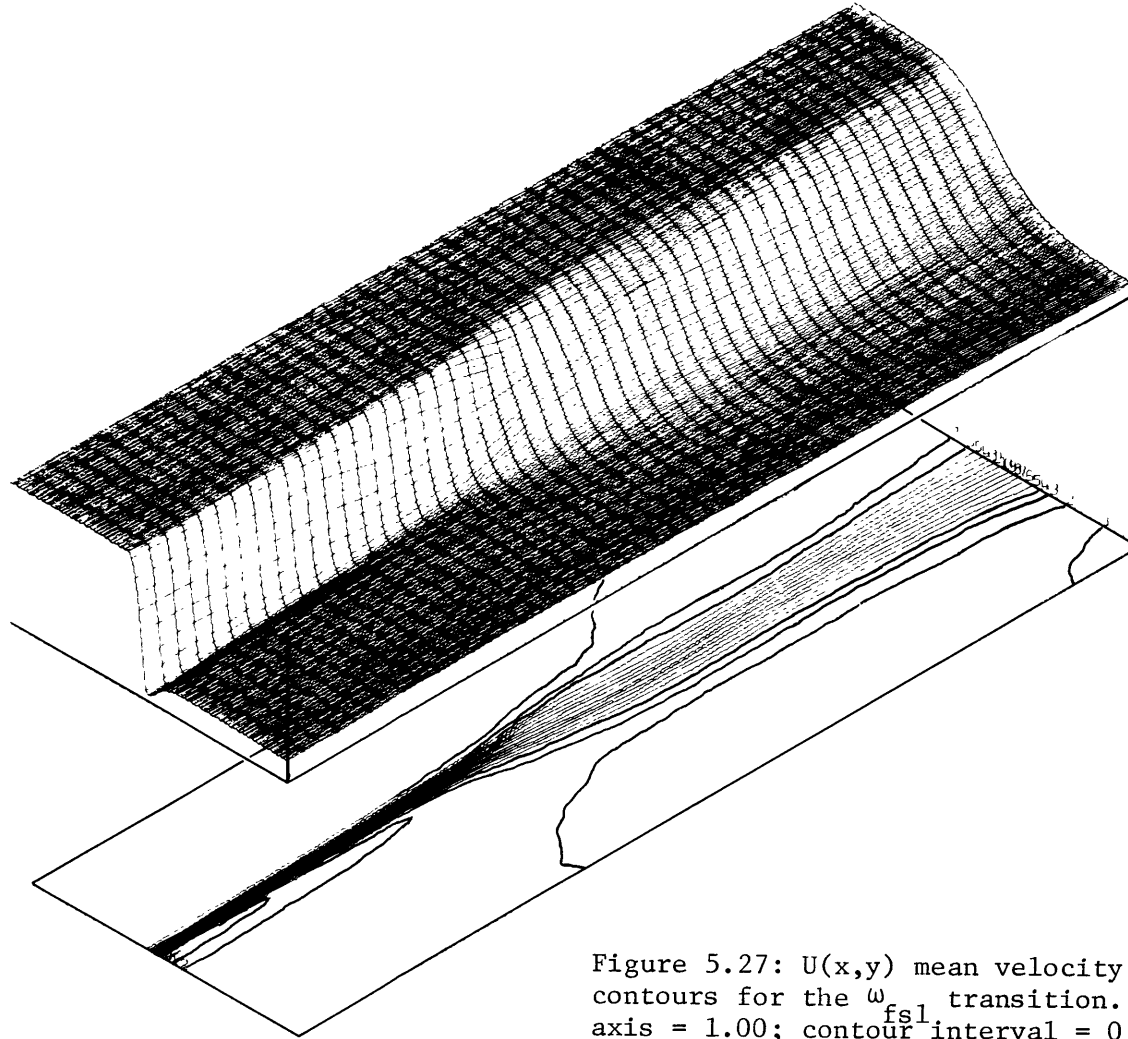


Figure 5.27: $U(x,y)$ mean velocity profiles and contours for the ω_{fs1} transition. U/U_T amplitude axis = 1.00; contour interval = 0.05.

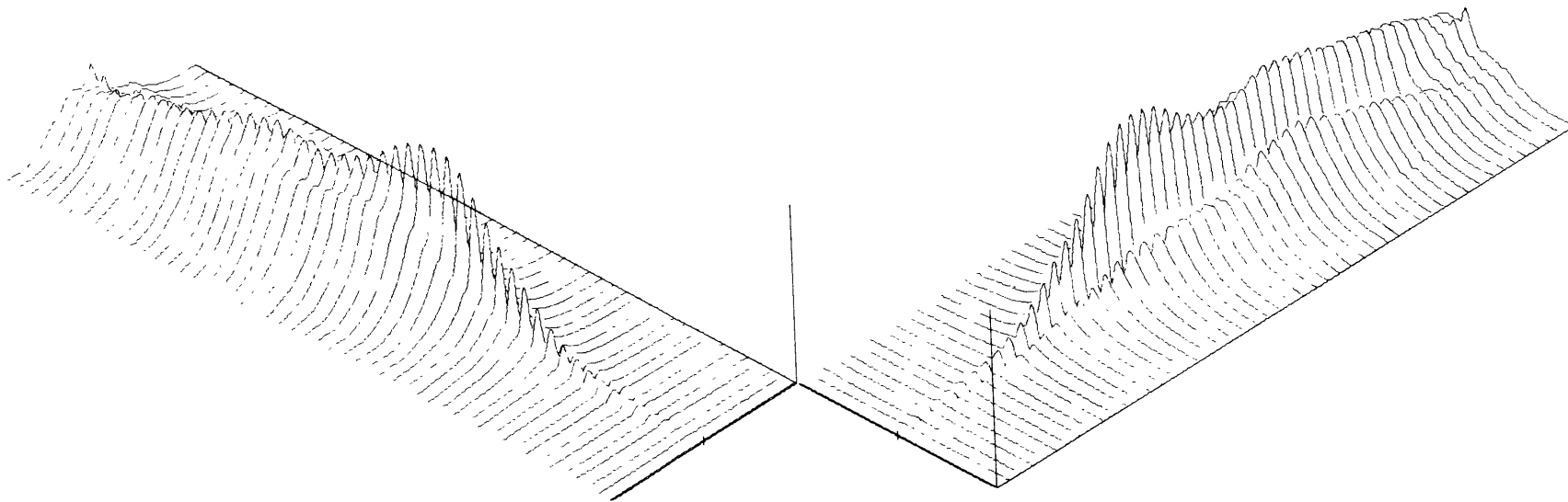


Figure 5.28: Downstream profiles of $u_{\text{rms}}(\omega_{\text{fsl}})$.
 u_{rms}/U_T amplitude axis = 5.5%.

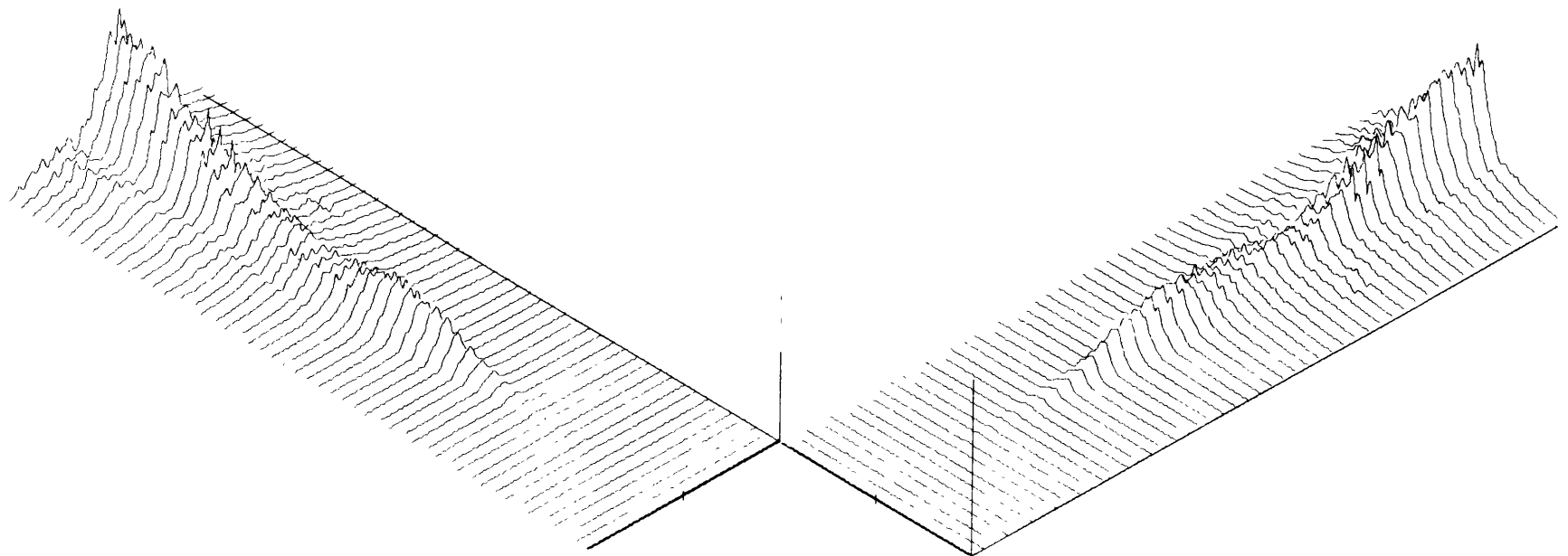


Figure 5.29: Downstream profiles of $u_{rms}(\omega_{fs1}/2)$
 u_{rms}/U_T amplitude axis = 15.5%.

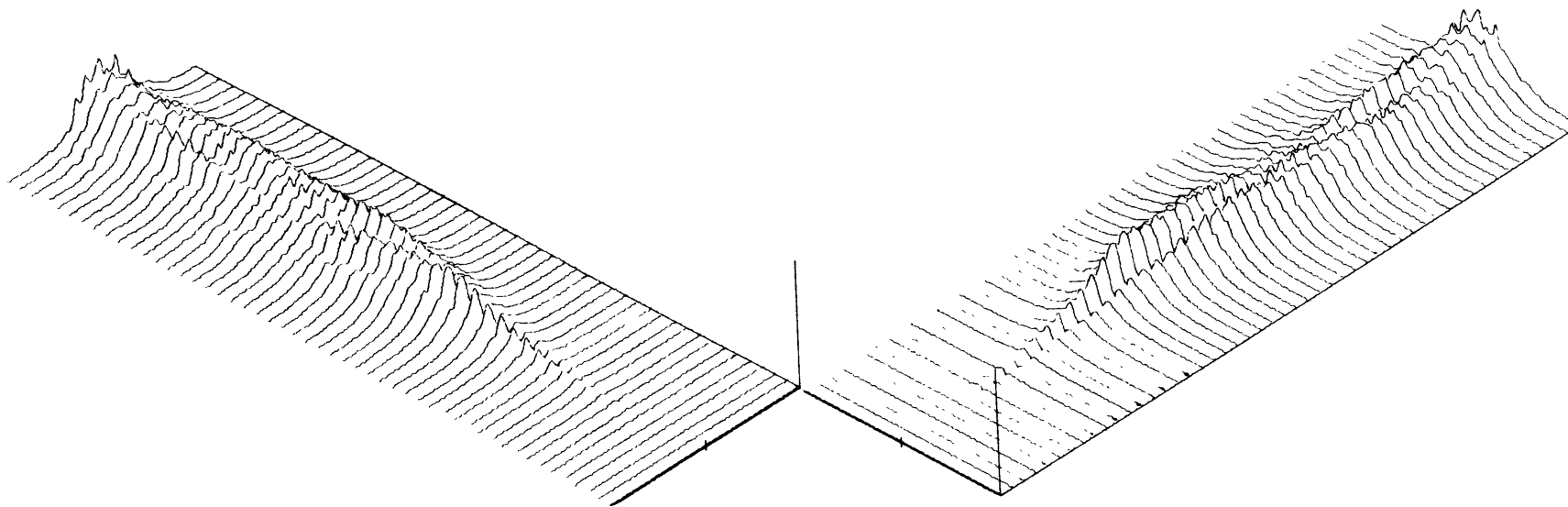


Figure 5.30: Downstream profiles of $u_{rms}(3\omega_{fs1}/2)$
 u_{rms}/U_T amplitude axis = 5.5%.

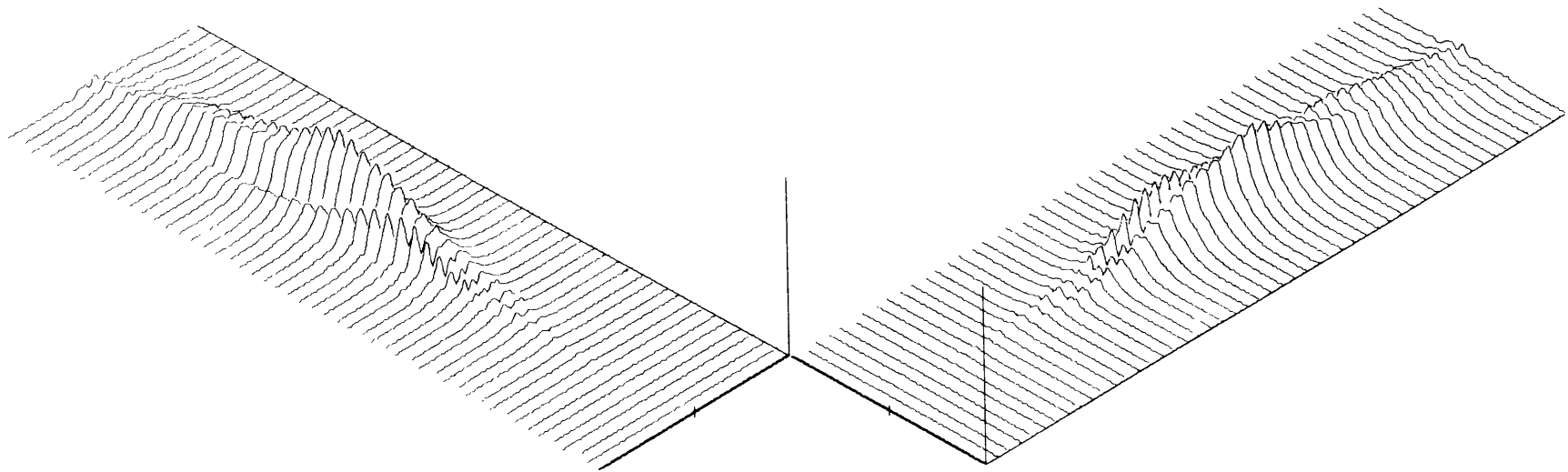


Figure 5.31: Downstream profiles of $u_{rms}(2\omega_{fs1})$.
 u_{rms}/U_T amplitude axis = 15.5%.

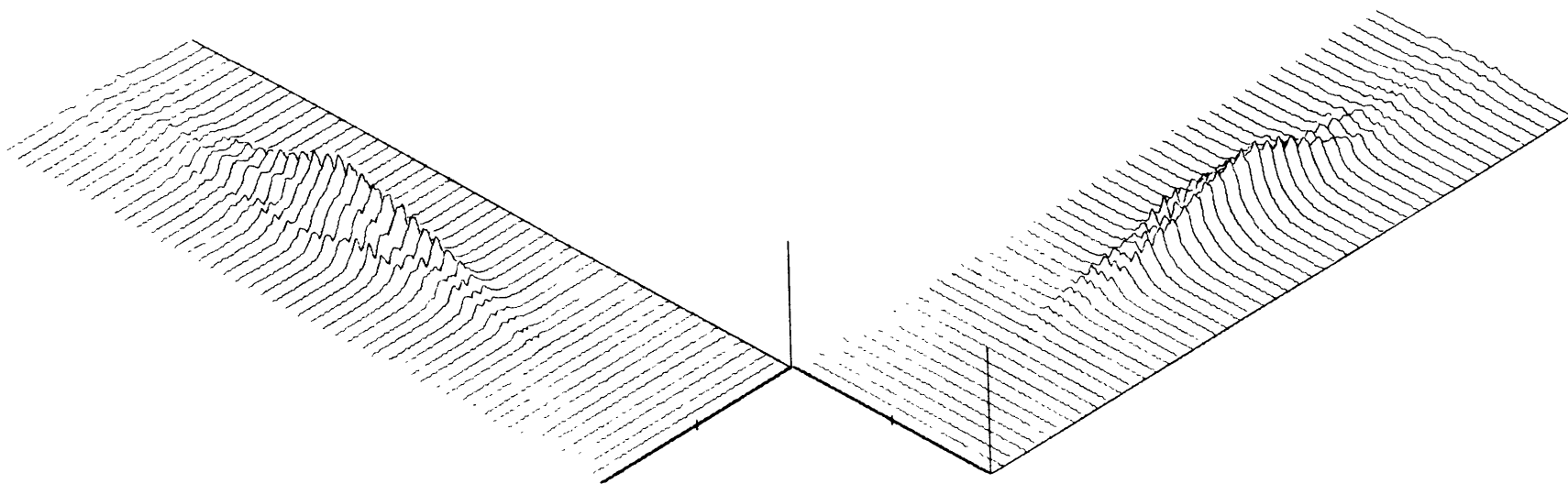


Figure 5.32: Downstream profiles of $u_{rms}(3\omega_{fs1})$.
 u_{rms}/U_T amplitude axis = 5.5%.

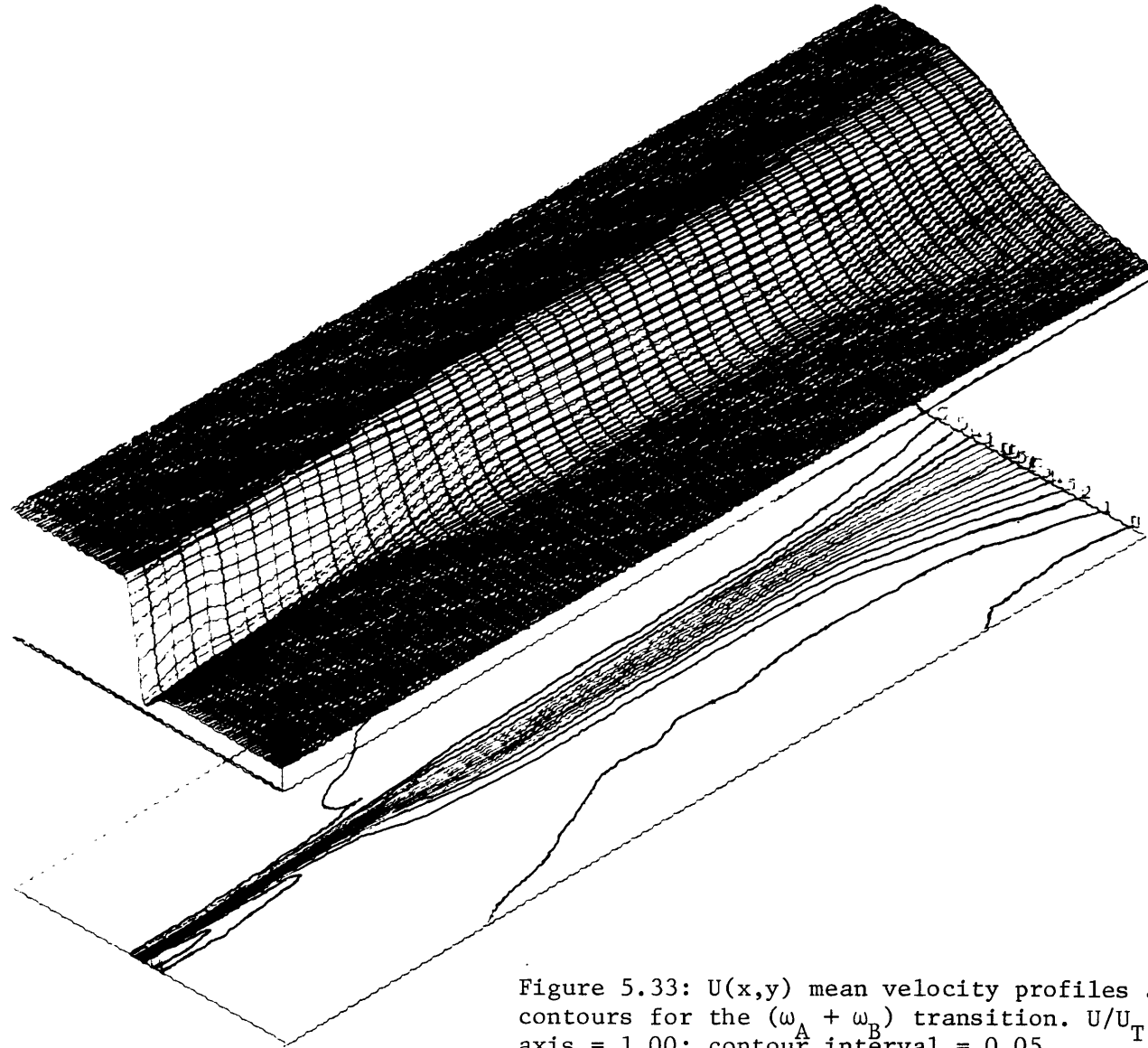


Figure 5.33: $U(x,y)$ mean velocity profiles and contours for the $(\omega_A + \omega_B)$ transition. U/U_T amplitude axis = 1.00: contour interval = 0.05.

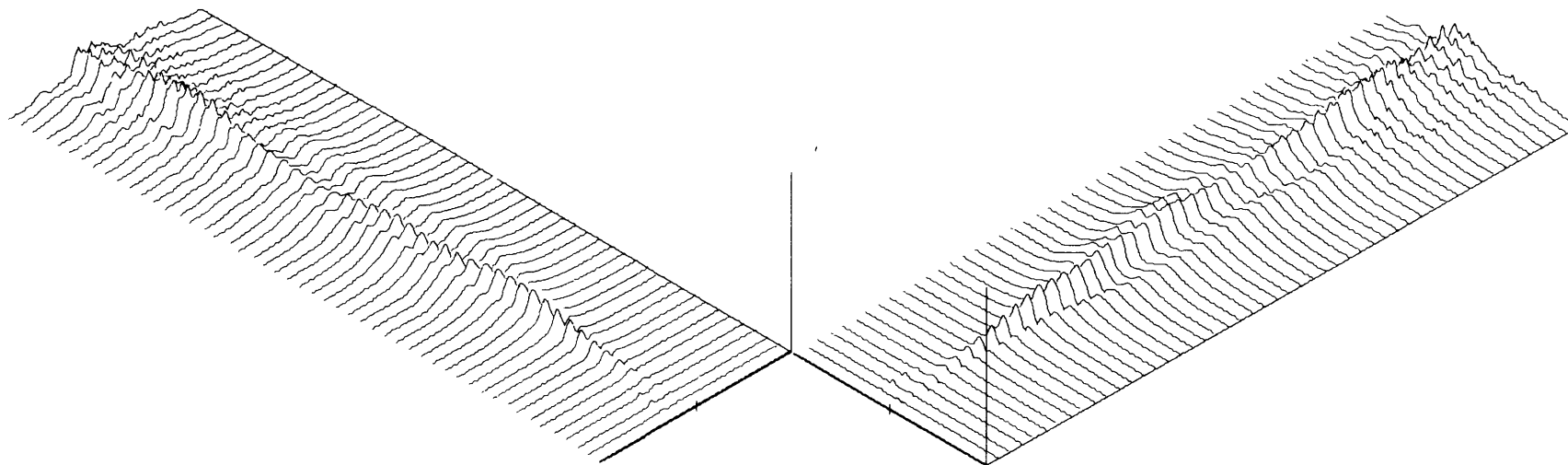


Figure 5.34: Downstream profiles of $u_{rms}(\omega_A)$.
 u_{rms}/U_T amplitude axis = 15.5%.

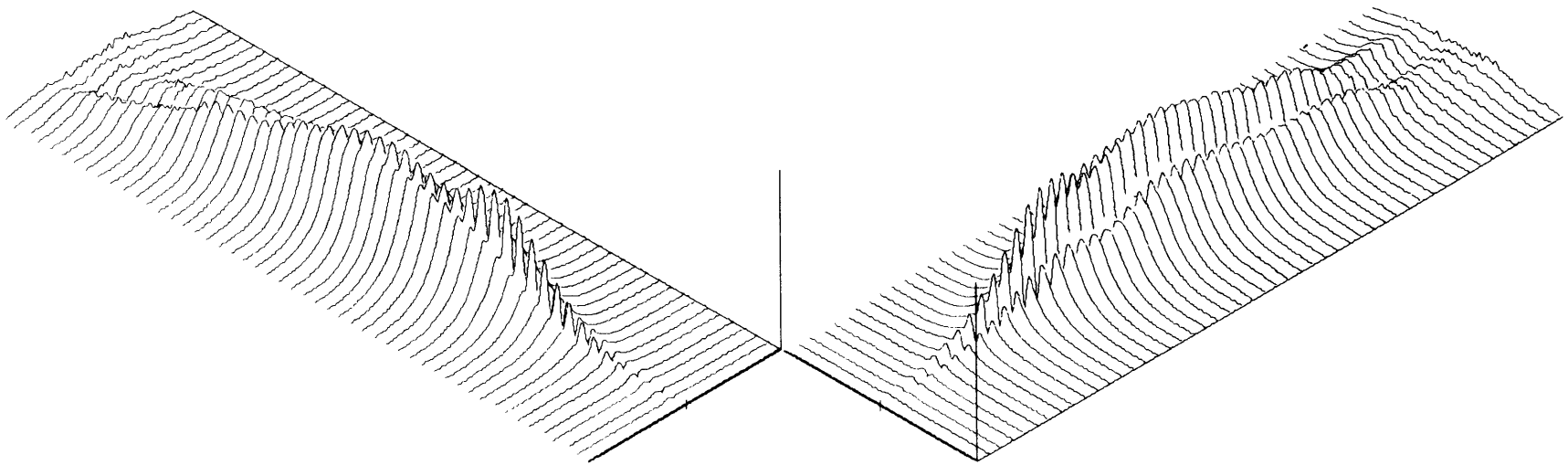


Figure 5.35: Downstream profiles of $u_{rms}(\omega_B)$.
 u_{rms}/\bar{U}_T amplitude axis = 15.5%.

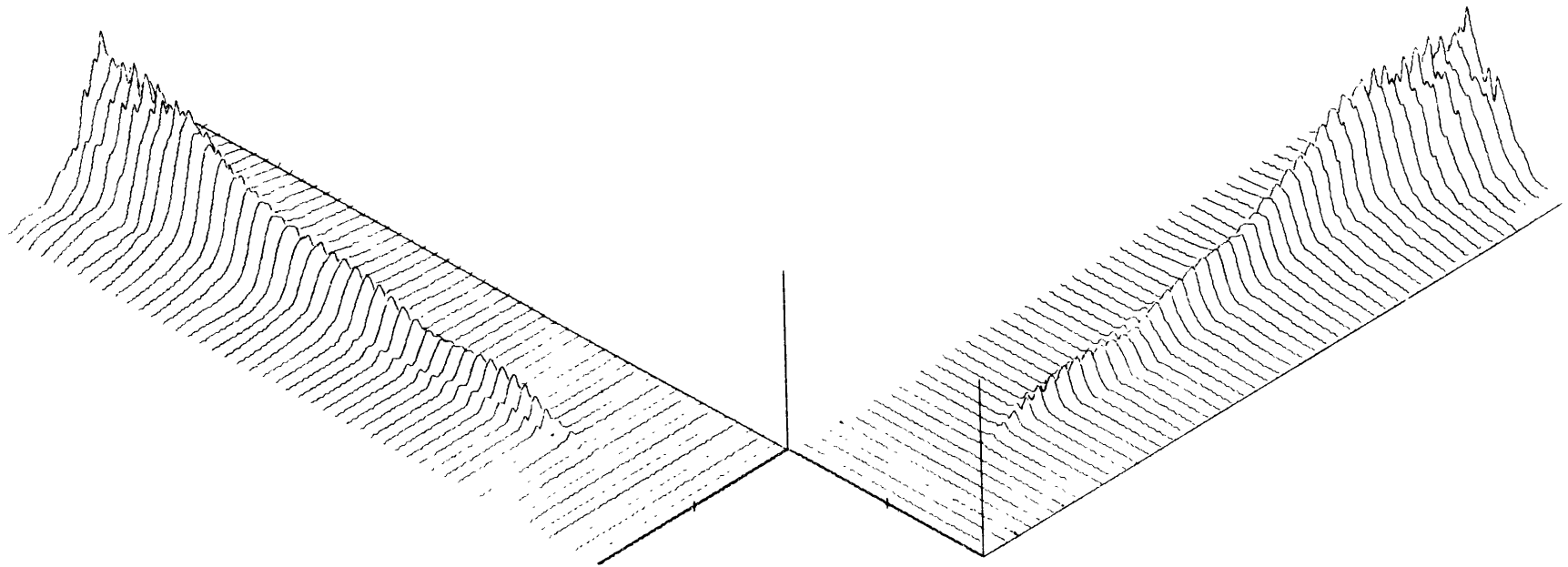


Figure 5.36: Downstream profiles of $u_{rms}(\omega_B - \omega_A)$.
 u_{rms}/U_T amplitude axis = 15.5%.

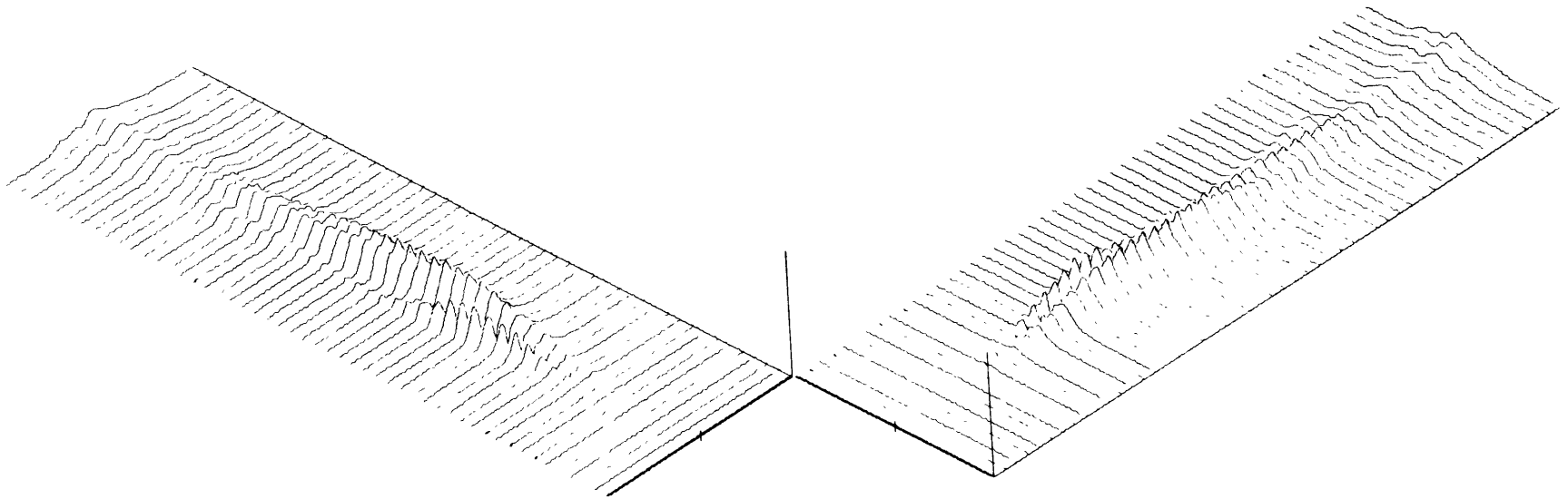


Figure 5.37: Downstream profiles of $u_{rms}(\omega_A + \omega_B)$.
 u_{rms}/U_T amplitude axis = 5.5%.

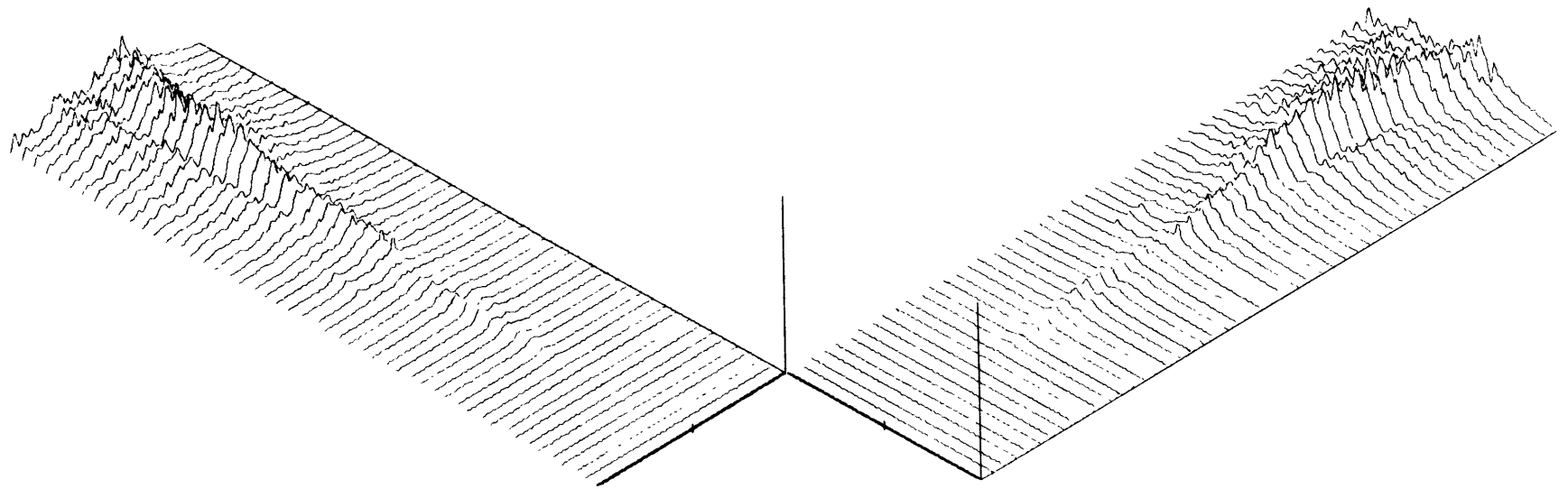


Figure 5.38: Downstream profiles of $u_{\text{rms}}(\omega_B/2)$.

u_{rms}/U_T amplitude axis = 15.5%.

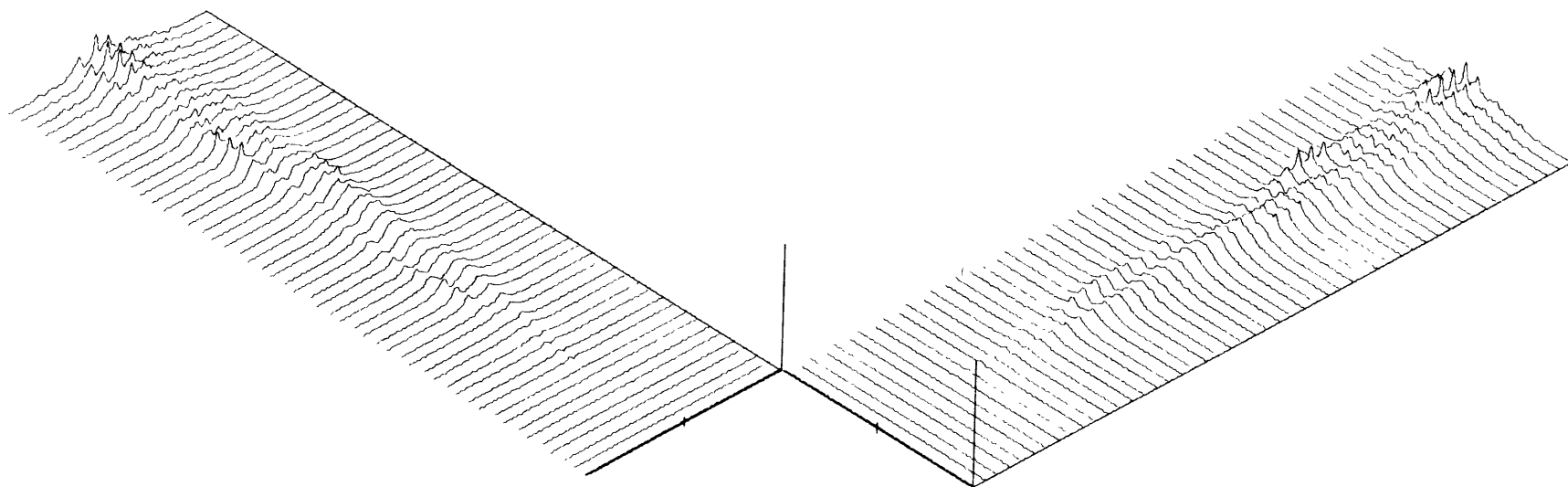


Figure 5.39: Downstream profiles of $u_{\text{rms}}(2\omega_A)$.

u_{rms}/U_T amplitude axis = 5.5%.

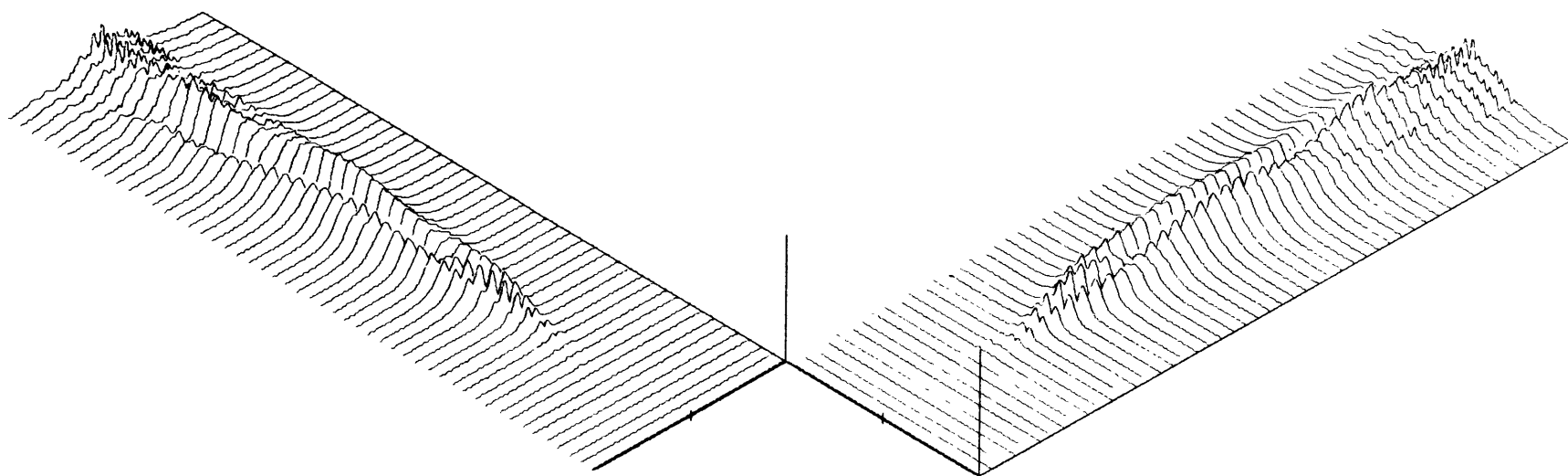


Figure 5.40: Downstream profiles of $u_{\text{rms}}(\omega_a + \omega_b/2)$.

u_{rms}/U_T amplitude axis = 5.5%.

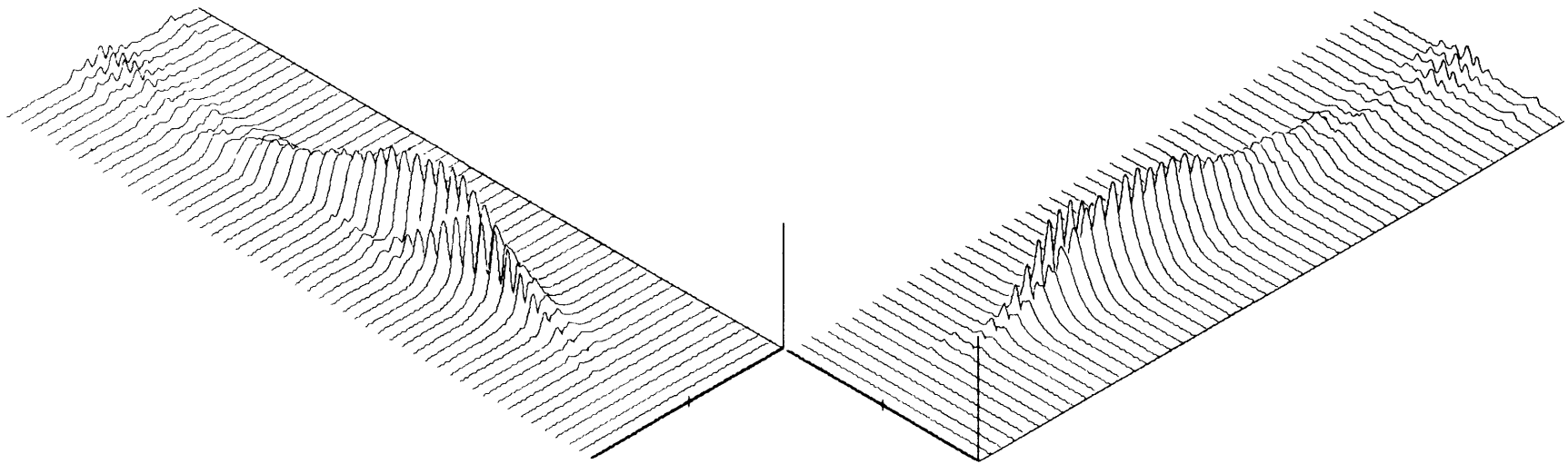


Figure 5.41: Downstream profiles of $u_{rms}(2\omega_B)$.
 u_{rms}/U_T amplitude axis = 5.5%.

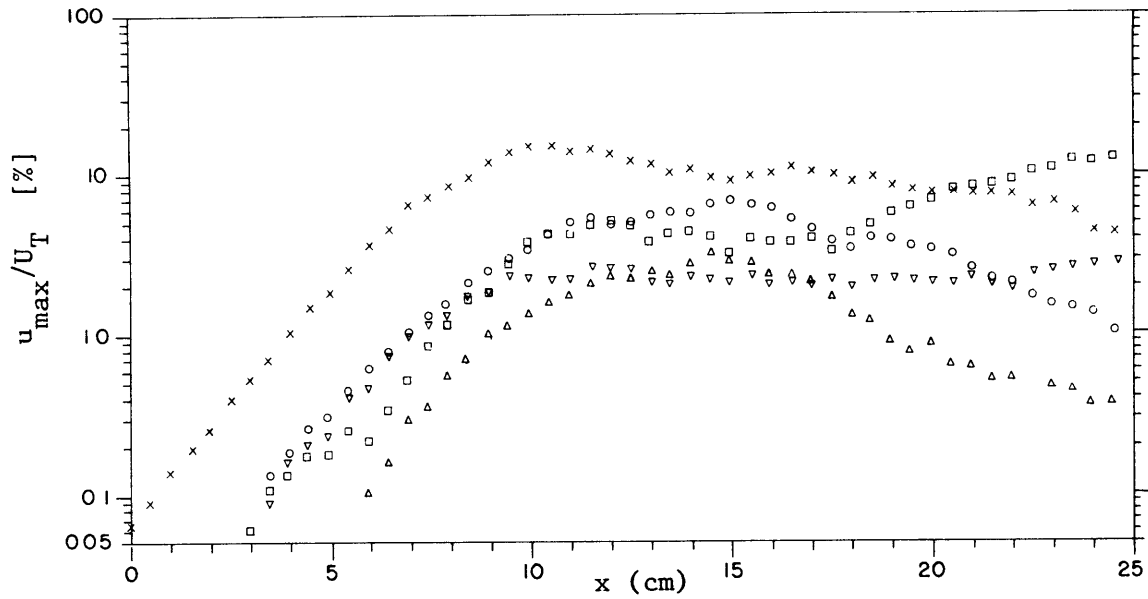


Figure 5.42: Downstream growth of the maximum u_{rms} velocity of each mode in the ω_{fs1} transition. [$x - \omega_{fs1}$; $\square - \omega_{fs1}/2$; $\nabla - 3\omega_{fs1}/2$; $\circ - 2\omega_{fs1}$; $\Delta - 3\omega_{fs1}$.]

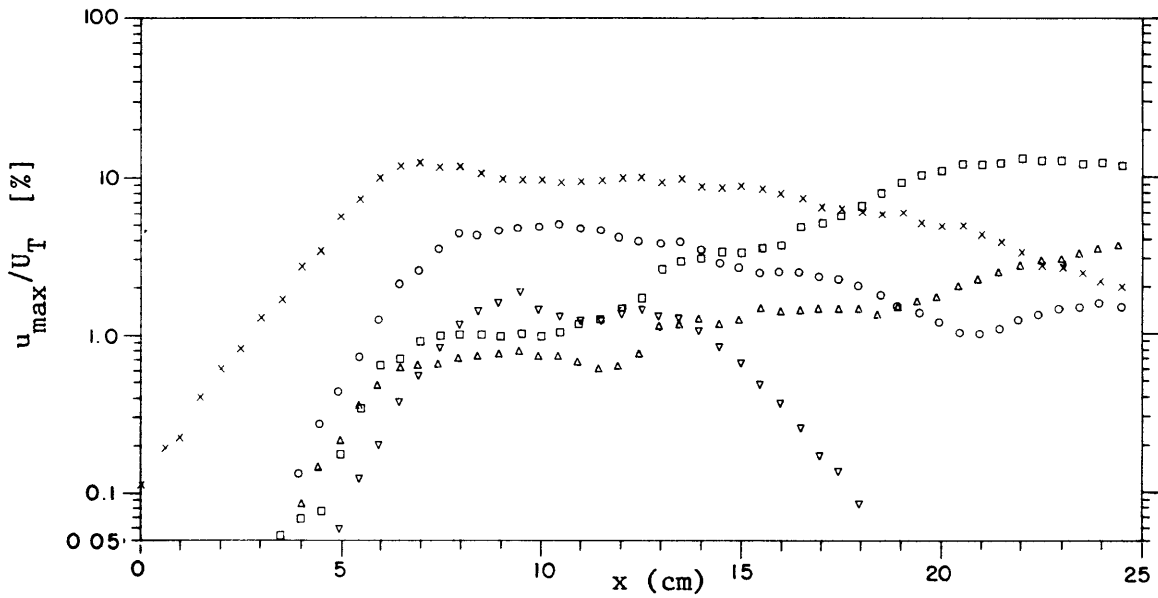


Figure 5.43: Downstream growth of the maximum u_{rms} velocity of each mode in the ω_{II} transition. [$x - \omega_{II}$; $\square - \omega_{II}/2$; $\Delta - 3\omega_{II}/2$; $\circ - 2\omega_{II}$; $\nabla - 3\omega_{II}$.]

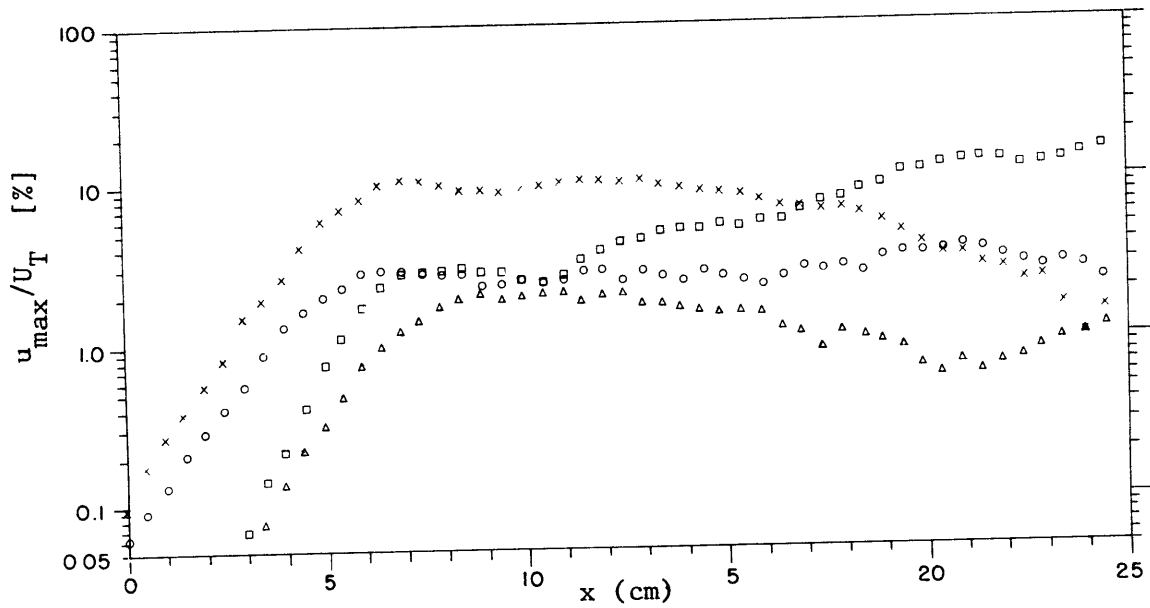


Figure 5.44a: Downstream growth of the maximum u_{rms} velocity of the significant modes in the $(\omega_A + \omega_B)$ transition.
 [x - ω_B ; O - ω_A ; \square - $(\omega_B - \omega_A)$; Δ - $(\omega_A + \omega_B)$.]

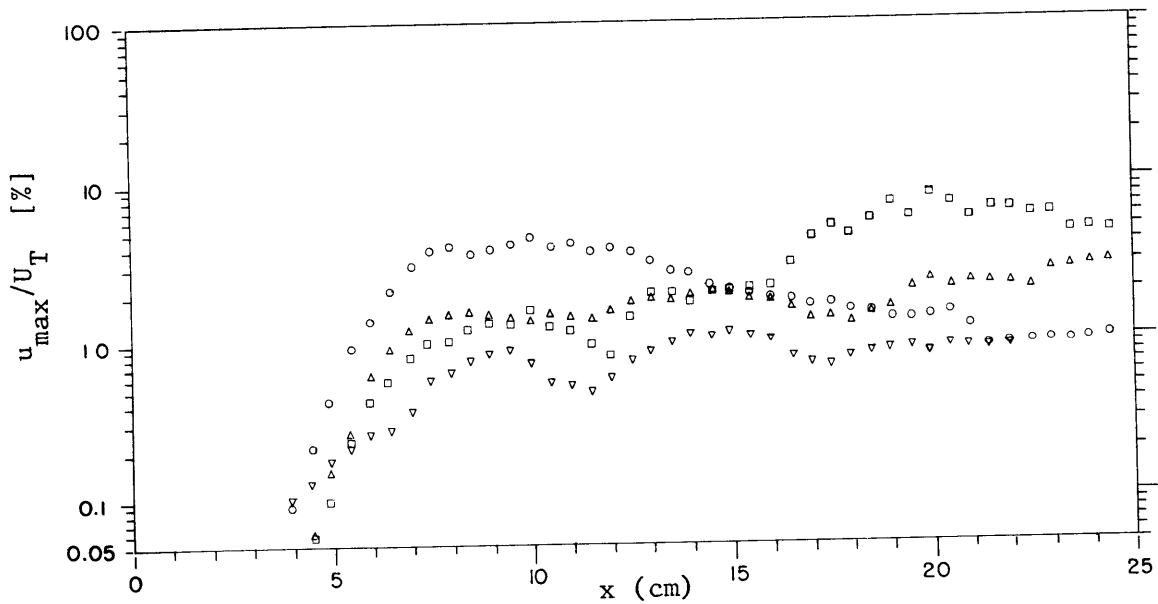


Figure 5.44b: Downstream growth of the maximum u_{rms} velocity of the significant modes in the $(\omega_A + \omega_B)$ transition.
 [\square - $\omega_B/2$; Δ - $(\omega_A + \omega_B)/2$; ∇ - $3\omega_B/2$; O - $2\omega_B$]

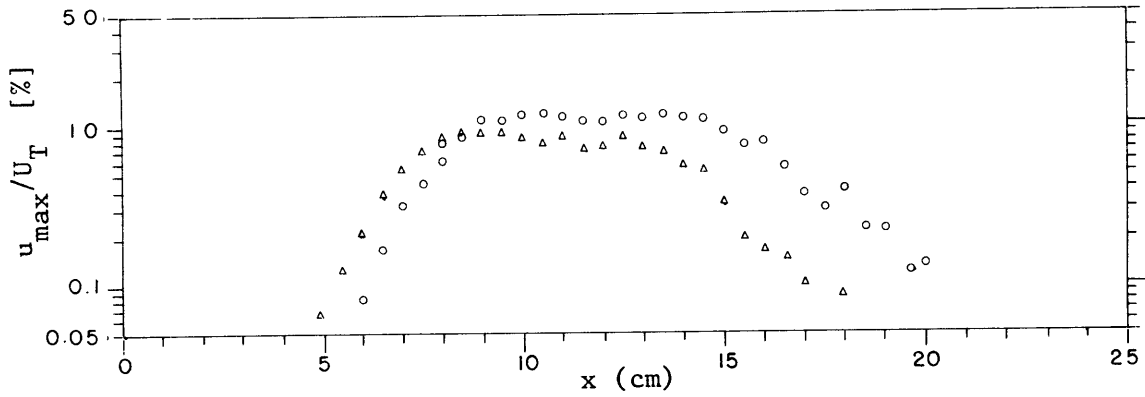


Figure 5.44c: Downstream growth of the maximum u_{rms} velocity of the significant modes in the $(\omega_A + \omega_B)$ transition.
 [$\circ - 3\omega_A; \Delta - (2\omega_B + \omega_A)$]

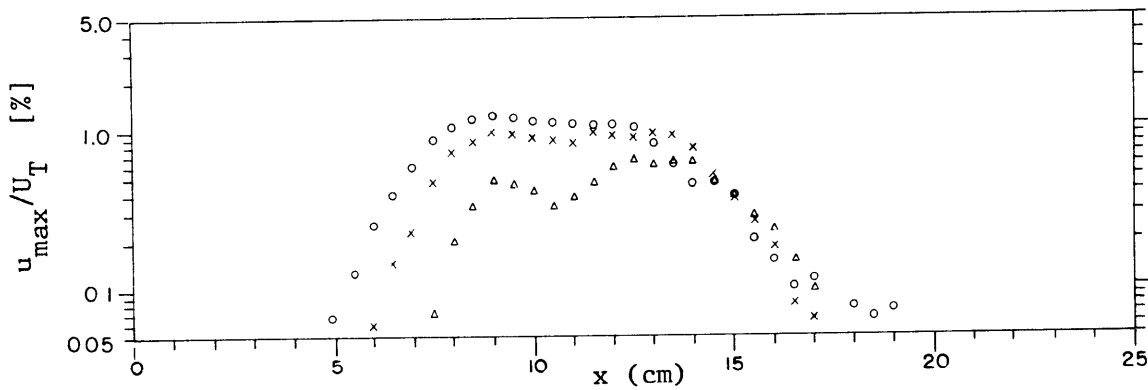


Figure 5.44d: Downstream growth of the maximum u_{rms} velocity of the significant modes in the $(\omega_A + \omega_B)$ transition.
 [$\circ - 3\omega_B; \times - (2\omega_A + \omega_B); \Delta - 2(\omega_A + \omega_B)$]

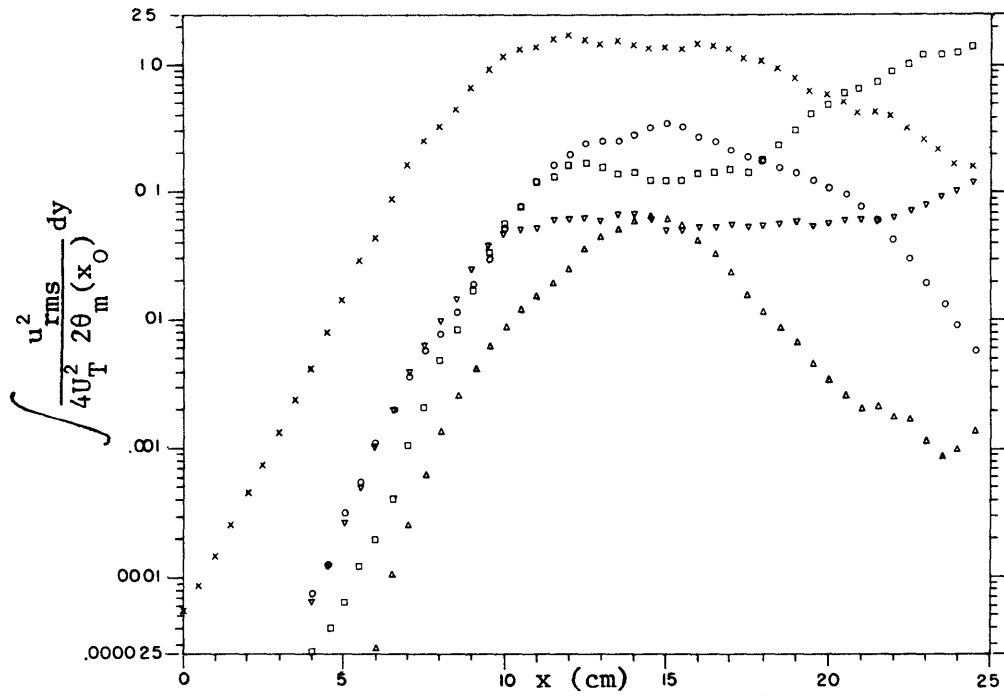


Figure 5.45: Vertically integrated u_{rms}^2 energy of the modes in the ω_{fsl} transition. [$x - \omega_{\text{fsl}}$; $\square - \omega_{\text{fsl}}/2$; $\nabla - 3\omega_{\text{fsl}}/2$; $\circ - 2\omega_{\text{fsl}}$; $\Delta - 3\omega_{\text{fsl}}$.]

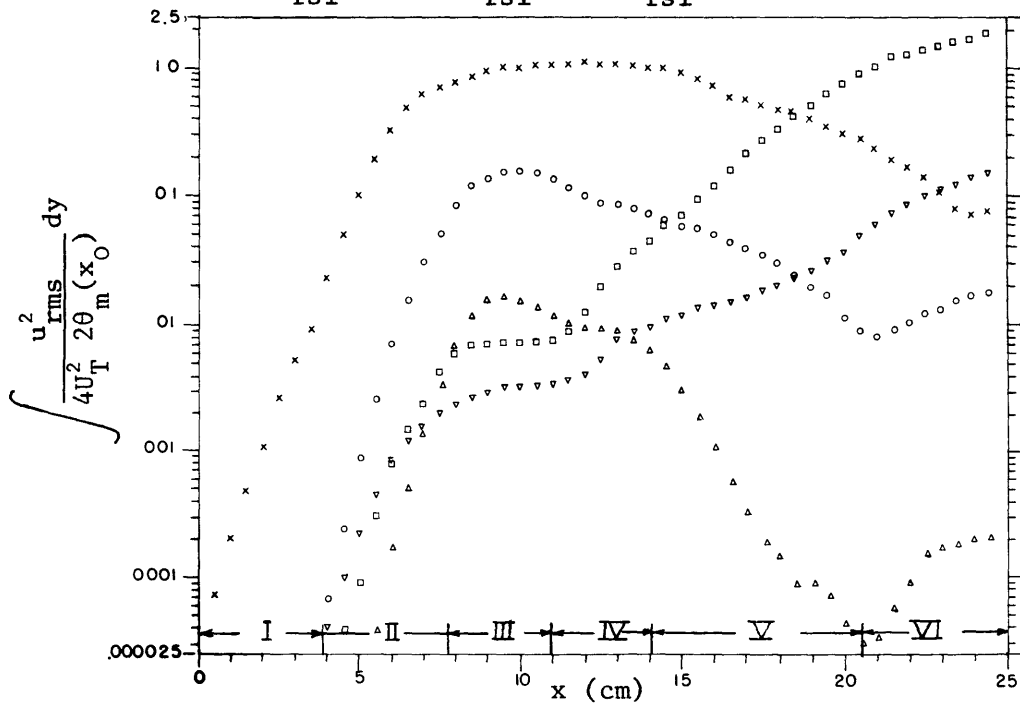


Figure 5.46: Vertically integrated u_{rms}^2 energy of the modes in the ω_{II} transition. [$x - \omega_{\text{II}}$; $\square - \omega_{\text{II}}/2$; $\nabla - 3\omega_{\text{II}}/2$; $\circ - 2\omega_{\text{II}}$; $\Delta - 3\omega_{\text{II}}$.]

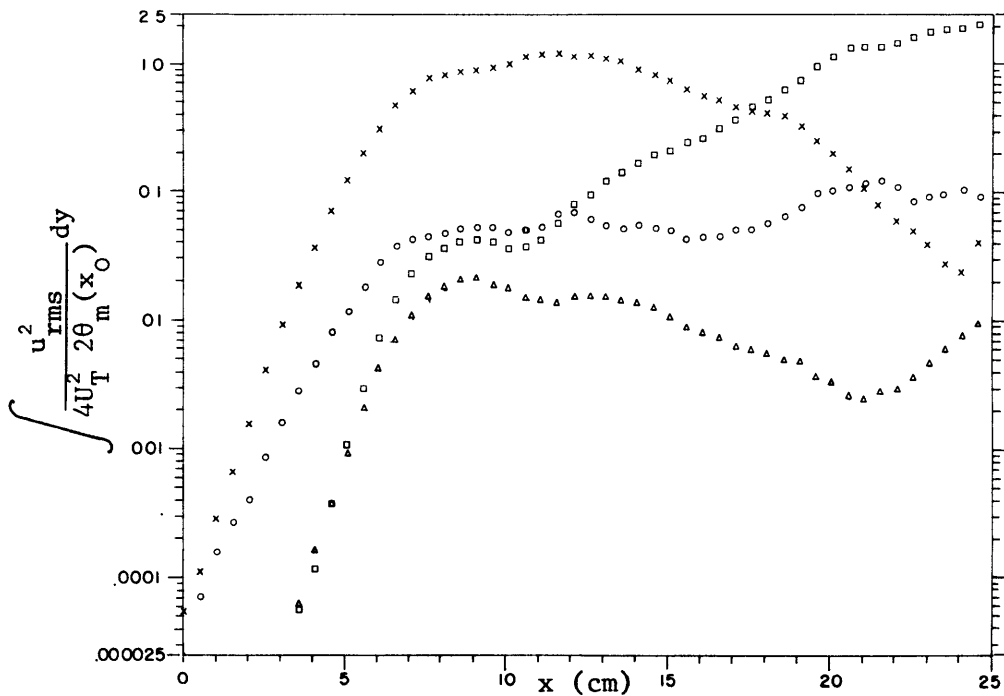


Figure 5.47a: Vertically integrated u_{rms}^2 energy of the modes in the $(\omega_A + \omega_B)$ transition. [$\circ - \omega_A$; $\times - \omega_B$; $\square - (\omega_B - \omega_A)$; $\Delta - (\omega_A + \omega_B)$.]

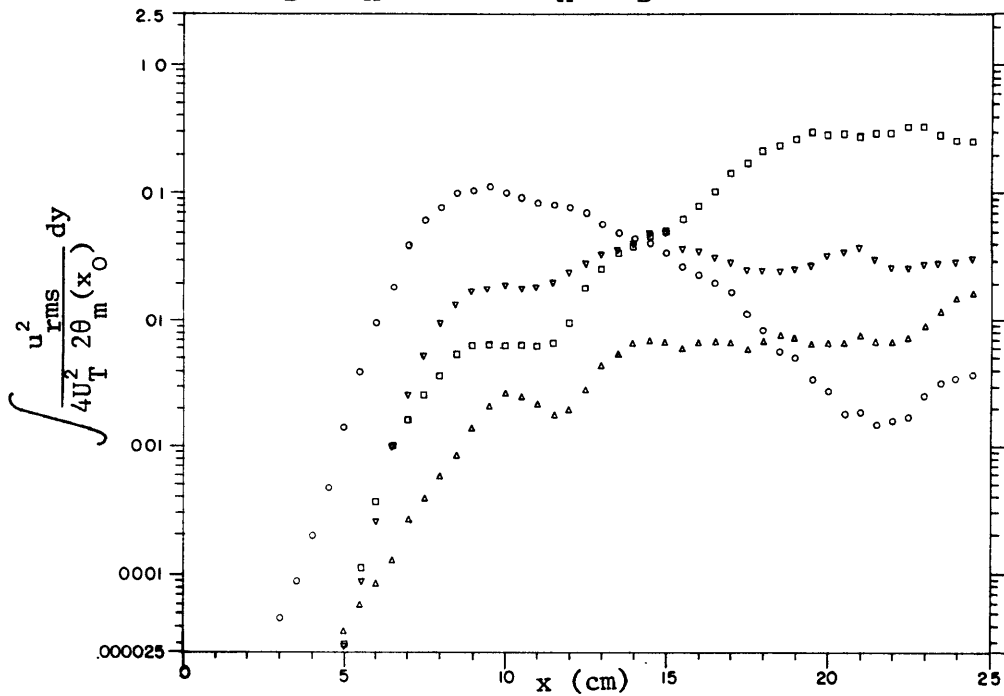


Figure 5.47b: Vertically integrated u_{rms}^2 energy of the modes in the $(\omega_A + \omega_B)$ transition. [$\square - \omega_B/2$; $\nabla - (\omega_A + \omega_B/2)$; $\Delta - 3\omega_B/2$; $\circ - 2\omega_B$.]

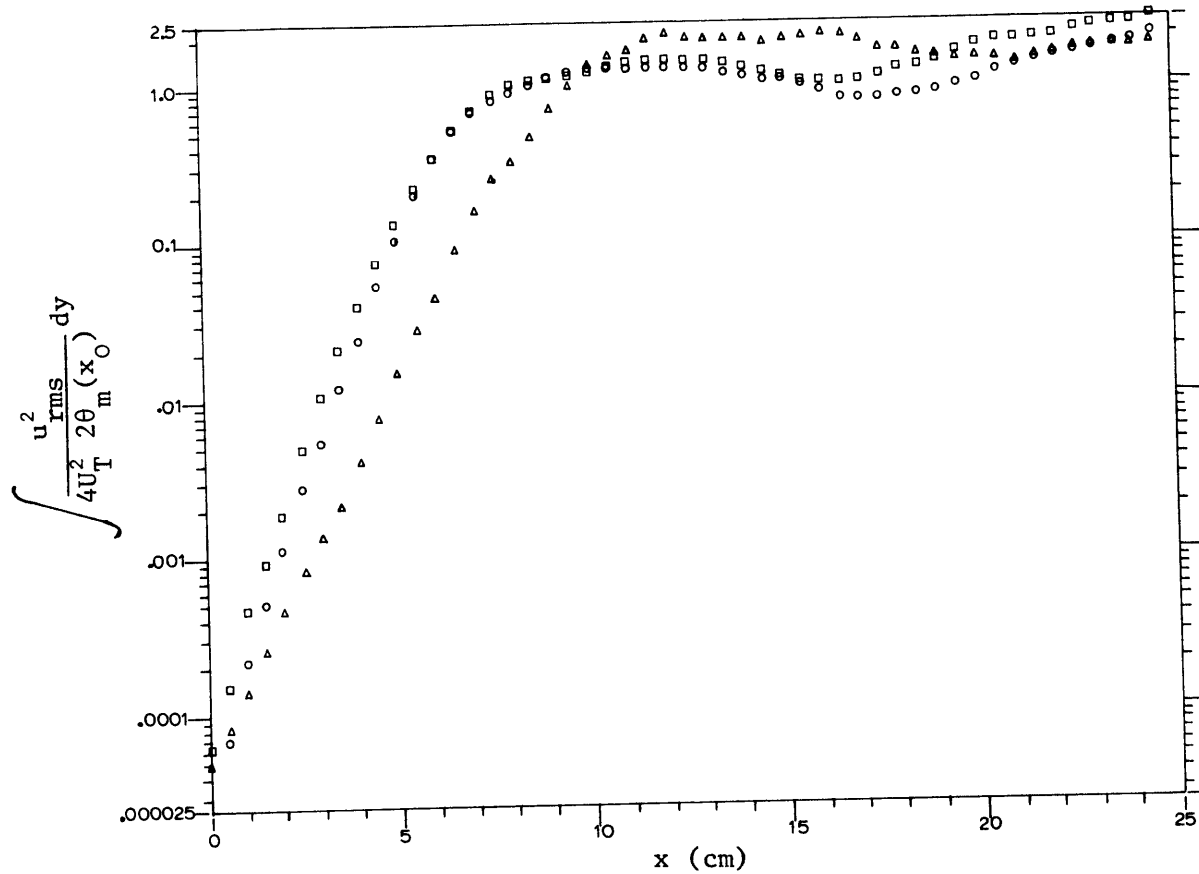


Figure 5.48: Total disturbance energy content, $E(\text{total})$, as defined by the sum of the vertically integrated energies of all modes present in each forced transition. [O- ω_{II} transition; Δ - ω_{fs1} transition; \square - $(\omega_A + \omega_B)$ transition.]

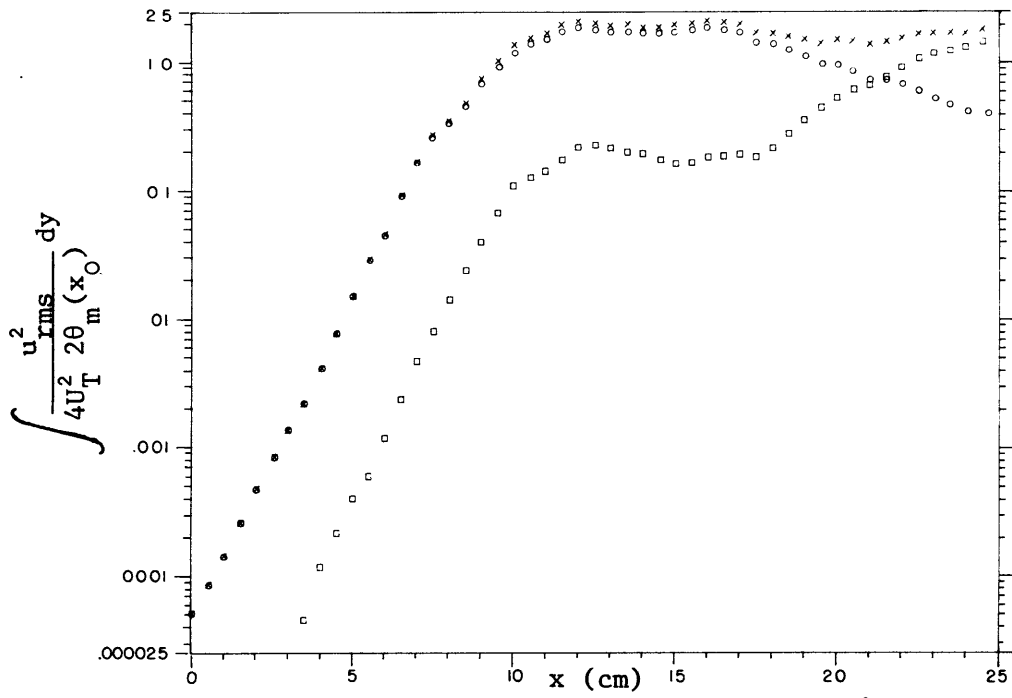


Figure 5.49: Sum of the vertically integrated u_{rms}^2 energy of the odd and even modes in the ω_{fsl} transition. [\square - EM(odd); \circ - EM(even); \times - E(total).]

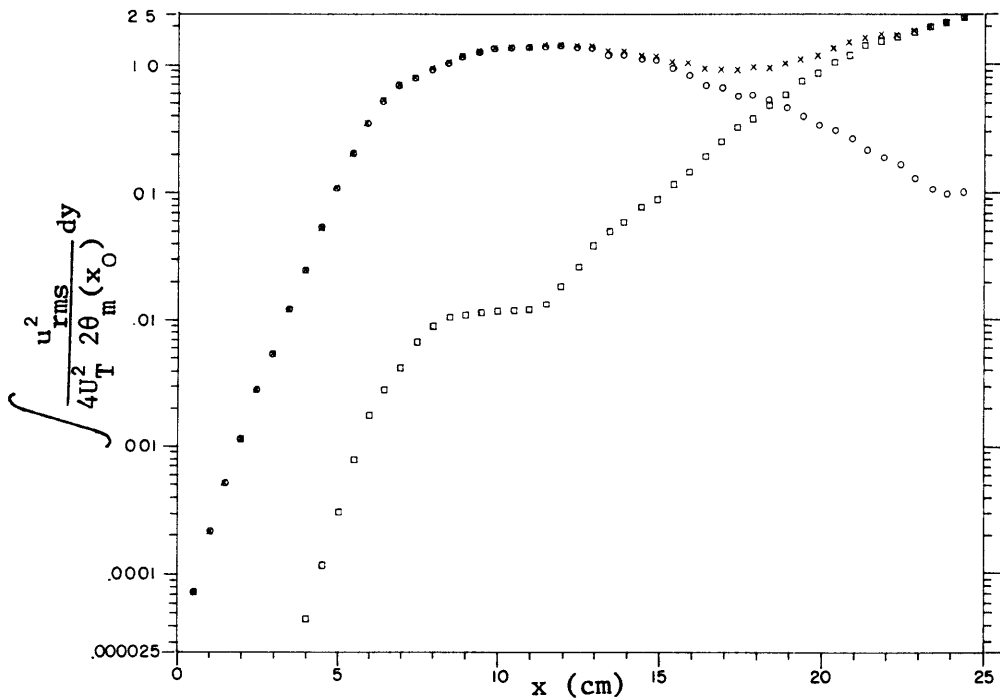


Figure 5.50: Sum of the vertically integrated u_{rms}^2 energy of the odd and even modes in the ω_{II} transition. [\square - EM(odd); \circ - EM(even); \times - E(total).]

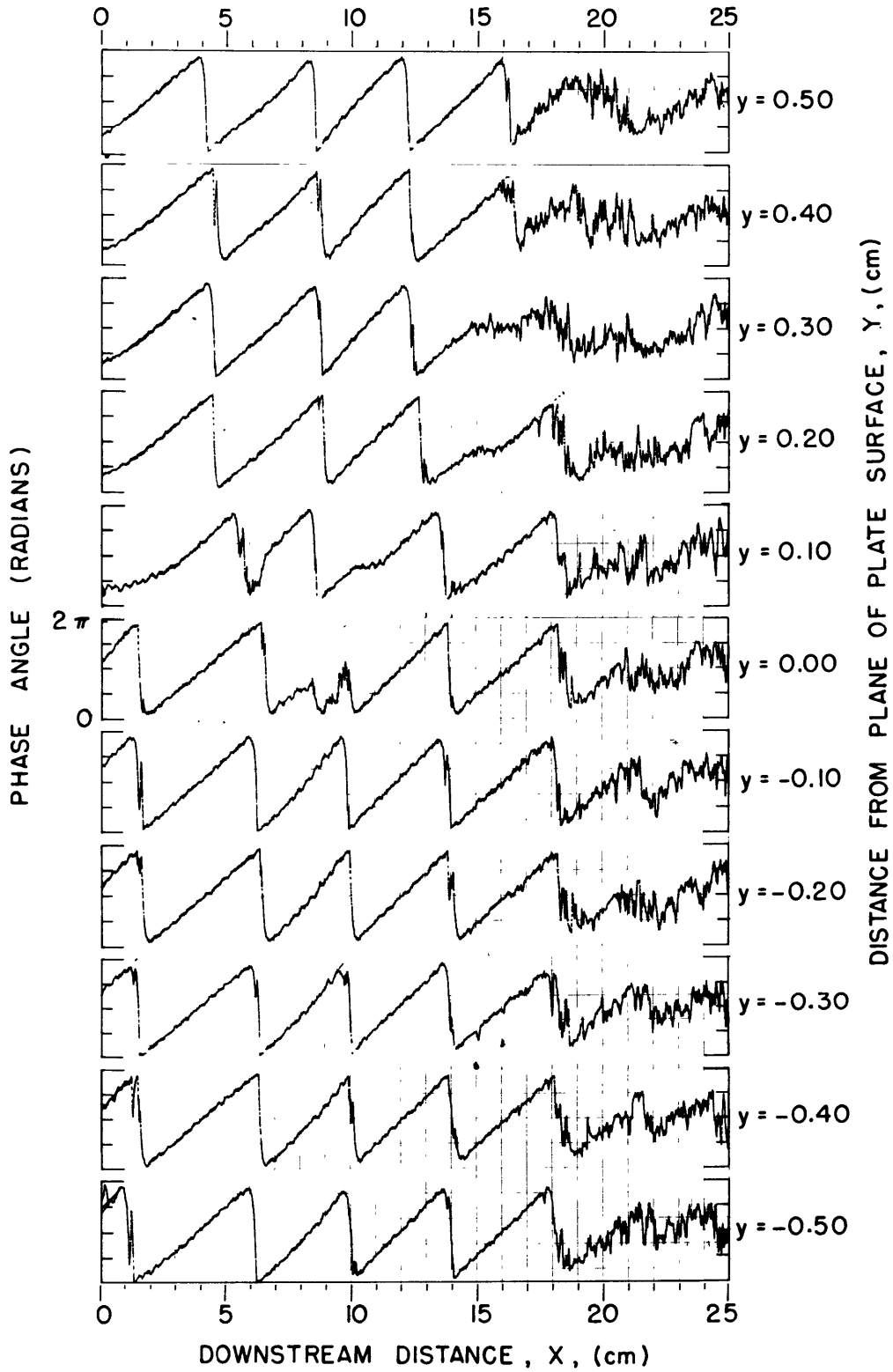


Figure 5.51: Downstream variations in the streamwise phase angle $\phi_1(\omega_{II})$ of the ω_{II} fundamental mode at different values of y .

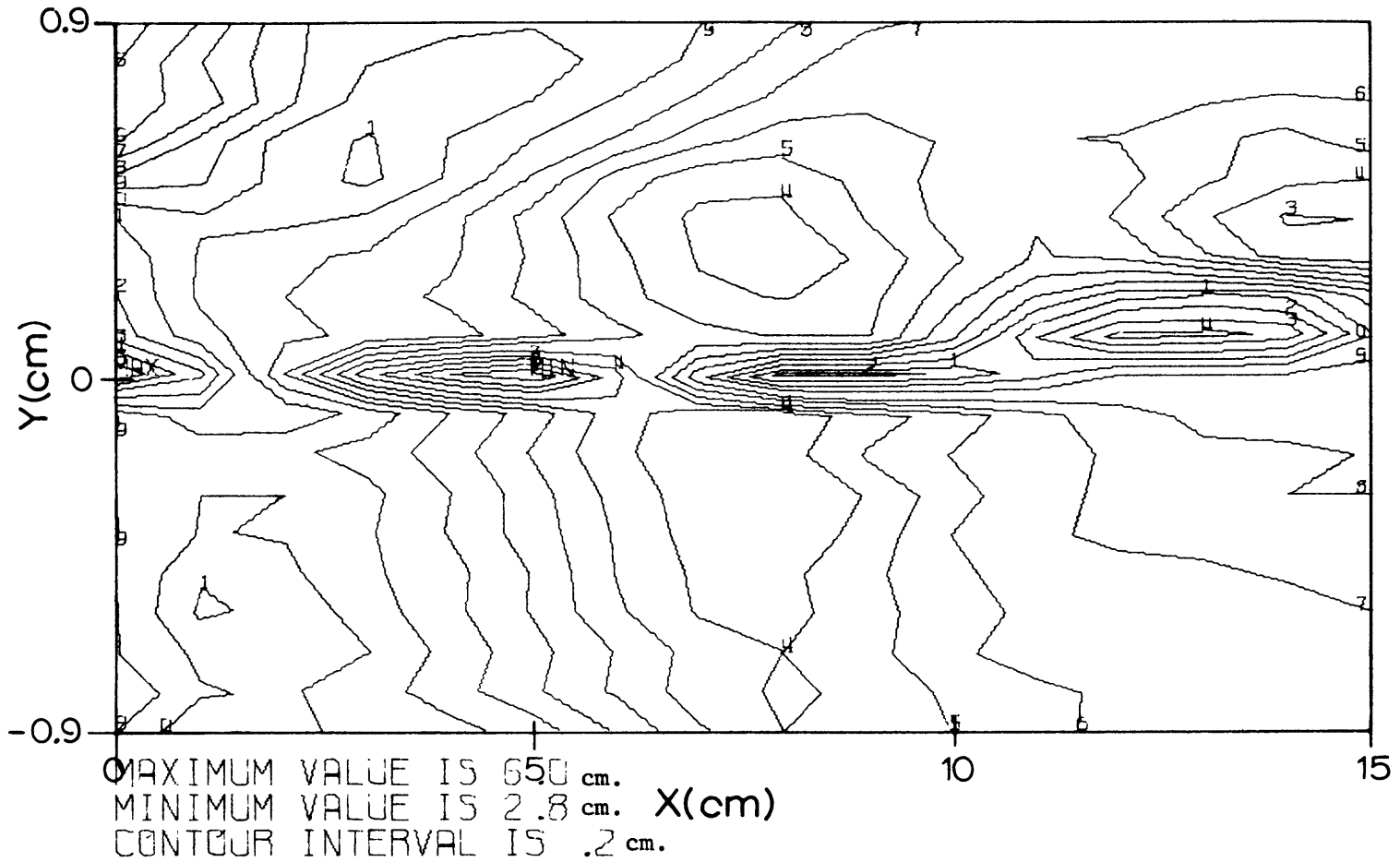


Figure 5.52: Contours of the downstream phase variations of the ω_{II} fundamental mode as seen in a coordinate frame moving with the ω_{II} phase velocity.

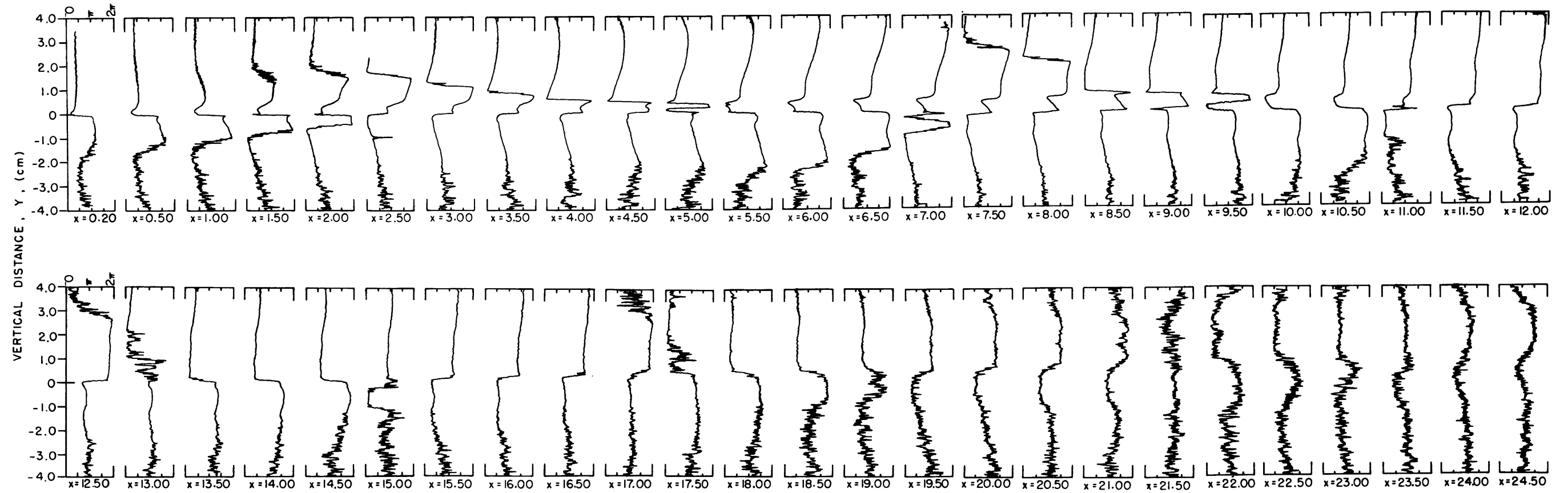


Figure 5.53: Downstream variations in the vertical phase angle profiles of the ω_{II} fundamental mode.

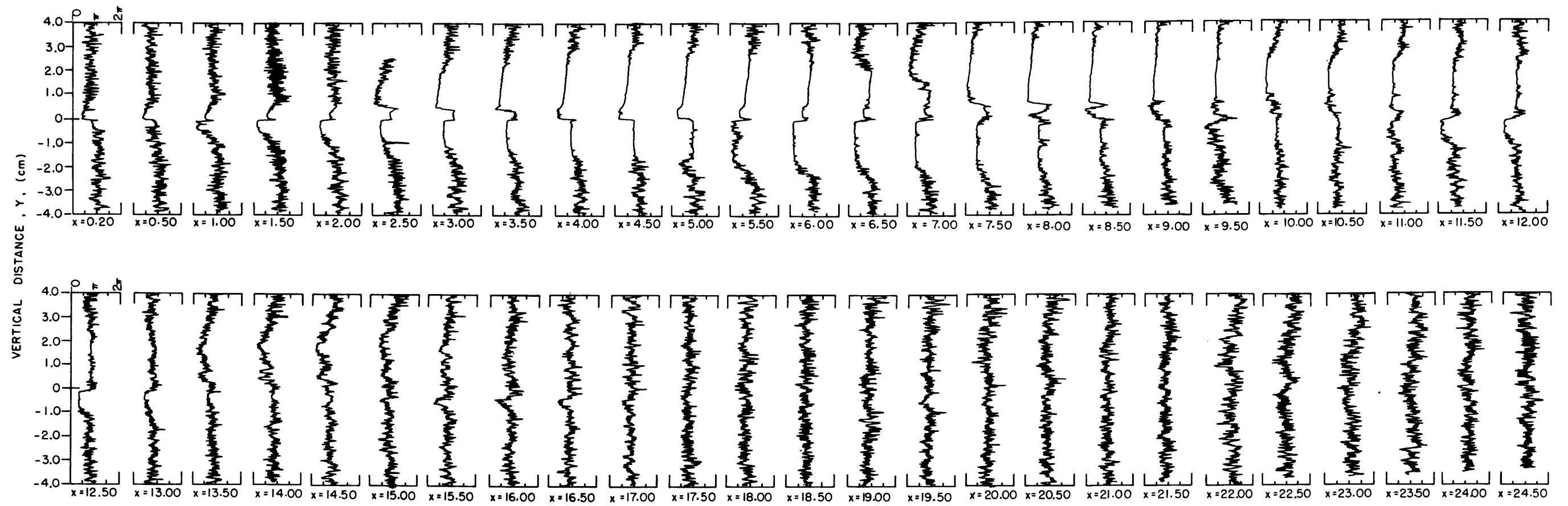


Figure 5.54: Downstream variations in the vertical phase angle profiles of the $\omega_{II}/2$ sub-harmonic mode.

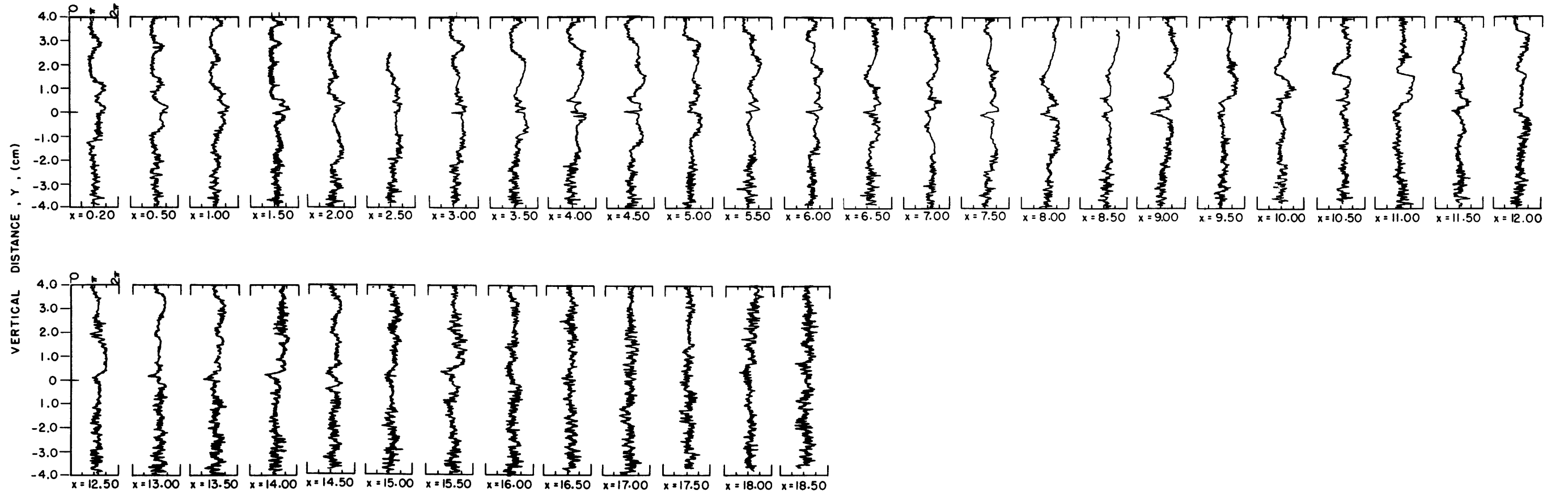


Figure 5.55: Downstream variations in the vertical phase angle profiles of the $3\omega_{II}/2$ harmonic mode.

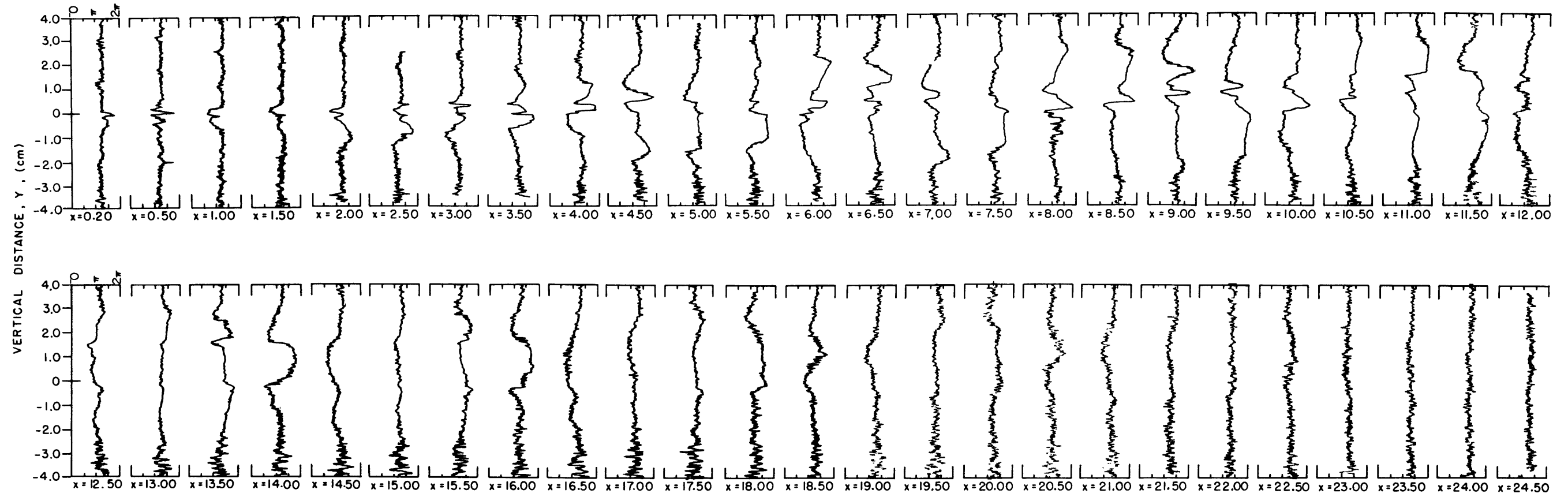


Figure 5.56: Downstream variations in the vertical phase angle profiles of the $2\omega_{II}$ harmonic mode.

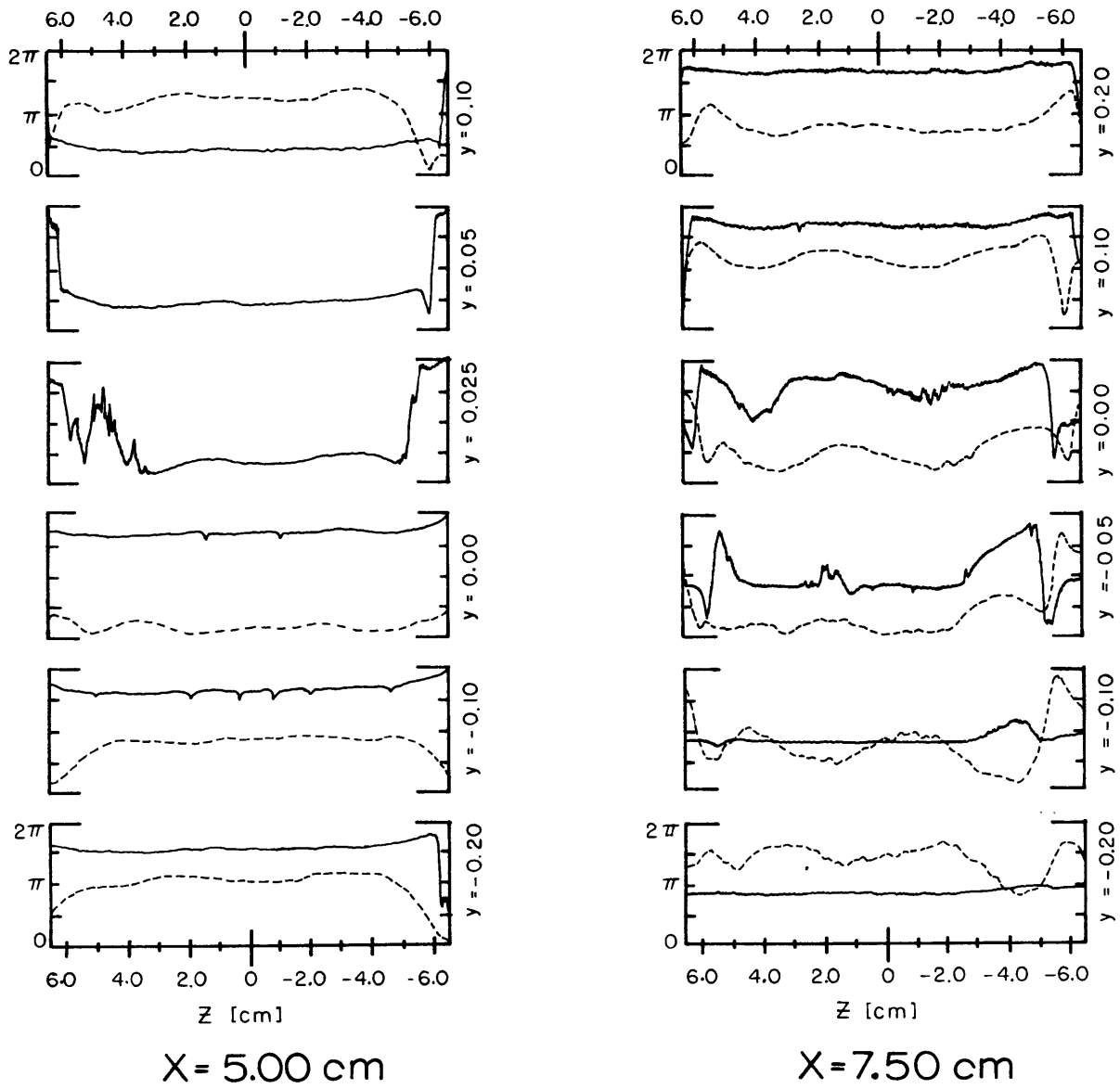


Figure 5.57: Spanwise variations of the spanwise phase angle and e_{rms} wave fronts of the ω_{II} fundamental mode at different values of y .
 — $\phi_3(\omega_{II})$; ---- $e_{rms}(\omega_{II})$

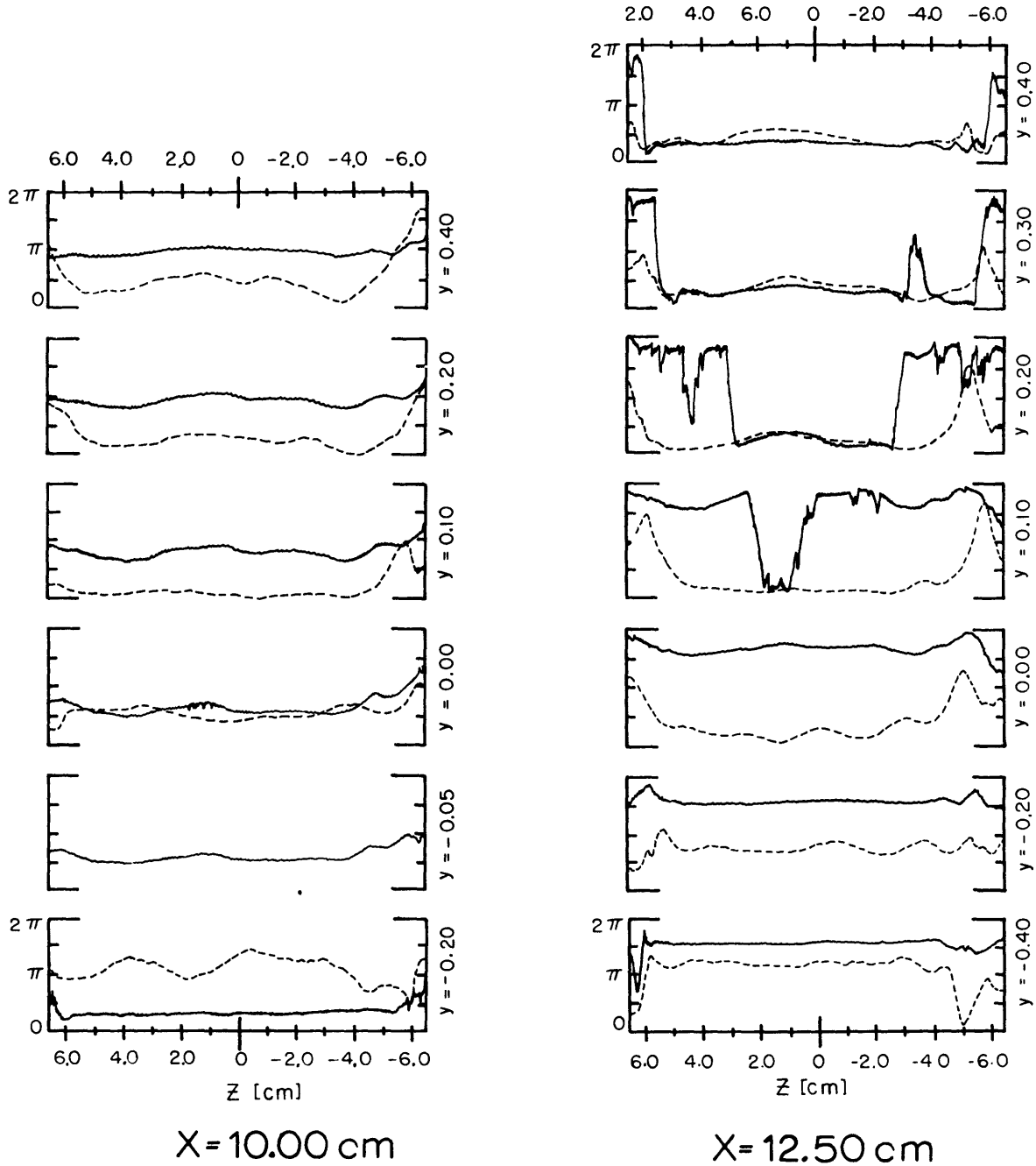
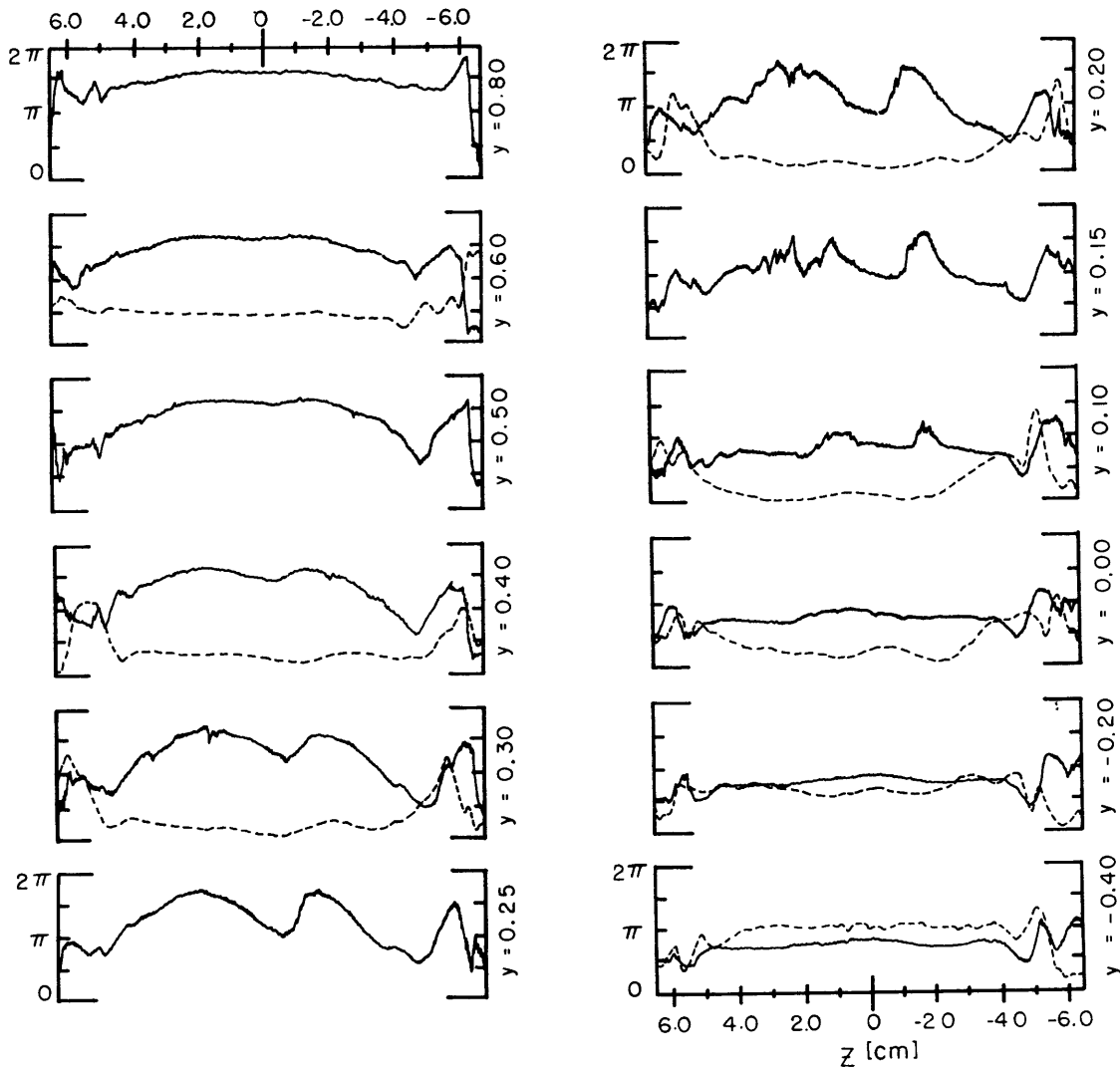
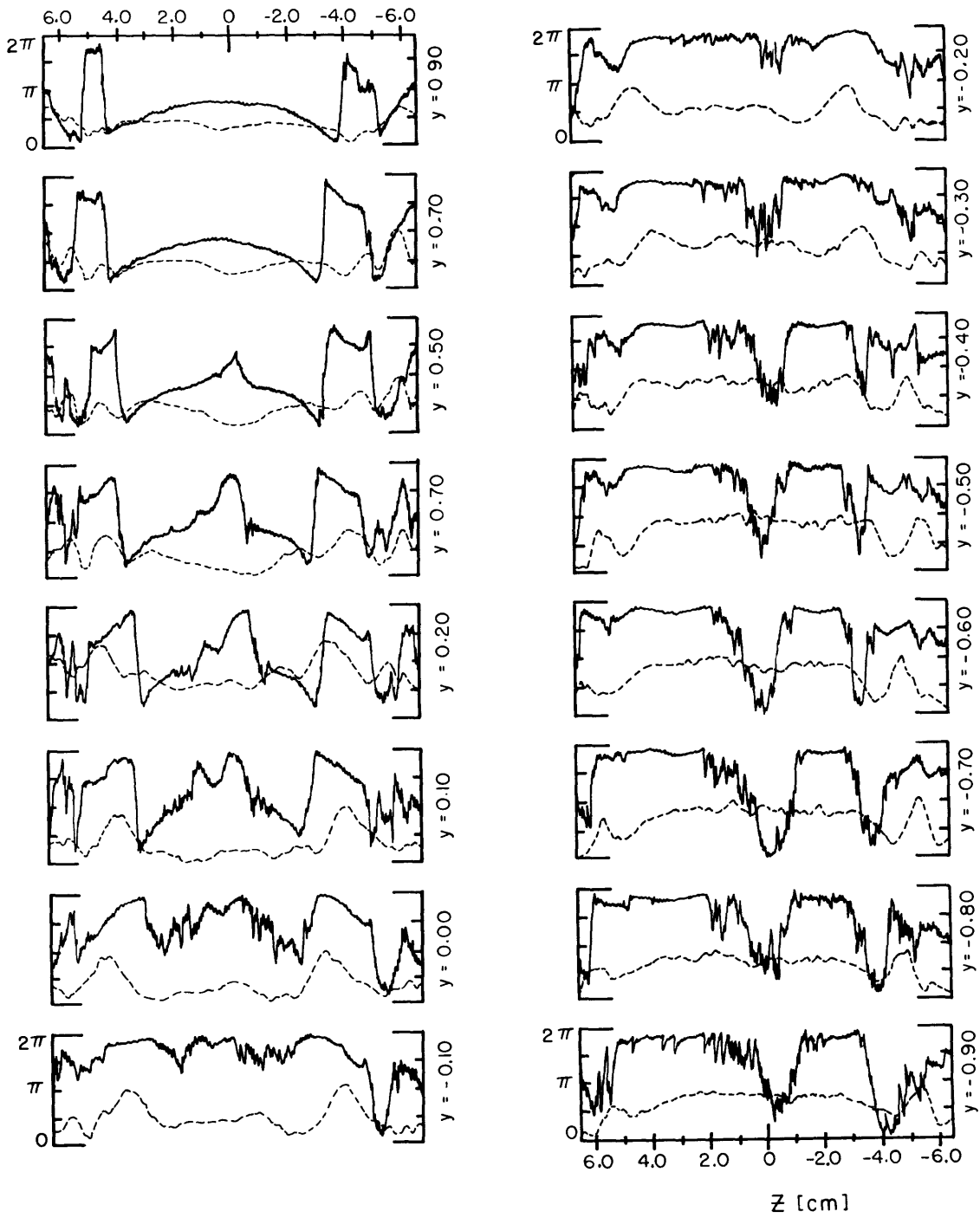


Figure 5.58: Spanwise variations of the spanwise phase angle and e_{rms} wave fronts of the ω_{II} fundamental mode at different values of y .
 — $\phi_3(\omega_{\text{II}})$; ---- $e_{\text{rms}}(\omega_{\text{II}})$.



X=15.00 cm

Figure 5.59: Spanwise variations of the spanwise phase angle and e_{rms} wave fronts of the ω_{II} fundamental mode at different values of y .
 — $\phi_3(\omega_{II})$; --- $e_{rms}(\omega_{II})$.



$X = 17.50 \text{ cm}$

Figure 5.60: Spanwise variations of the spanwise phase angle and e_{rms} wave fronts of the ω_{II} fundamental mode at different values of y .
 — $\phi_3(\omega_{\text{II}})$; --- $e_{\text{rms}}(\omega_{\text{II}})$.

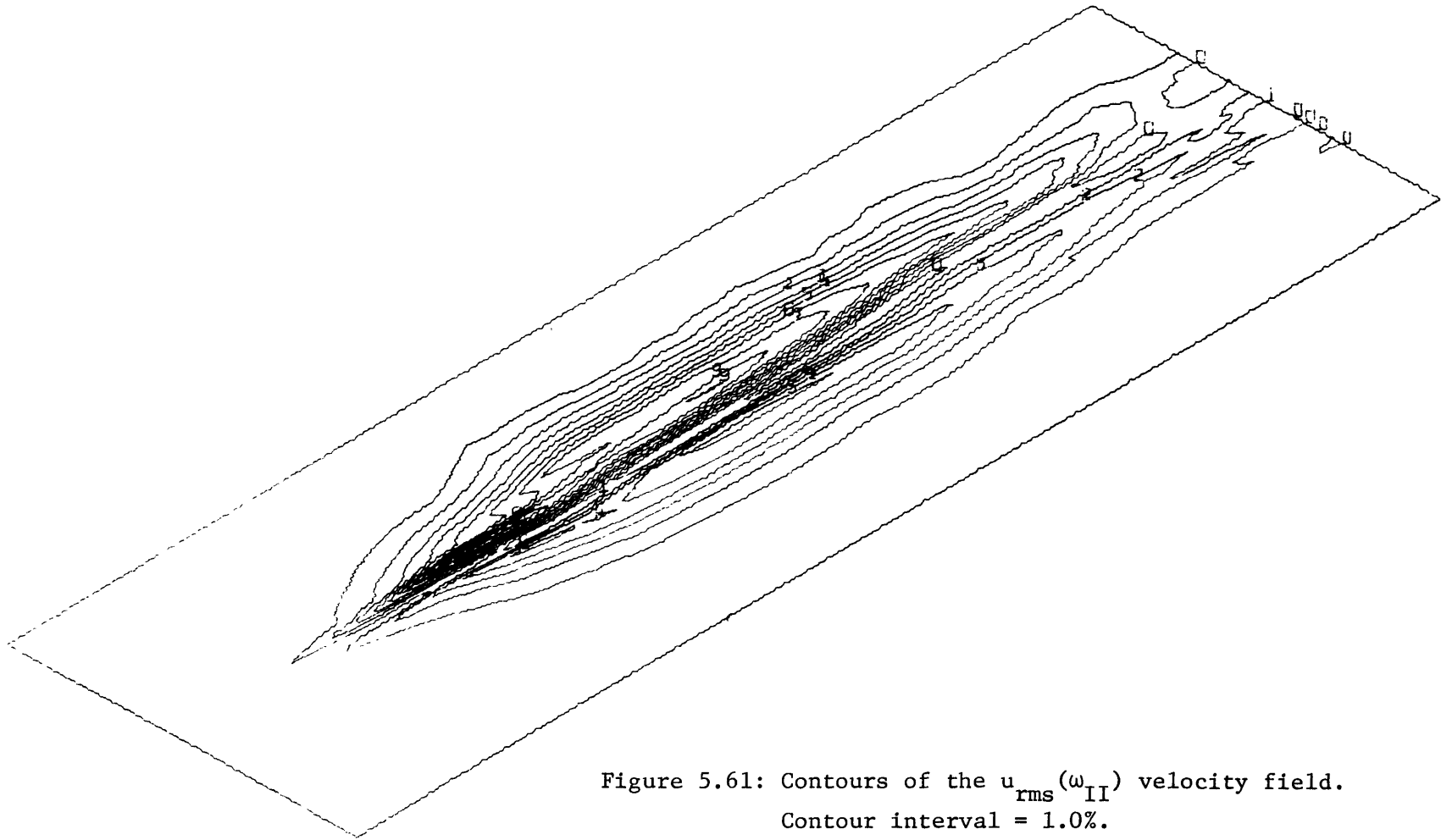
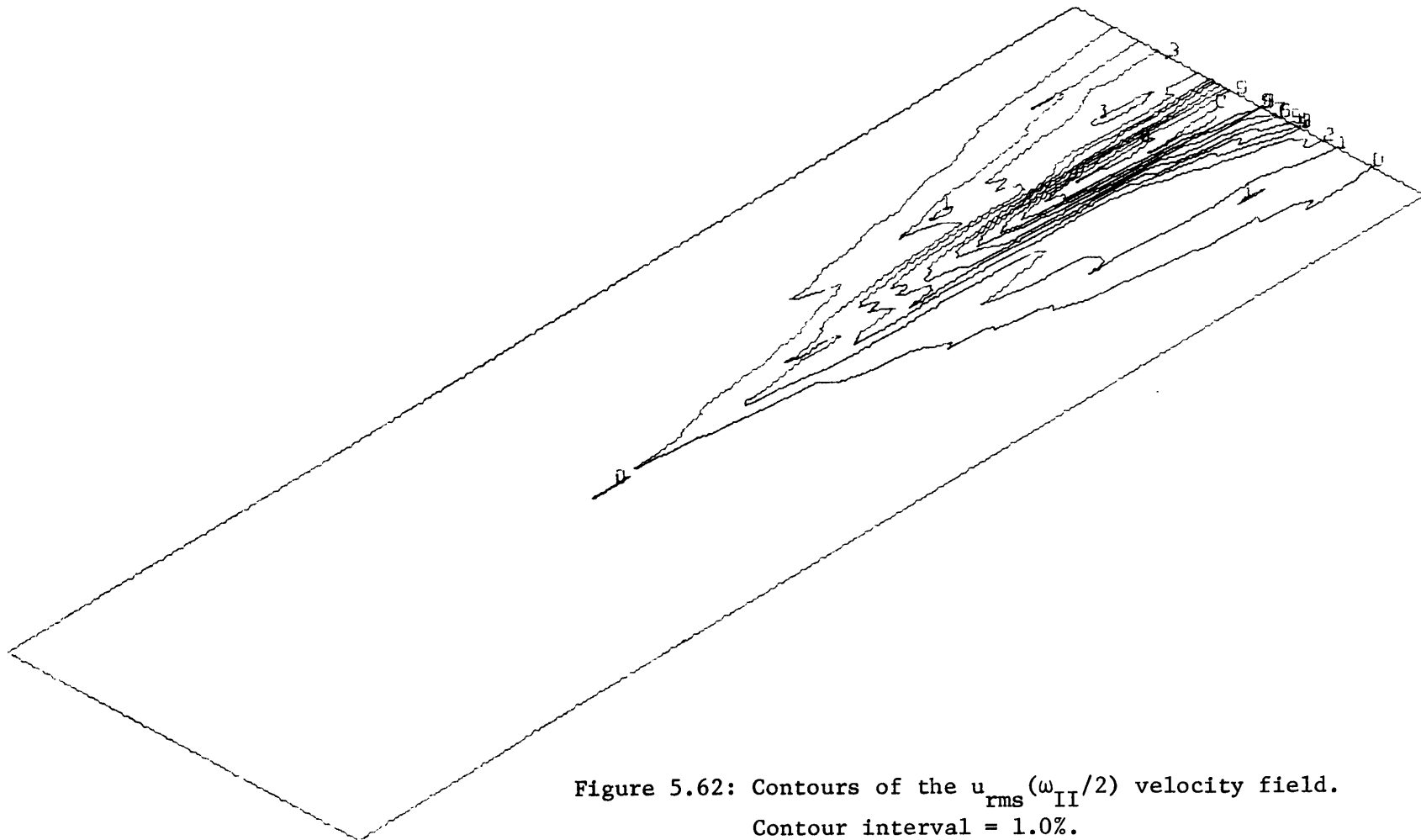
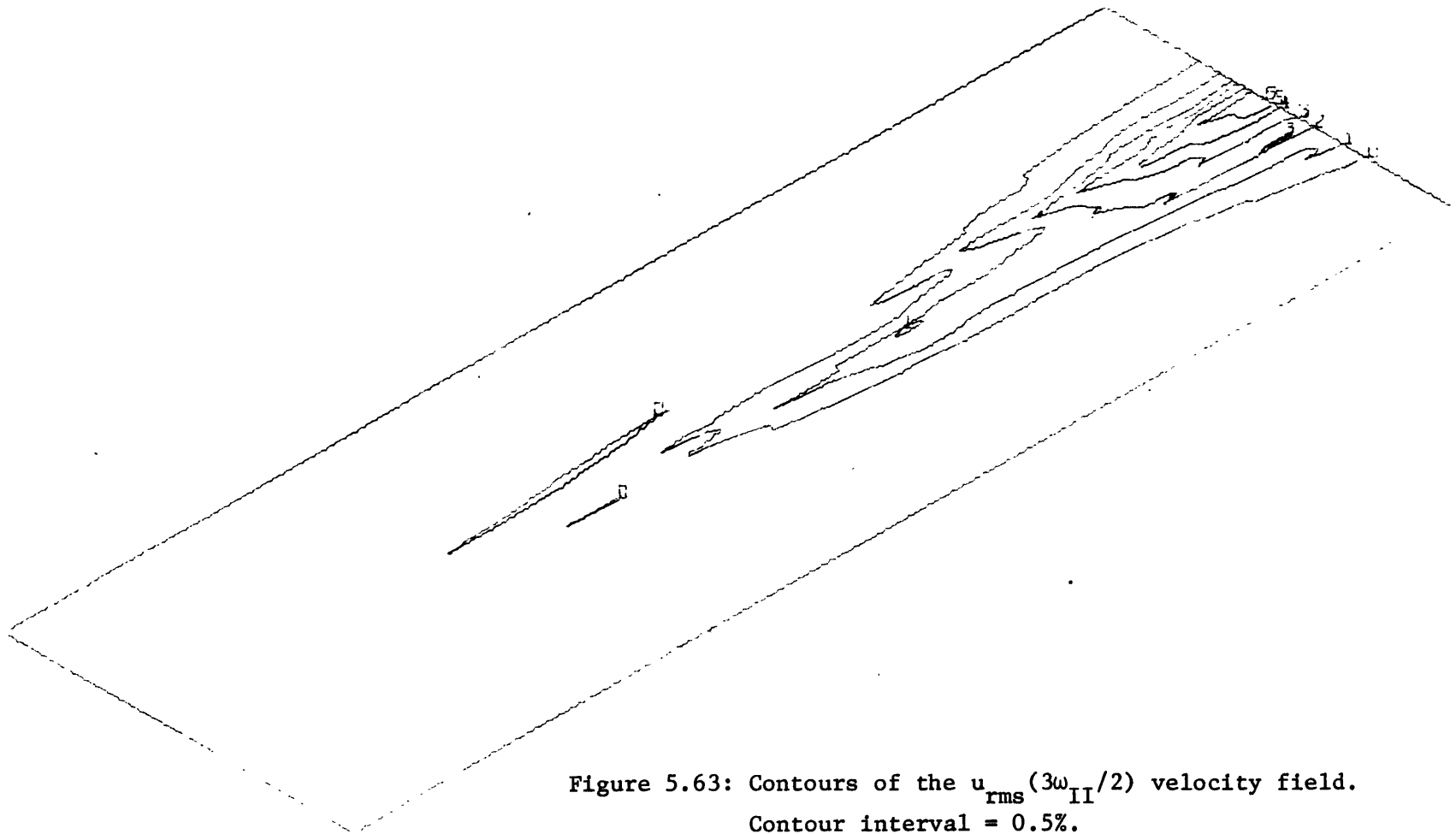


Figure 5.61: Contours of the $u_{\text{rms}}(\omega_{\text{II}})$ velocity field.
Contour interval = 1.0%.





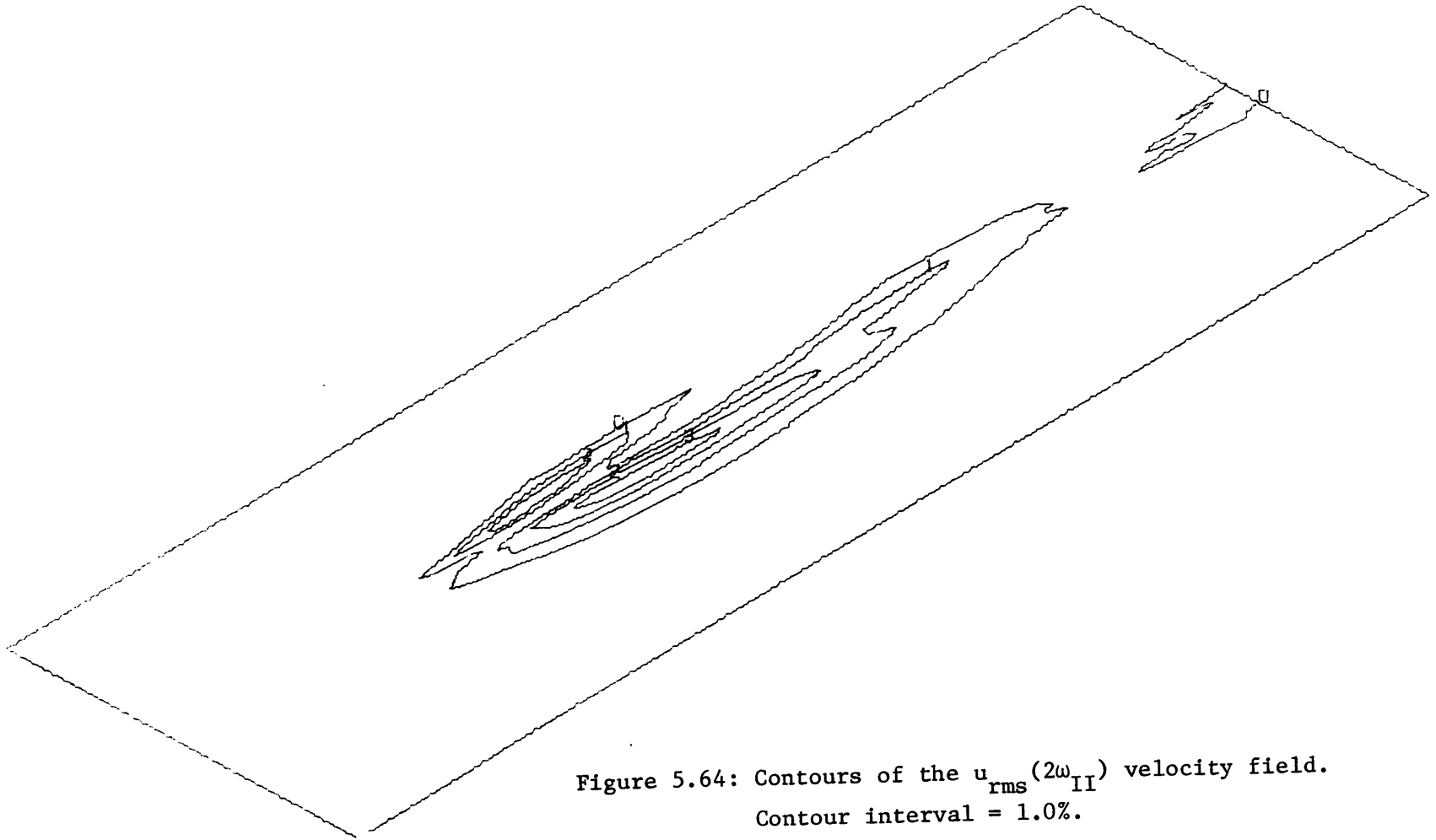


Figure 5.64: Contours of the $u_{\text{rms}}(2\omega_{\text{II}})$ velocity field.
Contour interval = 1.0%.

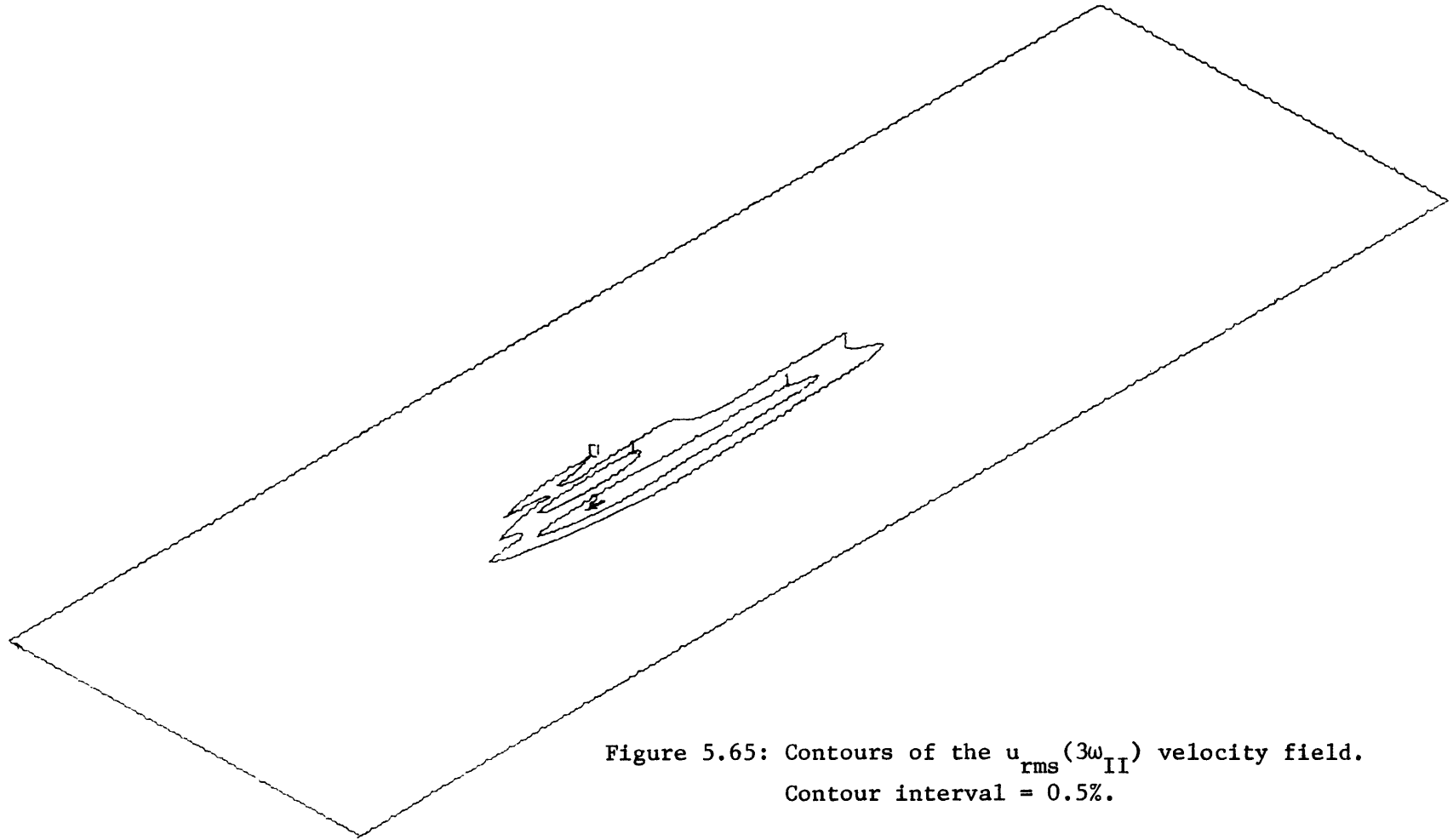


Figure 5.65: Contours of the $u_{\text{rms}} (3\omega_{\text{II}})$ velocity field.
Contour interval = 0.5%.

CHAPTER VI
DISCUSSION OF THE TRANSITION PROCESS

As briefly mentioned in chapter IV, the single mode forced transitions were characterized by six distinct regimes, each of which exhibited a particularly unique character. For convenience these will be referred to as regions I-VI. The identifying characteristics of each region are noted below for the ω_{II} transition.

| Region | Approximate Extent | Characteristics |
|--------|--------------------------------------|--|
| I | $0.0 \rightarrow 0.9 \lambda_{II}$ | Fundamental mode grows exponentially and obeys linear theory. No non-linear modes present. |
| II | $0.9 \rightarrow 1.8 \lambda_{II}$ | Fundamental mode continues to grow exponentially; exponentially growing non-linear modes appear. |
| III | $1.8 \rightarrow 2.5 \lambda_{II}$ | Fundamental mode reaches a finite amplitude equilibration state; non-linear modes also equilibrate. |
| IV | $2.5 \rightarrow 3.20 \lambda_{II}$ | Fundamental mode remains in equilibration; sub- and 3/2 harmonics start second region of growth; second and third harmonics start to decay. |
| V | $3.2 \rightarrow 4.75 \lambda_{II}$ | Termination of fundamental mode equilibration; second and third harmonics decay strongly; sub- and 3/2 harmonics change growth rates but continue to grow. Three-dimensional distortions of the fundamental appear. |
| VI | $4.75 \rightarrow 5.75 \lambda_{II}$ | Final breakdown of flow; disturbance spectra rapidly fill in; ω_{II} , $2\omega_{II}$, $3\omega_{II}$ start to grow again, $\omega_{II}/2$, $3\omega_{II}/2$ approach a second equilibration; strong three-dimensional distortions. |

Table 6.1: Identifying downstream characteristics of the ω_{II} Transition.

This chapter is presented in two segments. The first considers the detailed behavior of the single mode forced transitions and is divided into six sections, each concerning itself with a given region of transition. Primary emphasis is placed on the ω_{II} transition of the maximally unstable mode. The second segment concerns itself with the mixed mode $(\omega_A + \omega_B)$ transition.

The effects of forcing on the transition process, and the relative character of the forced and natural transitions have been discussed in chapter IV and will be drawn upon when needed; otherwise the following discussions will only be concerned with the forced transtions.

VI.I Single Mode Forced Transition

Region I: Linear Transition ($0.0 \rightarrow 0.9 \lambda_{II}$)

In order to interpret the experimental results in the linear transition zone, a series of stability calculations were made for various downstream mean velocity profiles. The mean profile at each station was approximated by a trapezoidal model (see below). The linear, inviscid limit was taken and the Rayleigh equation was solved. The resulting eigenvalue matrix was analyzed for both temporal and spatial instabilities.

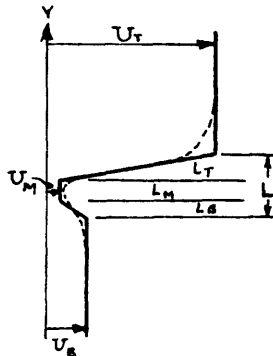


Figure 6.1: Trapezoidal approximation of a continuous velocity profile.

After several preliminary calculations both intuition and the general trend of the calculations indicated that the proper method of fitting the trapezoidal profile to the real data was to choose the slope and length scale of each segment to model the maximum mean shear as previously calculated from the experimental data. Since (U_T, U_B, U_M) are fixed by the experimental data, this technique introduced three length scales (L_T, L_B, L) or equivalently (L_T, L_B, L_M) . As might be expected, the calculations for the maximally unstable mode (which were due to the upper layer inflexion point) were not significantly affected by slight variations in L_M and L_B if the overall scale, L , was held constant. However, variations in L_T (which changed the maximum modeled vorticity) or in L (which altered the characteristic length scale) caused variations of 10 to 20% in the predicted growth rates and wavelengths.

(a) Stability of the Initial Wake Profile

Both temporal and spatial analyses were made for the initial profile at x_0 and the results are presented in figure 5.1. The spatial analysis presented convergence problems for large values of $|\alpha|$; this behavior has been noted by other authors, Mattingly (1968), in conjunction with continuous profiles. It seems to be an inherent problem with spatial models, and not one due to the trapezoidal approximations. The excessive computation costs involved with the spatial analysis precluded an attempt to calculate the eigenvalues for large values of $|\alpha|$ and once the maximally unstable mode was reached the calculations were terminated. The agreement between the spatial model and experimental data was quite good for small $|\alpha|$. The poorer agreement for larger values of $|\alpha|$ is to

be expected for a trapezoidal model.

Although the temporal and spatial models gave slightly different maximum growth rates, both were centered near the frequency of the experimentally determined maximally unstable mode. The results of both analyses are tabulated below along with the experimental values.

The pertinent results of previous workers on similar problems are also included for comparison. These comparative results were typically obtained for single inflexion point shear layers and correspond to the mode II upper inflexion point instability of the trapezoidal profile.

Table 6.2: Eigenvalues for the maximally unstable mode II disturbances

| <u>Model</u> | <u>Frequency</u> β_r | <u>Growth rate</u> | <u>Wave no.</u> | <u>Phase speed</u> |
|----------------------------|-------------------------------|--|-----------------|--------------------|
| Miksad (exp) | 0.2175 | $-\alpha_i = 0.1970$ | 0.380 | 0.570 |
| Miksad (spatial) | 0.2216 | $-\alpha_i = 0.2370$ | 0.414 | 0.536 |
| Miksad (temporal) | 0.2090 | $\alpha_r c_i / c_r = 0.1560$ $\alpha_r c_i / c_g = 0.1540$ | 0.396 | 0.547 |
| Browand (exp) | 0.227 | $-\alpha_i = 0.220$ | $0.36 \pm .08$ | 0.58 ± 0.11 |
| Sato (exp) | 0.2208 | $-\alpha_i = 0.184$ | 0.37 | $0.54 \pm .08$ |
| Freythuth (exp) | 0.2140 | $-\alpha_i = 0.180$ | ----- | ----- |
| Michalke (spatial) | 0.2067 | $-\alpha_i = 0.2284$ | 0.4031 | 0.5137 |
| Michalke (temporal) | 0.223 | $\alpha_r c_i / c_r = 0.1898$ | 0.4446 | 0.5000 |
| Lessen & Fox (temporal) | 0.220 | $\alpha_r c_i / c_r = 0.160$ $\alpha_r c_i / c_g = 0.150$ | 0.408 | 0.5400 |

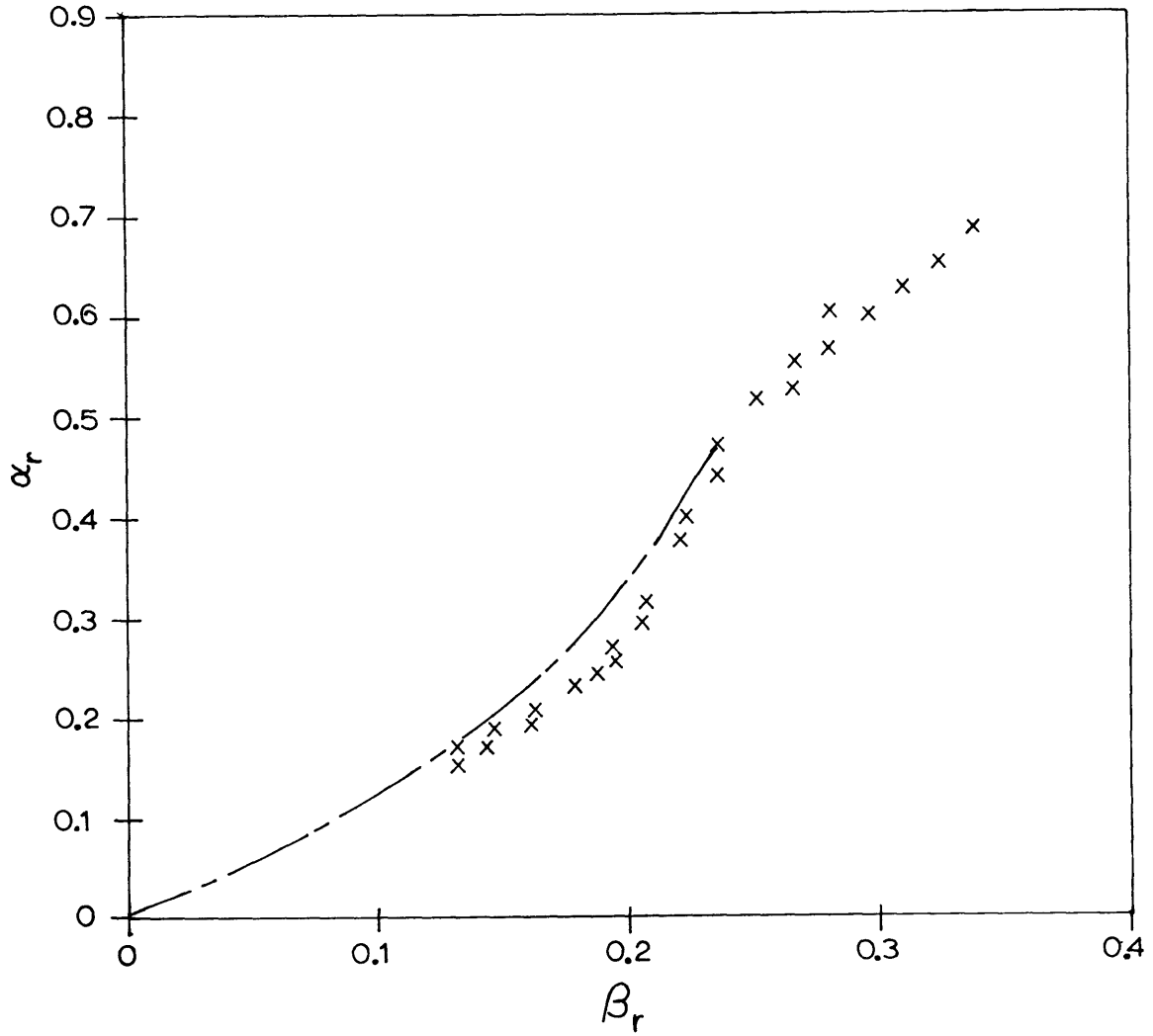


Figure 6.2: Experimentally measured wavenumber, α_r , versus frequency, β_r , relation for the fundamental modes. Dashed curve is the α_r vs β_r relation predicted by a spatial stability model at x_0 .

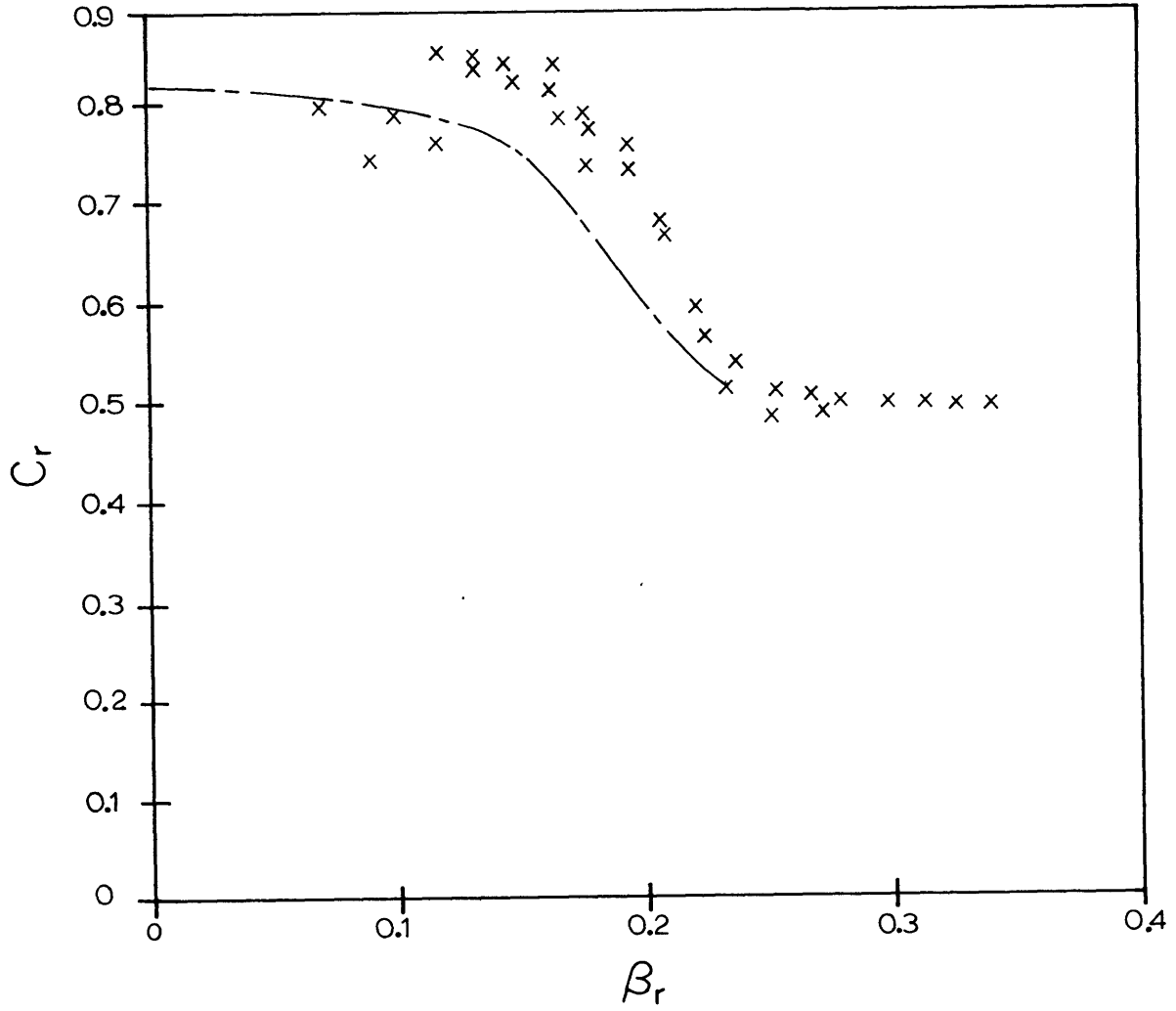


Figure 6.3: Phase speeds c_r of the fundamental modes versus frequency β_r . Dashed line is the c_r vs β_r relation predicted by a spatial stability model at x_0 .

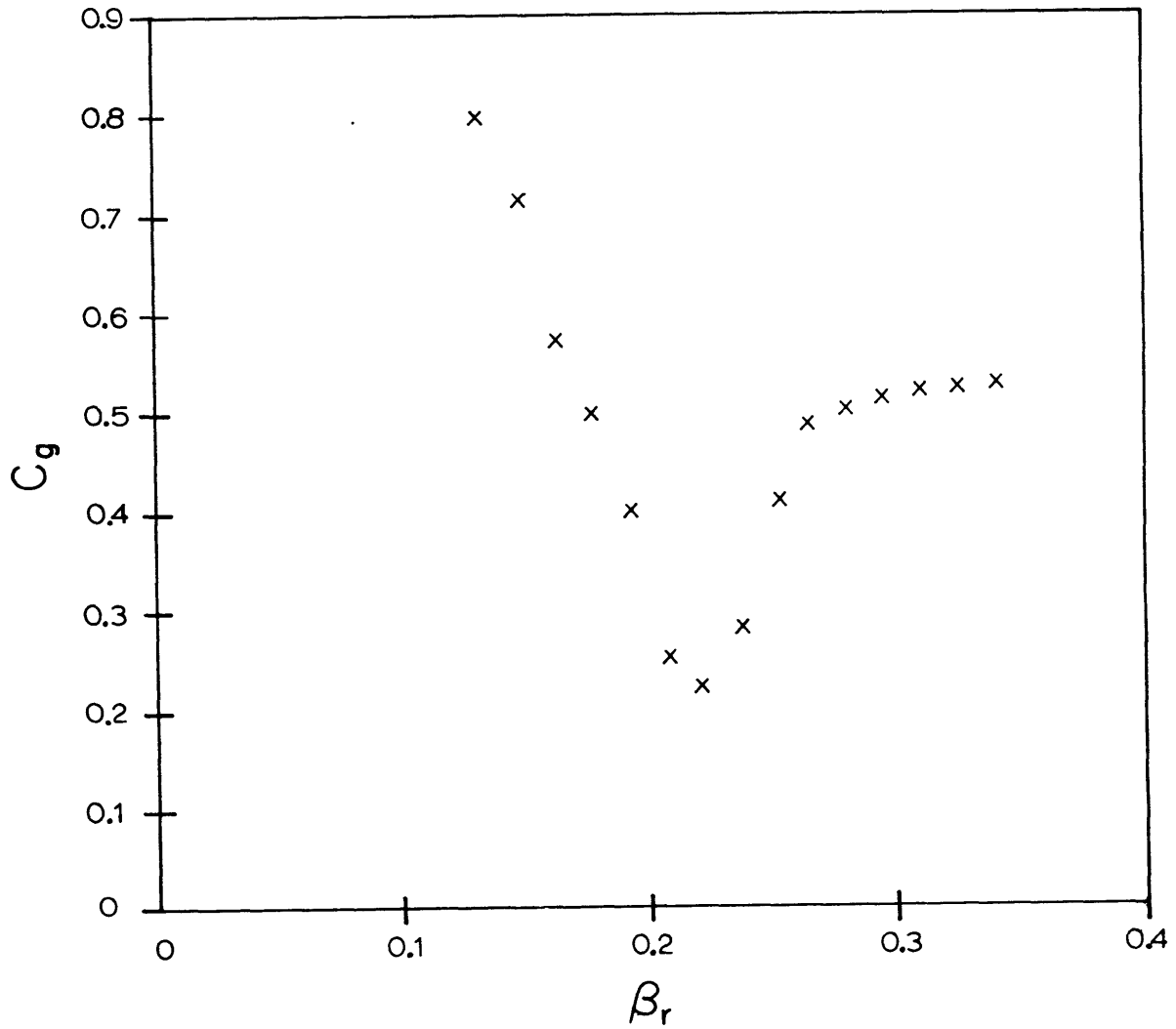


Figure 6.4: Group velocities, c_g , of the fundamental modes. Values are calculated from the slope of a least squares polynomial approximation of the (α_r, β_r) curve.

The eigenvalues of the spatial trapezoidal model at x_0 are plotted in figures 6.2, 6.3 and 6.4 together with the experimental data as measured in the linear transition zone. The dispersive nature of the spatially growing waves is evident from the wavenumber plot.

Perhaps the most interesting point to be noticed here is the fact that the group velocity is a minimum for the maximally unstable mode. This result implies that the most unstable mode is that mode whose energy travels at the slowest speed and hence can, so to speak, hang around longer and absorb more energy from the mean flow. Another way of looking at this is to note that the time scale over which the Reynolds stress can interact with the mean flow and transfer energy to the disturbance is a maximum when the group velocity is a minimum.

(b) Successive Downstream Quasi-Uniform Calculations

Using a quasi-uniform approach the local growth rate curves were calculated at each downstream station by considering successive local mean velocity profiles and assuming that each new profile represented a new parallel flow stability problem. The theoretically predicted variations were then compared to the experimental data.

The analysis was broken into two sections. The initial regions of transition in which the flow had an asymmetric wake configuration were analyzed with the trapezoidal model discussed earlier. The remainder of the flow could, for all intents, be considered as a single shear layer and was modeled by fitting a hyperbolic tangent profile to the local mean velocity. The results of Michalke's (1965) spatial analysis were used for the downstream profiles beyond 6 cm. It should

be emphasized, however, that for all intents linear approximations cease to be valid beyond 6cm. Thus, the application of Michalke's model should be viewed as a test to see just how bad linear theory is in a non-linear region.

The convergence problems associated with the spatial trapezoidal model, and the fact that linear transition was only one facet of this investigation, precluded detailed spatial calculations for downstream stations other than the first one at x_0 . Instead, since the temporal eigenvalues at x_0 are in reasonable agreement with experiment for the maximally unstable mode, temporal calculations were made for the downstream stations between x_0 and 6 cm. Of course, if the local details such as the eigenfunction structure or phase distribution are desired, a spatial analysis would be necessary.

The downstream variations of the growth rate and frequency are plotted in figure 6.5 for the trapezoidal wake as it evolves in the first six centimeters of transition. The neutral point, as well as the frequency and growth rate of the most unstable mode decrease with downstream distance. It should be noted that the validity of the trapezoidal approximation is questionable for the small wavelength modes near the neutral point. The calculated neutral points are lower than those obtained by other authors for continuous profile single inflexion point shear layers.

The variations in eigenvalues for the most locally unstable mode are given in table 6.3 for the first six centimeters of transition. It is apparent that by $x = 4.0$ cm, the locally preferred mode is $\beta_r =$

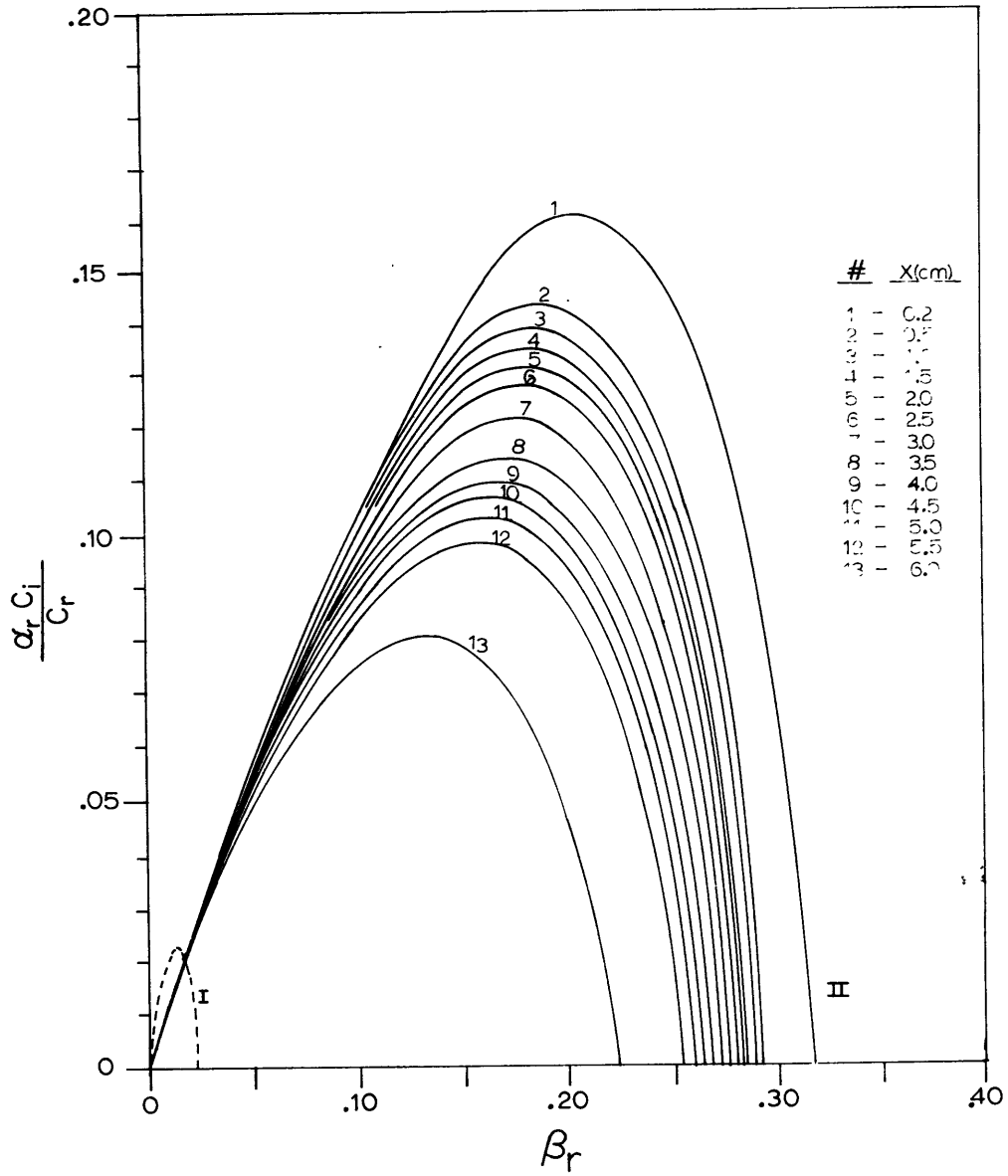


Figure 6.5: Downstream variations in the temporal growth rate curves as predicted by a series of quasi-uniform linear stability calculations. Calculations are based on a trapezoidal approximation to the experimentally measured mean velocity profiles in the first 6 cm. of transition. Dashed curve is the mode I instability at x_0 . All other curves are for the mode II instabilities of the upper shear layer.

$0.1633\omega_{fs1}$.

Table 6.3: Downstream variation of the eigenvalues of the most unstable mode as predicted by a series of quasi-uniform calculations based on a linear trapezoidal model.

| <u>x (cm)</u> | <u>β_r</u> | <u>α_r</u> | <u>c_r</u> | <u>$-\alpha_i$</u> | <u>Model</u> |
|---------------|-----------------------------|------------------------------|-------------------------|-------------------------------|--------------|
| 0.2 | .2216 | 0.4140 | 0.5361 | 0.2370 | Spatial |
| 0.2 | .2090 | 0.3822 | 0.5468 | 0.1562 | Temporal |
| 0.5 | .1891 | 0.3463 | 0.5461 | 0.1433 | Temporal |
| 1.0 | .1852 | 0.3380 | 0.5479 | 0.1364 | Temporal |
| 1.5 | .1821 | 0.3306 | 0.5505 | 0.1355 | Temporal |
| 2.0 | .1807 | 0.3264 | 0.5537 | 0.1308 | Temporal |
| 2.5 | .1780 | 0.3219 | 0.5570 | 0.1790 | Temporal |
| 3.0 | .1742 | 0.3105 | 0.5610 | 0.1218 | Temporal |
| 3.5 | .1666 | 0.2945 | 0.5656 | 0.1145 | Temporal |
| 4.0 | .1633 | 0.2866 | 0.5697 | 0.1094 | Temporal |
| 4.5 | .1630 | 0.2849 | 0.5721 | 0.1079 | Temporal |
| 5.0 | .1603 | 0.2785 | 0.5754 | 0.1032 | Temporal |
| 5.5 | .1570 | 0.2706 | 0.5800 | 0.0984 | Temporal |
| 6.0 | .1325 | 0.2266 | 0.5847 | 0.0817 | Temporal |

The change in the frequency and growth rate of the locally most unstable mode reflects the successive shrinking of the velocity deficit, and hence the maximum vorticity, as the flow approaches a free shear layer configuration. Once the wake structure was eliminated, a hyperbolic tangent model was applied. The results for the most unstable local mode are summarized in figure 6.6. In general, a direct relation exists between the local maximum vorticity and the locally preferred mode.

(c) Comparison of Experiment to the Quasi-Uniform Model

Indicated in figure 6.6 are the experimentally preferred modes of the natural transition at each downstream station. In the initial stages of transition the preferred natural mode remained relatively near

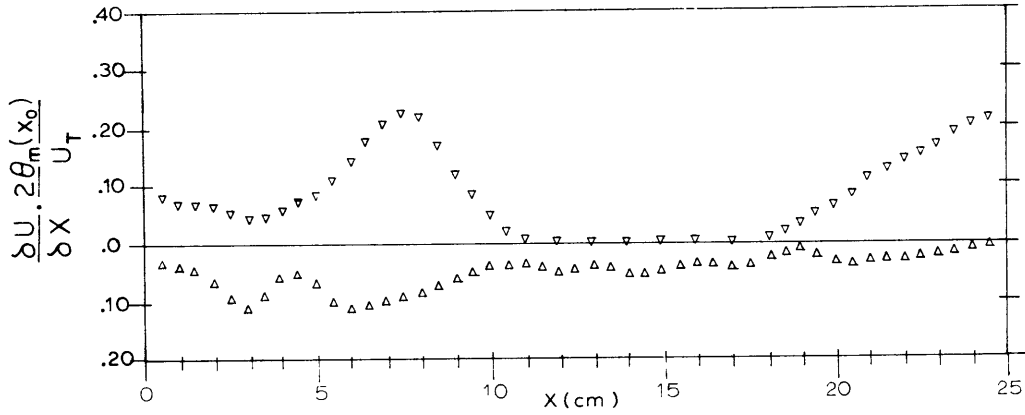


Figure 6.6a: Downstream variations of the maximums of $\partial U / \partial x$ mean shear [∇ - maximum value of $\partial U / \partial x$ below the center line; Δ - maximum value of $\partial U / \partial x$ above the center line.

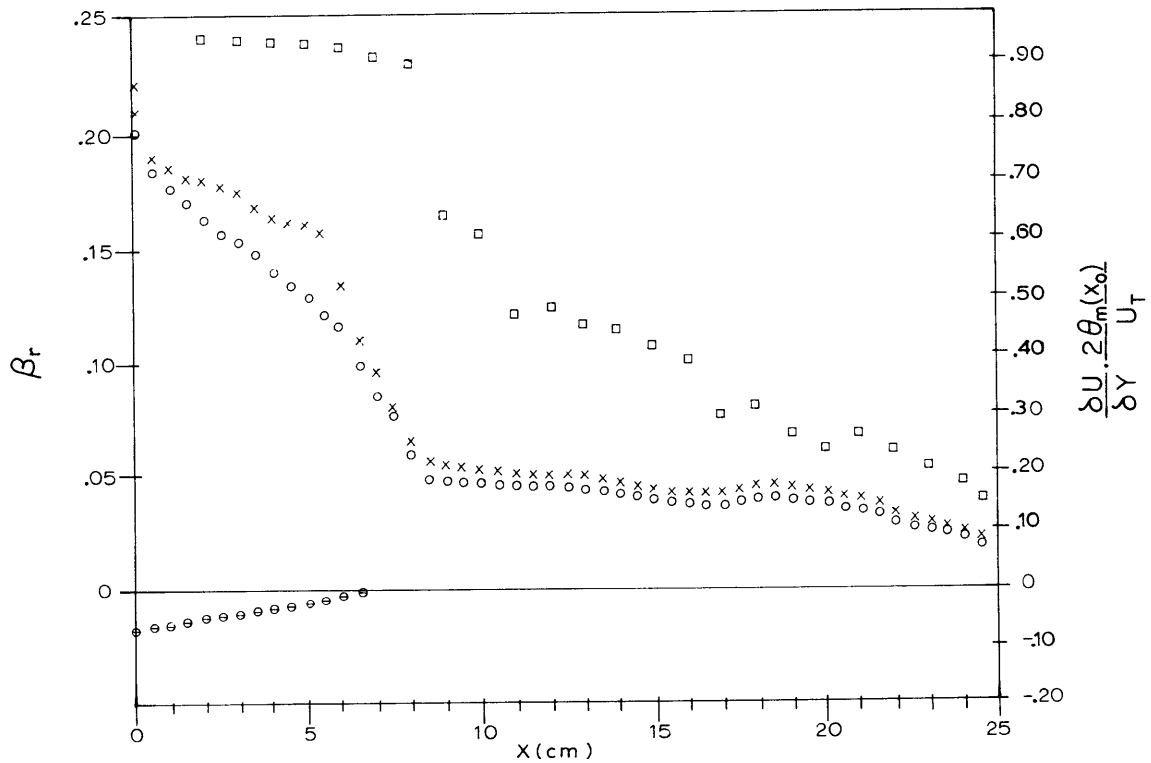


Figure 6.6b: Summary of downstream mean stability characteristics. [\square - maximum value of upper layer $\partial U / \partial y$; \circ - maximum value of lower layer $\partial U / \partial y$; x - favored local mode as predicted by a series of quasi-uniform linear stability calculations; \circ - experimentally favored local modes in the natural transition.

its value at x_0 . Not until a significant decrease in mean vorticity occurs do the natural modes decrease in an apparent response to local conditions.

The fact that the preferred natural modes do not exhibit a downward shift, as predicted by theory, may reflect the inability of the quasi-uniform approach to consider the strong upstream preference for energy input into the initially most unstable mode at x_0 . The stability characteristics of each upstream station act to organize and center the disturbance energy at the most unstable mode as befits its local conditions. Since the maximum vorticity and hence the most vigorous instability occurs at $x = x_0$, it is the initial profile which acts to center the disturbance energy most strongly, and the energy input at later stations will necessarily be centered at the frequency of the convected upstream energy. The shear layer scale does not change extensively in the initial stages of the natural transition and the x_0 mode can still fit in with the downstream local length scales. It is not until strong changes in scale occur, that the preferred upstream energy input can be overcome by changes in the local mean conditions.

The effect of local variations have even less influence on forced transitions. As was evident from the data of chapter V, the growth rates of the forced modes were also insensitive to local changes in the first wavelength of transition. They grew as predicted by the stability characteristics at x_0 . Apparently, the continuous energy input of the forcing field tends to mask and override all subtle changes due to evolving mean conditions.

Thus the disturbance evolution in both the natural and forced transitions can be modeled with reasonable accuracy in the initial stages of transition by a linearized parallel flow model based on the initial mean flow at x_0 . Even though local conditions may lead to a variation in predicted stability characteristics, the initial instability based on the upstream profile will dominate the downstream disturbance field .

However, as will be discussed in the next section, the local variations in scale and fundamental mode stability characteristics play an important role in determining which non-linear modes are preferred by the local mean conditions. In this vein, quasi-uniform calculations can be of great use, even though on their own right they cannot predict the actual behavior of the most unstable fundamental mode.

(d) The Effect of Local Scale Conditions on Non-Linear Activity

A comparison of the relative location of the points at which non-linear modes first appear, and the wake-like structure of the mean flow disappears, will illustrate some points concerning the importance of local scale effects on non-linear activity. In the ω_{II} and ω_{fs1} transitions, the wake structure of the mean flow disappears at different downstream distances. The absolute distances are in the ratio of the respective wavelengths of ω_{II} and ω_{fs1} . However, in both transitions, non-linear modes appear at about the same absolute location ($x \approx 4.0$ cm) and not at distances in proportion to the ω_{II} and ω_{fs1} wavelengths.

The dependence of mean flow erosion on fundamental mode wavelengths is quite understandable. The rate of disturbance erosion is really a

measure of mean energy loss. As the energy plots show, the fundamental modes absorb most of this energy. The initial rate at which mean energy is lost is basically expressed by the exponential growth rate $e^{-\alpha_i x}$ of linear theory, which in turn is really an expression of the rate at which Reynolds stresses transfer energy to the fundamental. The growth rates, $-\alpha_i$, of ω_{fs1} and ω_{II} vary in rough proportion to their wavenumbers. Thus, the two transitions will attain equal mean energy losses*, and hence roughly similar mean profiles at distances in proportion to their wavelengths. The disappearance of the wake structure can be expected to occur at distances in rough proportion to λ_{fs1} and λ_{II} .

The fact that non-linear modes appear at similar downstream distances indicates that factors other than growth rate must be considered. If non-linear activity depends solely on disturbance amplitude, then a critical amplitude would presumably exist. Growth rate considerations would indicate that the critical value would be reached at distances in proportion to the wavelengths of ω_{II} and ω_{fs1} .

The characteristic amplitudes of ω_{fs1} and ω_{II} when non-linear modes first appear are on the order of

$$\omega_{fs1} = 0[0.7-0.8\%]$$

$$\omega_{II} = 0[1.6-2.0\%]$$

The amplitudes are roughly in the ratio of 1:2 and there does not seem to be a specific critical amplitude for higher mode generation. Hence amplitude effects cannot be the sole factor in determining non-linear activity. Rather, it appears that in addition to amplitude, the vertical scale of the fundamental and non-linear modes must be considered.

* see figure 6.7

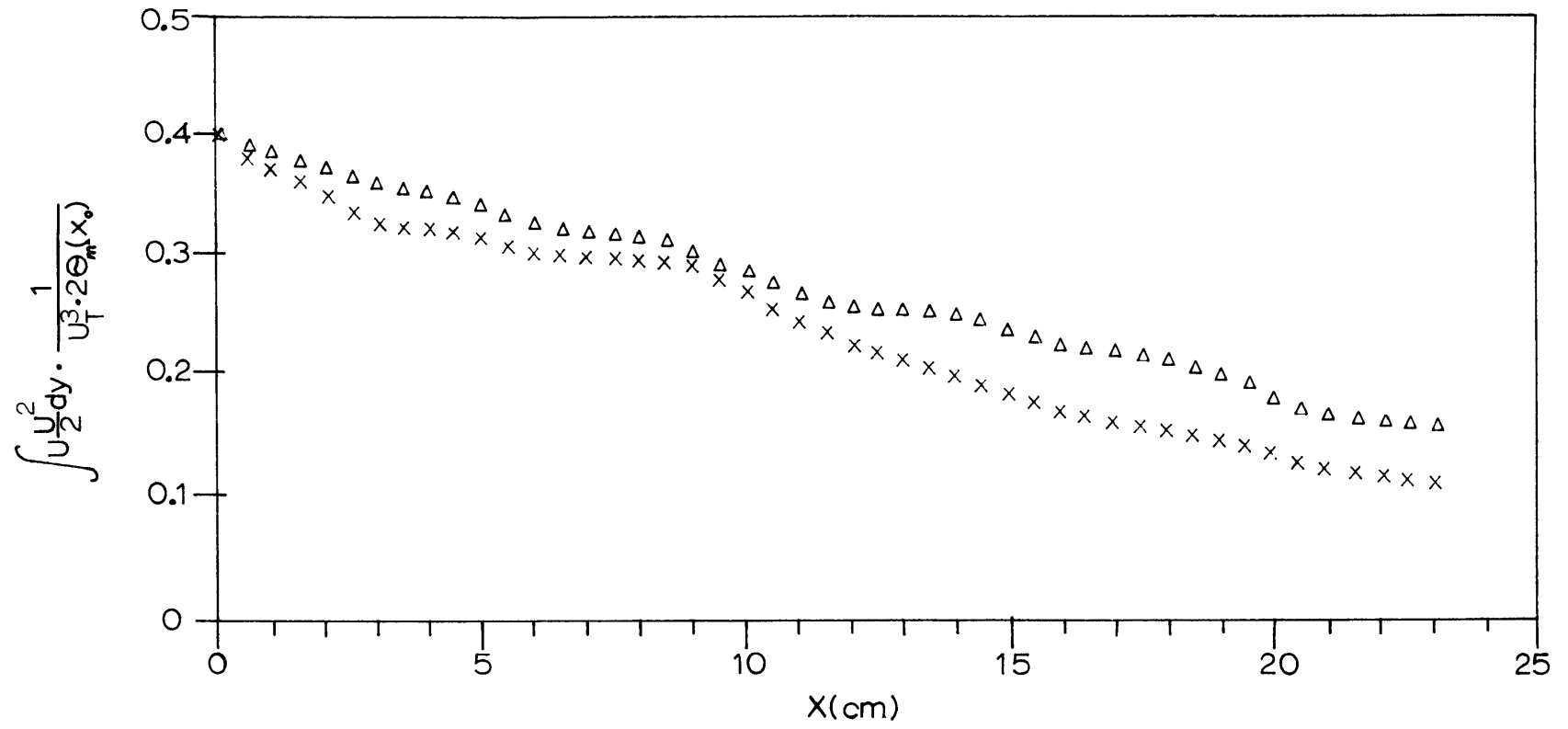


Figure 6.7: Downstream variations in the flux of mean energy in the ω_{II} and ω_{fs1} forced transitions. [x - ω_{II} transition; Δ - ω_{fs1} transition.]

The quasi-uniform calculations showed that at $x \approx 4.0$ cm the fundamental mode preferred by the local mean conditions is near ω_{fs1} . The appearance of harmonics of ω_{fs1} in the natural transition may indicate that the local conditions also favor the vertical modal structure of the non-linear modes of ω_{fs1} .

The mean flow is the initial source of all disturbance energy. The non-linear modes can derive their energy either directly from the mean flow or indirectly by taking energy from the fundamental which in turn derives its energy from the mean flow.

The basic energy transfer relations between the mean flow, the fundamental, and the non-linear modes can be expressed as *

$$\begin{aligned} \frac{\partial}{\partial t} \iint \frac{1}{2} (u'^2 + v'^2) dx dy &= \iint (-u'v') \frac{\partial U}{\partial y} dx dy - \iint u'v' \left(\frac{\partial u''}{\partial y} + \frac{\partial v''}{\partial x} \right) dx dy \\ &- \iint (u'^2 - v'^2) \frac{\partial u''}{\partial x} dx dy - \frac{1}{R} \iint \left(\frac{\partial v'}{\partial x} - \frac{\partial u'}{\partial y} \right) dx dy \end{aligned}$$

where u' is the fundamental mode, and u'' represents a harmonic mode. The interaction, and possible energy transfer between the fundamental and non-linear modes are expressed by the second and third terms on the R.H.S. of the above equation. A similar relation can be written for the harmonic mode, and along with terms

* see Stuart (1962)

representing the interaction with the fundamental. It will contain a term of the form $u''v'' \partial U/\partial y$ which represents direct interaction of the harmonic mode with the mean flow. The terms which express the interaction of the fundamental and non-linear modes with the mean flow are clearly dependent on the vertical scale of the disturbance modal structures. The mutual interaction terms between the two disturbances are also partially dependent upon the vertical scale of the disturbances.

If the non-linear modes obtain their energy from the fundamental then one must consider the efficiency of the fundamental in obtaining energy that it can pass on to the non-linear modes. The effectiveness with which the vertical scale of the fundamental mode fits in with the local mean shear profile is certainly as important as its amplitude is in determining the overall efficiency of the Reynolds stress in transferring energy to the fundamental; (i.e.) the proper matching of the maximums of $u'v'$ and $\partial U/\partial y$ is just as important as the value of the maximums themselves.

If the non-linear modes derive their energy directly from the mean flow, then certainly the same arguments which hold for the efficiency of the $u'v'$ fundamental mode Reynolds stress will apply equally as well to the $u''v''$ interaction of the non-linear mode with the mean flow.

The energy plots of chapter V indicate that the non-linear modes may not receive their energy at the expense of the fundamental. This brings up the interesting concept of the fundamental acting as a

'catalyst' for the direct transfer of energy from the mean flow to the non-linear modes. Physically, the catalyst behavior can be viewed in terms of the fundamental mode acting to alter or condition the vertical scale of the mean shear so that the $u''v''$ terms of the harmonic modes can interact in an efficient manner with the mean shear. Presumably, due to the interaction terms between the fundamental and non-linear modes, the vertical scale of the non-linear modes will be dictated by the scale of the fundamental. This behavior has been noted for the modal structure of the harmonic modes in symmetric free shear layers. It seems plausible then that if the scale of a specific fundamental mode is locally preferred by the mean flow, then so will those of its non-linear modes be.

The fundamental can condition or alter the vertical scale of the mean flow by its $u''v''$ Reynolds stress interaction. Those fundamentals with vertical scales near that preferred by the local mean conditions may not have to grow to as large an amplitude for effective conditioning, and subsequent matching of the disturbance and mean flow scales, as other locally less preferred modes may have to. This would explain the difference in amplitudes of ω_{II} and ω_{fs1} at the onset of non-linear activity.

(e) Effect of Test Section Boundaries

The results of a model by Howard (1964) were used to analyze the possible stabilizing influence of the boundaries on the disturbance oscillations. Howard considered the temporal stability of a hyperbolic tangent profile bounded by rigid walls at $y = y_0$.

The model showed that disturbances should be stabilized by the boundaries when

$$\alpha_r y_0 \leq 1.997$$

Thus long wave disturbances are more likely to be stabilized, and based on the geometry of the test section, waves with $\alpha_r \leq 0.20$ will tend to be influenced by the boundary constraints.

This behavior was observed experimentally for frequencies below $\beta_r \sim 0.150$ (i.e. $\alpha_r \leq 0.175$). Modes below $\beta_r = 0.150$ could be excited and were found to initially grow at the exponential rates predicted by theory. However, as the mean flow evolved towards a free shear layer configuration, the long wave modes equilibrated at smaller amplitudes than observed by previous investigators. These other experiments were typically conducted in tunnels of much larger geometry. Thus it appears that the test section geometry used here did have a stabilizing influence on long wave modes.

Both ω_{II} and ω_{fs1} were above the stabilization point and were not apparently affected by the boundaries. This was corroborated by checking the limiting amplitudes of each mode against the available results of other experimenters.

Region II: Weakly Non-Linear Behavior (0.9-1.8 λ_{II})

When the primary mode, ω_{II} , reached an amplitude of approximately 2%, the generation of non-linear modes was observed. The primary mode then continued to grow at almost the same exponential rate as it did in

the linear zone. The newly generated non-linear modes also grew exponentially, often at rates exceeding that of the fundamental. The region II growth rates of the ω_{II} and ω_{fs1} transitions are given below.

Table 6.4: Spatial growth rates of the fundamental and non-linear modes of the ω_{II} and ω_{fs1} transitions in region II.

| <u>Mode</u> | <u>$-\alpha_i = -\alpha_i^* \cdot 2\theta_m(x_0)$</u> | <u>Mode</u> | <u>$-\alpha_i = -\alpha_i^* \cdot 2\theta_m(x_0)$</u> |
|------------------|--|-------------------|--|
| ω_{II} | .200 | ω_{fs1} | .138 |
| $\omega_{II}/2$ | .247 | $\omega_{fs1}/2$ | .170 |
| $3\omega_{II}/2$ | .187 | $3\omega_{fs1}/2$ | .164 |
| $2\omega_{II}$ | .303 | $2\omega_{fs1}$ | .158 |
| $3\omega_{II}$ | .302 | $3\omega_{fs1}$ | .230 |

Spanwise phase measurements showed no three-dimensional distortions, and the non-linear interactions can be assumed to involve two-dimensional waves.

The relatively small amplitudes of the primary modes at the beginning of region II (i.e. 0.7→2.0%) indicate that the non-linear mechanisms can be investigated from the viewpoint of weakly non-linear interaction theory. It is interesting to note that Klebanoff (1962) also finds the linearity limit of the primary mode in boundary layer transitions to be of order 2%. Studies of free shear layers have typically found higher values nearer 4 to 5%.

The larger values of the later investigators were normally determined by investigating the point at which the growth rate of the funda-

mental mode deviated from exponential form. Their curves were typically determined from the growth of a given r.m.s. peak and often contained considerable scatter, or a minimum of points and only gross features could be observed.

It can be quickly ascertained from figures 5.42 and 5.43 for maximum amplitude growth, that the first significant departure from exponential growth does indeed occur at approximately 4% in this experiment also. However, this is a rather poor definition of linearity and the linear limit used here will be that point at which non-linear modes first appear. As will be seen in the mixed transition, this also corresponds to the point at which the superposition concept of linear theory breaks down.

It is not at all clear why other investigators, such as Browand have not observed the formation of sub- and 3/2-harmonics in region II. Browand's growth rate curves indicate that second harmonics were observed at $x \sim 0.7\lambda$ wavelengths downstream, which is roughly coincident with our region II. Sub- and 3/2-harmonics did not appear until the primary and second harmonics reached an equilibration point (i.e. our region III). The intermittency of $\omega_{II}/2$, $3\omega_{II}/2$ in region II, and their small amplitudes may have been a factor. With the exception of one point for the primary mode, Browand's data seem to start at some instrument threshold point of $u'/U_\infty \sim 2\%$. The instrumentation used here was sensitive to $0.05\% \pm 0.02\%$ fluctuations. The fluctuations in region II are seen to be normally below 1% and may have been below Browand's sensing range.

The exponential growth of the non-linear modes indicates that they may represent the non-resonant interaction of exponentially growing modes. Raetz (1959) has shown that the non-resonant interaction of two such exponentially growing modes can produce a third combination wave whose amplitude will grow exponentially and will be equal to the product of the exponential amplitudes of the interacting waves.

The growth rate of $2\omega_{II}$ was found to be roughly twice that of ω_{II} at x_0 and probably represents the self interaction of the primary mode. The exponential growth of $3\omega_{II}$, and its delayed appearance until $2\omega_{II}$ reaches a significant amplitude may infer a weak secondary non-linear interaction between ω_{II} and $2\omega_{II}$; the growth rates of ω_{II} and $2\omega_{II}$ do not sum to that of $3\omega_{II}$ however.

The origin of the sub-harmonic mode is not clear. However, several points do stand out. The sub-harmonic energy grows exponentially and not as the product of a secular term times an exponential (i.e. $xe^{\alpha_1 x}$) as might be expected for the result of a resonant interaction. In fact the sub-harmonic growth rate (as determined from the energy plots) is very close to the sum of $(\omega_{II} + \omega_{II}/2)$ as observed experimentally (see figure 5.1). Hence the sub-harmonic may represent the combination interaction of the primary mode with a latent sub-harmonic oscillation. However it is not evident why the sub-harmonic should be preferred for such an interaction*.

* Kelly (1967) has shown that just such a preference does exist when the fundamental reaches finite amplitude on the order of 10%.

The strong intermittency of the sub-harmonic in region II discounts the possibility that the speaker forcing field contains a sub-harmonic contribution which could directly excite $\omega_{II}/2$. Hence the generation of sub-harmonics in this region seems to be an inherent feature of the transition.

It is possible that a parametric resonance mechanism may be generating the sub-harmonic mode. In parametric resonance an oscillation of very small magnitude and frequency ω_o , without recourse to non-linear effects, can destabilize and amplify the half-frequency, $\omega_o/2$, by a periodic variation of the parameters of the system. This phenomenon has been discussed by Kelly (1965) for Kelvin-Helmholtz flows. The destabilized sub-harmonic is a solution of a Mathieu type equation and its amplitude can be shown to behave as $\exp(\pm \epsilon t/2)$ for small ϵ where ϵ is a measure of the periodic variation of the natural parameters.

It is interesting to note that if as an exercise (and with no rigorous physical justification) a Mathieu type equation is written for the velocity u_o of the sub-harmonic mode $\omega_{II}/2$, when the fundamental mode $u'(\omega_{II})$ is assumed to give a representative periodic variation,

$$\frac{d^2 u_o}{dt^2} + \left[\frac{\omega_{II}^2}{4} + u'(\omega_{II}) \cos \omega_{II} t \right] u_o = 0$$

then it can be shown that

$$\epsilon = \frac{u'(\omega_{II})}{\frac{\omega_{II}^2}{4}}$$

and using the growth rate of the sub-harmonic as $\epsilon/2 \approx .247$ implies

that a periodic oscillation of the fundamental mode of order

$$u' = 0[4\%]$$

can lead to a sub-harmonic parametric amplification of the observed rate of growth. This is near the value of u' that would be predicted from the u'_{rms} curves.

A parametric resonance mechanism may also be responsible for the direct excitation of harmonic modes as observed in figure 5.1 and section 5.2d. Excitation at 2ω for example, may parametrically excite ω . If the role of the fundamental, ω , is that of a catalyst then it may not have to grow to significant amplitudes to enact a passage of energy from the mean flow to the harmonic. The time necessary for the sub-harmonic effect to organize ω oscillations may explain the delay in the appearance of an effectively reinforced harmonic. The preferred reinforcement of 2ω by the forcing field may explain its large growth rate once the necessary energy transfer arrangements have been established.

Kelly has also discussed the importance of the dispersive nature of the system for effective parametric resonance. It may also be that the dispersive nature of the flow is responsible for the intermittency of the sub-harmonic modes. Both non-linear sub-harmonic resonance interactions, and parametric resonance mechanisms are strongly sensitive to phase synchronization effects. Slight changes in the local mean state, due to mean flow distortion by the growing primary mode, may cause commensurate changes in the frequency and phase characteristics of the instantaneously valid local free modes. Since the condition for resonant

energy transfer is dependent on the proper matching of the phase velocities of the interacting wave trains, it is apparent that any intermittent changes in the local phase velocities of the free mode can lead to intermittent energy transfers. This effect is discussed further in region IV and the arguments used there apply equally as well in this region.

Regardless of what mechanisms trigger the growth of the sub-harmonic and other non-linear modes, it is quite clear from the amplitude equilibrations in region III that non-linear mechanisms which can act as energy growth limiters must eventually become important in region II.

Region III: Finite Amplitude Equilibration ($1.8 \rightarrow 2.5 \lambda_{II}$)

As the amplitude of the fundamental mode approached a finite value of 4 to 5%, the disturbance growth rate deviated from its initial exponential value. At larger amplitudes of about 12% the fundamental mode and the growing non-linear modes equilibrated into oscillations of definite finite amplitude. The equilibration amplitude of the fundamental mode was found to be independent of its initial amplitude at x_0 . The ω_{II} transition exhibited the most clearcut tendency for fundamental and non-linear mode equilibration. The fundamental and sub-harmonic modes of ω_{II} undergo the most distinct equilibrations while the second and third harmonics start an immediate decay once a maximum is achieved.

The rate of loss of mean flow energy (figure 6.7) is also seen to level off as equilibration is approached.

(a) Equilibration Amplitudes

Representative values of the equilibration amplitudes, A_e , of the fundamental and non-linear modes are given below. Although ω_{II} is the maximally unstable mode, ω_{fs1} and its non-linear modes grow to larger amplitudes. This result was not entirely unexpected and will be discussed more fully later.

Table 6.5: Region III equilibration amplitudes of the fundamental and non-linear modes of the ω_{II} and ω_{fs1} transitions.

| Mode | Equilibration Amplitudes | | |
|-------------|------------------------------|-----------------------------|-------------------------------|
| | ω_{fs1} Transition | ω_{II} Transition | Browand Max. Unstable Mode |
| ω | 15.5% | 12.5% | 11.0% |
| $\omega/2$ | 5.1% | 1.0% | |
| $3\omega/2$ | 2.2% | 0.75% | |
| 2ω | 6.0% | 5.0% | 4.8% |
| 3ω | 3.1% | 1.5% | |

The non-linear modes are basically dependent upon the fundamental mode for their existence. Their respective equilibrations are apparently a direct result of the equilibration of the fundamental. The important aspect of the transition in region III is to consider just why the fundamental mode equilibrates.

The initial growth of ω_{II} is described by linear theory. Quasi-uniform linear calculations showed that downstream mean flow variations can alter growth rates somewhat, but cannot account for disturbance equilibration. As will be discussed in the following section, the finite

amplitude behavior of the fundamental and the presence of non-linear modes must be considered to describe the eventual equilibration of the fundamental mode.

The picture can be simplified by noticing that the second harmonic, $2\omega_{II}$, is the dominant non-linear mode in regions II and III, and to a good approximation, is the only non-linear mode that need be considered in the equilibration scheme. This does not necessarily imply that the third, sub-, and 3/2-harmonics do not play a role in the equilibration process. It only implies that their effects are probably of smaller magnitude than that of the second harmonic.

(b) Calculation of the Second Landau Coefficient

Liu (1969)^{*} has shown that if sub and 3/2-harmonics are neglected, and if the non-linear interaction of the fundamental with the mean flow and various non-linear modes is considered, then an equation governing the streamwise growth of the fundamental mode can be obtained from the equations of motion.

$$\frac{d|A(x)|^2}{dx} = 2a_0|A(x)|^2 + 2a_1|A(x)|^4 + 0|A(x)|^6 + \dots$$

This equation was first discussed by Landau (1944) and "a₁" is usually referred to as the second Landau coefficient. It represents the various first order, and often competing non-linear effects.

Since in the linear limit, the disturbance growth must be exponen-

* See Watson (1960) and Stuart (1960) also.

tial, $|A(x)|^{2m} \rightarrow 0$, $m \neq 1$, and $a_0 = -\alpha_1$, the growth rate of linear theory, and is positive in magnitude. If finite amplitude equilibration is to occur, then $d|A(x)|^2/dx \rightarrow 0$, and a_1 , the second Landau coefficient must be non-zero and negative ($a_1 < 0$).

The experimental growth rates and equilibration amplitudes were measured for the primary modes between ($0.133 < \beta_r < 0.390$) and the resulting second Landau coefficients were calculated.* Since the test section geometry precluded an unbiased study of non-linear effects for long waves, the data of Freymuth (1966) was used to calculate typical values of the second Landau coefficient for long wave modes. The equilibrium values $|A_e|$ of the fundamental modes of both investigations were found to vary with frequency, and are shown in figure 6.9.

The intensity of the non-linear effects, as represented by the magnitude of the second Landau coefficient, increases with frequency and hence wavenumber. Long wave disturbances which have smaller values of a_1 take longer to equilibrate and hence will grow to larger amplitudes. The trend of the data confirmed this behavior except for very long wave disturbances which were sensitive to boundary stabilization effects. These modes are circled in figure 6.10. The stabilizing influence of the boundaries cannot be accounted for in the Landau theory and in the context of the Landau relation they will appear as an apparent increase in non-linear activity.

Freymuth's test section essentially had infinite boundaries and he was able to measure much longer wavelength disturbances. If the boundary stabilized modes are ignored the values of this investigation fall along

* see figure 6.10

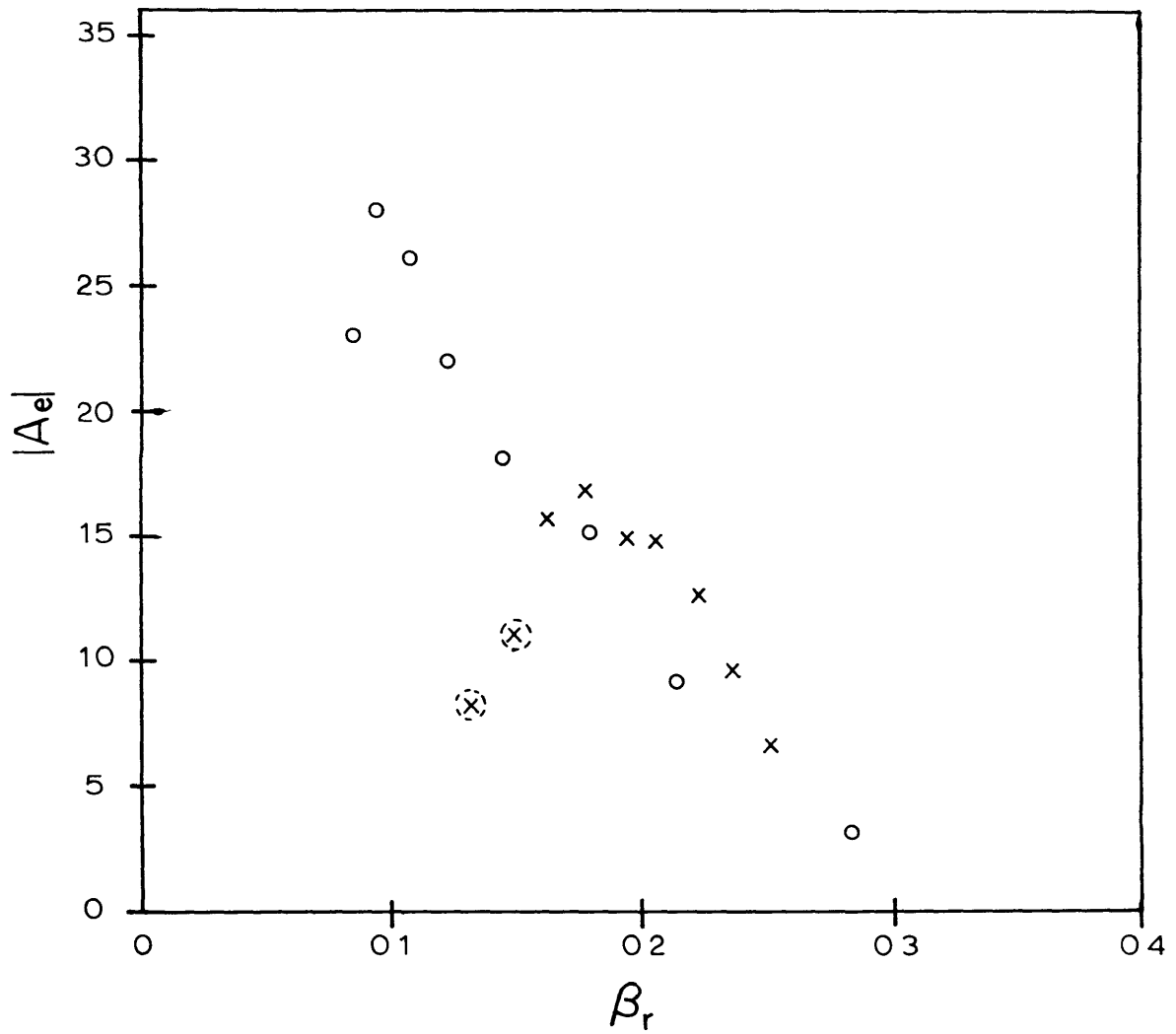


Figure 6.9: Equilibration amplitudes (A_e) of the fundamental modes vs frequency β_r . (x = value of this experiment; O - data of Freymuth (1966) (\otimes) - boundary stabilized modes.)

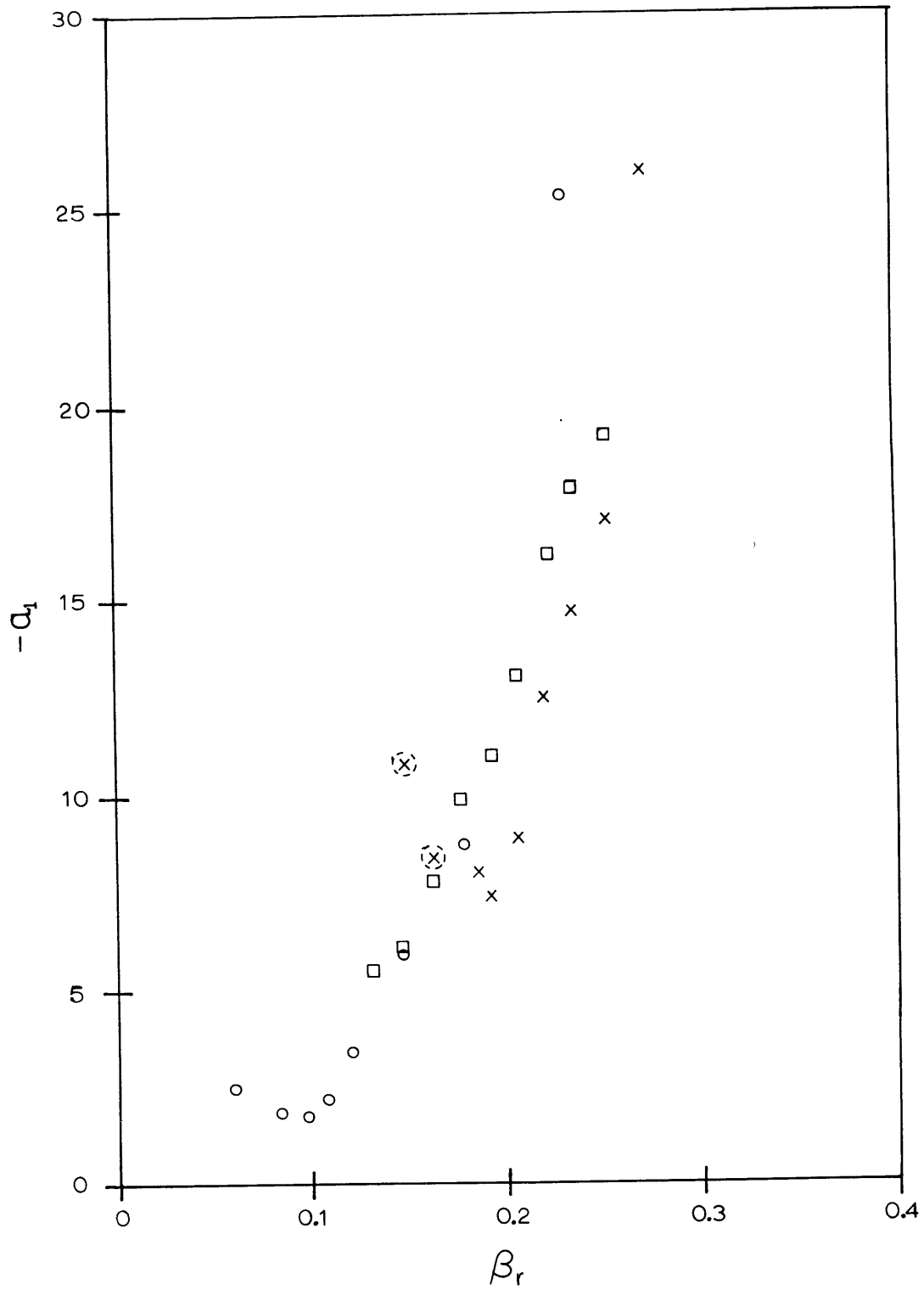


Figure 6.10: Values of the second Landau coefficients a_2 for the fundamental modes. (x - this experiment; O - Freymuth (1966), square - values of the second Landau coefficients when the generation of harmonic modes is neglected.

the same general curve that Freymuth's lower modes do. Also, the equilibration amplitudes and second Landau constants for the most unstable modes of both investigations agree reasonably well.

(c) Influence of the Critical Layer

The rapid increase of a_1 with frequency indicates an increasing influence of non-linear effects. Without a complete understanding of the internal structure of the second Landau coefficient it is difficult to pinpoint just which mechanisms dominate the equilibration process. The details of a_1 will be discussed shortly; however, it is of interest to consider the possible influence of the critical layer.*

As can be seen from the Orr-Sommerfeld equations, the disturbance eigenfunctions and eigenvalues are sensitive to the rate at which changes occur at the critical layer. Meskyn and Stuart (1951) have shown that finite amplitude oscillations can have a destabilizing influence at the critical layer.

Non-linear mechanisms distort the mean flow by interaction with the mean shear. Since the maximum mean shear occurs at the inflexion point y_0 , the destabilizing effects may be expected to increase as the critical layer y_c approaches the inflexion point y_0 .

The experimentally measured critical layer positions and thicknesses are given in table 6.6 along with the theoretically predicted critical

*The region where the disturbance phase velocity equals the local mean velocity.

layer thicknesses as given by $|\alpha R|^{-1/3}$. It is clear that $y_c \rightarrow y_0$ as β_r increases, and the critical layer of the higher frequency modes tends toward and often overlaps the inflexion point. Thus, the increase in a_1 with frequency may be due to an intensification of non-linear effects at the critical layer.

Table 6.6: Critical layer position where $U(y_c)=c_r(\beta_r)$ and theoretical critical layer thickness $|\alpha_r R|^{-1/3}$ for the fundamental modes at x_0 . Experimentally measured inflexion point location at x_0 is $y_0=0.240$ cm. Experimentally measured critical layer thicknesses based on cat's eye plots are $0.3 \rightarrow 0.4$ cm for $\beta_r=0.2178$, and $0.45 \rightarrow 0.6$ cm for $\beta_r=0.167$. Accuracy of y_c is $\pm 5\%$, and $|\alpha R|^{-1/3}$ is $\pm 10\%$.

| Dimensionless Radian Frequency β_r | Experimental Critical Layer Position y_c (cm) | Theoretical Critical Layer Thickness $ \alpha R ^{-1/3}$ (cm) |
|--|---|---|
| 0.133 | 0.410 | 0.401 |
| 0.148 | 0.406 | 0.385 |
| 0.163 | 0.404 | 0.372 |
| 0.178 | 0.378 | 0.354 |
| 0.194 | 0.356 | 0.338 |
| 0.207 | 0.322 | 0.318 |
| 0.222 | 0.302 | 0.298 |
| 0.237 | 0.284 | 0.284 |
| 0.252 | 0.266 | 0.286 |
| 0.266 | 0.265 | 0.262 |
| 0.281 | 0.250 | 0.248 |
| 0.296 | 0.243 | 0.420 |

(d) Dependence of Equilibration on Local Reynolds Number

The fundamental mode derives its energy from the interaction of the Reynolds stress with the mean flow, and as the oscillations grow in the

downstream direction they distort the mean flow. One might expect that there may exist a downstream location, unique for each frequency, at which the mean flow has become so distorted and non-linear effects have grown so strong that a continued increase in energy transfer to the fundamental is no longer possible. Equilibration can then occur. The local Reynolds number based on momentum thickness gives a measure of mean flow distortion and a relationship may exist between the equilibration amplitude and the local Reynolds number at which equilibration occurred. This idea was first put forth by Landau who assumed $A_e^2 \sim (R_e - R_{cr})$. Later work by Stuart (1958) showed that at least for Poiseuille flow the proper relation is

$$|A_e|^2 = \frac{K_e(R_e - R_{cr})}{\alpha R_e^2}$$

where R_{cr} is the critical Reynolds number for laminar instability; R_e is the local downstream Reynolds number at which equilibration occurs, and K_e is a measure of the competing non-linear mechanisms at equilibration. This relation was originally derived for a constant Reynolds number flow. However, the results of this section show that it holds for evolving flows which under "slow" transitions.

The experimentally measured equilibration amplitudes and Reynolds numbers were used to evaluate the above relation. The results are presented in figure 6.11. The local momentum thicknesses at equilibration were used to determine R_e while the curves of Betehov and Szewczyk (1963) were used to determine R_{cr} .

The experimental points fall along a relatively straight line with

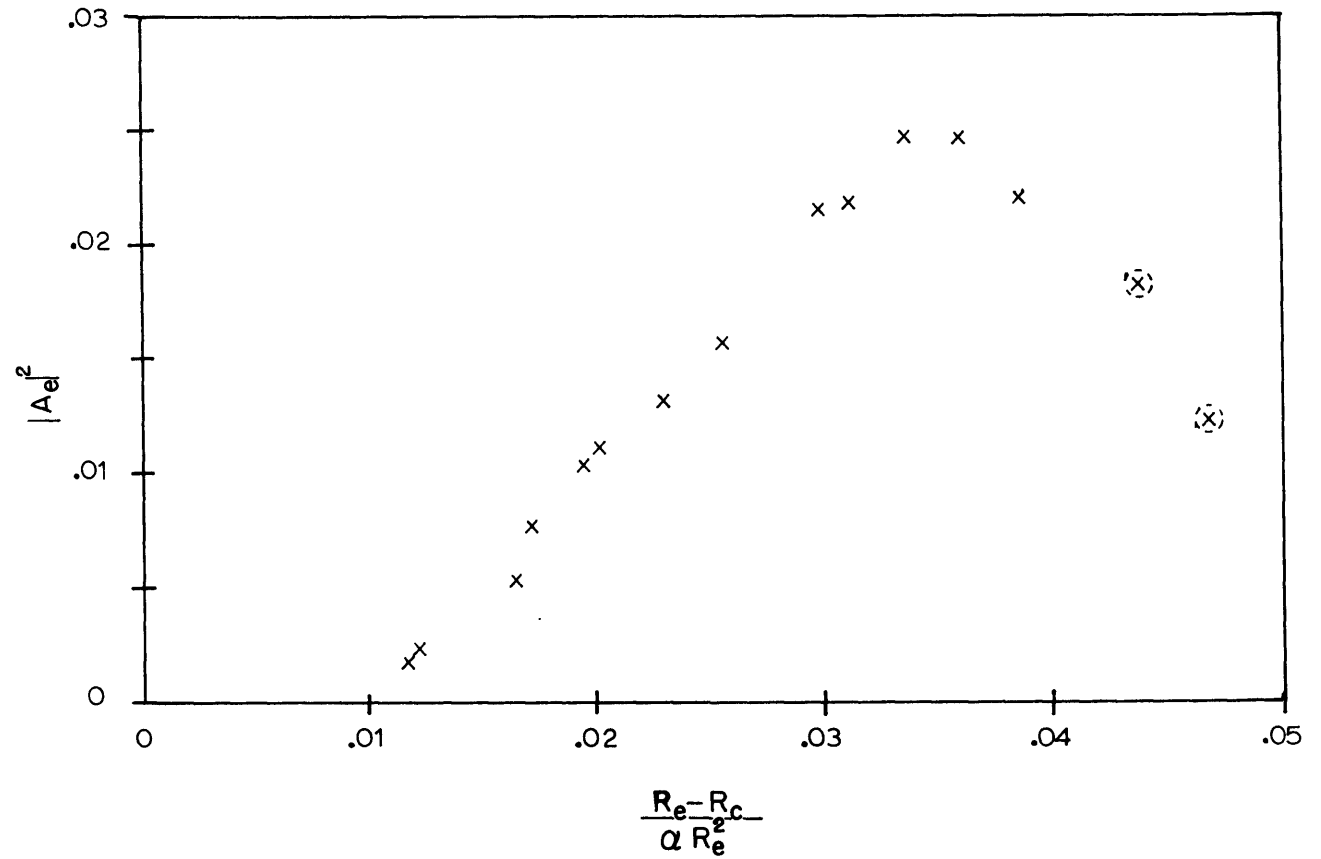


Figure 6.11: Dependence of the square of the equilibration amplitude $|A_e|^2$ on the local $(R_e - R_c) / R_e^2$ Reynolds number relation at equilibration. Circled points indicate the long wave modes for which boundary stabilization effects are important.

unit slope (i.e. $K_e \sim 1.00$) for all modes except the low frequency ones for which boundary stabilization effects are important. It is interesting to note that the experimental agreement with this simple relation extends over a wide range of Reynolds numbers: typically $(R_e - R_{cr})/R_{cr} \sim [10-20]$. This is in contrast to the theoretical restrictions on this relation which basically state that $(R_e - R_{cr})/R_{cr} \ll 1$.

A similar experimental relation has been found for Taylor flow transition. Taylor flows are an example of spectral evolution transitions and exhibit critical Taylor numbers for disturbance onset, and bands of Taylor numbers over which disturbance equilibration can occur. The existence of Reynolds number equilibration bands and critical values of a finite amplitude instability, demonstrate the hybrid, spectral evolution-catastrophic transition, nature of free shear layers which undergo slow transitions. The significant critical Reynolds numbers are summarized below.

Table 6.7: Critical local Reynolds numbers for significant stages of transition. Note that the mean velocity field evolves differently in each transition. Thus the local momentum thicknesses must be calculated from the velocity field of each transition.

| Transition | Value of Local Reynolds Number | | | |
|-------------------------|------------------------------------|--|---|---------------------|
| | Onset of Fundamental Equilibration | Onset of 2nd Region of Sub-Harmonic Growth | Termination of Fundamental Equilibration. | Turbulent Breakdown |
| ω_{fs1} | 248 | 470 | 480 | 577 |
| ω_{II} | 226 | 335 | 370 | 454 |
| $(\omega_A + \omega_B)$ | 206 | 320 | 354 | 523 |

The Reynolds number band over which equilibration occurs decreased with increasing disturbance frequency. This decrease may explain why the higher frequency harmonic modes have such narrow equilibration zones and decay almost immediately after equilibrating.

(e) Physical Significance of the Second Landau Constant

The details of the Landau equation and the internal structure of the second Landau coefficient have been discussed by Stuart (1958, 1962) and Liu (1969) for temporally and spatially growing disturbances. Their results show that the various non-linear effects which contribute to a_1 are physically similar in both cases and, in general, express the effects of mean flow-Reynolds stress interaction, viscous dissipation, harmonic mode generation, and harmonic mode interaction with the fundamental and mean flow, on the energy of the fundamental mode.

In specific, the Landau relation can be expressed as

$$\frac{d|A(x)|^2}{dx} = 2a_0 |A(x)|^2 + 2(K_1 + K_2 + K_3) |A(x)|^4 + 0 |A(x)|^6 + \dots$$

and the terms can be identified as having the following physical significance:

- a_0 : represents the initial rate of energy transfer from the mean flow, via the Reynolds stress, to the fundamental, minus the viscous dissipation of fundamental mode energy;
- a_1 : represents the restrictions imposed by the non-linear mechanisms on the flow of energy to the fundamental mode where
- K_1 : is the restriction on energy transfer due to Reynolds stress distortion of the mean flow;

K_2 : is the flow of energy from the fundamental to the non-linear harmonic modes; and

K_3 : contains two parts and represents the distortion of the structure of the fundamental mode by the interactions of the mean flow (K_{31}) and the second harmonic (K_{32}).

Since the non-linear second harmonics may also extract energy directly from the mean flow, one must also consider K_{20} , the direct transfer of mean flow energy to the harmonic as having a possible influence on the energy available to the fundamental.

The equilibration process of the fundamental can schematically be pictured as follows:

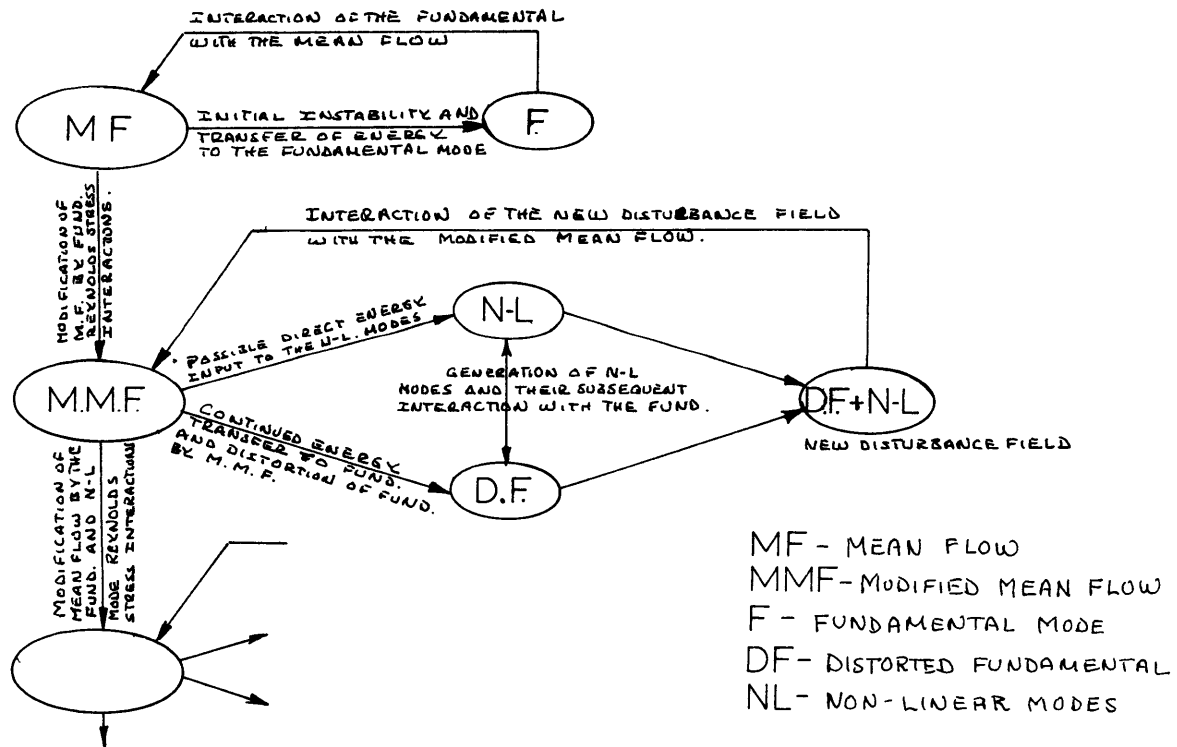


Figure 6.12: Basic non-linear mechanisms involved in the finite amplitude equilibration of the fundamental mode.

As will be seen in the next section, the actual equilibration process is significantly more simplified for free shear layers. However, as Davey (1962) has shown, all of the mechanisms discussed must be considered before specific conclusions can be drawn.

(f) Simplified Model of the Equilibration Process

Returning to the dependency between Reynolds number and the equilibration amplitude, Stuart (1958) has shown that if the presence of harmonic modes is neglected in the derivation of the Landau relation, then the equilibration constant K_e becomes

$$K_e \approx \frac{a_o \alpha R}{a_1}$$

where it has been tacitly assumed that $a_1 = K_1 + K_{31}$.

The experimental data plotted in figure 6.12 indicates that $K_e \sim 1.00$ and the above relation can be reduced to a simple expression for the second Landau coefficient.

$$a_1 \approx a_o \alpha R$$

This relation is plotted in figure 6.10 along with the results obtained from the rigorous Landau relation. The points calculated from the simpler relation agree reasonably well with the true Landau points. Thus, to a good approximation, the second Landau constant and hence the strength of the non-linear effects can be calculated from easily measured experimental variables.

The agreement of the simpler model with the Landau relation indicates that to a good approximation the effects of harmonic generation

and harmonic distortion of the fundamental and mean flow basically cancel each other out, so that

$$(K_2 + K_{20} + K_{32}) \ll (K_1 + K_{31})$$

and a_1 does equal $(K_1 + K_{31})$.

Thus, the generation of non-linear harmonic modes does not play a significant role in the equilibration of the fundamental mode in free shear layers. The important effects are due to a feedback system established by the distortion of the mean flow by the Reynolds stress of the fundamental, and the subsequent modification of the fundamental by the distorted mean flow.

Region IV: Second Region of Sub-Harmonic Growth ($2.5 \rightarrow 3.2 \lambda_{II}$)

(a) Sub-Harmonic Generation by Finite Amplitude Interactions

In contrast to the continued equilibration of the fundamental and the decay of the higher harmonic modes in region IV, the 1/2- and 3/2-harmonics undergo a very strong second region of growth. The existence of an equilibration zone between the two regions of sub-harmonic growth indicates that the responsible destabilizing mechanisms differ in each region. As indicated by the equilibration in region III the sub-harmonic mechanisms of region II are amenable to modification or counterbalancing by finite amplitude non-linear effects. In contrast, those in region IV seem to be dependent upon the existence of finite amplitude oscillations of the fundamental mode.

The disturbance energy curves show that the system prefers to keep

the fundamental in equilibration even though the sub-harmonic energy starts to grow again. This indicates that the sub-harmonic mode may not be deriving its energy from the fundamental. Instead it appears that the finite amplitude oscillations of the fundamental condition the flow so that a critical Reynolds number is achieved at which the flow is amenable to a new second type of instability, namely the finite amplitude sub-harmonic oscillations. In this respect the fundamental can again be considered as a catalyst which allows energy to be extracted from the mean flow and fed directly into a non-linear mode. The fact that the fundamental mode continues to equilibrate even after the critical Reynolds number is reached indicates that the critical Reynolds number for equilibration breakdown is higher than that for sub-harmonic initiation.

Sub-harmonic phase measurements show that although a mean relation does exist relative to the fundamental, there is no clear phase synchronization between the two. Assuming that a causal relation does exist between the fundamental and sub-harmonic modes it seems that the proper explanation of the sub-harmonics intermittent behavior involves the dispersive nature of the spatially growing disturbances.

Since the non-linear self-interaction of a wave can only produce higher frequency harmonics, sub-harmonic modes must come from the interactions between waves of different wavelength. Non-linear resonant mechanisms, and other mechanisms such as parametric effects, are very sensitive to the proper phase synchronization between the interacting disturbances. Physically, this is really a question of the characteris-

tic time during which resonating wave trains overlap such that energy can be effectively exchanged between the two. A physical example of this is the phase relations which are necessary for wind perturbation fields to generate amplifying ocean surface waves.

Spatially growing waves are dispersive and form packets of amplifying traveling waves. Hence, resonance conditions which only require the proper matching of wavenumber and frequency (and hence phase velocity) will not give a proper estimate of the interaction efficiency. The finite length of the wave packets and hence the characteristic time of overlap cannot be accounted for. Instead, the group velocity of the interacting waves must be considered. From figure 6.4 it can be seen that the group velocity of those modes near the sub-harmonic varies strongly with wavenumber. Since the group velocity is dependent upon the local dispersion relationship, any instantaneous variations of the local mean flow, or subsequent downstream deformations, can cause significant variations in the group velocity of the sub-harmonic and its immediate neighboring modes. One would expect then that due to slight changes in the local dispersion relation the proper group velocity necessary for efficient resonance with the fundamental will be intermittently attained by modes on either side of $\omega_{II}/2$. Hence the intermittent and broad band nature of the growing sub-harmonic oscillations are felt to be due to the intermittent shifting of the phase and group velocity matching conditions necessary for efficient interaction in a dispersive system.

Apart from the intermittency of the sub-harmonic response, the

essential features of this region are markedly consistent with the analysis of Kelly (1967). Kelly showed (from a temporal analysis of an asymmetric free shear layer) that a finite amplitude fundamental mode oscillation can serve as a vehicle by which sub-harmonic oscillations can be resonantly reinforced. A critical threshold amplitude of approximately 12% was found to be necessary for the fundamental mode. This compares favorably to the value found at the beginning of region IV. For fundamental modes of this value, Kelly found the growth rate of the destabilized sub-harmonic to be of the same magnitude as that of the fundamental as predicted by linear theory in region I. Calculations based on the energy curves show that the sub-harmonic growth rate was almost one half of that of the fundamental. Kelly considered only a temporal non-dispersive system, and the difference in growth rates may be due to the dispersive nature of spatially growing modes.

Within a short distance of sub-harmonic growth, the energy of the fundamental mode starts to decrease; this decrease is accompanied by a commensurate reduction of the sub-harmonic growth rate. It is interesting to note however that the fundamental mode energy did not decrease during the initial stages of sub-harmonic growth.

Spanwise wave deformations were only measured for the fundamental mode, and no indication of the spanwise structure of the sub-harmonic is available. However, it is interesting to note that the strong two-dimensional structure of the fundamental is lost at $x = 15.00$ cm (i.e. $\sim 3.5 \lambda_{II}$). The appearance of spanwise distortions of the fundamental

coincide with the first alteration of the sub-harmonic growth rate, and the decay of the fundamental mode energy from its equilibration value. Thus three-dimensional effects seem to play an important role in the breakdown of the equilibration zone. The commensurate decay of fundamental mode energy and sub-harmonic growth rates is very interesting and may be another check on the applicability of Kelly's analysis since his work indicates that the sub-harmonic growth rate will decrease slightly as the equilibration amplitude of the fundamental decreases.

It is also of interest to note that Kelly's model also indicates that the finite amplitude fundamental oscillations can interact with two disturbances, $\omega_{II}/2$ and $3\omega_{II}/2$ and act to destabilize the 3/2-harmonic. Since $\omega_{II}/2$ exists very strongly prior to the second growth of the 3/2-harmonic, this triad interaction may explain the coincident growth of $3\omega_{II}/2$.

(b) Vortex Model for Sub- and 3/2-Harmonic Generation

Smoke trace pictures indicated that the process of sub-harmonic generation may involve the mutual slipping of vortex pairs. Although one cannot attach great significance to smoke pictures* (i.e. they only represent instantaneous streak lines and not streamlines) many of the gross features of the sub-harmonic field can be described by a relatively simple model consisting of a double row of alternating vortices spaced at half-wavelength intervals on either side of the inflexion point.

* see figures 6.13 and 6.14

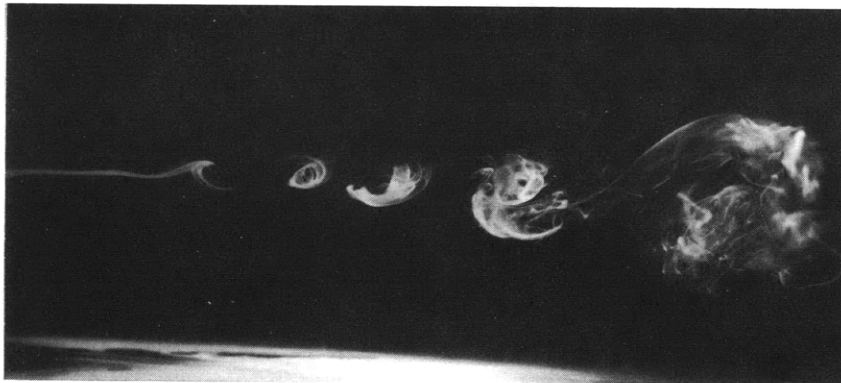
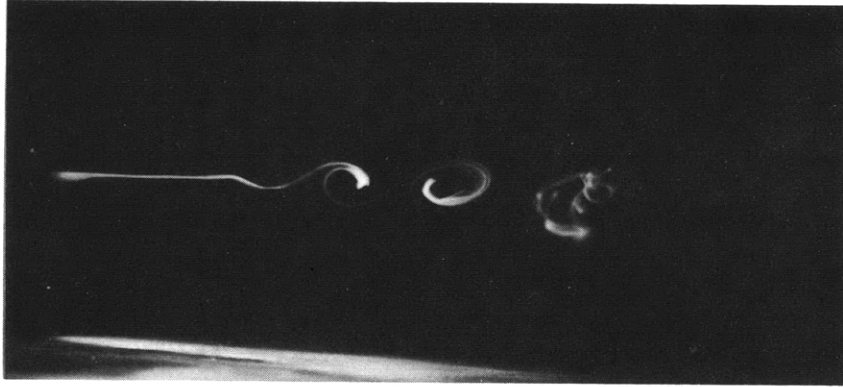


Figure 6.13: Sequence of smoke pictures taken at succeeding instants of time showing the formation of sub-harmonic oscillations by vortex slipping and fusion. Splitter plate is at the right-hand side of the picture. Left-hand edge is approximately 30 cm. downstream.

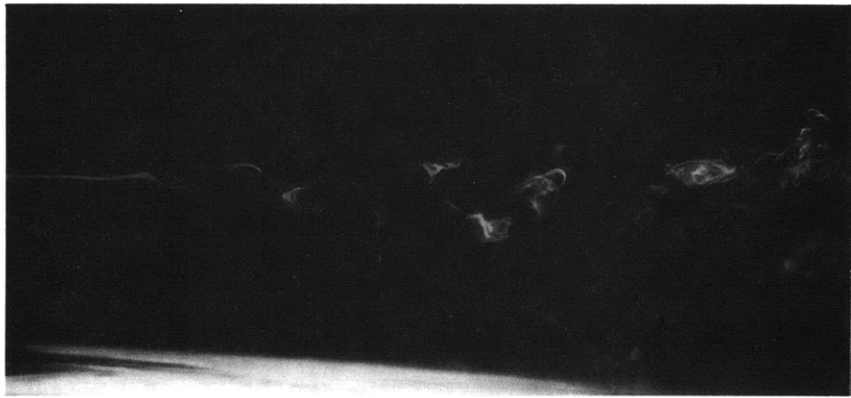
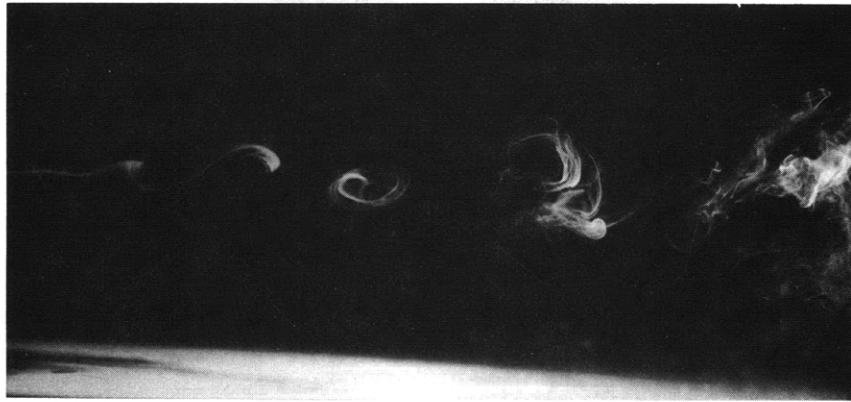


Figure 6.14: Top picture is the 4th instant of the series in figure 6.13. Middle picture taken with the stroboscope set at $3\omega_{II}/2$. Bottom picture shows the formation of second harmonics.

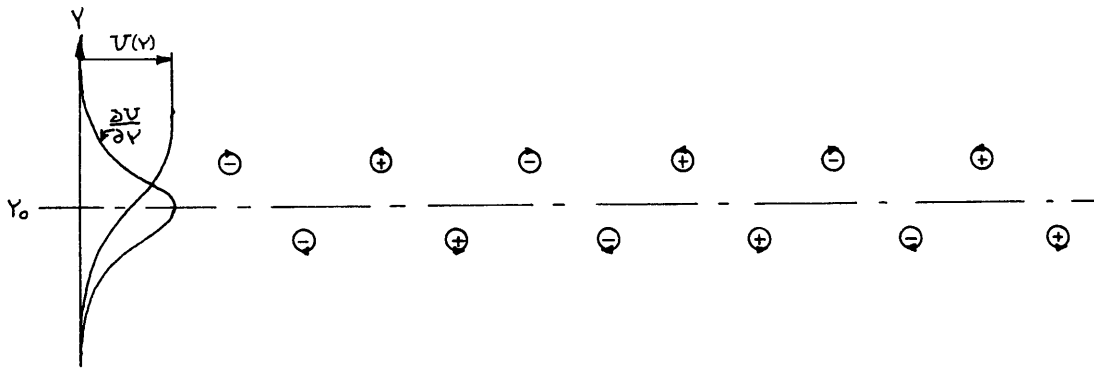


Figure 6.15 Possible finite amplitude vortex configuration prior to sub-harmonic generation.

This configuration has been discussed by Lighthill (1963) in conjunction with Blasius boundary layer instability. He notes that the velocity field induced by each disturbance augments the circulation of its neighbors; the induced velocity fields also augment the mean convective speed of each row so that they keep in relative step. Hence on its own right, it may be a possibly valid representation of the finite amplitude structure of the fundamental just prior to sub-harmonic generation.

In fact the vertical phase plots of the fundamental in figure from $x = 10.00$ to 12.00 cm show a phase structure qualitatively similar to that of Lighthill's model. Note how the characteristic dip in phase

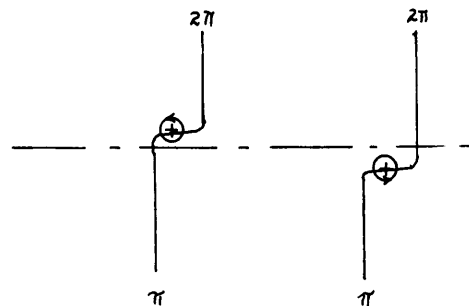
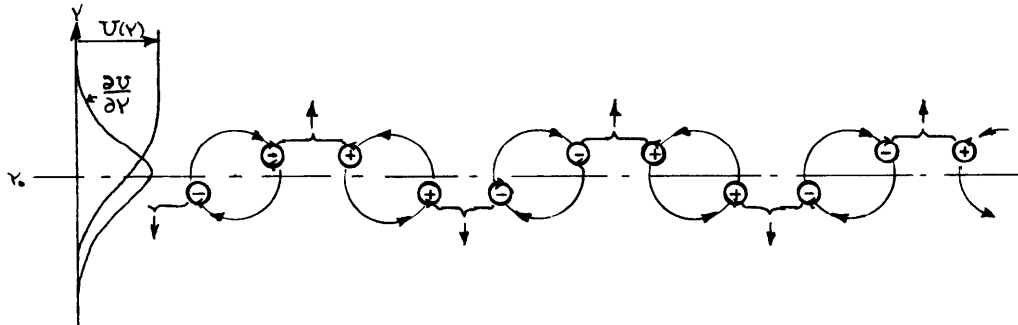


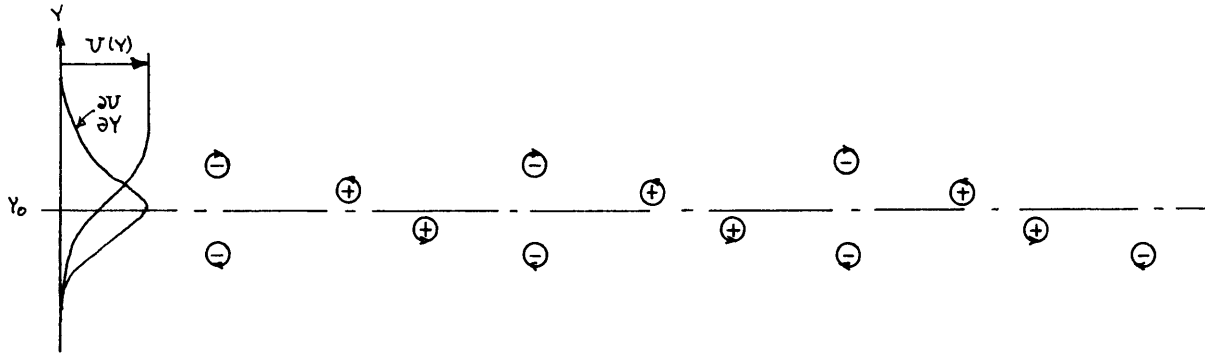
Figure 6.16 Alteration of phase angle distribution in vortex model.

alternates to either side of y_0 just as it does in the model above.

Using the arguments of Broward (1966), one can show that the sense of the restoring (or destabilizing) acceleration exerted on a displaced vortex will be given by the product of the signs of the disturbance circulation and the local mean vorticity gradient. (Note that the mean vorticity gradient changes sign at y_0 .) One can then show that the mean vorticity field will act to inhibit vortex slipping of like signed vortex pairs as arranged in this initial configuration. However, if the vortices are assumed to be subjected to some finite perturbations which displace each vortex towards and across the inflexion point, one can show (again using the same arguments) that the mean vorticity field will act to produce the following configuration. As indicated adjacent pairs of opposite signed vortices will tend to translate outward, (and hence cause wake spreading) while adjacent pairs of similar circulation will tend to induce a mutual rotation about a common axis.



A little consideration will show that the mean vorticity gradients will act to inhibit the mutual rotation of the positive vortex pairs while it will aid the rotation of the negative ones, at least until they reach the quasi-equilibrium position indicated below.



In this configuration the induced velocity fields of the \ominus vortices will tend to move the \oplus ones closer to the inflexion point, while the mean vorticity gradients will inhibit their crossing. Similarly, the \oplus vortices will tend to keep the \ominus vortices near their indicated positions. The mutual action of the induced disturbance velocity fields and the mean vorticity fields will probably act to cause slight oscillations about the indicated positions and hence cause some intermittency. This configuration would then show intermittent sub and $3/2$ -harmonics along the center line, as well as two smaller sub-harmonic contributions to either side. The r.m.s. velocity distributions suggested by this model

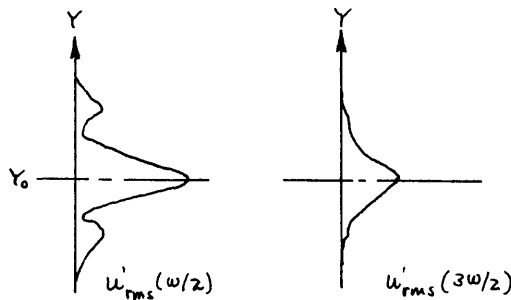


Figure 6.17: R.M.S. distributions predicted by vortex model after slipping has occurred.

are remarkably similar to the measured sub and 3/2-harmonics.

Of course this is a very crude model which is subject to many assumptions concerning the relative strength of the vortex slipping effects and mean vorticity field stabilization strength. However it does seem to account for many of the observed features of the sub-harmonic generation. Browand (1966) has also presented several vortex models for sub-harmonic generation. However the possibility of vortex slipping was not considered.

Similar arguments may also be used to give a physical explanation as to why sub-harmonic oscillations are not observed in symmetric, narrow jets and wakes. These flows have two inflexion points and hence two closely spaced vorticity peaks of opposite sign. In this situation the downward displaced unstable vortices of the upper row for example, will, upon traveling a very short distance, find themselves in the vorticity field of the lower layer. A little consideration will show that those vortices which are destabilized by the positive vorticity gradient in the lower part of the upper layer will receive a counteracting upward restoring force due to the negative gradients of vorticity in the upper portion of the lower layer. Similarly, unstable vortices of the lower layer will be retarded by the positive vorticity gradient in the lower portion of the upper layer. Hence a disturbance configuration conducive to vortex slipping will not be achieved.

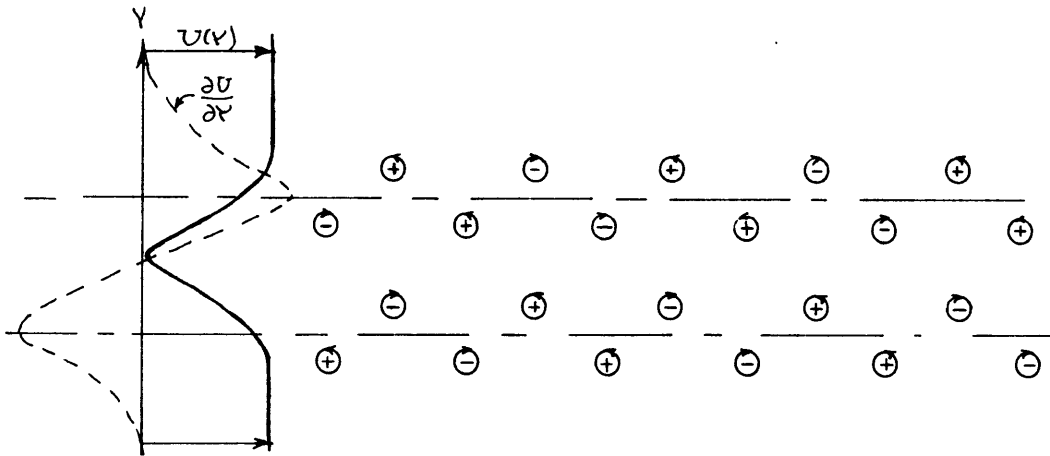


Figure 6.6 : Vortex model for symmetric jets and wakes. Note how the lower vorticity field of opposite sign stabilizes unstable vortices from the upper layer and hence inhibits the slipping of vortex pairs.

Region V: Onset of Three-Dimensional Behavior and the Termination of Fundamental Mode Equilibration. (3.2-4.75 λ_{II})

The fundamental mode equilibration zone terminated at about 3.2 wavelengths downstream. Three-dimensional distortions appeared at this point, and it appears that a new critical Reynolds number has been reached for the presence of yet another new type of instability. The Reynolds number at equilibration breakdown is of order 450.

This region marks the first point where strong periodic spanwise activity, as indicated by the spanwise phase measurements, appears. Earlier distortions of r.m.s. wavefront profiles were observed but they were not accompanied by periodic phase variations. Wavefront distortions alone do not imply periodicity, and it is felt that phase variations are the best indication of developing three-dimensional activity.

Slight spanwise phase distortions did appear near the onset of equilibration in region III. However, they were not periodic or extensive, and did not signify three-dimensional activity.

The onset of spanwise activity is accompanied by a noticeable decay of the fundamental mode energy along the $z = 0$ center plane. It is hard to tell whether this reduction is due to a spanwise transfer of energy. One curious feature is the apparent smoothing out of previous distortions in the r.m.s. wavefront. This smoothing may indicate that weak spanwise energy transfers may be occurring in such a manner that they act to fill in undesired distortions as a precursor for setting up a more preferred spanwise structure.

By $x = 17.50$ cm, significant spanwise distortions of both phase and r.m.s. wavefronts have been established and the structure of the phase plots indicates the development of a secondary flow consisting of several streamwise longitudinal vortices. The exact details of this secondary flow were not investigated but several features were evident. The cross-stream scale (i.e. diameter) of the vortices varied with spanwise location and tended to decrease with downstream distance. This decrease in scale was accompanied by an increase in three-dimensional activity. At $x = 15.00$ cm the spanwise wavelength varied between (2.5-3.0) cm, while at $x = 17.50$ cm, the characteristic wavelength had decreased to (1.2-2.0) cm. The major activity of the rolls was confined to a region near the critical layer of the fundamental mode. The vertical scale of the rolls was smaller than the lateral scale, the rolls being somewhat ellipsoidal in cross-section. The erratic nature of the fluctuations

in the final stages of breakdown precluded further downstream investigations of the secondary vortex structure.

These results are all in agreement with the Benney-Lin mechanism (1961) in which it was shown that a two- and three-dimensional disturbance can interact to reinforce spanwise distortions of the fundamental and subsequently generate a secondary longitudinal vortex structure. The theoretical spanwise wavelength of the vortex structure was found to vary from the wavelength of the fundamental mode for weak three-dimensional effects, to one half the fundamental wavelength when strong three-dimensional effects dominated the transition. As noted earlier, a similar reduction in wavelength was experimentally observed as three-dimensional activity increased.

Similar three-dimensional distortions have also been observed for symmetric jets and wakes in the final stages of transition. Symmetric wakes do not exhibit sub-harmonic oscillations and it seems unlikely that the onset of three-dimensionality in asymmetric wakes can be directly attributed to the presence of finite amplitude sub-harmonic oscillations.

This last stage of transition where three-dimensional distortions appear may be a necessary precursor for turbulence. Since turbulence is a three-dimensional phenomenon, it seems logical that the final instability just prior to turbulent breakdown will be one that can condition the flow for acceptance of strong three-dimensional motions. Viscous boundary layers, symmetric jets and wakes, and asymmetric jets and wakes all seem to exhibit some sort of three-dimensional vortex structure just prior to turbulent breakdown. The Benney-Lin mechanism, or some modifi-

cation of it, thus seems to play an important role in the breakdown of shear layers in general.

It is not clear if the cross-stream boundaries exert any spanwise constraints in this region. At best one could only hope to fit in two or three fundamental mode wavelengths in the cross-stream direction. This certainly is not a sufficient degree of freedom to eliminate boundary effects. I do not wish to pursue the question of spanwise boundary constraints further. However, it is a subject which must be explored in order to understand the representativeness of the three-dimensional mechanisms observed in this experiment.

One other notable feature of region V is an extremely strong, almost exponential decay of the third harmonic.

Region VI: Final Breakdown ($4.75-5.75 \lambda_{II}$)

After about five wavelengths of transition the disturbance spectrum abruptly spread into a broad band spectrum. Phase measurements showed that all synchronization with the upstream fundamental was lost. The flow is certainly three-dimensional and although oscilloscope traces indicated the presence of weak, intermittent, secondary instabilities at the upper edge of the shear layer, no evidence of high frequency bursts were found. The secondary instabilities seemed to generate frequencies in the range ω_{II} to $3\omega_{II}$ and may have been due to instantaneous mean flow distortions caused by the secondary vortex structure of region V.

As indicated in figure 5.48 the total disturbance energy starts to

increase in this region to levels above the apparent upper bounds present in regions III, IV and V where a discrete transition spectrum existed. This growth of total energy seems to coincide with an apparent second equilibration region for the sub-harmonic which has now become the dominant disturbance. The spectra plots indicate a grouping of energy near the sub-harmonic and this second equilibration may represent yet another step in Landau's successive instabilities concept. Here, the sub-harmonic seems to be playing the same role as the fundamental did in earlier regions.

It is not at all clear as to just what role three-dimensional effects play in the second sub-harmonic equilibration. However, it does appear that unlike the fundamental and sub-harmonic mode equilibration in region III, strong three-dimensional effects, probably due to the secondary vortex structure, are necessary for the second sub-harmonic equilibration. It is curious, and perhaps significant, that a slight indication of three-dimensionality also appeared just prior to region III equilibration. In that case the influence of three-dimensionality was not deemed important. It may however be an integral part of the equilibration mechanism and poses a question that should be investigated.

VI.2 Mixed Mode Transition

The mixed mode experiments were conducted mainly out of curiosity. However it was evident, even before actually running the experiments, that in addition to obtaining the usual phenomenological information on shear layer transition (as were taken for the ω_{II} transition) several

basic stability concepts could be tested independent of the particular details of the flow being studied.

In brief, the excitation of two growing fundamental modes allowed the following points to be investigated:

- (a) the validity of the linear superposition principle which asserts that component oscillations can exist independently of each other;
- (b) the importance of the generation of non-linear combination modes (due to the interaction of the fundamental modes) in the transition process;
- (c) the role which non-linear mode competition plays in the transition process.

A fourth, but initially unappreciated factor, is the role played by the relative phases of the excited disturbances in the transition. Perhaps by inertia and habit, a great deal of quantitative data was accumulated for the mixed mode transition. However, the points just mentioned were of greatest interest to the author, and are the only ones that will be discussed.

(a) Validity of the Linear Superposition Principle

The mixed transition experiment provided a classic example of the limits to which the linear concept of disturbance superposition can be extended. The ω_{fs1} and ω_{II} experiments established the behavior of the isolated transitions of the two respective fundamental modes. It was clear from the energy and r.m.s. plots that for infinitesimal amplitudes ω_A and ω_B grew in a manner identical to the growth of their single mode

counterparts, ω_{fs1} and ω_{II} . However, significant differences occurred when ω_A and ω_B reached respective finite amplitudes of 1 and 2%. At this point, the rate of growth of ω_A abruptly declined. In contrast, ω_B continued to grow at the same rate that its single mode counterpart had. Non-linear modes also appeared at this point.

Since the growth of ω_B does not deviate in any significant manner from that of ω_{II} , it appears that the amplitude of ω_B determines when superposition will break down. The breakdown of superposition is reflected in the alteration of the growth characteristics of ω_A and the appearance of non-linear modes. The 2% value for ω_B marks the upper limit to which the principle of superposition can be extended. As such, it can be taken as the best criterion for determining the extent to which linear theory can describe the mechanics of shear layer transition.

(b) Role of Non-Linear Combination Modes

In the mixed mode experiments, non-linear sum and difference combination modes appear along with the usual harmonic and sub-harmonic modes of each individual fundamental. The combination modes interact with the two fundamentals and the other non-linear modes and can extensively organize the transition spectra. As many as 25 different non-linear modes appear in the transition spectrum. Most of these modes were observed to initially grow at an exponential rate, and the dominant non-linear modes are tabulated in table 6.8 along with their initial exponential growth rates. Additional information is presented in the data of chapter V.

Table 6.8: Spatial growth rates of the dominant modes in the $(\omega_A + \omega_B)$ transition in regions I and II.

| <u>Mode</u> | <u>$-\alpha_i = -\alpha_i \cdot 2\theta_m(x_0)$</u> | <u>Mode</u> | <u>$-\alpha_i = -\alpha_i \cdot 2\theta_m(x_0)$</u> |
|-------------------------|--|-------------------------|--|
| ω_A | 0.144 | $\omega_B/2$ | 0.285 |
| ω_B | 0.198 | $\omega_A + \omega_B/2$ | 0.276 |
| $(\omega_B - \omega_A)$ | 0.246 | $3\omega_B/2$ | 0.109 |
| $(\omega_B + \omega_A)$ | 0.209 | $2\omega_B$ | 0.220 |

The mixed mode transition is obviously more complicated than the normal single mode transition. In many respects it may be more representative of a natural transition. In natural transitions many discrete disturbances are randomly introduced and trigger the grow of many fundamental modes which then proceed to interact among themselves just as ω_A and ω_B do.

As can be seen from figures 5.46 and 5.47a, the growth of ω_B energy is almost identical to the growth of ω_{II} energy. Also, as shown in figure 5.48, the total disturbance energy of the mixed transition is almost identical to that of the ω_{II} transition. It appears that the combination modes obtain their energy at the expense of ω_A and its non-linear modes, and not from ω_B . Also, since the total disturbance energy does not differ in any significant manner from the ω_{II} transition, the presence of combination modes induces a redistribution of energy among the disturbances and not an increase.

An interesting aspect of the mixed transition was the observation

that the generation of the $\omega_A/2$ sub-harmonic mode was suppressed in favor of the $(\omega_B - \omega_A)$ combination mode. In contrast, $\omega_B/2$ was not noticeably affected.

Combination modes are generated by the direct non-linear interaction of ω_A and ω_B . Since ω_A and ω_B have constant relative phase angles the sum and difference modes can be expected to be more sharply centered and less intermittent than the broad band sub-harmonics are. Resonance reinforcement mechanisms can be expected to be more efficient for the difference frequency $(\omega_B - \omega_A)$ than for the sub-harmonic modes. The broad band of disturbances that amplify in the $\omega_A/2$ sub-harmonic band overlap the $(\omega_B - \omega_A)$ frequency. The strong centering of $(\omega_B - \omega_A)$ apparently interferes with an efficient sub-harmonic reinforcement of $\omega_A/2$. In contrast, $\omega_B/2$ is much further away from the difference frequency and does not experience a competition for energy input.

(c) Mode Suppression Due to Non-Linear Effects

As the mixed mode transition proceeds downstream, an equilibration zone (similar to that observed for ω_{fs1} and ω_{II}) appears. It is here that the coupling between the two fundamental modes becomes apparent. The equilibration amplitude of ω_B is almost identical to that of ω_{II} , while ω_A equilibrates much earlier and at a much lower level than ω_{fs1} did. This result demonstrates the crucial role which the linear zone plays in establishing the initial conditions for the downstream non-linear regions. The most efficient organizer of upstream energy is the maximally unstable mode $\omega_{II} \approx \omega_B$, and it appears that as long as the flow is destabilized at this frequency, the overall character of the

non-linear regions of transition will be dominated by this mode. The other fundamentals, if present, seem to enter into the picture mainly through their interaction with the most unstable mode to generate combination modes and other higher order non-linear effects.

Stuart (1962) considered the mutual influence of two growing fundamentals on the equilibration process. The analysis resulted in two mutually coupled Landau equations, one for the amplitude A of ω_A and one for the amplitude of B of ω_B . Based on the work of Liu, these will be written in their spatial form.

$$\frac{d|A|^2}{dx} = 2|A|^2 \{-\alpha_i(\omega_A) + a_A|A|^2 + a_B|B|^2 + \dots \}$$

$$\frac{d|B|^2}{dx} = 2|B|^2 \{-\alpha_i(\omega_B) + b_B|B|^2 + b_A|A|^2 + \dots \}$$

where a_B and b_A represent the non-linear coupling between ω_A and ω_B .

Since the growth rates and equilibration amplitudes of ω_B and ω_{II} are almost identical, the equilibration of ω_B must be relatively insensitive to the presence of a second fundamental mode: It seems reasonable to assume that

$$b_B \gg b_A$$

and to a good approximation, the equilibration of ω_B is governed by the same mechanisms as the ω_{II} equilibration, the distortion of the mean flow by the ω_B fundamental and the subsequent modification of ω_B by the distorted mean flow.

However, it is evident that the equilibration of ω_A is extremely sensitive to the presence of ω_B . The influence of ω_B on the ω_A equilibration is expressed by a_B , where

$$a_B = \frac{\alpha_i(\omega_A) - a_A \cdot |A_e|^2}{|B_e|^2} \approx -\{168 + 17.3 a_A\}$$

If, as an exercise, the value of the second Landau coefficient for the ω_{fs1} transition is taken to be representative of a_A , the effect of ω_B on the equilibration of ω_A can be estimated as

$$a_B \approx -312 = 37.4 a_A$$

The non-linear coupling effects of ω_B on the equilibration of ω_A , are seen to be 40 times as great as the effects of ω_A on itself. Hence, even though the equilibration of ω_B is virtually unaffected by the presence of ω_A , the non-linear coupling between ω_A and ω_B acts to strongly suppress the growth of ω_A . This is an example of non-linear mode competition.

(d) Role of Disturbance Phase in Shear Layer Breakdown

As discussed in appendix A.3, the wavenumber and frequency characteristics of a disturbance are determined by the spatial and time variations of the disturbance phase $\theta(\underline{x}, t)$. The valid variations of $\theta(\underline{x}, t)$ (and hence α_r, β_r) are governed by the local dispersion relation of the flow*

*The term 'dispersion relation' is used in a very loose sense to describe the constraints of the mean flow field and boundary conditions on the allowable degrees of freedom the disturbance oscillations may have.

If we consider a flow with one or two amplifying fundamental mode disturbances

$$u_1(x) e^{i\theta_1(x,t)}, \quad u_2(x) e^{i\theta_2(x,t)}$$

then as these modes grow to finite amplitudes they will interact with and distort the mean flow field. The mean flow distortion is dependent on the particular disturbances which are present. Hence the local dispersion relation is sensitive to variations in θ_1 and θ_2 . Variations in phase and dispersion relations will be reflected as variations in the wavenumber and frequency of the disturbance field.

If θ_1 and θ_2 are assumed to be constant, then the transition will be dominated by two specific wavenumber and frequency pairs, the values of which are determined by θ_1 and θ_2 and the constant, local dispersion relation.

If, however, the phases θ_1 and θ_2 are allowed to vary on a random or intermittent basis, as is observed just prior to turbulent breakdown, then the local mean conditions, and hence the local dispersion relation will also vary on a random or intermittent basis. Variations in θ_1 and θ_2 will cause an observer to see variations in wavenumber and frequency. Variations in the dispersion relation will alter the wavenumber and frequency combinations which are instantaneously valid. The coupled variations in phases and dispersion relation will thus cause the appearance of a wide range of disturbance wavenumbers and frequencies. The introduction of only a few disturbances with random phases can thus cause a broad band filling in of the wavelength and frequency spectrums. The

presence of non-linear modes, whose phases are also sensitive to variations in the phases of the fundamental modes will further augment the chaotic nature of the disturbance spectrum.

Thus the intermittent or random behavior of just a few amplified disturbances can describe many facets of the abrupt transition to turbulence observed in shear layers.

As was seen in the ω_{II} , ω_{fs1} and $(\omega_A + \omega_B)$ transitions, the disturbance spectrum at turbulent breakdown is sensitive to the upstream initial conditions. The unstable normal modes of the linear region dominate the non-linear regions and persist in influence into the turbulent region. Turbulence is a statistical phenomenon and it would be interesting to conduct an experiment in which the phases θ_1 and θ_2 of the unstable upstream disturbances varied on a controlled basis according to some given statistical relation. Then the effects of the initial input statistics on the transition process and the final turbulent field could be investigated. Also, since turbulent Reynolds stresses only have meaning on a statistical basis, it may prove possible to isolate specific features of the turbulent Reynolds stress in the normally organized, and well studied, non-linear regions of transition. In this manner, Reynolds stress due to statistically excited disturbances could be compared to the organized Reynolds stress induced by a coherent single or multi-mode excitation field.

In either case, a controlled statistically excited experiment would give a more representative model of the natural behavior of an unstable system.

APPENDIX

A-1 Linear Trapezoidal Stability Model

Using a streamfunction $\psi(x, y, t) = \phi(y) e^{i\alpha(x-ct)}$

the Rayleigh equation for inviscid parallel flow can be written as

$$\phi''(y) - \alpha^2 \phi(y) = \frac{V''}{V-C} \phi(y) \quad (\text{A-1-1})$$

where primes indicate derivatives with respect to the y coordinate, and α is the x coordinate wavenumber.

Equation A-1-1 has the Greens function solution

$$G(y, \xi) = -\frac{1}{2\alpha} e^{-\alpha|y-\xi|} \quad (\text{A-1-2})$$

hence

$$\phi(y) = -\frac{1}{2\alpha} \int_{-\infty}^{\infty} \frac{V''(\xi)}{V(\xi)-C} e^{-\alpha|y-\xi|} \phi(\xi) d\xi \quad (\text{A-1-3})$$

where

$$\begin{aligned} \alpha &= \alpha_r + i\alpha_i \\ C &= C_r + iC_i \end{aligned} \quad (\text{A-1-4})$$

For a trapezoidal profile, $V''(\xi)$ is identically zero at all points except at the N points (a_i) where the straight line profiles intersect. Thus,

$$\phi(y) = -\sum_{i=1}^N \phi(a_i) \frac{e^{-\alpha|y-a_i|}}{2\alpha[U(a_i)-c]} \int_{y-a_i}^{y+a_i} U''(\xi) d\xi \quad (\text{A-1-5})$$

giving

$$\phi(y) = -\sum_{i=1}^N \phi(a_i) \frac{e^{-\alpha|y-a_i|}}{2\alpha[U(a_i)-c]} \{U'(y+a_i) - U'(y-a_i)\} \quad (\text{A-1-6})$$

The solution, by nature of the Greens' function, satisfies the necessary boundary conditions $\phi(\pm\infty) \rightarrow 0$. The importance of choosing the right mean velocity slope (i.e. vorticity) in fitting the trapezoidal model to the real profile is clearly evident from equation (A-1-6).

When evaluated at each of the (a_i) points, the above equation gives N equations in N unknowns and leads to the eigenvalue problem

$$[A_{ij} - \delta_{ij}c] \{\phi(a_i)\} = 0 \quad (\text{A-1-7})$$

where

$$A_{ij} = A_{ij}(\bar{\sigma}_{T,M,S}, L_{T,M,S}, \alpha_r, \alpha_i)$$

and can be solved for complex values of c and α . Since ψ can be written as

$$\begin{aligned} \psi(x,y,t) &= \phi(y) e^{i(\alpha_r + i\alpha_i)(x - c_r t - i c_i t)} \\ &= \phi(y) e^{i(\alpha_r x - \beta_r t)} \cdot e^{-(\alpha_i x - \beta_i t)} \end{aligned} \quad (\text{A-1-8})$$

where

$$\begin{aligned}\beta_r &= \alpha_r C_r - \alpha_i C_i \\ \beta_i &= -\alpha_r C_i - \alpha_i C_r\end{aligned}\tag{A-1-9}$$

and the valid spatially growing solutions are those for which $\beta_i = 0$, and α_i is negative. The solution for ($\alpha_i = 0, \beta_i > 0$) corresponds to the temporal problem.

A-2 Sound generation of vorticity perturbations

The mechanics by which sound waves generate perturbation fluctuations in a moving, non-uniform, sheared flow are not well understood. In the simplest case of a uniform stream at rest, the sound induced velocity field is irrotational. One would expect that the basic perturbation field for a sound excited, low Mach number flow would also be basically irrotational.

However, linear stability models show that valid perturbations are rotational and it is unlikely that a sound induced potential velocity field could directly trigger the actual flow instability. Rather a mechanism for the production of perturbation vorticity is needed.

If the total velocity field is expressed as a sum of an irrotational and rotational perturbation superposed on a sheared mean flow, then

$$\underline{u} = \underline{U} + \underline{u}'_I + \underline{u}'_R \quad (\text{A-2-1})$$

where

$$\begin{aligned} \underline{u}'_I &= \nabla \phi(x, t) \\ \underline{u}'_R &= \text{curl } \psi(x, t) \end{aligned} \quad (\text{A-2-2})$$

If the respective equations governing the potential and rotational components are separated from that of the mean motion, then it can be shown (Mollo-Christensen [1969]) that (1) the basic sound induced velocity field is irrotational, and (2) a mechanism does exist by which the irrotational perturbation field can interact with the mean vorticity to produce perturbation vorticity.

The first statement is evident from the equation for \mathbf{u}'_F which is basically the forced wave equation and can be expressed as*

$$\frac{\partial^2}{\partial t^2}(\nabla\phi) - a^2 \nabla^2(\nabla\phi) = C(x, \bar{\sigma}, \psi, \phi, P, \beta, S, T) \quad (\text{A-2-3})$$

The R.H.S. expresses the local generation and interaction mechanisms. For a far-field approximation, this reduces the retarded potential problem. If the effects of the R.H.S. are assumed small (see Mollo-Christensen) then it reduces to the equation for a potential perturbation field, and the sound waves will produce a basically irrotational perturbation field.

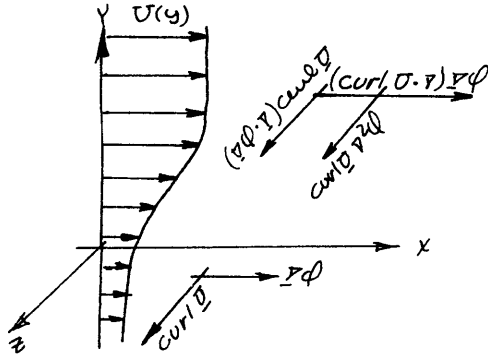
The equation for \mathbf{u}'_R expresses the production of perturbation vorticity in a sheared flow in which irrotational disturbances are present. For our purpose it can be expressed as

$$\begin{aligned} \left(\frac{\partial}{\partial t} + \bar{\sigma} \cdot \nabla \right) \nabla^2 \psi &= \left\{ (\nabla\phi \cdot \nabla) \text{curl } \bar{\sigma} + (\text{curl } \bar{\sigma} \cdot \nabla) \nabla\phi + \text{curl } \bar{\sigma} \nabla^2 \phi \right\} \\ &+ \left\{ \text{viscous terms} \right\} + \left\{ \psi, \nabla\phi \text{ interaction terms} \right\} \\ &+ \left\{ \psi, \text{curl } \bar{\sigma} \text{ interactions} \right\} + \left\{ \text{baroclinic terms} \right\} \end{aligned} \quad (\text{A-2-4})$$

It is apparent from the first term on the R.H.S. that sound generated potential field perturbations can interact with the mean shear (i.e. mean vorticity) to produce perturbation vorticity. If baroclinic effects are neglected, then this term provides the only mechanism by which disturbance vorticity can be produced by a potential perturbation field.

*See Mollo-Christensen (1969)

Considering the relative importance of the three components of the first term it can be shown that terms (i) and (iii) will generate spanwise vorticity perturbations

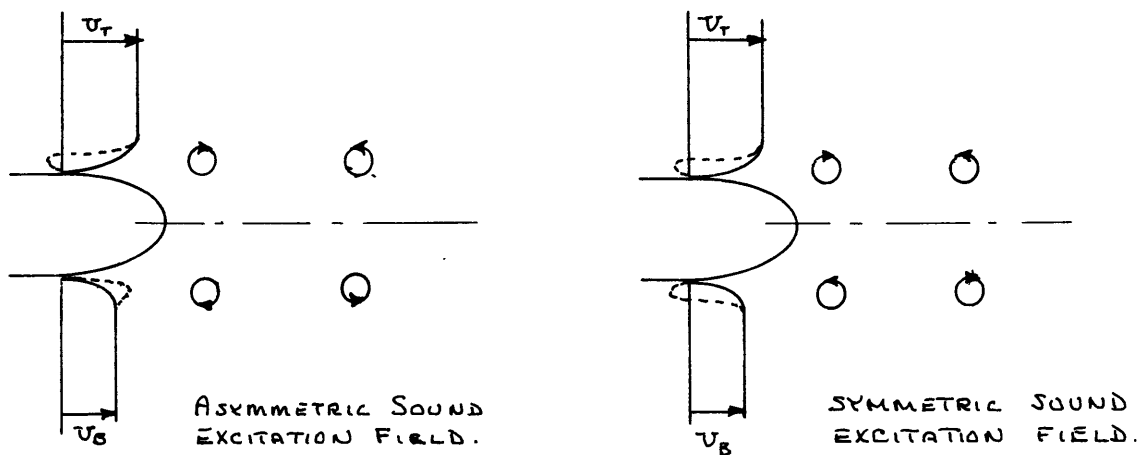


Since the largest values of $\text{curl } D$ and its derivatives exist near the edge of the splitter plate, one can expect this region to be the most efficient producer of perturbation vorticity. It is clear, however, that the interactions can occur throughout the mean shear field.

Physically, these three terms indicate that the potential fluctuations can act to instantaneously alter the mean velocity field. Thus the mean vorticity field is instantaneously altered, which in effect is a generation of perturbation vorticity.

The symmetry or asymmetry of the generated perturbation vorticity field will be dependent on the symmetry or asymmetry of the potential perturbation field and the character of the mean shear profile.

A physical explanation of how long wave sound perturbations can generate small scale vorticity perturbations can be illustrated by considering the effect of the sound pressure field on the velocity and pressure distributions at the splitter plate edge.



An asymmetric sound field will produce pressure fluctuations which alternatively shift the local pressure distribution from one side of the splitter plate edge to the other. The local boundary layers will be alternatively distorted by the shifted pressure distribution, so that perturbation vorticity of similar sign will be effectively generated at the same instant of time. These will then be swept downstream into the test section by the mean flow. The downstream length scale of the convected vorticity field will be determined by the ratio of the mean velocity to the forcing field frequency and

$$\lambda \sim O\left[\frac{U}{\omega}\right] = O[6 \text{ cm}]$$

for ω_{II} forcing if $U = U_T$. If the mean convective velocity is used and $U \sim (U_T + U_B)/2$, then $\lambda \doteq 4$ cm. In either case, the convective disturbance field will not be a simple sinusoid and will contain oscillations near the value of the actual ω_{II} wavelength. The flow can then pick out its preferred wavelength.

A symmetric sound field will induce the same instantaneous distortion on both sides of the stagnation point and will hence produce vorticity perturbations of opposite sign on both sides of the plate. This would then give a symmetric downstream perturbation field.

A-3 Wavelength, Phase Speed and Phase Angles

Although the actual disturbance measured by the hot wire probe is normally viewed as being a travelling wave with a local wavelength, phase speed and phase angle, the hot wire probe can only measure the amplitude of the wave and the frequency at which variations in amplitude sweep past it. Wavelengths, phase speed, phase angles, the instantaneous directional sense of fluctuation, and relative position in the fluctuation cycle must be inferred from a general phase function $\theta(\underline{x}, t)$. The phase function cannot be directly measured, but must be reconstructed from measurements of its space and time variations. The measurements are then referred to the behavior at a reference point in the flow in order to establish a consistent reference phase.

The probe senses the total local velocity component $u_N(\underline{x}, t)$ normal to the wire,

$$u_N(\underline{x}, t) = \bar{U}_N(\underline{x}) + u_N'(\underline{x}, t) \quad (\text{A-3-1})$$

and responds with an analog voltage signal of the form

$$e_w(\underline{x}, t) = E_w(\underline{x}) + \sqrt{2} e_{rms}'(\underline{x}) e^{i\theta(\underline{x}, t)} \quad (\text{A-3-2})$$

By the reduction schemes discussed in Appendix A.4 the fluctuating component of velocity can be constructed from the local values of the r.m.s wire voltage, and phase function,

$$u_N'(\underline{x}, t) = \sqrt{2} u_{rms}'(\underline{x}) e^{i\theta(\underline{x}, t)} \quad (\text{A-3-3})$$

The spatial variations of $u_{rms}(\underline{x})$ are normally measured separately as they are the easiest to obtain. Measurements of $\theta(\underline{x}, t)$ are more difficult. Since $\theta(\underline{x}, t)$ gives the behavior at one point in (\underline{x}, t) space relative to another, its variations can be measured relative to any convenient reference point or signal with no loss of information.

Variations of the phase $\theta(\underline{x}, t)$ in (\underline{x}, t) space can be expressed as

$$\theta(x,t) = \theta(x_r, t_r) + \bar{\alpha} \cdot (x - x_r) + \text{higher order spatial terms} + \theta_t (t - t_r) + \text{higher order temporal terms} \quad (\text{A-3-4})$$

If for simplicity the disturbance is assumed to be a constant frequency travelling wave, moving in the downstream direction at a constant speed, then the higher order temporal and x-coordinate terms $\rightarrow 0$, and the wave structure is determined by

$$\alpha = \frac{\partial \theta}{\partial x} = \text{downstream wave number} \quad (\text{A-3-5})$$

$$\beta = -\frac{\partial \theta}{\partial t} = \text{radian frequency}$$

$$\phi_2 = \left\{ \frac{\partial \theta}{\partial y} \cdot (y - y_r) + \frac{\partial^2 \theta}{\partial y^2} \cdot (y - y_r)^2 \text{ terms} \right\} = \text{vertical phase angle.}$$

$$\phi_3 = \left\{ \frac{\partial \theta}{\partial z} \cdot (z - z_r) + \frac{\partial^2 \theta}{\partial z^2} \cdot (z - z_r)^2 \text{ terms} \right\} = \text{spanwise phase angle.}$$

Based upon measurements giving the spatial and temporal variations of phase, the true disturbance wave form can be reconstructed

as

$$u(x,t) = \frac{1}{\sqrt{2}} u_{rms}(x) e^{i\{\alpha x - \beta t + \phi_2 + \phi_3\}} \quad (A-3-6)$$

where θ_r , λ_r and t_r can be taken as zero for convenience.

It is clear, for example, that if a periodic spanwise phase variation is observed, then the higher order z-coordinate derivatives of θ must approach zero. A shift in terminology would then be made, and the periodic spanwise structure would be defined by a **spanwise** wavenumber.

Variations of the spatial structure of $\theta(\underline{x}, t)$ are measured by a phase meter. As the probe is traversed through space, the meter will register the instantaneous difference in phase as sensed by two probes located at different spatial positions. The probes, and hence the meter, can only view disturbances in the time domain, and they see signals of the form

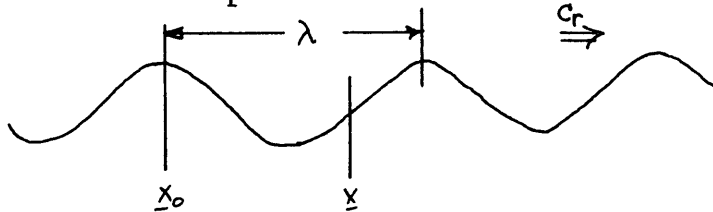
$$e^{i\{-\beta t + \text{phase variations due to the spatial structure of } \theta(\underline{x}, t)\}}$$

or equivalently

$$e^{i\{-\beta t + \Phi(x)\}} \quad (A-3-7)$$

Recourse to a simple model will demonstrate how only spatial variations in phase are measured by the phase meter. Temporal variations are of course measurable by a frequency counter.

Consider a sinusoidal travelling wave of downstream wavelength λ and phase speed c_r ,



Two probes stationed at $\underline{x}_0 = (x_0, y_0, z_0)$ and $\underline{x} = (x, y_0, z_0)$ will sense respective signals of the form *

$$\textcircled{\text{a}} \underline{x}_0 \quad e^{i\theta(\underline{x}_0, t)} = e^{i\{-\beta t + \Phi(\underline{x}_0)\}} = e^{i\{-\beta t + \alpha x_0 + \phi_2(\underline{x}_0) + \phi_3(\underline{x}_0)\}} \quad (\text{A-3-8})$$

$$\textcircled{\text{a}} \underline{x} \quad e^{i\theta(\underline{x}, t)} = e^{i\{-\beta t + \Phi(\underline{x})\}} = e^{i\{-\beta t + \alpha x + \phi_2(\underline{x}) + \phi_3(\underline{x})\}}$$

These two signals are the inputs to the phase meter which in turn responds with an analog output proportional to the phase difference

$$\Delta\theta = \theta(\underline{x}, t) - \theta(\underline{x}_0, t) = \Phi(\underline{x}) - \Phi(\underline{x}_0) \quad (\text{A-3-9})$$

Since $\phi_2(\underline{x}) - \phi_2(\underline{x}_0) = 0$, if $y = y_0$, and $\phi_3(\underline{x}) - \phi_3(\underline{x}_0) = 0$ if $z = z_0$, then if an x-coordinate traverse is made

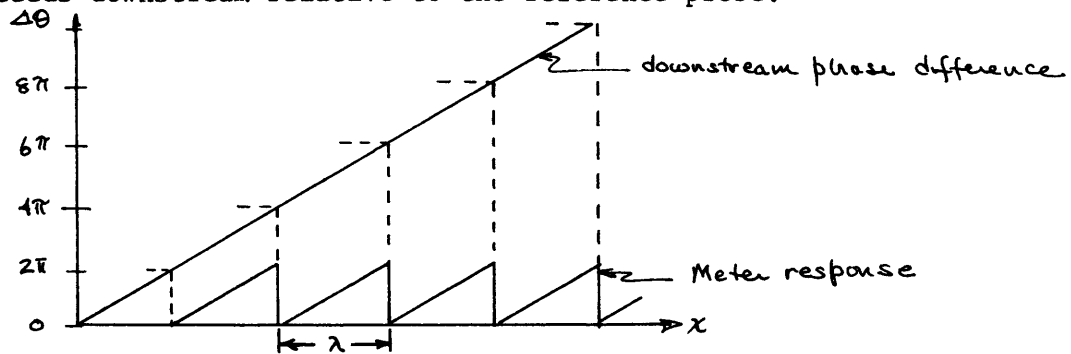
$$\Delta\theta = \alpha(x - x_0)$$

Thus, as far as the phase meter output is concerned, all time dependence has been eliminated. Only the relative phase angle differences, due to spatial variations in $\theta(\underline{x}, t)$ are recorded. Physically, this is equivalent to riding with the phase speed of the wave.

* The meter operation is independent of the amplitude of the disturbances and only unit amplitude signals will be considered.

Hence, an effective Galilean transformation has been made, and the flow stream lines are now steady. In a sheared flow, this will give the Kelvin's cats eyes, discussed in section (5.5b).

The meter response goes from $0 \rightarrow 2\pi$ and back to zero as $\bar{\Phi}(\underline{x}) - \bar{\Phi}(\underline{x}_0)$ increases from $2\pi n$ to $2\pi(n+1)$ etc. Hence the meter output has the following form as the measuring probe proceeds downstream relative to the reference probe.



The distance between zeros corresponds to

$$\Delta\theta = 2\pi = \alpha(x-x_0)$$

or

$$(x-x_0) = \frac{2\pi}{\alpha} = \lambda$$

and hence gives wavelength increments.

Similar arguments will show that if phase angle variations exist along the vertical or spanwise coordinates, then (x_0, y, z_0) traverses will give the vertical phase angle variations

$$\theta(x_0, y, z_0, t) - \theta(x_0, y_0, z_0, t) = \phi_2(x_0, y, z_0) - \phi_2(x_0, y_0, z_0)$$

and (x_0, y_0, z) traverses will give the spanwise phase angle variations

$$\theta(x_0, y_0, z, t) - \theta(x_0, y_0, z_0, t) = \phi_3(x_0, y_0, z) - \phi_3(x_0, y_0, z_0)$$

Of course, real unstably growing wave trains are not simple sinusoidal travelling waves. Non-linear effects can alter the local dispersion relations and hence the wavelengths and phase speed. Experimentally, however, only errors due to wavelength variations can be detected since the input signals to the meter are filtered in the time domain so that $\beta = \text{constant}$.

The hot wire probe and associated measuring circuitry can not distinguish between a linear wave train and a non-linear one. It can not be programmed to follow a given wave train as it passes through space and perhaps changes its wavelength and frequency due to local or non-linear effects. The circuitry can only make a Fourier decomposition of the local signal in the analog time domain and then map out the spatial phase behavior of a given frequency. It can not tell whether a wave that earlier had a given local frequency and wavelength has now had its frequency and wavelength altered and hence appears to the probe as a different frequency and hence a new wave. Thus the behavior of a given frequency, as it evolves in the laboratory frame may be an actual composite behavior of many waves whose frequency and wave numbers are altered according to their local dispersion relation and interaction with the mean flow and other disturbances.

A-4 Hot-Wire Calibration

Considerable attention has been paid to the calibration, and operating characteristics of hot-wire anemometers. Excellent discussions have been given by Corrsin (1963), Hinze (1959), and Collis and Williams (1959). The basic result is that the response of a heated cylindrical wire in a mean flow of a sufficient velocity to insure forced convection heat transfer, is given by:

$$\frac{I^2 R_w}{R_w - R_c} = A + B U_w^n \quad (A-4-1)$$

where: U_w is the total velocity normal to the wire, and A, B, and n, are calibration constants determined by the physical characteristics of the wire and the medium in which it is operating. R_c and R_w are the cold and operating resistances of the wire and $(R_w/R_w - R_c)$ is usually referred to as the hot-wire overheat ratio. I is the operation hot-wire current.

The response equation can be linearized for small velocity fluctuations, and separated into equations governing the mean and fluctuating components of velocity.

$$U(x) = \left[\left\{ \frac{I R_w}{R_w - R_c} - A \right\} \frac{1}{B} \right]^{\frac{1}{n}} \quad (A-4-2)$$

$$u'(x,t) = \frac{e'(x,t)}{\left\{ \frac{(R_w - R_c)^2 \cdot n \cdot B U^{(1-n)}}{I R_c} \right\}} \quad (A-4-3)$$

where $E_w = E_w + e'$ is the sensor voltage, and $U_N = U + u'$ are the mean and fluctuating velocity components. The work of Roshko (1954) on the shedding frequency of a cylinder in a mean flow was used to determine A and B. As given by Roshko:

$$f_{\text{SHEDDING}} = \frac{1}{d} \left\{ 0.212 U_N - \frac{4.5D}{d} \right\} \quad 50 < Re < 300 \quad (\text{A-4-4})$$

where the Reynolds number is based on the cylinder diameter "d".

The calibration procedure consisted of inserting a cylinder of known diameter in the free stream flow. The hot-wire probe was then positioned behind the rod and the eddy shedding frequency was monitored by a digital counter. Roshko's relation was then used to compute U_N . The rod was withdrawn and the true current and operating and cold resistances of the wire were measured for the given mean velocity. By varying the tunnel velocity over a wide range, a series of calibration points were obtained. These were then fitted to equation A-4-1 by a least squares fit, where "n" was taken to be 0.45 as suggested by Collis and Williams. The fitted curve was extrapolated for velocities lower than 20 cm/sec.

For computational analysis, the response equations A-1-1 and A-1-2 were rewritten in terms of the measured variables (i.e. voltage, current, and cold wire resistance).

$$U(x) = \left[\left\{ \frac{E_w(x) \cdot I(x)^2}{E_w(x) - I(x) \cdot R_c} - A \right\} \frac{1}{B} \right]^{\frac{1}{n}} \quad (\text{A-4-5})$$

$$w'(\underline{x}) = \frac{e'(\underline{x})}{\left\{ \frac{(E_w(\underline{x}) - I(\underline{x}) \cdot R_c)^2 \cdot B \cdot n}{I(\underline{x})^3 \cdot R_c \cdot U(\underline{x})^{(1-n)}} \right\}} \quad (\text{A-4-6})$$

or

$$w'(\underline{x}) = \frac{e'(\underline{x})}{FS(\underline{x})} \quad (\text{A-4-7})$$

If A, B, n, and R_c , are known, then the mean velocity and fluctuation sensitivity $FS(x_i)$, can be computed from a knowledge of the mean hot-wire voltage, $E_w(x_i)$ and current, $I(x_i)$ at each point in space.

Bibliography

- Abernathy, F.H. and Kronauer, R.E. 1962 The formation of vortex sheets. J. Fluid Mech. 13, 1.
- Bendat, J.S. and Piersol, A.G. 1966 Measurement and Analysis of Random Data. John Wiley and Sons.
- Benney, D.J. and Lin, C.C. 1960 On the secondary motion induced by oscillations in shear flow. Phys. Fluids. 3, 656.
- Benney, D.J. 1961 A non-linear theory for oscillations in a parallel flow. J. Fluid Mech. 10, 209.
- Betchov, R. and Criminale, W.O. 1967 Stability of Parallel Flows. Academic Press.
- Betchov, R. and Szewczyk, A. 1963 Stability of a shear layer between parallel streams. Phys. Fluids. 6, 1391.
- Bradshaw, P. 1966 The effect of initial conditions on the development of a free shear layer. J. Fluid Mech. 26, 225.
- Browand, F.K. 1966 An experimental investigation of the instability of an incompressible separated shear layer. J. Fluid Mech. 26, 281.
- Coles, D. 1965 Transition in circular Couette flow. J. Fluid Mech. 21, 385.
- Collis, D.C. and Williams, M.J. 1959 Two dimensional convection from heated wires at low Reynolds' numbers. J. Fluid Mech. 6, 357.
- Corrsin, S. 1963 Turbulence: Experimental methods. Handbuch der Physik, VIII/2. S. Flugge and C. Truesdell. Springer-Verlag.
- Davey, A. 1962 The growth of Taylor vortices in flow between rotating cylinders. J. Fluid Mech. 14, 336.
- Drazin, P.G. and Howard, L.N. 1962 The instability to long waves of unbounded parallel inviscid flow. J. Fluid Mech. 14, 257.
- Esch, R.E. 1957 The instability of a shear layer between two parallel streams. J. Fluid Mech. 3, 289.

- Fjortoft, R. 1950 Applications of integral theorems in deriving criteria of stability of laminar flow and for the baroclinic circular vortex. Geofys. Publ. 17, 1.
- Freythuth, P. 1966 On transition in a separated laminar boundary layer. J. Fluid Mech. 25, 683.
- Gaster, M. 1962 A note on the relation between temporally increasing and spatially increasing disturbances in hydrodynamic stability. J. Fluid Mech. 14, 222.
- Gaster, M. 1965 The role of spatially growing waves in the theory of hydrodynamic stability. Prog. Aeron. Sci. 6, 251.
- Helmholtz, H. 1868 On discontinuous movements of fluids. Phil Mag. 4, 337.
- Hinze, J.O. 1959 Turbulence. McGraw Hill Book Company.
- Howard, L.N. 1964 The number of unstable modes in hydrodynamic stability problems. Journal de Mecanique. 4, 433.
- Howard, L.N. and Drazin, P.G. 1965 Hydrodynamic stability of parallel flow of inviscid fluid. Advances in Applied Mechanics. Academic Press.
- Kelly, R.E. 1965 The stability of an unsteady Kelvin-Helmholtz flow. J. Fluid Mech. 22, 547.
- Kelly, R.E. 1967 On the stability of an inviscid shear layer which is periodic in space and time. J. Fluid Mech. 27, 657.
- Kelvin, W. 1871 The influence of wind on waves in water supposed frictionless. Phil. Mag. 4, 368.
- Klebanoff, P.S., Tidstrom, K.D. and Sargent, L.M. 1962 The three-dimensional nature of boundary layer instability. J. Fluid Mech. 12, 1.
- Ko, D.R.S., Kubota, T. and Lees, L. 1969 Finite disturbance effect on the stability of a laminar incompressible wake behind a flat plate. Hypersonic Research Project, Memorandum No. 72. Grad. Aero Labs, California Institute of Technology.
- Lanchon, H. and Eckhaus, W. 1964 Sur l'analyse de la stabilite des e conlements faiblement divergents. J. Mecan. 3, 445.

- Landau, L.D. 1944 On the problem of turbulence. C.R. (Doklady) Acad. Sci. U.R.S.S. 44, 311.
- Lessen, M. and Fox, J.A. The stability of boundary layer type flows with infinite boundary conditions. Fifty Years of Boundary Layer Research. Vieweg, Braunschweig.
- Lin, C.C. 1955 The Theory of Hydrodynamic Stability. University Press.
- Lin, C.C. and Benney, D.J. 1964 On the instability of shear flows and their transition to turbulence. Proc. XI Intern. Congr. of Appl. Mech., Munich, 1964. 797.
- Liu, J.T.C. 1969 Finite-amplitude instability of the compressible laminar wake. Weakly nonlinear theory. Phys. Fluids. 12, 1763.
- Lorenz, E.N. 1969 How much better can weather prediction become. Technology Review, 71, 31.
- Mattingly, G.E. 1968 The stability of a two-dimensional incompressible wake. Ph.D. thesis, Princeton University.
- Michalke, A. 1964 On the inviscid instability of the hyperbolic tangent velocity profile. J. Fluid Mech. 19, 543.
- Michalke, A. 1965 On spatially growing disturbances in an inviscid shear layer. J. Fluid Mech. 22, 371.
- Mollo-Christensen, E. 1969 Lecture notes on jet noise. M.I.T.
- Orr, W.M.'F. 1907 The stability or instability of the steady motions of a perfect liquid and of a viscous liquid. Proc. Roy. Irish Acad. 27A, 9.
- Rayleigh, J.W.S. 1878-1919 Scientific Papers, Cambridge, University Press.
- Reynolds, O. 1883 An experimental investigation of the circumstances which determine whether the motion of water shall be direct or sinusoidal, and the law of resistance in parallel channels. Scientific Papers, 2, 51, Cambridge, University Press.
- Roshko, A. 1954 On the development of turbulent wakes from vortex streets. NACATR 1191.

- Sato, H. 1956 Experimental investigation on the transition of laminar separated layer. J. Phys. Soc, Japan. 11, 702.
- Sato, H. 1959 Further investigation on the transition of two-dimensional separated layer at subsonic speeds. J. Physical Soc. Japan. 14, 1797.
- Sato, H. 1960 Transition of a two-dimensional jet. J. Fluid Mech. 7, 53.
- Sato, H. and Kuriki, K. 1961 The mechanism of transition in the wake of a their flat plate placed parallel to a uniform stream. J. Fluid Mech. 11, 321.
- Sato, H. and Okada, O. 1966 The stability and transition of an axisymmetric wake. J. Fluid Mech. 26, 237.
- Schade, H. 1964 Contribution to the nonlinear stability theory of inviscid shear layers. Phys. Fluids. 7, 623.
- Schubaner, G.B. and Skramstad, H.K. 1943 Laminar boundary layer oscillations and transition on a flat plate. NACA Tech. Dept. No. 909.
- Sommerfeld, A. 1908 Proc. Fourth Intern. Cong. Mathematicians, Rome, 116.
- Starr, V.P. 1968 Physics of Negative Viscosity. McGraw-Hill Book Co.
- Stuart, J.T. 1958 On the non-linear mechanics of hydrodynamic stability. J. Fluid Mech. 4, 1.
- Stuart, J.T. 1960a On the non-linear mechanics of wave disturbances instable and unstable parallel flows, I. The basic behavior in plane Poiseuille flow. J. Fluid Mech. 9, 353.
- Stuart, J.T. 1960b On three dimensional non-linear effects in the stability of parallel flows. Adv. Aero Sciences. 3, 121.
- Stuart, J.T. 1962 Non-linear effects in hydrodynamic stability. Proc. Tenth Intern. Congr. Appl. Mech. Elsevier, Amsterdam.
- Stuart, J.T. 1967 On finite amplitude oscillations in laminar mixing layers. J. Fluid Mech. 29, 417.
- Taylor, G.I. 1923 Stability of a viscous liquid contained between two rotating cylinders. Phil. Trans., A. 223, 289.

- Taylor, G.I. 1915 Eddy motion in the atmosphere. Phil. Trans. Roy. Soc., A. 215, 1.
- Tollmien, W. 1929 Vber die entstehung der turblinz, Gesellschaft der Wissenschaften, Gottingen, Mathematisch, Naturwissenschaftlicher Klasse, Nachrichten, 21.
- Tollmien, W. 1935 Ein allgemeines Kriterium der instabilitat laminarer geschwin dig keitsverteil ungen, translated 1936. Nat. Adv. Comm. Aero. Technology Memo, No. 792.
- Watson, J. 1960 On spatially-growing finite disturbances in plane Poiseuille flow, II. The development of a solution for plane Poiseuille flow and for plane Couette flow. J. Fluid Mech. 9, 371.
- Wille, R. 1963 Growth of velocity fluctuations leading to turbulence in free shear flow, AFOSAR Tech. Rept. Contract AF 61(052)-412, Hermann-Fottinger, Inst TU Berlin.

DEDICATION

To my brother Steven Charles Miksad TM3 and his fellow crewmen of the USS Scorpion (SSN-589). Their love of the ocean knew no bounds, and their stay within its depths will know no end.

Acknowledgement

I would like to express my gratitude to the many persons who have made my stay at M.I.T. an enlightening and rewarding experience. I would especially like to thank Professor Erik Mollo-Christensen whose incisive perspectives always served to bring order to what often appeared to be insurmountable experimental chaos. A special note of thanks is extended to Professor Henry Houghton. It has been a pleasure to know him both as a scientist and as a person.

I am also very grateful to the National Science Foundation who supported my research work.

Biographical Sketch

The author was born on August 24, 1940 in Trenton, New Jersey. He attended the elementary school system of Yonkers, New York and graduated from Saunders Trade and Technical High School. His undergraduate education was in mechanical engineering and he received the degree of B.S.M.E. from Bradley University in 1963. He attended the graduate school of Cornell University under a Sloan Foundation Fellowship and received the M.S. degree in 1964. His master's thesis was concerned with the idiosyncrosics of thermionic plasma diodes. The following summer was spent designing second stage propulsion units for Polaris missiles. The Ford Foundation then funded a year's stay with the direct energy conversion group at the University of Pennsylvania. During this stay the author met Professor Kenneth Wiskind who was instrumental in introducing the author to the field of oceanography. A succeeding summer of sailing and several awe-inspiring Caribbean storms convinced the author that his intrigue with the ocean was one he wished to pursue further. To the end he enrolled in the Department of Meteorology at M.I.T. in the fall of 1965.